SPACE DIVISION

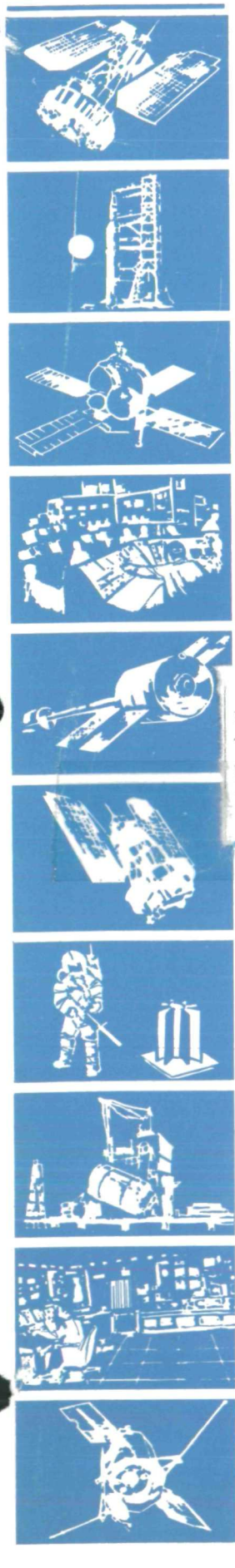

NASA CR-112212
MARCH, 1973

DEVELOPMENT OF A BREADBOARD MODEL CORRELATION INTERFEROMETER FOR THE CARBON MONOXIDE POLLUTION EXPERIMENT

GENERAL ELECTRIC

NASA CR-112212
MARCH, 1973

DEVELOPMENT OF A BREADBOARD MODEL CORRELATION INTERFEROMETER FOR THE CARBON MONOXIDE POLLUTION EXPERIMENT

PREPARED FOR

NASA/LANGLEY RESEARCH CENTER

UNDER CONTRACT NAS1-10139

BY

M.H. BORTNER
R. DICK*
H.W. GOLDSTEIN
R.N. GRENDA
G.M. LEVY*

* BARRINGER RESEARCH LIMITED

SPACE DIVISION
Valley Forge Space Center
P. O. Box 8555 • Philadelphia, Penna. 19101

GENERAL ELECTRIC

ABSTRACT

The breadboard model of the correlation interferometer for the Carbon Monoxide Pollution Experiment has been designed, fabricated, and tested. Laboratory, long-path, and atmospheric tests which were performed show the technique to be a feasible method for obtaining a global carbon monoxide map and a vertical carbon monoxide profile and that similar information is readily obtainable for methane as well. In addition, the technique is readily applicable to other trace gases by minor instrumental changes. As shown by the results of Section 7 and the conclusions of Section 8, it has been determined that CO and CH_4 data can be obtained with an accuracy of 10% using this technique on the spectral region around 2.3μ.

FOREWORD

This report was prepared for NASA as part of contract NAS1-10139 with Langley Research Center under the Advanced Applications Flight Experiments (AAFE) Program. The objective of this contract is the development of the Carbon Monoxide Pollution Experiment ("COPE"). This experiment is designed to obtain data for the investigation of mechanisms by which CO is removed from the earth's atmosphere. The approach uses an orbiting platform to remotely map global CO concentrations and determine vertical CO profiles using a correlation interferometer measurement technique being developed by Barringer Research Ltd. The instrument is to be capable of measuring CO over the range 0.02 to 20 atm.-cm. and of measuring other trace atmospheric constituents.

This report covers one aspect of the study -the breadboard instrument, its design, fabrication, and testing. A previous report (ref. 1) was concerned with an analysis of the feasibility of the experiment. In the future, the design, fabrication and testing of the engineering model, currently under test, will be reported. Results described herein are for measurements of carbon monoxide and methane. The technique is, of course, suitable for the measurement of other atmospheric trace species, and such applications are currently under study.

ACKNOWLEDGEMENT

The authors would like to express their appreciation to several co-workers who have contributed significantly to the work described herein and to related work - specifically, to G. R. Liebling who participated significantly in the treatment of the data; to A. E. Kraft who assisted with the GE multiple chamber tests; to W. Rohrbach and L. Mayo of NASA/LRC who assisted with the tunnel tests; to J. C. Burns who made numerous helpful suggestions and reviewed much of the work; to M. Jarrett of NASA/LRC who assisted with the computer treatment of the tunnel data; and R. H. Kummler who contributed many valuable suggestions in his consultation throughout the work.

The support of NASA and the cooperation of P. J. LeBel, NASA/LRC Technical Project Manager on the "COPE" program, are much appreciated.

TABLE OF CONTENTS

LIST OF CONTENTS (Cont)

LIST OF ILLUSTRATIONS

LIST OF ILLUSTRATIONS (Cont)

LIST OF TABLES

LIST OF TABLES (Cont)

LIST OF TABLES (Cont)

LIST OF TABLES (Cont)

1. INTRODUCTION

The Carbon Monoxide Pollution Experiment (COPE) is designed to obtain the global carbon monoxide concentration map and the vertical carbon monoxide concentration profile by use of the correlation interferometer mounted on board a satellite orbiting the earth at altitudes above most of the earth's atmosphere. Within this objective, a major goal is the development of the correlation interferometer instrument for quantitative measurement of carbon monoxide, and other trace constituents in the atmosphere. This report presents the details of the design, construction, and testing of the breadboard correlation interferometer. An interpretation of the results obtained with this instrument is given in Section 8 of this report. Previous reports have discussed the atmospheric CO problem (ref. 2)* and the feasibility of the experiment (ref. 1).

The specific objectives of this phase of the program (phase two) were, by building and testing a breadboard interferometer, to establish the feasibility of the method, to gain operational experience and experimental data on the interferograms of the gases of interest and to obtain inputs for the design of an engineering model. These objectives imply that the breadboard has provision for independently varying several of its parameters, so that the effects of these parameters could be investigated. This means that the breadboard instrument is more complex than later versions, in which these parameters will have optimum, fixed, values selected on the basis of experience with the breadboard. One such parameter was the wavelength. The breadboard was built for operation at both 2.35 micron (first overtone of CO) and at 4.6 micron (fundamental of CO). Based on the results obtained and presented in this report and on the analytical results previously presented (ref. 1), the 2.35 micron band was chosen for the engineering model.

The experiments described were designed to determine the feasibility of using a correlation interferometer to identify the expected CO sink by testing the breadboard instrument developed on this program. The two potential types of sinks are the upper atmospheric sink and the ground level sink to be looked for by the limb experiment and the mapping experiment, respectively. The limb experiment requires an ultimate sensitivity which will permit the locating of the sink at altitudes in the 20 to 40 km range where the optical thicknesses will be of the order of 1 and 0.1 atm. -cm., respectively. Thus the tests should cover the range from 1 to something less than 0.1 atm. -cm., a reasonable lower limit being 0.02 atm. -cm. The limits imposed by the mapping experiment are somewhat more stringent. The ground level sinks considered cause changes of optical thickness which require that a decrease of the order of 10% be detectable. This corresponds to our 0-3 km sink model and means that the instrument must be sensitive to a change of this magnitude in relative signals. However, the absolute limit of sensitivity should be such that a column density of 0.02 atm. -cm. (1/10 that of the nominal unpolluted atmosphere) is measurable.

*See Appendix D for references.

The experiments were planned to test the ability of the breadboard model correlation interferometer to measure carbon monoxide in its optical line of sight to levels as low as those associated with a surface sink region (i.e., 0.02 atm. -cm.). Since the capability of making these CO measurements with sufficient accuracy in the presence of atmospheric constituent gases which interfere spectrally with CO is the primary question to be answered, the tests must set up realistic combinations of carbon monoxide and and interferent gases over as wide a range of conditions as is practical.

The first series of tests were designed to verify the instrument operation in the laboratory using the General Electric multiple chamber system. In this facility the carbon monoxide and selected interferent gases can be introduced into the optical line of sight of the instrument in known quantities, and the effects of gas temperature and pressure on the measurements can be studied. The limitation of these tests is that not all of the atmospheric constituent gases can be introduced into the chambers in sufficient quantities to approximate atmospheric amounts. Water vapor is a major interferent whose effect can not be simulated in these laboratory tests.

However, the laboratory tests provided a first check on the instrument operation at the minimum CO level which one wishes to detect. The laboratory tests were carried out using the 2.3 micron overtone band and using the 4.6 micron fundamental band.

The second phase of the tests was a series of outdoor measurements with the instrument looking through an actual atmospheric path at sunlight. These outdoor tests indicated the sensitivity of the correlation instrument measurement of CO over a range of atmospheric parameters which were covered in this test period. However, these tests did not permit the instrument response to be evaluated over the full range of atmospheric parameters to be encountered on a long term seasonal and latitudinal basis. The outdoor tests were carried out using the 2.3 micron overtone band.

The third phase of the tests was a series of measurements with the instrument looking through a 430-foot tunnel at NASA/LRC. The composition of the gas in the tunnel, including an appreciable amount of water, was controlled.

2. PRINCIPLES OF OPERATION

The instrument being developed for the COPE program is a heterodyned refractively scanned field-widened correlation interferometer (refs. 3, 4, 5).

2.1 Interferometer

2.1.1 Concept. - The basic operation of an interferometer is illustrated in Figure 2.1.1. Radiation entering the field stop F is collimated before passing to the beamsplitter B, which divides the amplitude to give two beams which traverse the arms of the interferometer and return to the beamsplitter after reflection in the mirrors M1, M2. Depending on the difference in travel time for the two arms, the recombining beams will interfere constructively or destructively. Thus, if the delay is varied, then the intensity of radiation, at wavenumber σ, seen by the detector D will vary cosinusoidally about a mean value, as shown in the figure.

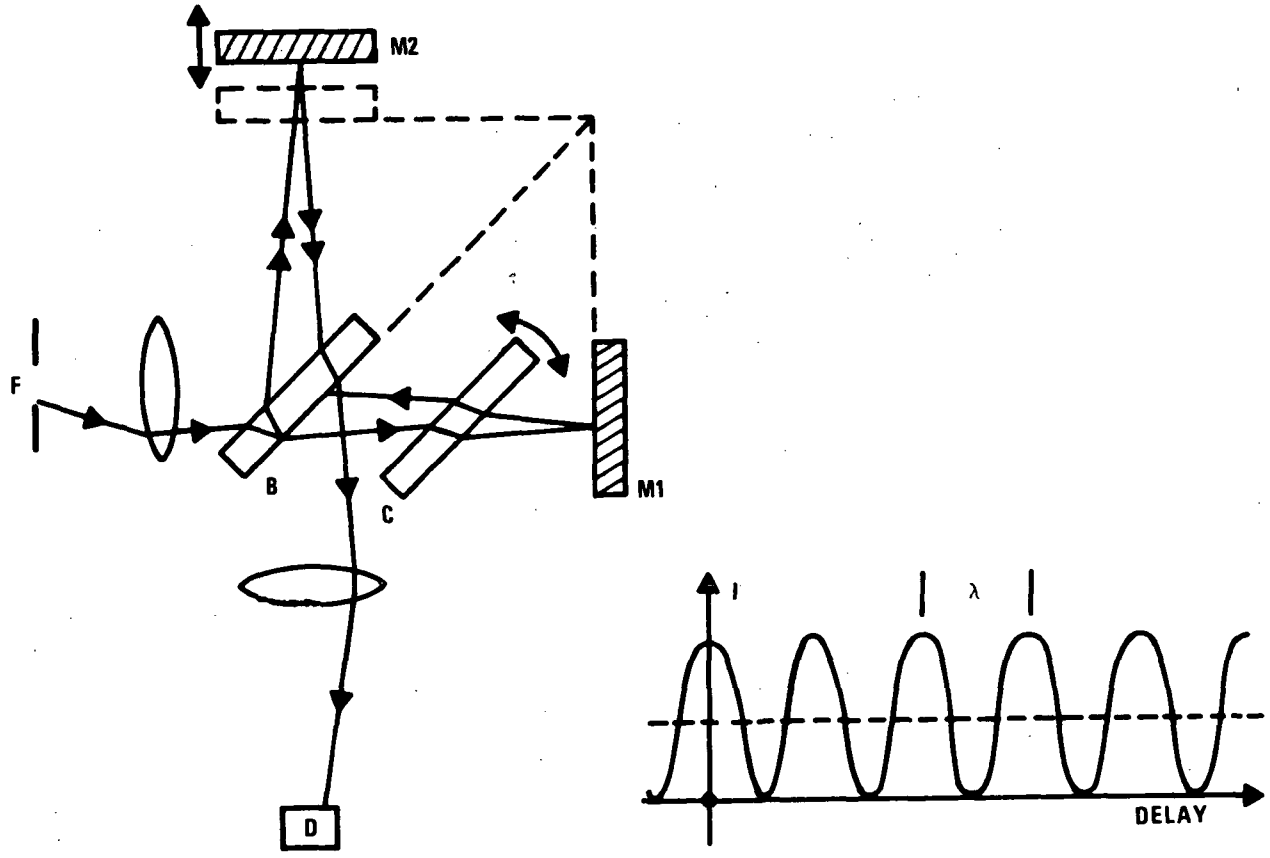

Figure 2.1.1. Interferometer

If radiation having an extended spectrum $\beta(\sigma)$ is input then the detector sees the interferogram

$$I(x) = K \int_0^\infty \beta(\sigma)\,(1 + \cos 2\pi x \sigma)\, d\sigma \qquad (1)$$

$$= K_1 + K_2\, b(x)$$

where x is the path difference between the arms, i.e., the delay divided by the speed of light.

K is a constant describing the efficiency and light gathering power of the interferometer.

b(x) is the cosine Fourier transform of $\beta(\sigma)$

The delay x, as well as being a function of the position of the mirrors and the amounts of refractive material in each arm, depends on the angle at which the radiation traverses the system. Thus, for a finite field of view, (1) must be integrated over angle. Since (1) represents a linear transformation, I(x) contains as much information about the radiation as does $\beta(\sigma)$. In some special cases certain information may be more easily derived from the interferogram.

2.1.2 The Direct Use of the Interferogram. - Consider, for example, absorption by the 2-0 overtone band of CO at 2.35 microns. Since each branch of the absorption spectrum (Figure 2.2.1) consists of a limited number of narrow lines with nearly equal spacing, $\Delta\sigma$, it may be approximated as the product of a rectangular function and a Dirac comb, so that the interferogram should be a series of isolated signatures separated by $1/\Delta\sigma$, corresponding to a cosine modulated by the convolution of a sine function with a Dirac comb. The experimental interferogram of 1 atm.-cm. of CO (2%) with a 22 cm^{-1} filter centered at 4245 cm^{-1}, also shown in Figure 2.2.1 displays the CO signatures at 2.25 mm and 4.5 mm path difference. This may be compared to the interferogram of methane, one of the principal atmospheric interferents, taken with the same spectral filter. The lines in the methane spectrum are irregularly spaced, so that the interferogram is spread over all delays.

Since the effect of CO is confined to a narrow spectral band, the sampling theorem implies that its interferogram can be completely specified by samples spaced by $1/(\sigma_1 - \sigma_2)$, where σ_1 and σ_2 are the limits of the spectral band. Further, the regular line spacing implies that these samples will be zero except in limited ranges of path difference. Thus, the entire information content may be obtained from a smaller number of sample values.

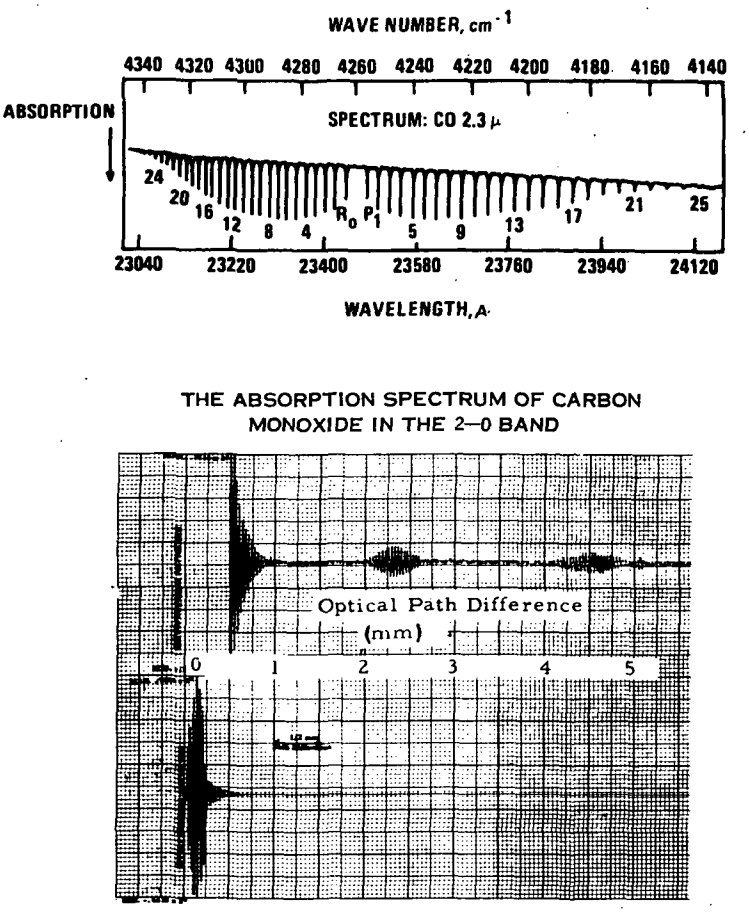

Figure 2.2.1. CO Overtone Spectrum and Interferogram

It is perhaps informative to look at the spectra and interferogram in the region of the CO bands. Figures 2.2.2a and 2.2.2b show, respectively, the spectra of CH_4 and of CH_4 with CO in an approximately 3:2 ratio. A close comparison shows that high resolution would be required to separate out the CO lines, especially with an atmospheric ratio of CH_4 to CO which is an order of magnitude higher than that used for these spectra. Here only the P6, P7, P8, R4, R5, and R8 lines stand out to any extent.

Figures 2.2.3.a and 2.2.3.b show the interferograms resulting from these spectra with an optical filter centered in the P region at about 4210 cm^{-1}. The corresponding CO interferogram is that shown above. The interferograms are quite different in various parts of the delay range, such as between 2.5 and 3 mm. A similar difference is observed when looking at the interferograms obtained with a filter centered in the R-branch. Most of the data presented herein were obtained with the latter filter since the other major interferent, water, has less effect on the interferogram using that spectral region.

Thus, the correlation interferometry technique takes advantage of the obvious differences in interferograms of different gases and combinations of them by direct use of the interferograms, or more specifically, those parts of the interferograms

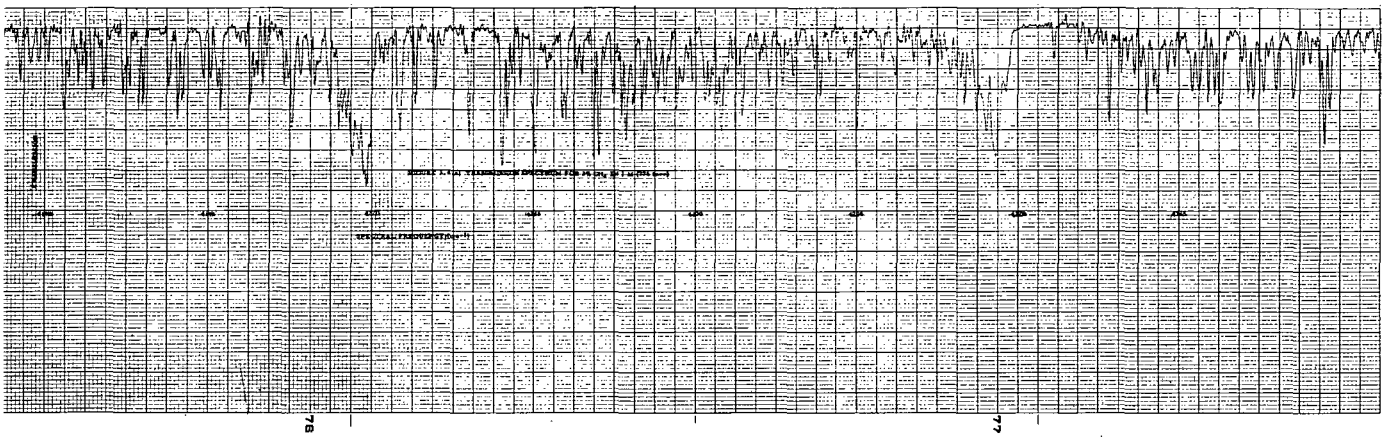

Figure 2.2.2.a. Spectra of CH_4 (3 atm.-cm.)

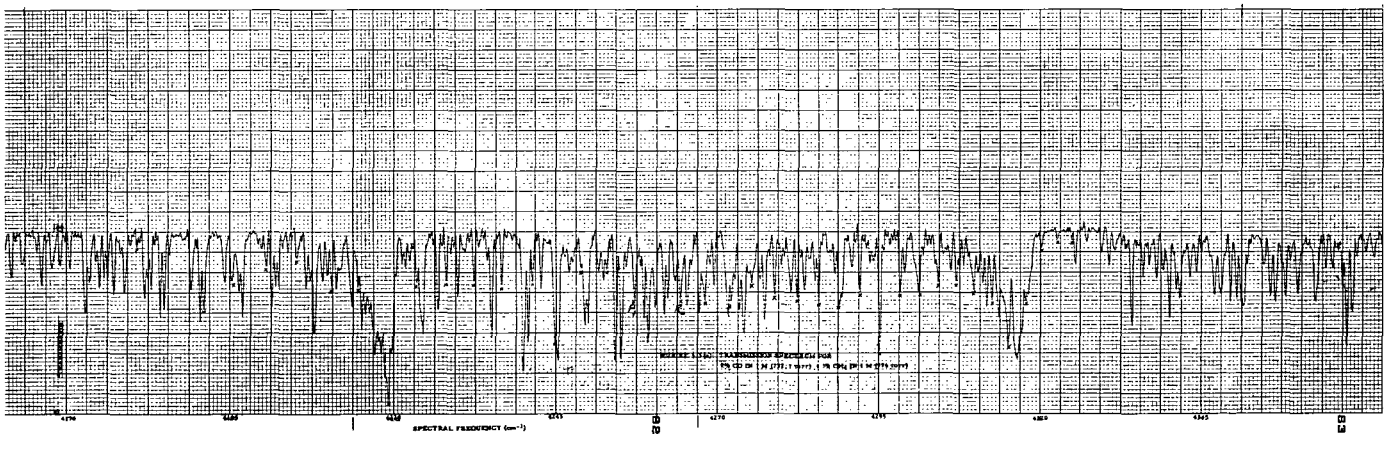

Figure 2.2.2.b. Spectra of CH_4 (3 atm.-cm.) + CO (2 atm.-cm.)

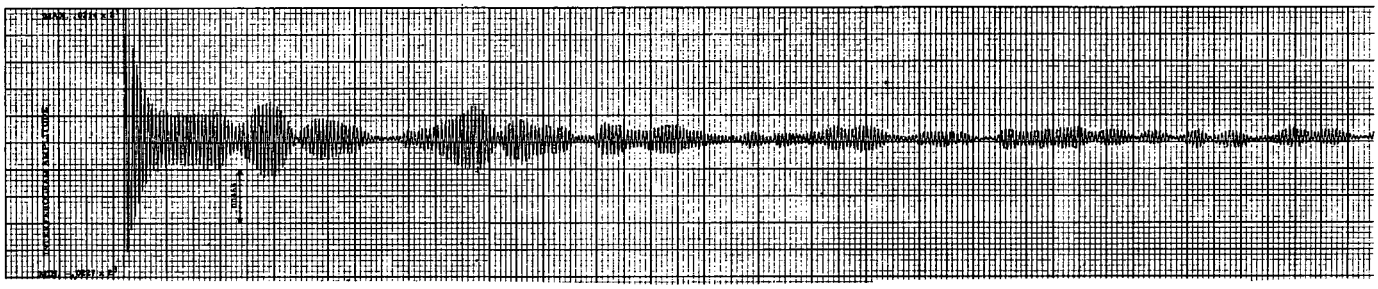

Figure 2.2.3.a. Interferogram of CH_4 (3 atm.-cm.)

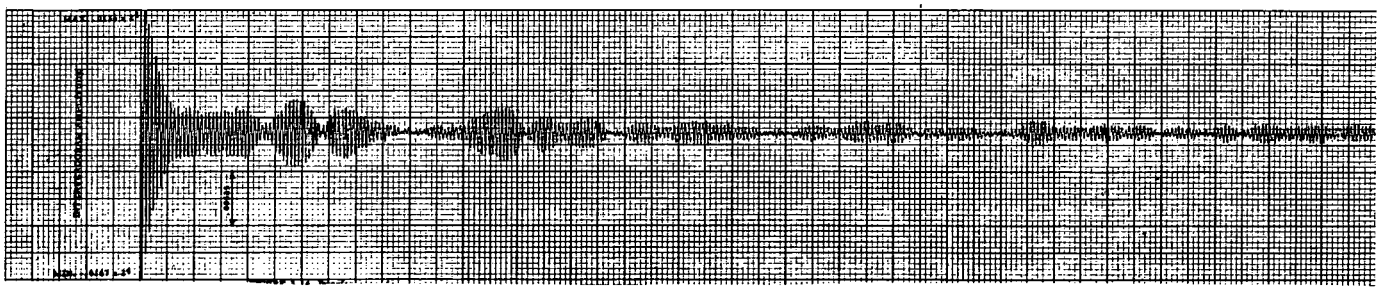

Figure 2.2.3.b. Interferogram of CH_4 (2 atm.-cm.) + CO (atm.-cm.)

which are most directly affected by the gases of interest. It is to be stressed that the interferograms are not converted back into the spectra but rather the analysis is made directly on the most appropriate parts of the interferogram. The results presented later in the report were obtained by analysis of interferograms (similar to those of Figures 2.2.1, and 2.2.3) obtained with the correlation interferometer.

2.2 Refractive Scanning

An interferometer can be scanned by moving one of the mirrors or, if only a limited scan range is required, as in the present case, by tilting a refractive plate in one arm. The limitation arises because the optical thickness of the tilted plate varies for different parts of the field of view, so that the resultant interferogram is the sum of many interferograms of different phase. This spread in phases, which increases with increasing plate angle, reduces the amplitude of the resultant interferogram.

In cases where only a limited scan range is required, refractive scanning has three significant advantages over mechanical translation of the interferometer mirrors. These are: (a) accurate rotation is easier to achieve than strictly linear motion, (b) the scan plate system is much more tolerant of random displacements than is the mirror, where a 1/2 wavelength movement produces a whole wavelength change in delay, and (c) the movement of the refractive scan plate can be achieved without using sliding surfaces, which are undesirable in space applications, especially where smooth motion is required.

2.3 Field Widening

The variation of path difference with angle can be minimized by suitable choice of the difference in thickness between the scanning plate and the beamsplitter substrate, so that a larger field of view can be tolerated for a given level of modulation in the interferogram. The choice of plate thicknesses which maximizes the switched power, i.e., maximizes the product of field of view and modulation, is known as the field-widened condition. The theory of field widening for a refractively scanned interferometer is given in Appendix B.

2.4 Correlation

The basic principle of correlation operation may be understood from Figure 2.4.1. The first two curves show (purely pictorially), the interferograms of a "target" and an "interferent", for example, CO and H_2O. We shall assume initially that the interferogram

amplitudes are proportional to the amounts of gas present and that if both are present their effects combine linearly. This is not strictly true but the departures can be taken into account. If only random noise were obscuring the CO signal, the optimum means of processing would be to multiply the signal by a stored replica of the noise-free CO interferogram and integrate the result over delay. This stored replica may be described as a correlation or weighting function, W. When we wish to reject interferents as well as random noise we can alter the shape of W so that it satisfies three conditions.

- (W x interferent) summed over delay = 0
- (W x target) summed over delay = (CO amount)
- (W x random noise) summed over delay = minimum

In practice, it is found that the shape of W which rejects the interferents is still very similar to the shape of the CO interferogram. The mathematical theory of the derivation of correlation functions is given in Appendix A.

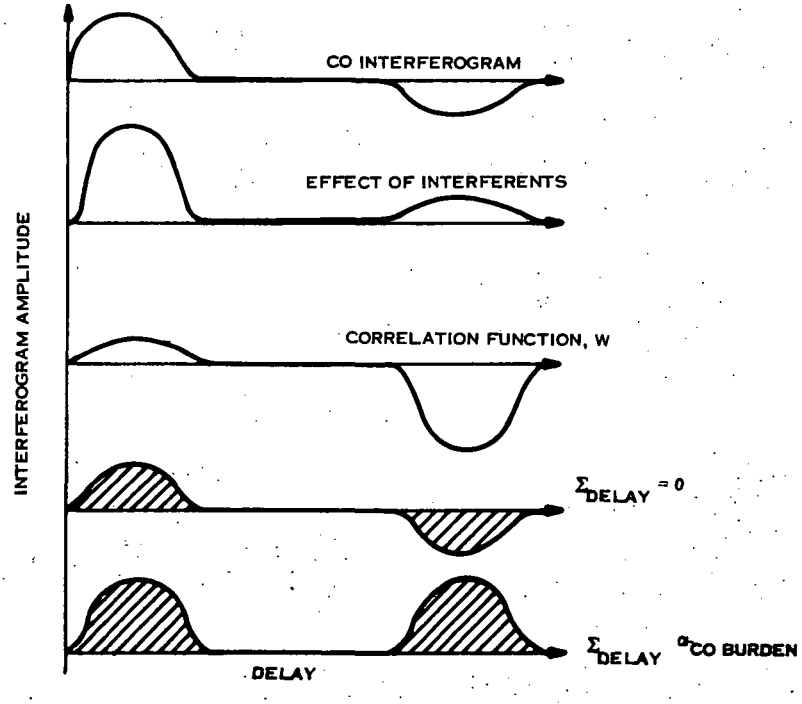

Figure 2.4.1. Principles of Measurement

2.5 Heterodyning

As mentioned in Section 2.1 above, the spectra of interest are band limited and, thus, the interferograms have the form of a phase and amplitude modulated cosine wave of the form $I(x) = A(x) \cos (2\pi \sigma_o x + \phi(x))$, where A and ϕ are slowly varying functions of the path-difference x and σ_o is the center wavenumber of the spectral band. The analogue of the result given by the sampling theorem, namely that I(x) need only be measured at points spaced by Δ, the reciprocal of the spectral bandwidth, may be roughly expressed by saying that A and ϕ will not vary significantly in distances much less than Δ. Thus, the sampling position accuracy required if A and ϕ are measured is much less than would be required when sampling the actual interferogram, the ratio being of the order $2 (\sigma_1 - \sigma_2)/(\sigma_1 + \sigma_2)$.

A and ϕ may be measured by using a reference source of wavelength within or close to the range of wavelengths of interest. The use of a reference channel is a common practice in a good deal of Michelson interferometry, allowing the delay of the interferometer to be continuously monitored. Such a source produces its own interferogram, which may be written (apart from DC terms) as a function of interferometer delay x.

$$I_o (x) = A_o (x) \cos (P_o (x))$$

If the source is monochromatic, A_o varies quite slowly with x, and P varies at the uniform rate of 2π per change of one wavelength in x:

$$P_o (x) = K_o x; K_o = 2\pi/\lambda_o = 2\pi f_o$$

For more complicated spectra the variations become more complex.

In a similar manner, a component at wavenumber "f" in the target spectrum produces an interferogram component. $I_f(x) = A_f(x) \cos (K_f x)$

If the interferogram is multiplied by a cosine varying in the same manner as does the reference interferogram, the result for spectral frequency f is a new interferogram.

$$I'(x) = A_f(x) \cos (K_o x) \cos (K_f x)$$

$$= A_f(x) (\cos (K_f + K_o) x + \cos (K_f - K_o) x)/2$$

The resulting interferogram can thus be considered as the sum of two interferograms, one with fringes varying at a rate corresponding to the sum of the spectral frequencies, the other with fringes varying at a rate corresponding to the difference of the frequencies. If the frequencies are sufficiently close the component at the sum may be removed by a low pass filter, leaving only the component at the difference. This basic procedure has been described by Mertz (ref. 6). The result of this procedure is twofold. First, the degree of severity of small changes in path is much reduced by using a reference source which undergoes the same changes in path. For change in path sufficient to cause a change in phase dP for fringes corresponding to spectral frequency f,

$$dP = K_f dx$$

$$= 2\pi f dx$$

or $$dx = dP/(2f),$$

the corresponding change in phase of the difference fringes is only

$$dP' = (K_f - K_o)\, dx$$

$$= \left(\frac{f - f_o}{f}\right) dP$$

A shift of the order of a wavelength at f results in only a fraction of a fringe shift in the difference interferogram, so that the requirements on mechanical stability and reproducibility are proportionately less when heterodyning is employed.

To preserve S/N in the regions where

$$(K_f - K_o)x = (2n-1)\pi/2$$

a second, parallel, channel is required, in which the interferogram is multiplied by $\sin K_o x$.

The simplest method of minimizing the difference frequencies, so as to obtain the maximum advantage from the hetrodyning process, is to use, as reference, blackbody radiation which has passed through the same spectral filter as the main signal and through a sample of the infrared-active atmospheric gases. This can be closely approximated using an incandescent source and an absorption cell containing about 1.75 atm.-cm. of methane, which is the principal atmospheric absorber in the 2.3 microns region.

3. BREADBOARD DESIGN

3.1 System Functions and Signal Flows

This section describes the subsystems which make up the breadboard, the functions of each subsystem and the resulting signal flow through the system. The functions, which are summarized, in order, in Figure 3.1.1 are as follows:

1. To collect radiation in sufficient quantity from a field of view appropriate to the mapping task.

2. To limit this radiation to the narrow spectral band where absorption by CO occurs.

3. To form the interferogram of the radiation as a function of time and convert it to a time-varying voltage for signal processing. Since the radiation is limited to an optical band of $\sigma_0 \pm \Delta\sigma$ the voltage is band limited to frequencies $S\sigma_0 \pm S\Delta\sigma$ where S is rate of scanning path difference.

4. To normalize the signal amplitude in terms of the total received power in the spectral band. This is required because the observable which is related to the CO amount is the transmission of the atmosphere, i.e., the quantity $1 - (I_0 - I)/I_0$ where $I_0(\sigma)$ is the irradiance entering the atmosphere and $I(\sigma)$ is that at the instrument.

5. To move signal frequency band (from $S\sigma_0 \pm S\Delta\sigma$ to $O \pm S\Delta\sigma$) by synchronous detection and smoothing. The use of synchronous detection (or hetrodyning) gives better S/N ratio for small signals than linear or square law detection (ref. 7) and does not require that the signal frequency be maintained exactly at the peak of a narrow band electrical filter. Transforming to zero frequency minimizes the position accuracy required on subsequent sampling, as explained in Section 2.5

6. To sample the smoothed signal, at known points in the interferogram over a range of delay centered around the CO signature. The spacing of the points to be that dictated by the bandwidth and the sampling theorem, i.e., at least one point every $1/2A\Delta\sigma$ units of delay.

7. To accumulate the value of each sample over a number of scans and then output the accumulated values, so that they can be used to compute a correlation (weighting) function, as described in Appendix A.

- COLLECT RADIATION
- LIMIT SPECTRAL BAND TO $\sigma o \pm \Delta\sigma$
- FORM INTERFEROGRAM AS A FUNCTION OF TIME
- CONVERT INTERFEROGRAM TO TIME-VARYING VOLTAGE
  - THIS SIGNAL IS BAND-LIMITED TO $\sigma oS + \Delta\sigma S$, WHERE S IS RATE OF SCANNING PATH DIFFERENCE
- NORMALIZE IN TERMS OF TOTAL RECEIVED POWER (AGC)
- MOVE SIGNAL BAND FROM $S\sigma_0 \pm S\Delta\sigma$ TO $0 \pm S\Delta\sigma$ (SYNCHRONOUS DETECTION AND SMOOTHING)
- SAMPLE SMOOTHED SIGNAL AT INTERVALS OF 1/2 $S\Delta\sigma$ (AT LEAST)
- OUTPUT SAMPLED VALUES OR
- MULTIPLY SAMPLED VALUES BY STORED COEFFICIENTS
  - ACCUMULATE PRODUCTS
  - OUTPUT RESULT

Figure 3.1.1. System Functions

or

To multiply the accumulated values by a stored weighting function, sum the products over the length of the scan and output the result, which is the measurement of the amount of target gas in the radiation path.

For the special purpose of the breadboard, it is also required that several parameters be selectable viz., sample length, number of samples per scan, number of scans to be co-added and the delay region covered by the scan.

The means by which these functions are implemented are shown in Figure 3.1.2 and described below. The parameters of the various subsystems are listed in Table 3.1.1.

Incident radiation is collected by an 8-inch diameter, f/2 Newtonian telescope with a 2^o field stop. The spectral band is defined by a temperature controlled Fabry-Perot interference filter near the focal plane of the telescope. A chopper blade driven by a step-motor and located in focal plane of the telescope, serves to 100% modulate the radiation when required for AGC. The radiation is re-collimated by a silicon lens and enters the field-widened refractively-scanned interferometer as a 7^o beam. Increasing

Table 3.1.1. Breadboard System Parameters

Aperture	
• Interferometer	6.6 cm Diameter
• Telescope	22.0 cm Diameter
Field of View	
• Interferometer	0.12 Radian Diameter
• Telescope	0.034 Radian Diameter
Spectral Bands	4240 - 4340 cm^{-1} (2000 - 2200 cm^{-1})
Delay Scan Range	2.5 - 4.0 mm
No. of Sample Points	0 - 64
Sample Length	1 - 63 Fringes
Scan Rate	1 Hz
No. of Scans Accumulated	1 - 500
Noise Equivalent Power	1.6 E - 11 Watt/$Hz^{1/2}$
Noise Equivalent CO Amount (3% Albedo, τ = 1 Sec)	0.004 Atm-cm
Detector 2.3μ	LN_2 Cooled PbS Immersed on Sr Ti O_3
(4.6μ	LN_2 Cooled InSb)
Weight	
• Interferometer	15 Lb
• Telescope	10 Lb
• Electronics	60 Lb
Power	100 Watts

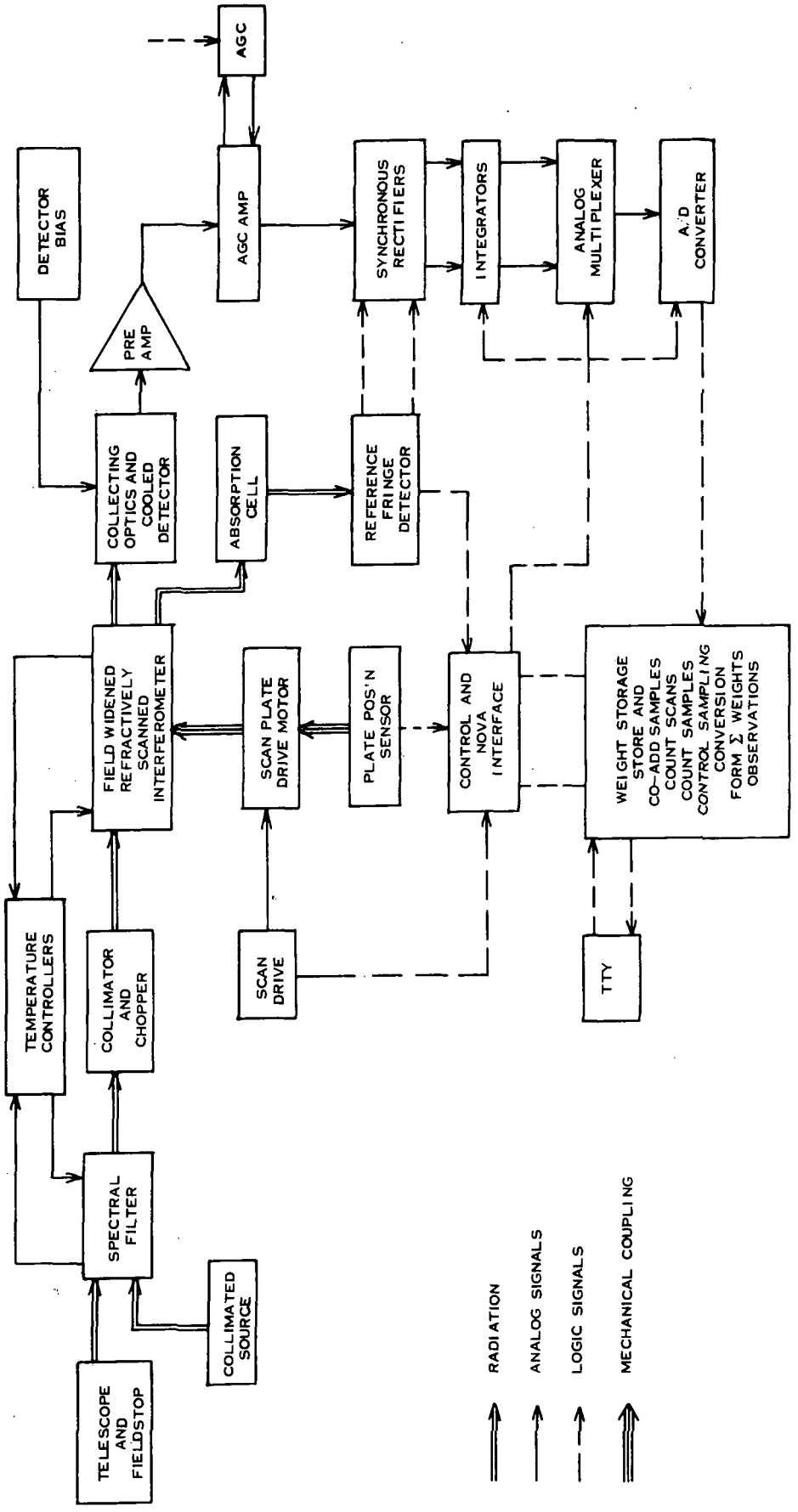

Figure 3.1.2. Breadboard Block Schematic and Signal Flow

the field angle in this way, to the maximum which can be accepted by the interferometer, permits the size of the interferometer to be minimized while maintaining the required radiation collecting ability (etendue).

The path difference in the interferometer is scanned by tilting the scan plate by means of a torque motor, using a drive waveform shaped so that the path difference decreases linearly over 3/4 of the scan, the plate returning rapidly to zero during the remaining 1/4. The interferogram leaving the interferometer is imaged by a second silicon lens onto the main detector element which is a liquid notrogen-cooled immersed lead sulphide unit. A second coaxial optical path (the reference channel) takes radiation from the incandescent lamp, located in the center of the telescope primary, through the spectral filter, the interferometer and a gas cell containing methane, the resulting reference interferogram being sensed by a separate room temperature PbS detector. After passing through the variable gain AGC amplifier, the signal from the main detector is input to two synchronous rectifiers, which are just electronic switches opened and closed by square waves derived from the peaks and zero crossings, respectively, of the reference interferogram. Two channels are used, separated by 90^{o} in phase, because, as explained in Section 2.5, the main interferogram is, in general, out of phase with the reference interferogram.

The outputs of the synchronous rectifiers are supplied to two dumping integrators whose outputs are sampled and reset to zero at fixed increments of path difference, as determined by counting the zeros of the reference interferogram. The integrator outputs are sampled, sequentially, by a 12-bit A/D converter. The digitized values (2 per sample) are stored in the Nova minicomputer and co-added over a number of scans.

As well as storing and accumulating the sample values, the Nova is used to control the operation of the breadboard, as shown in the flow-chart in Figure 3.1.3. The control program is conversational, via a teletype, and permits the operator to set the number of samples/scan and the number of scans to be co-added, and to have the accumulated sample values either printed out and/or punched on paper tape or to have them multiplied by any one of a set of 8 stored correlation functions and output the sum of the resulting products. The stored correlation functions are input, as required, from paper tape and there is also the facility to re-enter previous set of sample values from tape and treat it with correlation functions. All operator input points in the program are trapped to prevent accidental overwriting of stored program or data and the A/D converter input is trapped for overflow.

The time sequence of operation is shown in Figure 3.1.4. The interferogram is generated during the "forward" position of the scan and, during the flyback period, as the scan plate returns to the starting position, the total radiation entering the system is modulated by the chopper in the telescope. The "total radiation" signal is used to set the gain of the AGC amplifier. This gain, which is held fixed during the forward scan, is set so that the total radiation signal amplitude, multiplied by the gain, is equal to a fixed reference level. Thus, the interferogram amplitude observed at the output of the

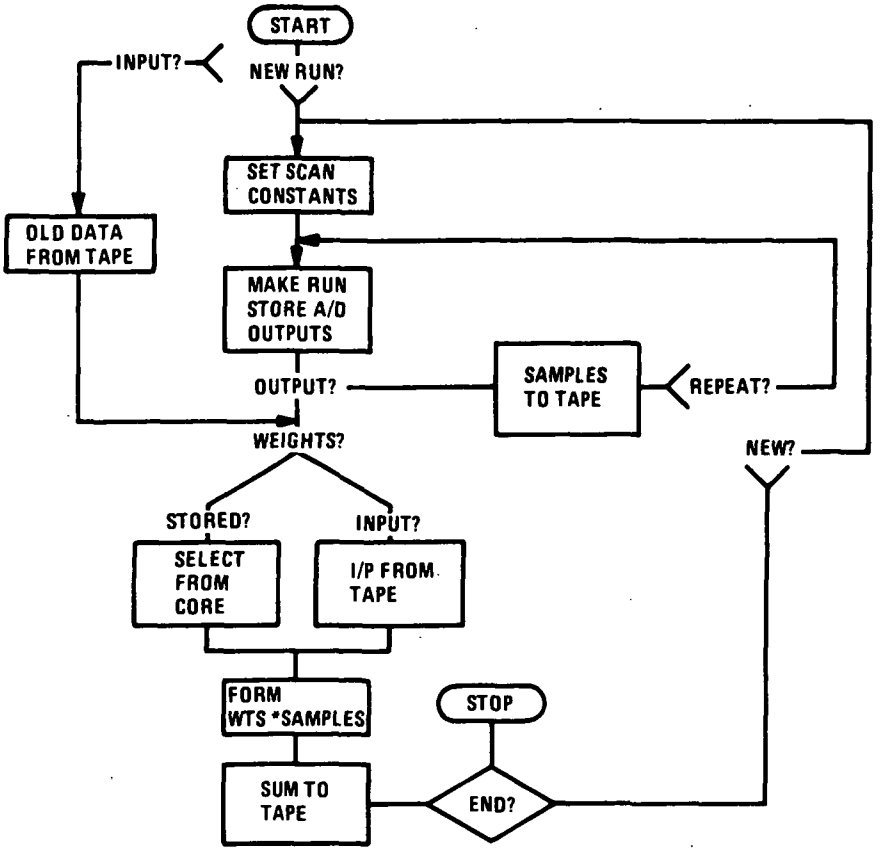

Figure 3.1.3 Nova Program Flow

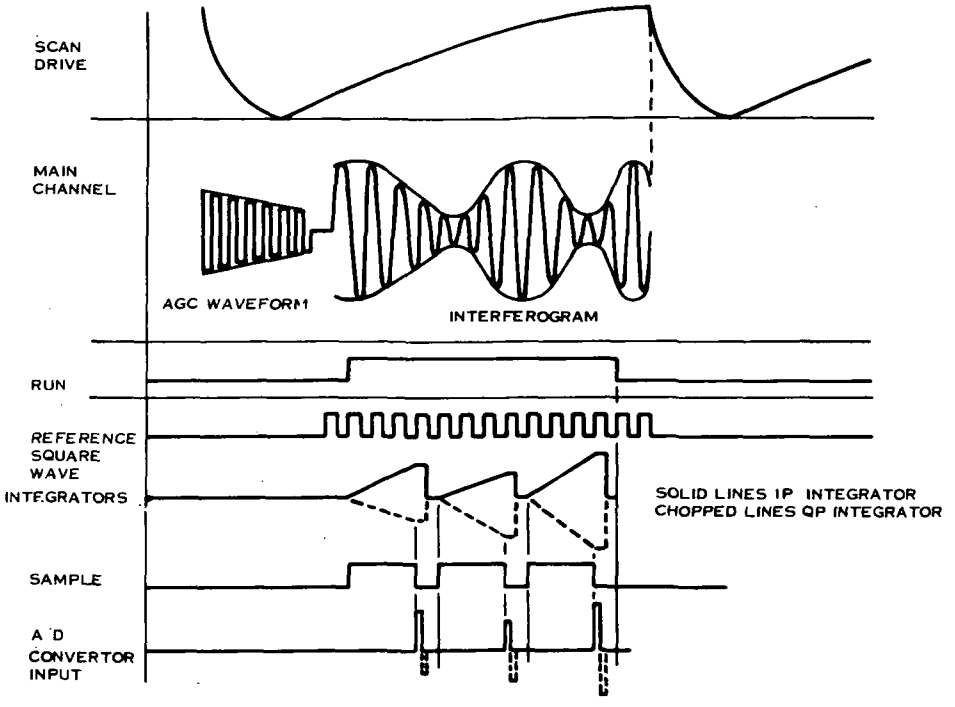

Figure 3.1.4, Breadboard Timing Sequence

AGC amplifier is proportional to the interferogram amplitude at the detector, divided by the total radiation entering the system, i.e., it represents the fraction of received radiation which is modulated by the interferometer.

The portion of interferogram sampled is delimited by the "run" pulse, which goes high when the scan plate passes through a given position, as determined by a LED/photo diode sensor, and goes low after m x n zero crossings of the reference interferogram, where m is the length of a sample and n is the number of samples/scan. The integrators are allowed to run for m-1 cycles of the reference, the remaining cycle being used to dump the accumulated charge.

For operation at 4.6 micron, the main channel radiation is diverted by an auxiliary mirror to a cooled InSb detector, the reference channel detector is replaced by a second InSb unit, the absorption cell is replaced by one containing carbon monoxide, the spectral filter is changed to the appropriate spectral band and the electronic bandpass center frequency is adjusted from 1 kHz to 500 Hz since the interferogram fringe frequency varies inversely with the spectral wavelength. The mode of operation at 4.6 microns is exactly as described above for 2.3 microns.

The temperatures of the spectral filter and of the enclosure containing the interferometric components are both controlled above ambient by proportional and integral controllers and thermistor sensors. Even though the path difference in the interferometer is stabilized by the use of an ultra low expansion structure and by temperature control, so that the delay is essentially controlled by the position of the scan plate, it is also advisable to have a means of monitoring the absolute delay, so as to check for any long term drifts or displacements due to mechanical shock. This can be done by detecting a peak in the reference interferogram. The peak amplitude of each fringe is detected and compared with the amplitude of the preceding fringe stored in a "sample and hold" circuit.

A logic one or zero is stored depending on whether the peak amplitude has decreased or increased, i.e., if the slope is +ve or -ve. This is then compared with the result for the next pair or peaks; if there is a change, then a pulse is generated, indicating a local maximum (or minimum) in the envelope of the reference interferogram. This pulse is coincident with the fringe peak immediately following the turning point.

The direction of change which corresponds to the sign of the second derivative, indicates whether the turning point is maximum or minimum.

3.2 Choice of System Parameters

This section describes the criteria used to determine the system parameters in the original design. These parameters are listed in Table 3.1.1. A later section on the construction and testing of the breadboard will show how some of these were slightly modified during construction and also outline the extent to which the predicted performance was realized.

The breadboard interferometer is to be used to gain experimental experience applicable to the design of flight models for atmospheric CO measurement. Accordingly, the sensitivity and accuracy of the breadboard should approach, as nearly as possible, the values thought to be necessary for detection of the CO sink. Parameters for best attaining these values were determined to be

- External field of view, $2^{o} \times 2^{o}$
- Measurement time, 1 second
- Minimum detectable amount of CO, 0.01 atm.-cm.

Further, all the critical components or functions should be consistent with space operation.

Appendix A describes how the several noise mechanisms, which limit sensitivity, and the uncertainties in operating environment, which limit accuracy, combine to effect the system. The noise terms depend on all the physical parameters of the instrument, while the errors due to interferents depend on the weighting function and the size and location of the delay scan.

The fundamental limit at 2.3 microns is the noise generated by the infrared detector. Accordingly the first task was to find the range of parameters for which signal/detector noise ratio was ≥ 2.5 for a change of 0.01 atm.-cm. in CO amount. This level was chosen because it appeared that the other sources of (system generated) noise, e.g., AGC errors, errors in scan speed and application of weights, could be kept below this level by careful electronic design. Considering only detector noise, the signal/noise ratio is given by

$$S/N = \frac{2 R \epsilon \tau A \Omega V D^*}{(A_1)^{1/2}} (\pi T)^{1/2} \qquad (1)$$

where R is the terrain radiance in watts/cm^2 sterad cm^{-1}

ϵ is the beamsplitter efficiency

τ is the transmission of the optical system including the peak transmission of the spectral filter

A is the area of the collecting aperture (cm^2)

Ω is the external field of view (steradians)

V (Ω, θ) is the visibility parameter which varies with Ω and scan plate angle as shown in Appendix B

D* is the detectivity in cm $Hz^{1/2}$/watt

A_1 is the detector area (cm^2)

T is the measurement time (seconds)

W is the normalized change in signal processor output for unit change in CO amount; it is computed by the program of Appendix A as an equivalent width in cm^{-1}, and includes total atmospheric composition

The detector area is given by

$$A_1 = \frac{4}{\pi} \frac{A f^2 \Omega}{G^2} \tag{2}$$

where f is the f/# of the detector optics and G the minification of any immersion element used.

Combining (1) and (2) gives

$$S/N = \frac{R \epsilon \tau (A\Omega)^{1/2} V G}{f} \pi T^{1/2} W D^* \tag{3}$$

Numerical values can be assigned to some of the factors in (3) thus

R = 1.6×10^{-8} watts/cm^2 sterad (cm^{-1})
(for 3% terrain reflectance)

ϵ = 0.21 (both polarizations)

τ = $(0.9)^3$ $(0.93)^7$ · 0.6 = 26.2%
(3 mirrors, 7 lenses and windows, narrowband filter)

f = 1.5, G = 3.5 (immersed system)

f = 1.0, G = 1 (unimmersed system)

The value for R is from reference (8) adjusted to air mass = 2. The values for f and G are based on ray traces for two-element detector optics and angular fields about 7^o.

Thus (3) becomes

$$S/N = 8.0 \times 10^{-9} (A\Omega/\pi)^{1/2} T^{1/2} VWD^* \quad (4)$$

The value of $\Omega^{1/2} V$ is determined by the scan range required and $A\Omega$ by the external field of view and size constraints on the optics. Using the program MAPEM (described in Appendix A) and interferograms of synthetic spectra covering the range of temperatures, water and methane amounts given by the GE model atmospheres, it was determined that the S/N had values close to maximum for any scan which includes the region from 2.8 to 3.6 mm delay. This result is not greatly affected by the relative magnitudes of the various noise mechanisms. The magnitude of errors produced by uncompensated interferant changes also show a broad minimum for scans covering the same range. Small changes in scan range redistribute the error magnitudes without significantly altering their RMS value. Since the actual conditions cannot be more precisely defined at this stage of the program, it was assumed that all variations described by the GE model atmospheres were equally probable so that there are several scan ranges which appear equally usable. Accordingly, the scan mechanism was designed to cover the maximum range, centered at 3.2 mm, as determined by the field-widening criteria, the external field of view and the S/N requirements. Figure 3.2.1 (based on the theory of Appendix B)shows that, for any given scan range, there is an angular field which maximizes the quantity $V\Omega^{1/2}$ and thus maximizes the S/N. Figure 3.2.2 shows how this optimum field varies with scan range.

Using program RUNEM (Appendix A) and considering the R branch of the 0-2 band we find W = 1.2 10^{-3} cm^{-1} for a change of 0.004 atm.-cm. CO amount. The R-branch was chosen because it is stronger and less masked by the most variable interferent (water vapor). Inserting the value of W in (4) along with the optimum field angles from Figure 3.2.1 gives the relation between interferometer collecting area and D* for a "noise equivalent amount" of 0.004 atm.-cm. CO, assuming a 1-second integration time and an immersed detector. This is also shown in Figure 3.2.2.

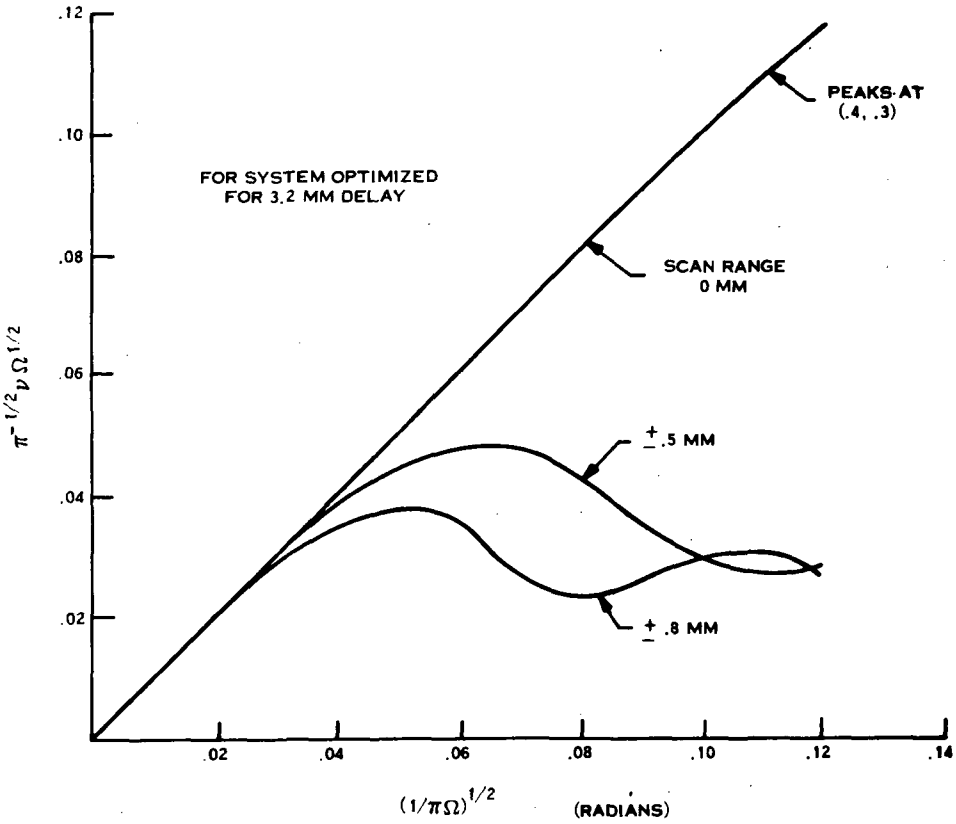

Figure 3.2.1. Switched Power as a Function of Field Angle and Delay Scan

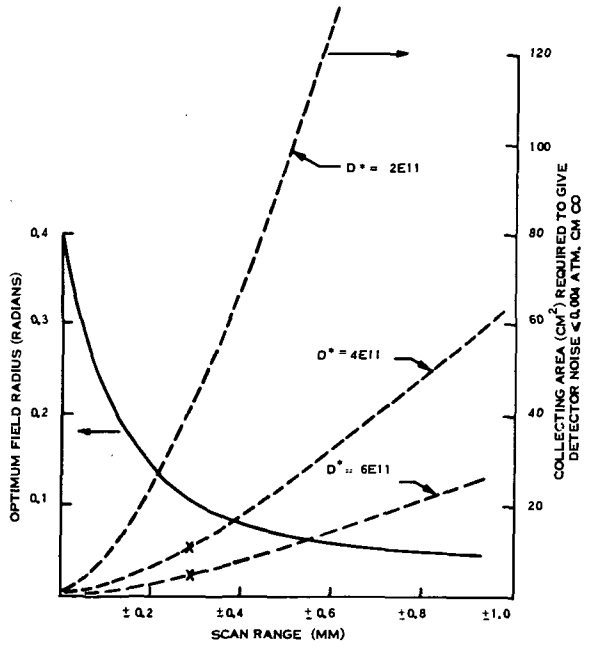

Figure 3.2.2. Field Aperture and D* as a Function of Scan Range

From Figure 3.2.2 it is apparent than an immersed detector with $D^* \geq 3 \times 10^{11}$ is necessary to achieve the required scan range and sensitivity with reasonable sized optics. This in turn implies the use of cooled lead sulphide, a detector material, which can be easily immersed, maintains D* even in large areas, and can be gain-controlled by varying the bias voltage. This detector can be operated at 77°K or 193°K; LN_2 operation was chosen for the breadboard, for simplicity, but thermoelectric cooling (to 193°K) may offer advantages for airborne/satellite use. The D* at 1 kHz signal frequency is comparable for 193°K and 77°K cooled-filter operation, but if scintillation frequencies were low enough to permit operation at 100 Hz, a D* of 6×10^{11} would be possible at 193°K, with a consequent reduction in instrument size.

Since the visibility, V, at the optimum field of view is practically a constant, the lines of constant D* on Figure 3.2.2 are also lines of constant $A\Omega$. Thus, assuming that the instrument has the optimum Ω for the scan range covered, we may plot "Noise Equivalent Amount" of CO as function of D* and $A\Omega$. Further, since the interferometer must be matched to the $2^o \times 2^o$ (1.1×10^{-13} steradian) external field of view, by a telescope of the same $A\Omega$, we may plot NEA vs D* and telescope diameter. (Figure 3.2.3).

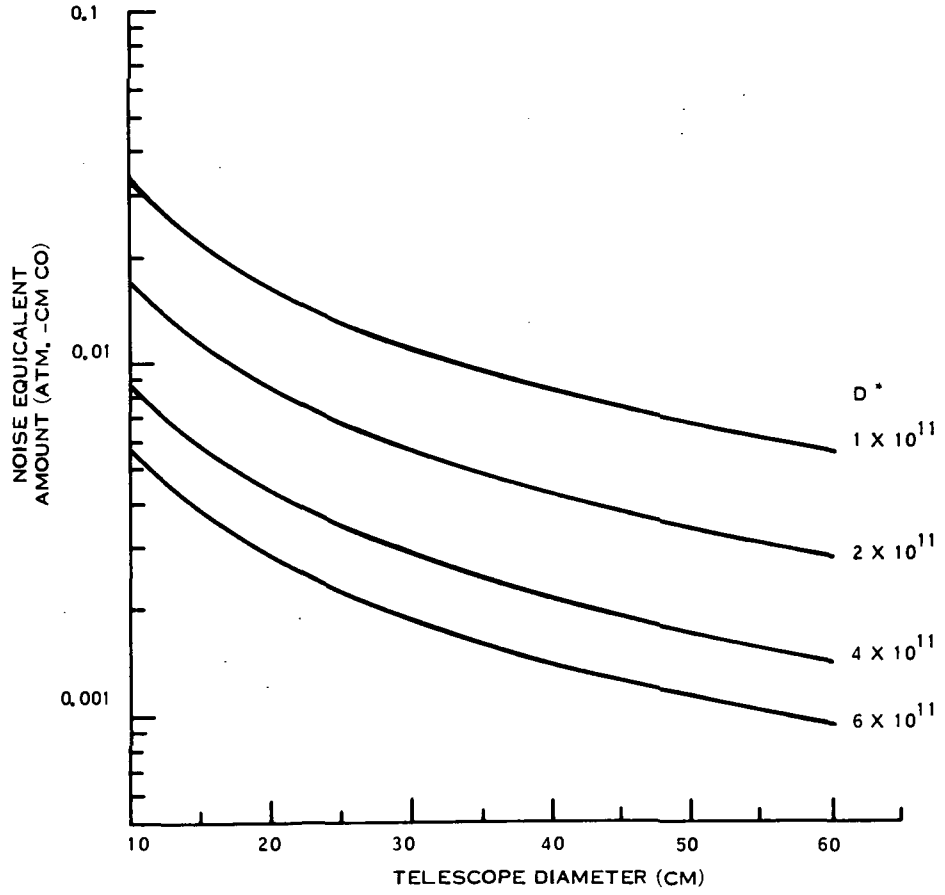

Figure 3.2.3. NEA as a Function of D* and Diameter

Based on manufacturers responses to request for quotation, a figure of $D^* = 4 \times 10^{11}$ cm $Hz^{1/2}$ watt was assumed. From Figure 3.2.3 an 8 inch telescope is then required to give adequate S/N and this is also a convenient size for a moveable instrument and not inconsistent with a satellite system. Since it is hoped to obtain experimental improvement of breadboard parameters, the scan range was chosen as $\pm$ 0.6 mm to allow for comparison with the minimum $\pm$ 0.4 mm range indicated by the modeling. This in turn gives a 0.12 radian field and a 2.6 inch aperture stop for the interferometer, which are compatible with available detector and dewar sizes and the maintenance of adequate optical flatness.

These values of the principal parameters (see also Table 3.1.1) seem to afford the best compromise consistent with the constraints. If these constraints were to be changed, the improvements in S/N would occur as follows:

- increasing the time allowed for a measurement would reduce the detector noise and the random system noise (or any scintillation noise in the region below the fringe frequency) by an amount proportional to the square root of the time.

- increasing the allowable external field would reduce the telescope size and weight and it could be eliminated for a 7° field, with a saving in transmission and reflection losses of about 20%. Still larger fields, up to the limit of 9° imposed by the minimum scan range, would permit a corresponding linear improvement in S/N or reduction in interferometer size.

The other major parameter of the system is the operating temperature range. By using a monolithic, ultra low expansion framework to position the interferometric components, the effect of temperature is reduced to: (a) the change in size and refractive index of the uncompensated refractive material in one arm, and (b) the temperature shift of the spectral filter used to define the operating wavelength. From the computer effect of interferogram and filter shifts, it is easily shown that the errors from these causes may be kept to less than 0.01 atm.-cm. CO by controlling the interferometer temperature to $\pm$ 10°C and the filter temperature to $\pm$ 1°C and this was done for the breadboard.

The parameters for the reference channel are governed by an equation similar to (3) with some added constraints. These are that: (i) the source must be located in the telescope primary if the two channels are to share the same spectral filter (ii) the maximum beam diameter at any aperture stop must be less than 1/4 of the main beam diameter at that point, (iii) the beam divergence in the interferometer must be $\leq$ 0.12 radian, and (iv) the source should be mechanically stable and have minimum power consumption. One of the small compact filament quartz-iodine automobile lamps makes an ideal source. Operated at 2000°K, it has indefinite life, low power consumption and 2.3 micron radiance equal to 1000°C blackbody. The reference channel optics were designed to give maximum $A\Omega$ and minimum detector size consistent with the constraints listed

below. The source consists of a quartz-iodine lamp with a 0.05 x 03 inch filament and a 1.5 inch diameter f/2.4 lens. The detector lens are 1 inch focal length f/1.4 and the detector is a 3 x 3 mm room temperature PbS element.

The resulting parameters are:

$R = 6.2 \times 10^{-4}$ watt/cm^2 sterad cm^{-1}

$A\Omega = 0.036$ cm^2 sterad

$f = 1.4$

$G = 1$

$\tau = 0.08$

$\epsilon = 0.2$

$V = 0.8$

$1/2\pi T = 1000$ Hz

$W = 0.3$ cm^{-1} (average for 2 atm.-cm CH_4)

$D^* = 1 \times 10^{-11}$

Giving an expected S/N of 220:1. At this level the number of spurious zero crossings should be negligible (ref. 9).

3.2.1 Mechanical Design. -

(a) The Interferometer Frame. - The interferometer frame has to provide constant relative position of the interferometer main optical elements. Therefore a high stiffness and low thermal expansion coefficient are important. In parallel with the design of an invar structure, we investigated the use of alternate materials, with a view to obtaining increased stability and a reduction in weight.

The alternate investigated were:

Cervit ceramic*

Titanium silicate**

Carbon filament epoxy matrix

*Manufactured by Owens-Illinois.
**Ultra low expansion material (ULE) manufactured by Corning.

The carbon filament material is anisotropic, and being at present still in development, is only obtainable in simple shapes. The best dimensional stability can be achieved with the ceramics. The ULE has the advantage that it can be fused to form a monolithic structure, while Cervit must be cast, which increases the cost of low volume production and also limits the possible shapes. Fusion of the glass frame components results in a structure with high stiffness and minimum weight. The weight of the glass structure is 1.5 kgm, compared to 6.1 kgm for invar, the elastic modulous is approximately 1/3 and the expansion coefficient ($3 \times 10^{-8}/^{o}C$) is only 1% of that of invar.

Some relevant properties of the materials are listed below:

	CERVIT	ULE	INVAR
Thermal expansion per ^{o}C	1.5×10^{-7}	3×10^{-8}	1.5×10^{-6}
Thermal conductivity cal/cm/sec/^{o}C	0.004	0.0032	0.04
Density	2.5	2.2	8.2
Yong's modulus, psi	13.4×10^{6}	10×10^{6}	30×10^{6}
Modulus of rupture psi	7×10^{3}	7×10^{3}	YIELD P, 4×10^{4}
Knoop	540	460	140 BRIN
Possibility of fusing	no	yes	no
Possibility of casting	yes	no	no
Conventional Fabrication	no	no	yes

Because glass is a fragile material, fastening of all the components on the frame must be different from normally used methods. All constraints are chosen according to strictly kinetic principles to be sure that forces on the frame do not exceed tolerable values and that they are exactly defined. Where, for reasons of mechanical accuracy, a direct contact of other components with the frame is necessary one of the contact surfaces has a spherical shape, to provide a limited and defined local pressure, causing stresses smaller than the rupture stress. Where the accuracy requirements are not critical, invar blocks are cemented onto the frame, providing supports for other components. The cement used is a flexible, low expansion type of epoxy (Eccobond 45).

The design of the frame has been carried out in consultation with the material manufacturer. Fused titanium silicate optical structures have been used in several satellite and balloon programs because of their high strength/weight ratio and ability to be finished to optical tolerances.

The glass version of the interferometer frame is illustrated in Figure 3.2.4.

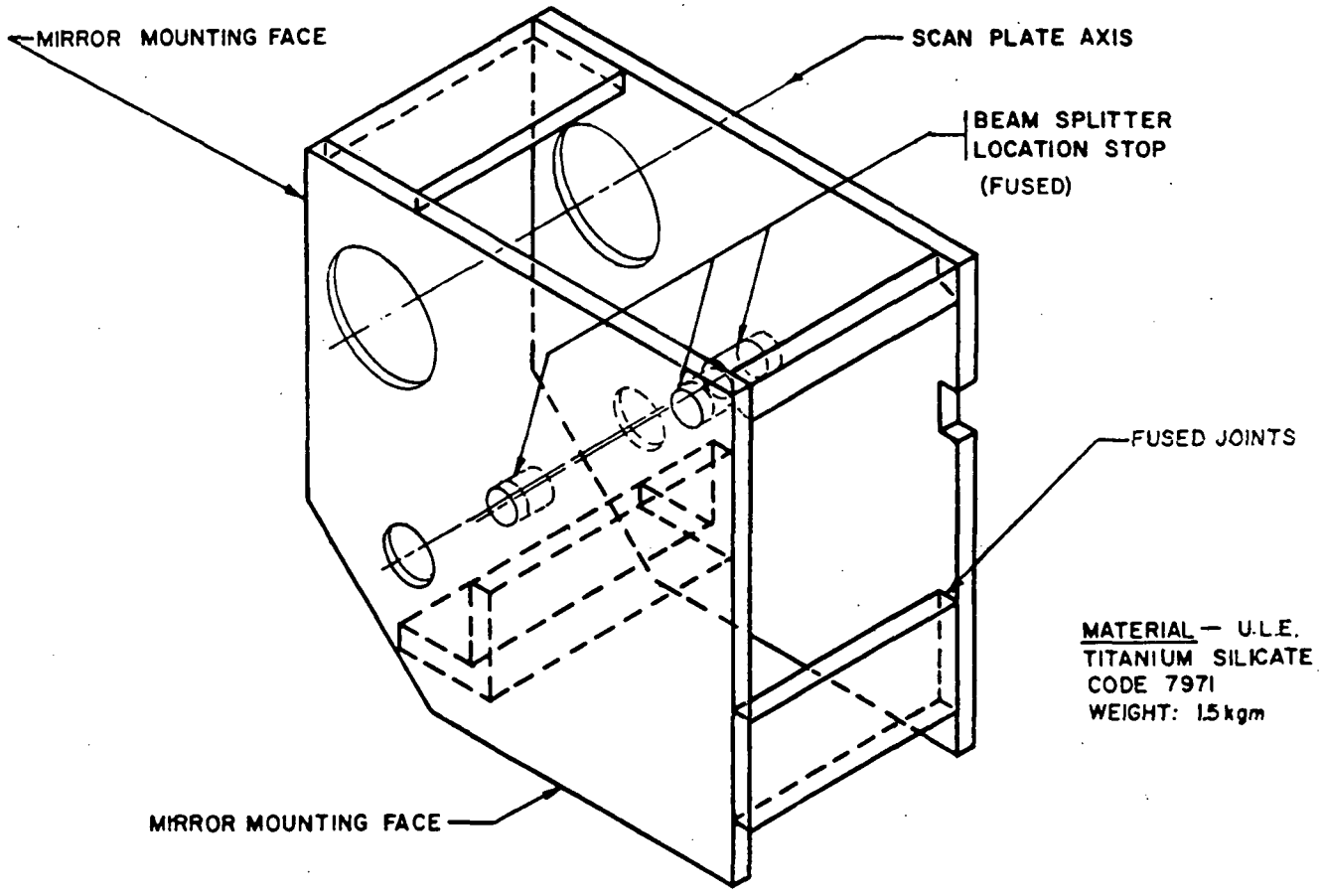

Figure 3.2.4. Main Frame

(b) Scanning Mechanism. - The scanning mechanism provides reproducible movement of the scanning plate and is composed of flexible pivots, torque motor, magnetic damper and photoelectric position detector.

For the selection of bearings, the following was taken into account:

- No ball bearings applicable
- Indefinite pivot life
- Resistance to accelerations (20g gives 10 lb. loading)
- Sufficient deflection ($\pm 8^{o}$ or if possible 16^{o} one way, to avoid using the additional spring)
- Tolerable center shift

Double ended standard pivots (Bendix type 6016-800), dia. 0.5", load capacity 35 lb., deflection 13^{o} for indefinite life (19^{o} for 2×10^{5} cycles), have been selected.

Requirements on the torque motor:

- Low power to minimize temperature changes and power needed
- Sufficient torque
- Large internal viscous damping to minimize size of the additional dampers
- Low weight, reasonable size
- Brushless, pancake version (Aeroflex Lab. torque motor 2.5 inch dia. (TQ25-6P) was selected)

Scanning Plate Position Detector

We considered:

- A synchro attached to the plate axis
- An induction potentiometer
- A photoelectric potentiometer
- A photoelectric incremental encoder composed of a recticle with parallel lines, fastened to the plate, and of a point light source.

The synchro accuracy is about 20 sec. of arc (about 1/2 a fringe) but the price of a pancake version is high ($2,200) and a special power supply is needed. Accuracy of the induction potentiometer and of the special photoelectric potentiometer was insufficient.

The incremental encoder used has a recticle with 500 lines/inch, 3/4 inch long. The light spot size is approximately 1/4 of the recticle spacing. One pulse given by this position detector corresponds approximately to 3 fringes path difference change.

Magnetic Damper

The magnetic damper is composed of permanent magnetis (Alnico 507) connected with a transformer steel plate into a system of magnetic circuits and of a copper blade moving in the magnetic field.

The proportionality constant between the torque of the damper and the angular velocity is for this configuration given approximately by the following equation:

$$F = \frac{B^2 \ell^2 R^2 b t}{\rho \cdot s} \times 10^{-12} \text{ (gr cm/rd/sec)}$$

where B is the induction (approximately 11,000 gauss)

ρ is the specific resistance of copper (1.72×10^{-5} Ω/cm^3)

R is the radius on which the damping is applied (10 cm)

ℓ is the length of the magnet (1.9 cm)

t is the conductive material thickness (0.04 cm)

s is the average length of the conductive path in conductor (approx 4 cm)

b is the average width of the current leading portion of the conductor (0.8 cm)

Values s and b do not have an exact geometrical meaning and were estimated in an experiment on a damper with a geometry similar to ours. For critical damping (F = 120 gm cm/rd/sec) 6 pairs of Alnico 5-7 magnets 0.5 x 0.75 inch on radius 4.9 inches are required. For the optimum air gap and copper thickness, the above equation and demagnetization curves for Alnico 5-7 give:

For clearance between copper and magnets (inch)	0.006	0.008	0.01
Copper thickness is (inch)	0.017	0.016	0.015
Induction is (gauss)	11,300	11,000	10,700

Temperature Dependence of the Damping

The main temperature changes are caused by induction change (about 0.2%/°C for materials similar to Alnico 5-7) and by copper conductivity change (about 0.4%/°C). The above equation:

$$F = \text{const} \times \frac{B^2}{\rho}$$

gives $\frac{\Delta F}{\Delta T} \approx 0.8\%$ F per °C.

Scan Dynamics

The spring rate for two flexible pivots K = 1880 gm cm/rd. The moment of inertia of the silicon plate M_1 = 1.1 gm cm^2, rotor inertia M_2 = 0.28 gm cm^2, damper M_3 = 0.4 gm cm^2, together with other mechanical parts the total moment of inertia is M = 2 gm cm^2.

The critical damping coefficient

$$F = 2\,(K \times M)^{0.5} = 122 \text{ gm cm/rad/sec}$$

Resonance frequency

$$W = (K/M)^{0.5} = 30.6 \text{ sec}^{-1}$$

$$f = 4.9 \text{ cps}$$

The differential equation for the scanning plate

$$M \frac{d^2 \alpha}{dt^2} + F \frac{d\alpha}{dt} - K (\alpha - \alpha_o) = \text{TORQUE (t)}$$

was programmed and response of the mechanism was computed for various functions "TORQUE (t)" introduced by torque motor and its drive.

The required response is such, that in the effective part of the scanning cycle the fringe rate has to be approximately constant. To express this condition mathematically, the expression for the path difference D in a tilted plate

$$D = 2 h [n - \cos (\alpha - \beta)] / \cos \beta$$

where α is angle of incidence

β = arcsin $(\frac{\sin \alpha}{n})$

h = plate thickness

n = refractive index

must be modified to get α as a function of time, which would correspond to a constant change in path difference D, i.e., to the constant fringe rate. This modification gives

$$\cos \beta = \frac{D^2 - 4h^2(1 - n^2)}{4 h n D}$$

and $\alpha = \arcsin (n \sin B)$.

Within accuracy of 1 - 2% this function can be approximated by

$$\alpha - \alpha_o = 0.874 (1 - \exp (-0.15 (D - D_o))$$

for plate thickness h = 9 mm and n = 3.4425, $\alpha_o = 0.576$ rd (33^o) and $D_o = 46.09$ mm. (Effective scan starts at 35^o, to give plate time to accelerate.)

To achieve this response, several various torque functions were tried, such as saw tooth or exponential function combined with a part of a sinusoidal function.

A relatively good response is yielded by the simplest solution where time function of the torque corresponds to the time function of the angular deflection:

$$\text{TORQUE}(t) = 1900 (1 - \exp (-0.15 \times \frac{D-D_o}{T_1} t))$$

where T_1 is the effective scan time which is 0.75 - 0.8 of the entire period of time T.

For $\text{TORQUE}(t) = 1900 (1 - \exp (-0.375t))$

and for $0 \leq t \leq 0.8$

$\text{TORQUE}(t) = 0$ for $0.8 \leq t \leq 1$

and angular deflection ($\alpha - \alpha_o$) is depicted in Figures 3.2.5 and 3.2.6 for three degrees of damping F = 122 (critical), F = 90 and F = 60 gm cm/rd/sec and for two different torque functions. Figure 3.2.7 shows the change in scanning speed caused by a change in damping coefficient from F = 122 to F = 90, which would correspond to a temperature change of about 30^oC.

(c) Optical System Design. - All lenses, the scanning plate and beamsplitter are made from silicon, selected because of its good transmission in the IR, high refractive index and therefore small spherical aberration, mechanical strength, low solubility and comparatively low price. It does not transmit visible light which is a disadvantage requiring more complicated alignment.

Efficiency of anti-reflective coatings was optimized for both spectral regions and a polarization-independent coating on the beamsplitter was used. All mirrors including the primary, have aluminum coating on a pyrex substrate with MgF_2 protective overcoating.

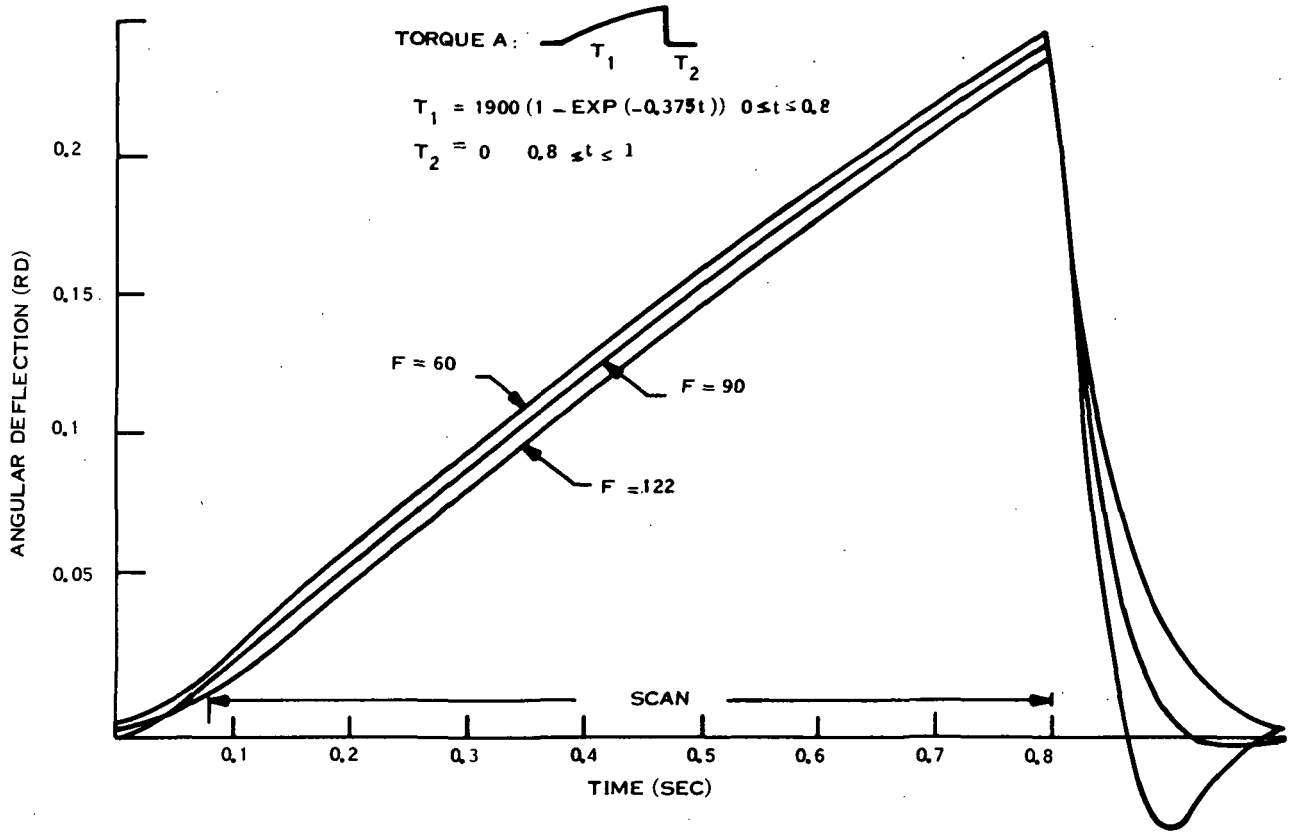

Figure 3.2.5. Angular Deflection as a Function of Time

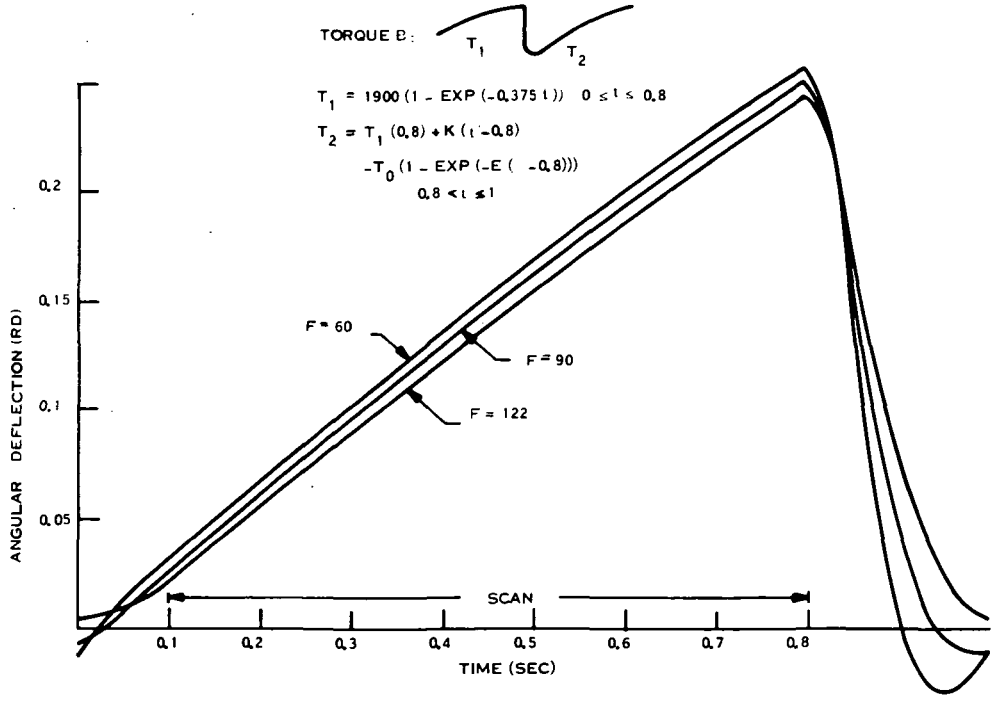

Figure 3.2.6. Angular Deflection as a Function of Time

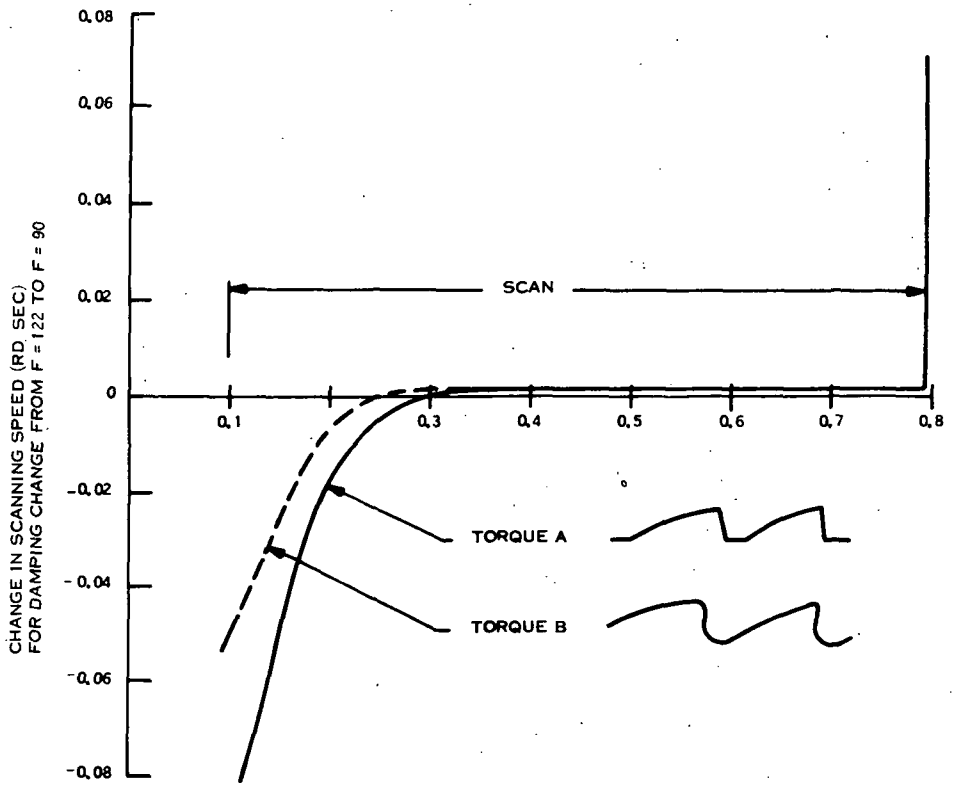

Figure 3.2.7. Scanning Speed of Various Damping Coefficients

For the breadboard, the increased reflectivity of a gold coating was not thought to compensate for the increased risk of mechanical damage.

Spherical lens and mirror surfaces were chosen since they are completely adequate for all applications except of the limb experiment, for which the main mirror could be exchanged for a parabolic if necessary. Spherical aberrations of lenses are minimized by using optimum lens shape.

The optical aberrations of the signal and reference channels have been minimized by computation, so as to provide the smallest possible detector area. The resulting configuration of the optics, with an immersed detector, is shown in Figures 3.2.8 through 3.2.10. In case an unimmersed detector is to be used (e.g., 4.6 micron operation) an alternative field lens has been computed and is also shown in Figure 3.2.8. Auxiliary plane mirror serves to select the unimmersed channel if required. The abberations of the interferometer were computed as well. Plate and beamsplitter thicknesses were optimized for field widening, as described in Appendix B.

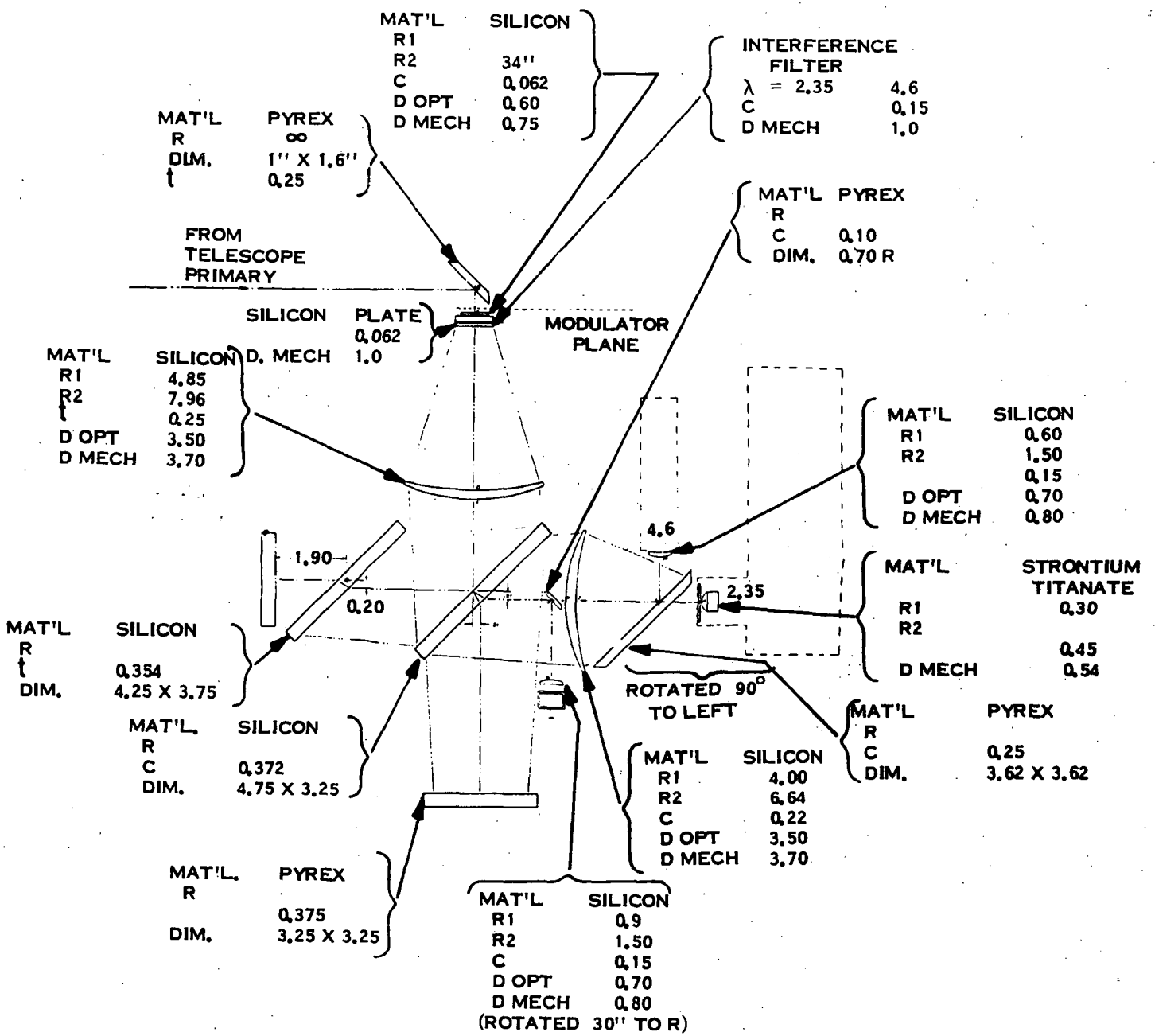

Figure 3.2.8. Optical Layout

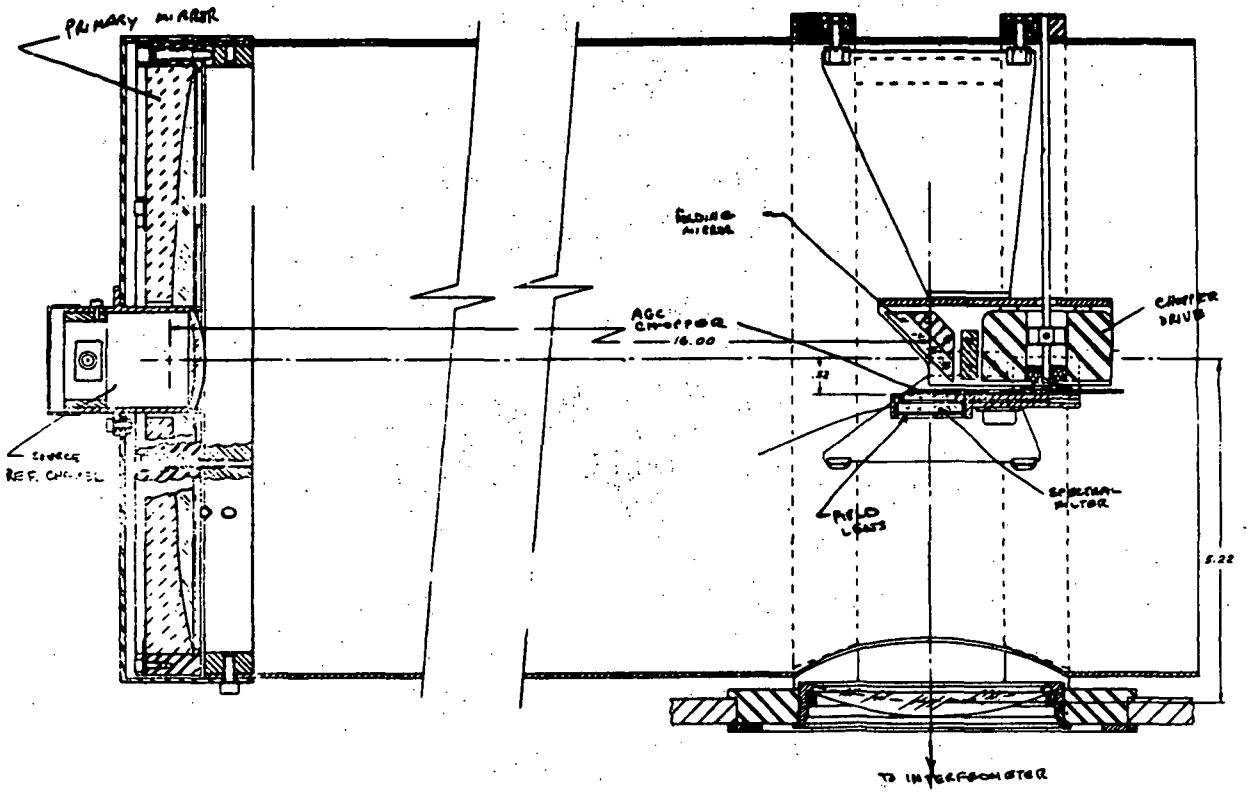

Figure 3.2.9. Fore Optics

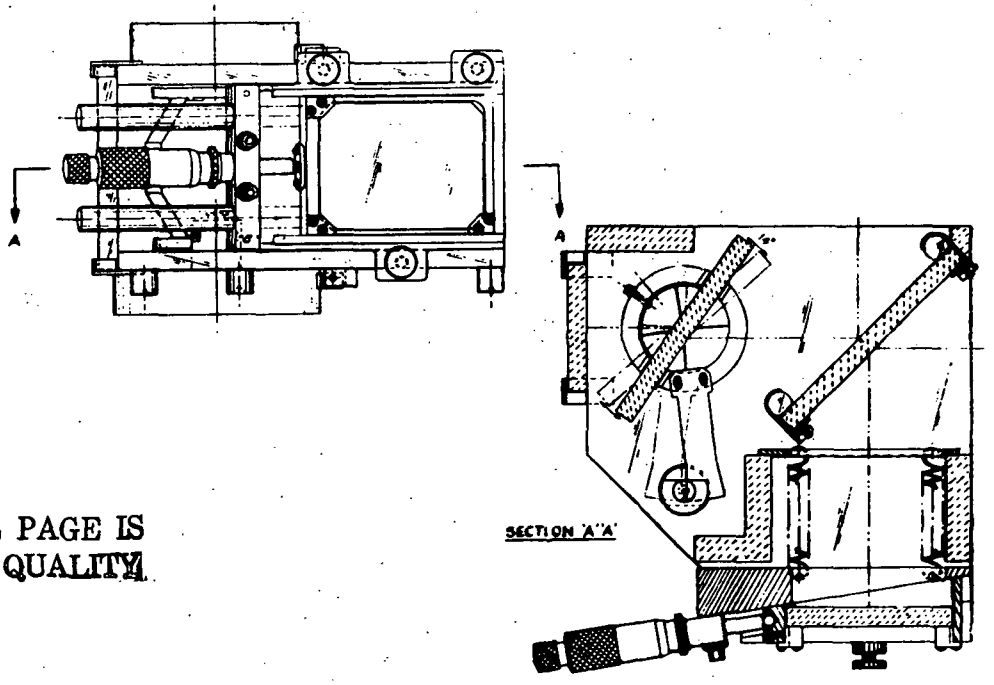

ORIGINAL PAGE IS
OF POOR QUALITY

Figure 3.2.10. General Assembly

3.3 Electronics

3.3.1 Concepts. - The scanning interferometer will see an interferogram of general shape as in Figure 3.3.1, showing the envelope of fringes in arbitrary light units as a function of the interferometer delay. The data processing concept calls for sampling the interferogram in k points inside the region of interest, between ΔS_1 and ΔS_2.

Two different approaches to realization of this concept were considered, either continuous scanning with sequential detection and integration of small portions of the interferogram (1-15 fringes) at selected sampling points, or noncontinuous scan utilizing an indexed scan plate which would stop at desired points plus a fast scanning plate which would scan up and down over a small number of fringes in the vicinity of the sampling point.

For an interferometer of given physical size, region of interest as long as 1000 fringes, and the fringe rate limited to 1 - 2 kHz properties of PbS detector, we obtain the following typical scan times and duty ratios (time utilization of light input):

	Continuous	Noncontinuous
Scan time	0.5 - 1 sec	5 - 10 sec
Duty ratio	5%	15%

Considerations of the scintillation noise spectrum seen by a satellite-borne instrument were the major points in deciding to maintain the scan time as short as possible, i.e., to implement the continuously scanning system. The same also resulted in the design concept of AGC loops.

Figure 3.3.2 shows the region of interest and the basics of interferogram processing. Numbers 1 to n have been assigned to the fringes in the region of interest. A set of marks m_i (i(l,k)) determines the sampling points. In each of the sampling points a sample of interferogram, ΔL is detected by in-phase and quadrature-phase synchronous detectors and integrated. The result of 1 scan is a set of in-phase and quad-phase integral products IP_i, QP_i. These are a function of the spectral modulation and are also directly proportional to the average light level I_o and to the time spent on the relevant sample Δt_i. Therefore, the processed signal has to be normalized with respect to variations of I_o and Δt_i. This is done in the following way:

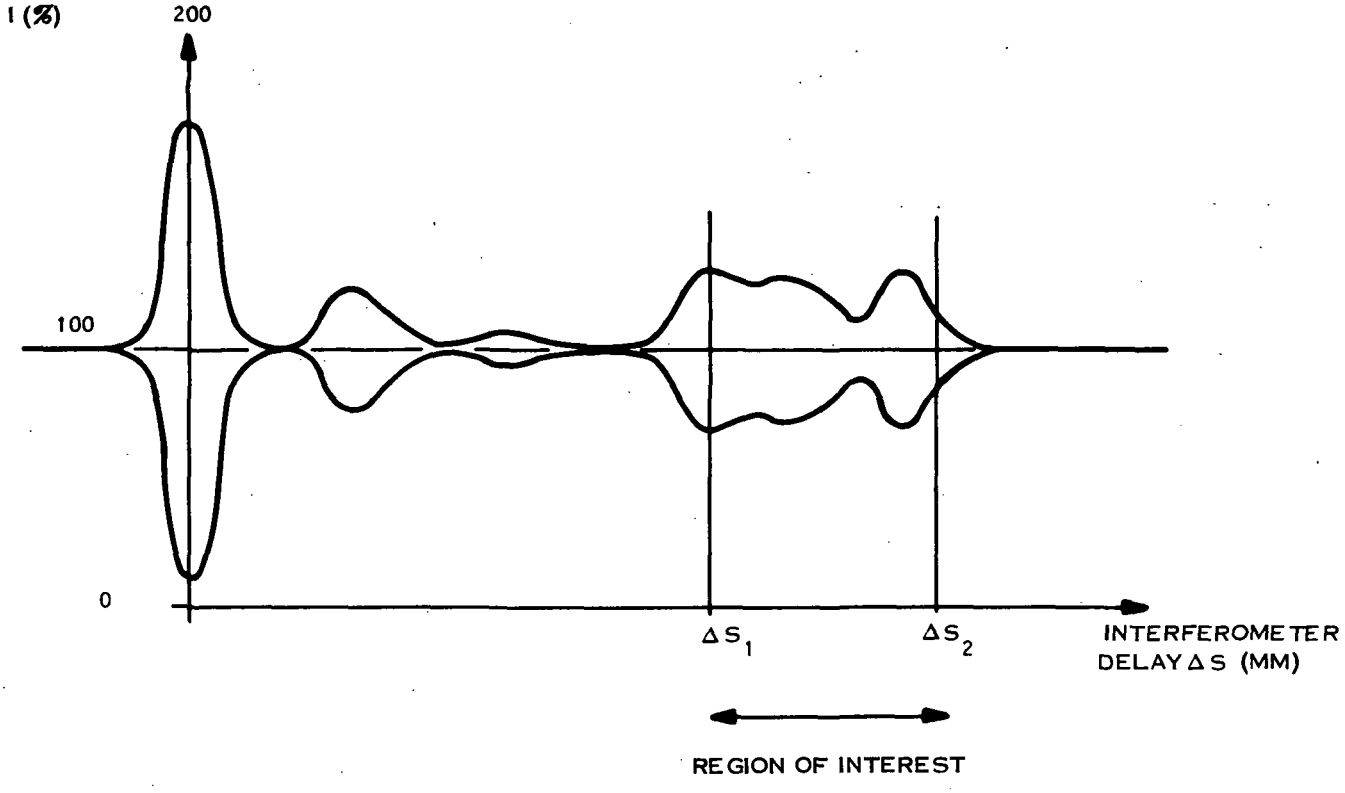

Figure 3.3.1. Output Light Intensity

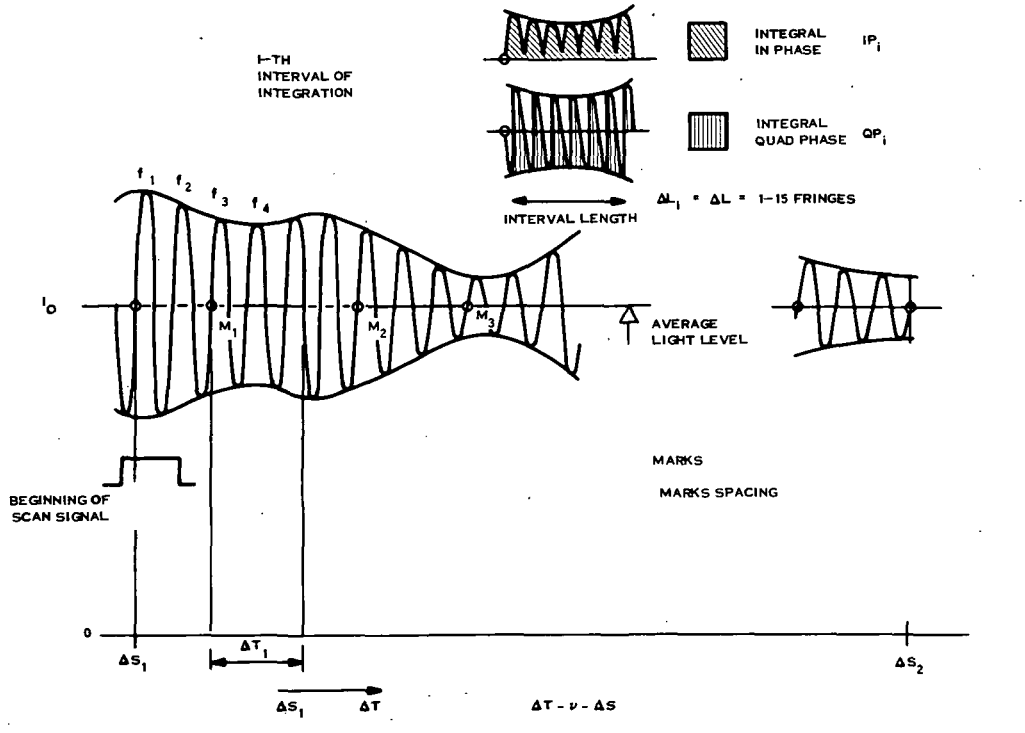

Figure 3.3.2. Interferogram Processing

1. Absolute AGC. As the value of I_o or corresponding voltage is inaccessible during the scan, the return scan is used to measure the value of I_o and set the gain in an automatic AGC loop to obtain normalized output. As DC measurement is impossible due to the time varying properties of the IR detector, chopping of input light is used. The settling time of the loop must be shorter than that of backward scan, dynamic range greater than 100:1, accuracy better than 10^{-2} to match the overall target accuracy of 1%, these implying the chopper frequency as high as possible, but safely distinguishable from the interferogram frequency. The gain is set and the absolute AGC is disabled during the forward scan.

2. Fast AGC. This loop is designed to take care of the variations of limited amplitude ($\pm$ 20% I_o) due to image motion. Unlike the absolute AGC, this one is functioning during the forward scan and disabled during return.

Accuracy is more critical, as to match the overall target figure of 10^{-2}, the integral products IP_i and QP_i must be measured with accuracy 10^{-3}. Errors due to varying scaling along the scan by fast AGC must not exceed this figure. Since I_o is inobtainable, variations δI_o are measured and the scaling factor

$$\frac{I}{I_o} = 1 - \frac{\delta I_o}{I_p}$$

is computed in an analog network and applied as a divisor in the signal path. Apparently the required accuracy of the fast AGC loop is < 0.5% of span, for the span of 20% I_o and output accuracy 10^{-3}.

$$20\% \times 0.5\% = 0.1\%$$

Fast AGC must not distort the interferogram pattern but must take care of the wide spectrum of variations. Variations slower than the scanning rate are compensated by absolute AGC and are irrelevant to the one cycle function of fast AGC. Therefore the fast AGC passband will have the low cut-off well below the scanning frequency and the high cut-off close to but safely below the interferogram frequency (see Figure 3.3.3). Since the breadboard was not intended for flight use, work on fast AGC was confined to design effort.

3. Scanning Velocity. During the forward scan, scanning velocity is a simple exponential function (See Section 2) to achieve uniform interferogram output at approximately constant frequency ($f_f \simeq$ 1 kHz). Theoretically, the velocity may be an arbitrary function, but it must be highly repeatable. For target accuracy 10^{-3} among the elements IP_i, QP_i, repeatability of the velocity function should be at least of the order of 3×10^{-4} averaged over the scan. With the scan mechanism described in Section this means that the shape of the drive waveform must have this degree of stability and the circuit used

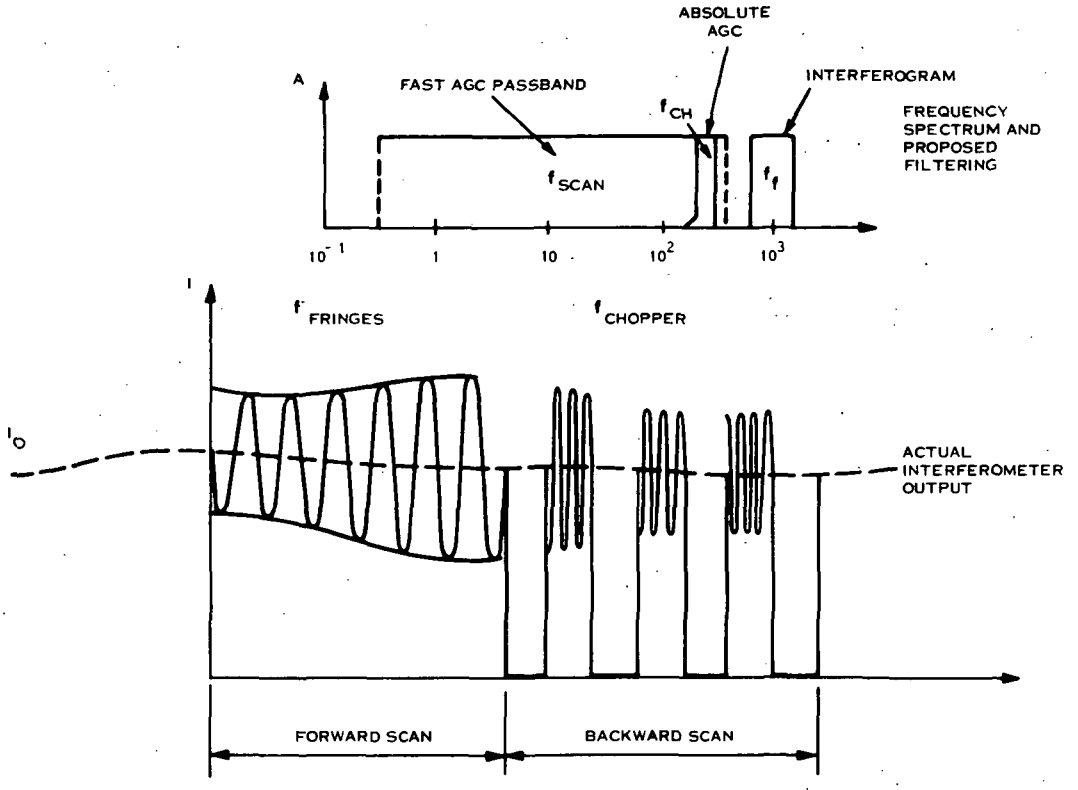

Figure 3.3.3. AGC Bandpass

is expected to achieve this. However, if for some reason variations $\delta t_i < 3 \times 10^{-4} t_i$ prove impossible to achieve by simple means, the times t_i can be measured by a real time clock and used to normalize the integral products IP_i, QP.

Figure 3.3.4 shows the actual hook-up of the signal preamplification and AGC. The reference channel observing an interferogram of a reference gas sample provides the phase reference necessary for synchronous detection. Note that both signal and reference channel contain matched filters (F1) to minimize differential phase shifts, even if these are designed for low phase-shift.

The remaining operations are carried out on the normalized interferogram. The processor evaluates scans as follows: Starting at the beginning of scan pulse - perform the inphase and quadrature-phase synchronous detection; integrate over Δt_i obtaining the integrals for the ith sampling point and jth scan IP_{ij}, QP_{ij}; multiplex these into one channel; and convert these analog values to digital numbers; accumulate each of these in the sample accumulators for the ith sampling point, continuing to the kth sample at the end of the region of interest; repeat over S scans to obtain the 2k numbers:

$$A_i' = \sum_{j=1}^{S} QP_{ij} \qquad A_i = \sum_{j=1}^{S} IP_{ji} \quad ;$$

then multiply by the weight coefficients W_i, W_i'; and sum over i to obtain

$$M = \sum_{i=1}^{k} A_i W_i + A_i' W_i'$$

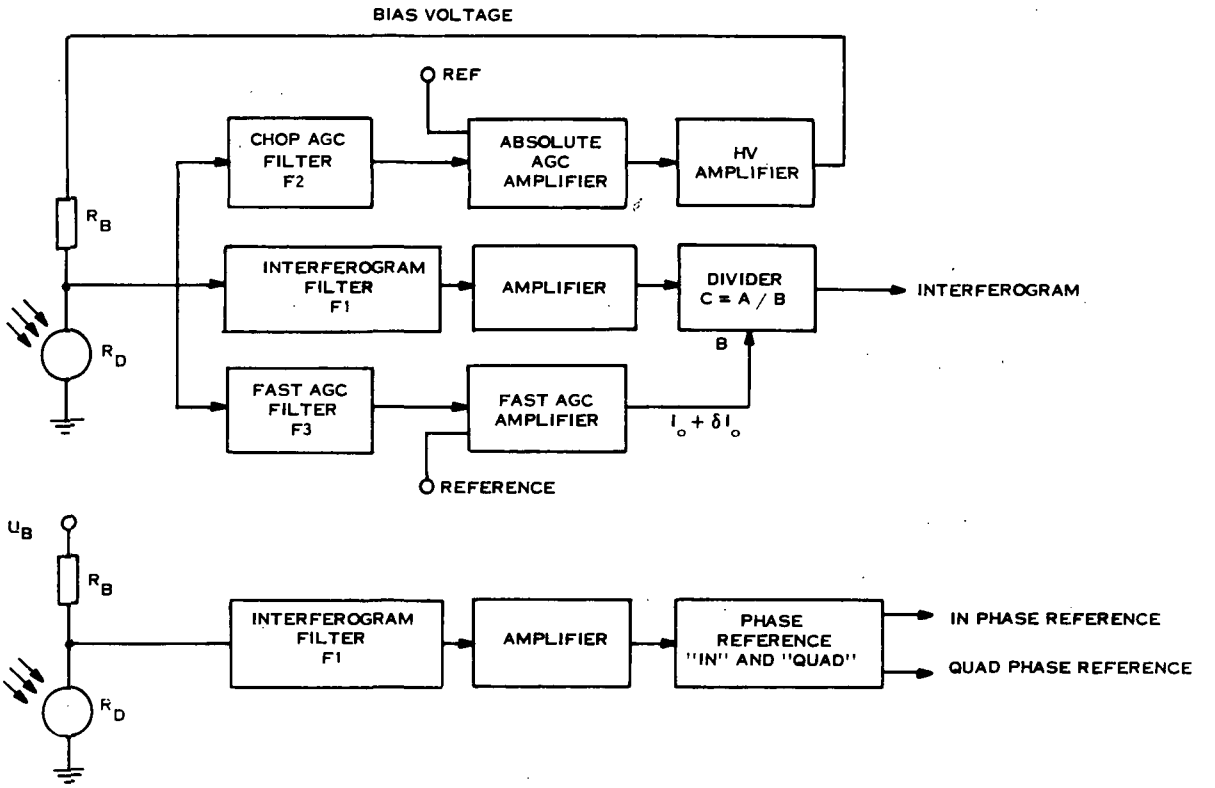

Figure 3.3.4. Signal Preamplification and AGC

Determination of position along the interferogram (i.e., timing of sample points) is by counting the fringes of the reference interferogram starting from a beginning of scan, synchronous pulse. This pulse is either the first reference zero crossing following the mark from the scan plate position sensor, or the mark from the reference point detector which identifies a maximum in the envelope of the reference interferogram.

Originally, it was proposed to build the entire electronic package necessary to carry out these functions including the facility to accumulate and output values for each sample point separately and to vary the sample length, number of samples/scan and number of scans co-added. While this package was being designed it became apparent that: (a) a large fraction of the digital circuitry would be devoted to accumulating separate samples and controlling sampling parameters and (b) that the recent advances in cost/performance ratio of mini-computers made it much more economical to use a mini-computer for these functions. It should be realized that the mini-computer is used purely as an experimental

convenience for the developmental breadboard instrument. In a final version there would be no need for accumulation of individual samples nor for adjustment of scan parameters so that the small amount of arithmetic involved in the actual correlation process can easily be implemented in a small dedicated electronic package. Indeed, several alternatives exist for the processor for a satellite instrument, as illustrated in Figure 3.3.1 to 3.3.9 and as described below.

Alternative 1.- Hybrid Data Processing (Figure 3.3.5). This is basically a simplified version of the breadboard system, hardware solution (Figure 3.3.10). The integral products are multiplied in a hybrid multiplier by weights selected from a ROM. An A to D conversion follows and the summing is digital. Output data for telemetry is digital.

Alternatives 2 and 3 introduce purely analog processing, which may be of some advantage provided that the overall number of sampling points is reasonably low.

Alternative 2, Figures 3.3.6 and 3.3.7 utilize a series of sample hold circuits to store the integral products. The summing network provides the weighting (see Figure 3.3.7) and the output for telemetry is analog.

Alternative 3, Figure 3.3.8 and 3.3.9 uses a low-drift integrator as the accumulator. As Figure 3.3.9 suggests, the weights are set either by various resistors for each sample or by different time Δt_i spent on each sample E_i. The output for telemetry is analog again.

3.3.2 Breadboard System.- The actual breadboard electronic processor is designed to process the signal as outlined in Section 3.3.1 with the following parameters:

Maximum scan length ΔS_{max} = 1000 fringes

Maximum number of sampling points = 64

Sampling interval width ΔL = 1 to 63 fringes

Number of scans to be evaluated = 1 to 999

Weighting coefficients = 128 12 bit numbers

Processing accuracy: better than $1:10^{-3}$ between samples +
better than $1:10^{-2}$ long term

Two alternative solutions were worked out, see Figure 3.3.10, Hardware Solution, and Figure 3.3.11, Minicomputer Solution.

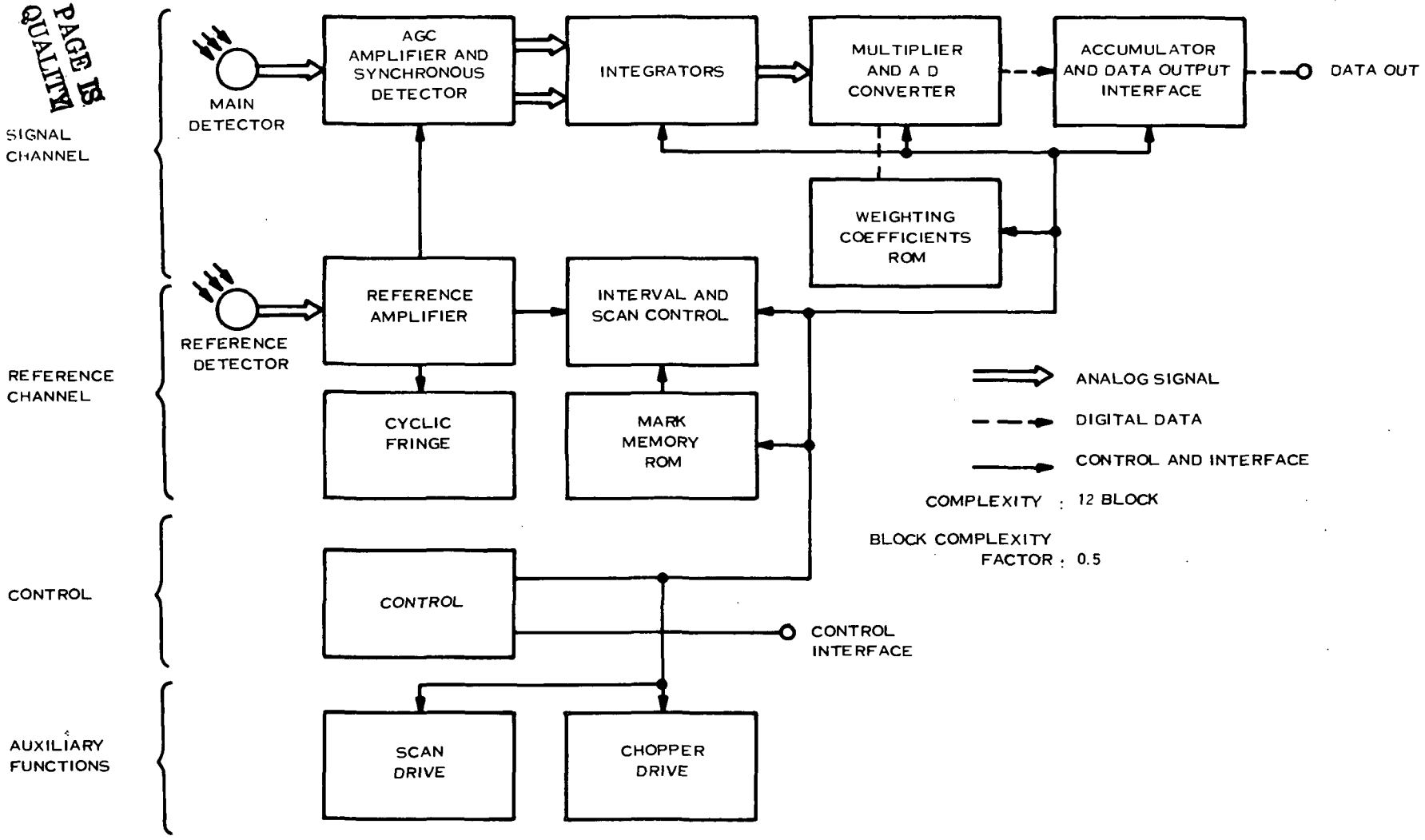

Figure 3.3.5. Satellite Electronics, Alternative I, Hybrid Data Processing

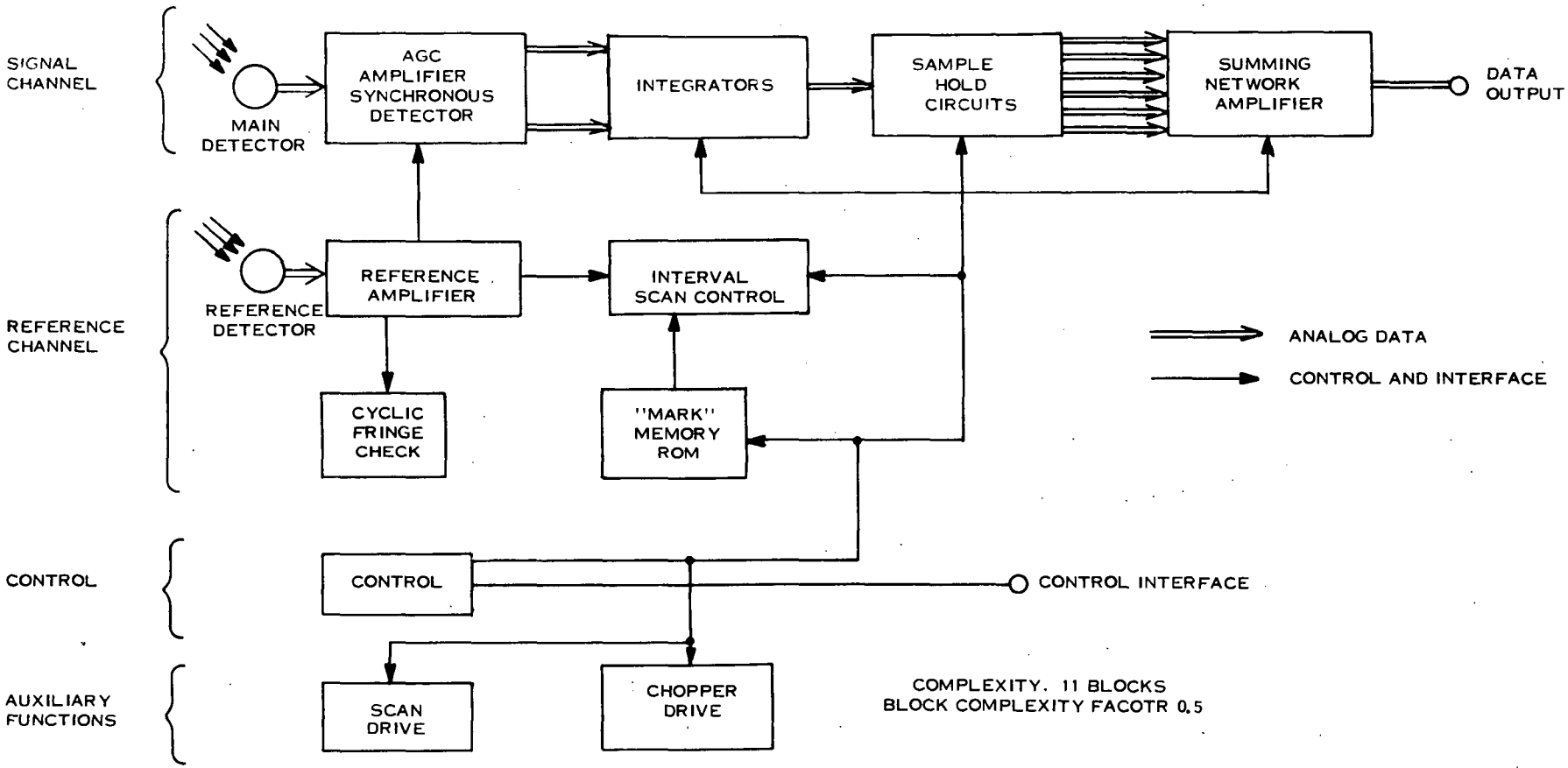

Figure 3.3.6. Satellite Electronics, Alternative II, Analog Processing 1

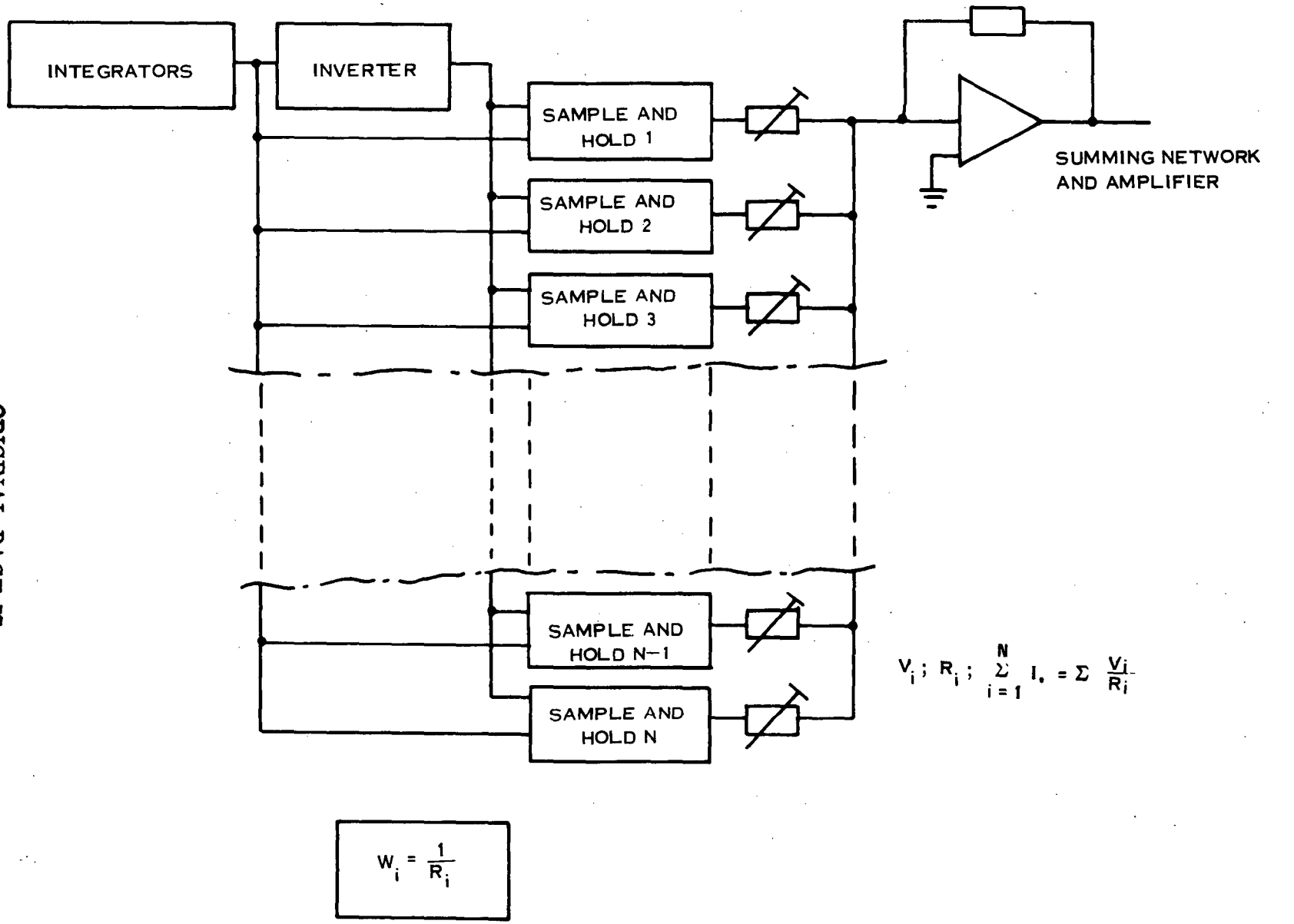

Figure 3.3.7. Satellite Electronics, Alternative II, Summing Network

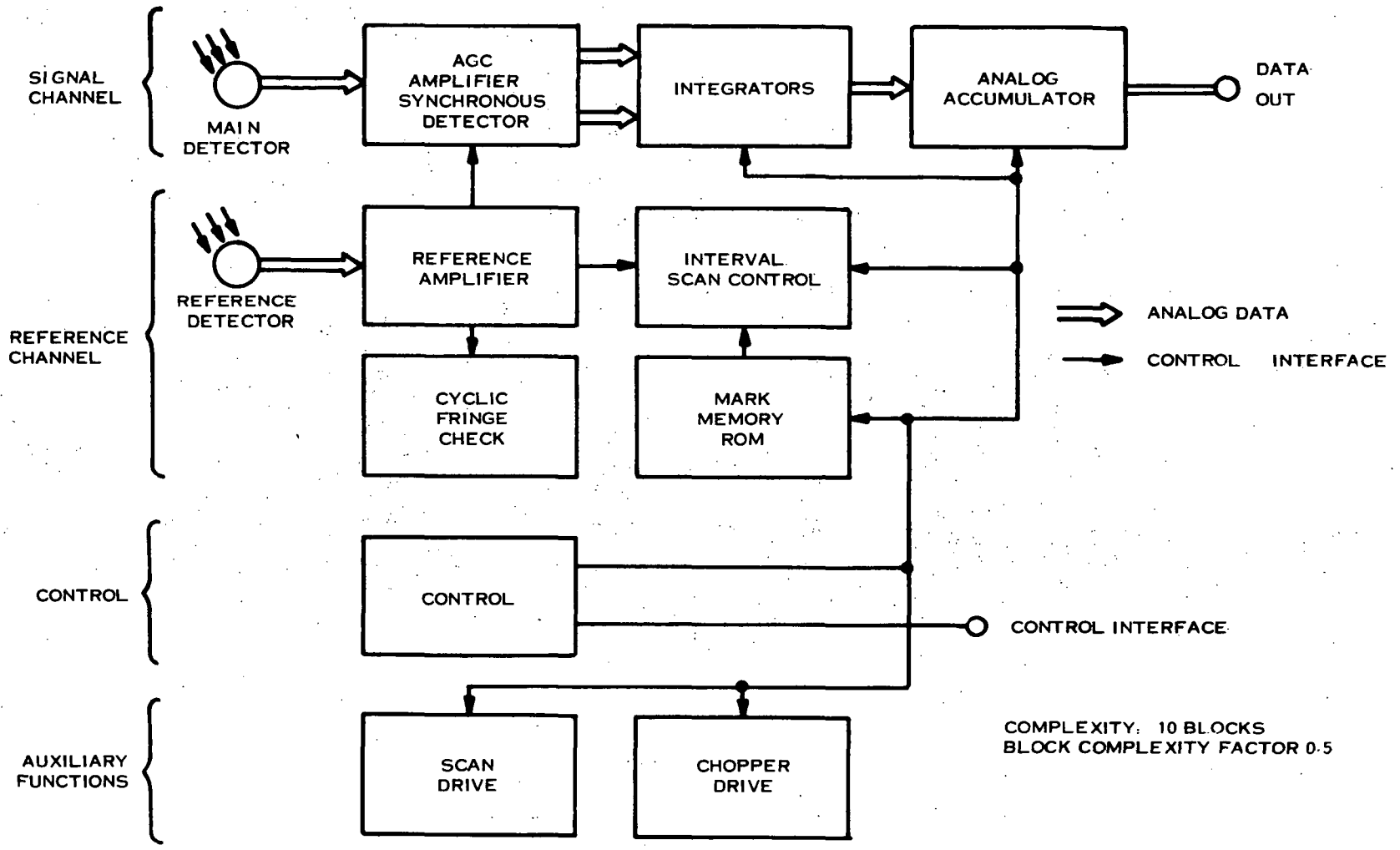

Figure 3.3.8. Satellite Electronics, Alternative III, Analog Processing 2

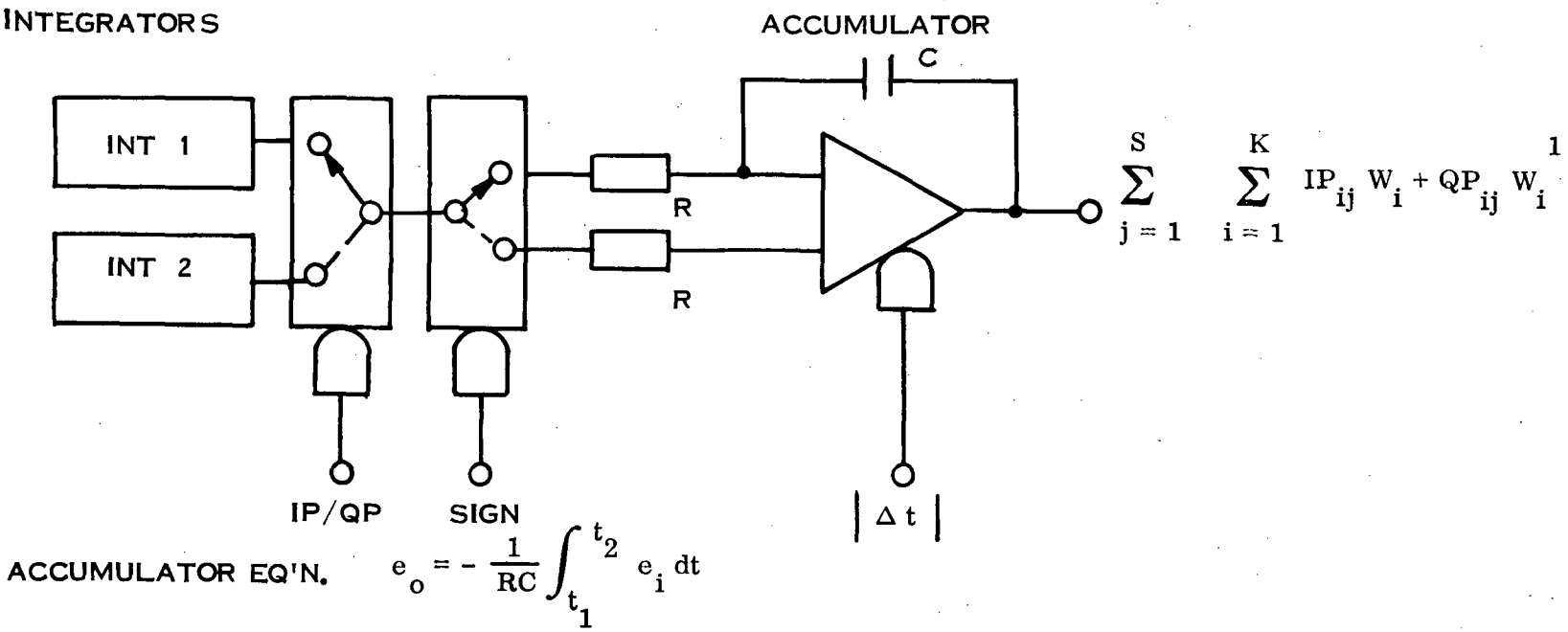

FOR $e_i = E_i = \text{CONST.}$

$$E_o = -\frac{1}{RC} E_i (t_2 - t_1)$$

1. EITHER SET

$$t_2 - t_1 = \Delta t_i = W_i$$

$$E = \sum E_o \approx \sum E_i W_i$$

2. OR SET

$$W_i = \frac{1}{R_i}$$

$$E = \sum E_o \approx \sum \frac{1}{R_i} = \sum E_i W_i$$

Figure 3.3.9. Satellite Electronics, Alternative III, Summing Network

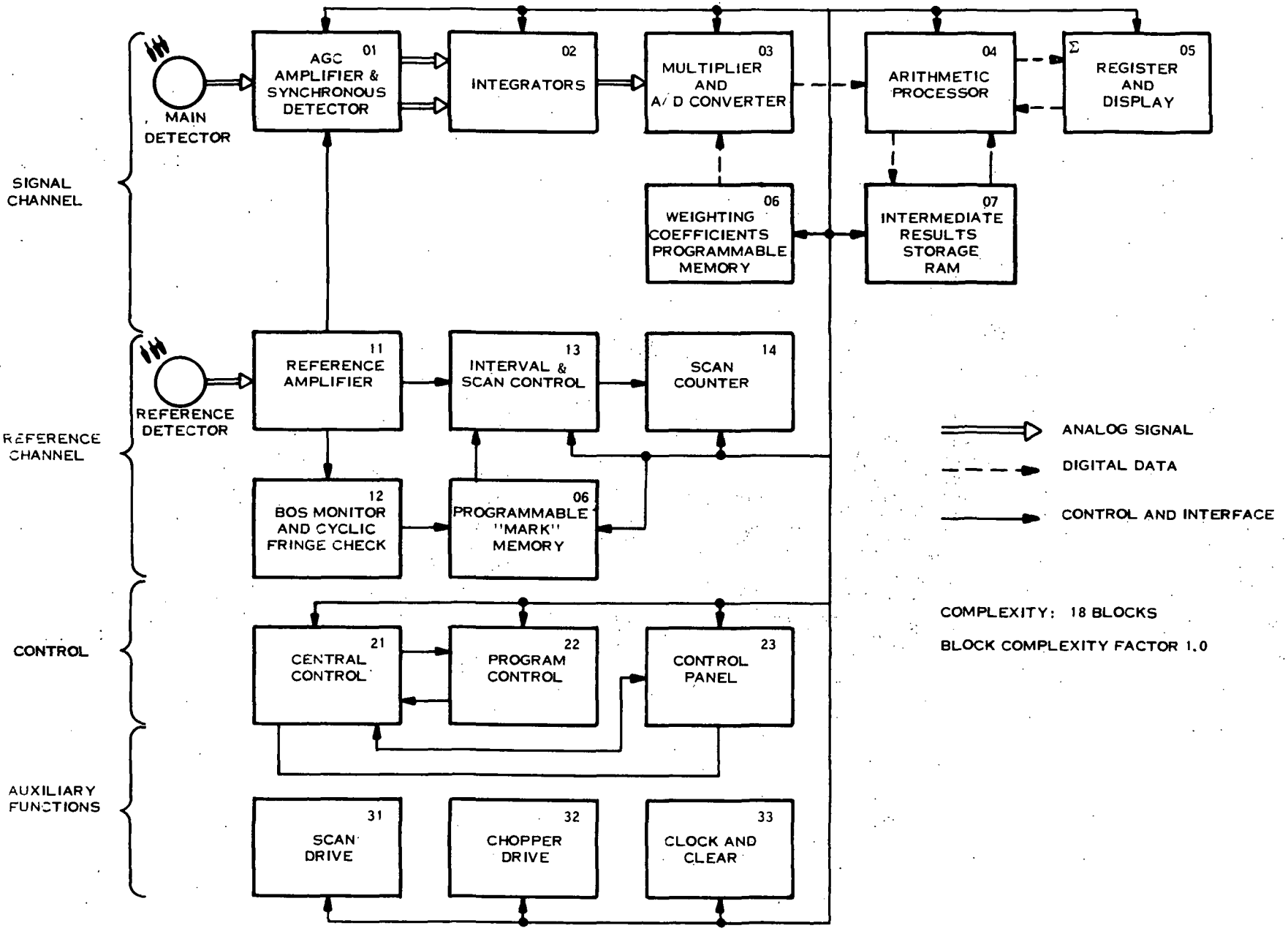

Figure 3.3.10. Breadboard Electronics, Alternative I, Hardware Solution

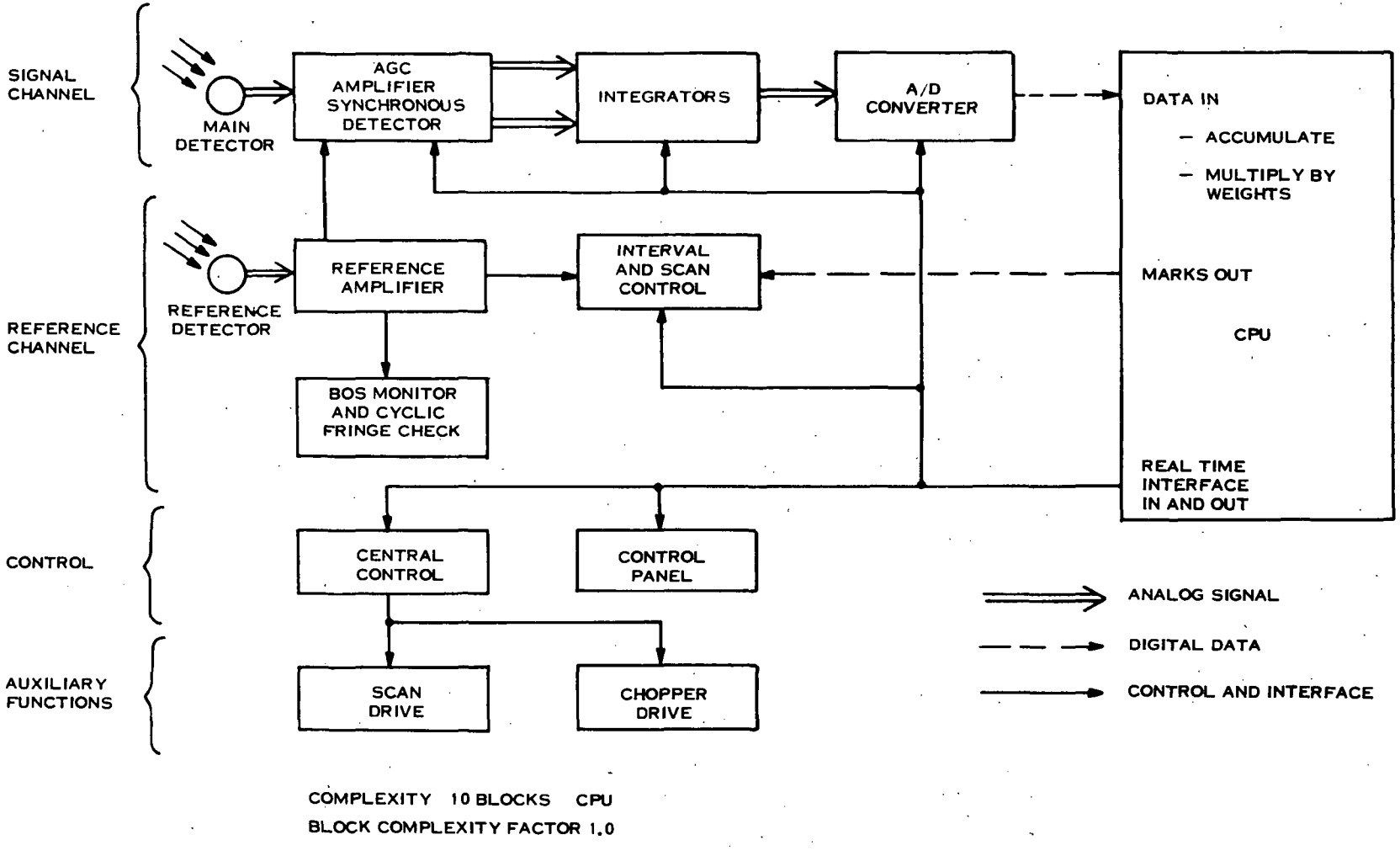

Figure 3.3.11. Breadboard Electronics, Alternative II, Minicomputer Solution

The first scheme consists of 18 building blocks, their complexity given by the above outlined specifications. Comparative complexity factor set to 1.0.

In the second scheme, a commercial minicomputer replaces 8 blocks (complexity factor being the same, 1.0) taking over arithmetic processing, memory and control functions.

Minicomputers capable of real time processing of the interferometer output are presently available at prices below $10,000. Costs involved in building either system are essentially the same. However, the minicomputer scheme offers higher capacity of memory and arithmetic processing and vast amount of added flexibility in setting experiment parameters, which may be varied simply in software, compared to the wired-in program of the hardware scheme. For these reasons, the minicomputer approach was adopted for the breadboard. The choice of the Data General Nova computer was based on the cost/performance indices for units with 16-bit word length costing less than $10K.

The following is a brief description of the Hardware Solution (Figure 3.3.10) and shows its increased complexity compared to the Minicomputer approach.

The signal channel consists of the AGC amplifier and synchronous detectors (01), integrators (02), multiplier and A/D converter (03), Arithmetic Processor (04) Σ Register and Display (05), Weighting Coefficients Programmable Memory (06) and Random Access Memory (07). The functions are as outlined in Section 3.3.1 and the circuits incorporate various control inputs, check and error indicating and other auxiliary circuitry. The structure of the arithmetic processor and memory, as constituted by modules 94, 05, and 07 is illustrated in Figure 3.3.12.

The reference channel contains the Reference Amplifier (11) including a differentiator. This module produces the in-phase and quadrature-phase reference for synchronous detectors. Module 12 generates the Beginning of Scan (BOS) pulse, monitors its positions relative to the reference interferogram and checks that the number of fringes evaluated in consecutive scans is the same. Module 13 counts the fringes of the reference interferogram, regarding BOS as origin, compares the fringe number with the numbers stored in the "Mark" memory (equivalent 06) (End of Integration) marks, maintaining the set integration interval width. The Scan Counter (14) counts the processed scans and generates the EOO (End of Operation) signal.

The control channel consists of three modules. Central Control (21) receives manual commands as well as responses of the system. It distinguishes 4 modes: STOP, START, OPERATION and INTERRUPT. It also contains 8 error memories to indicate the source of error within the system and interrupt the operation. Program Control (22) generates the routines for handling data after the end of each period of integration. The example of routines RUN1 and RUN2 is in Figure 3.3.13.

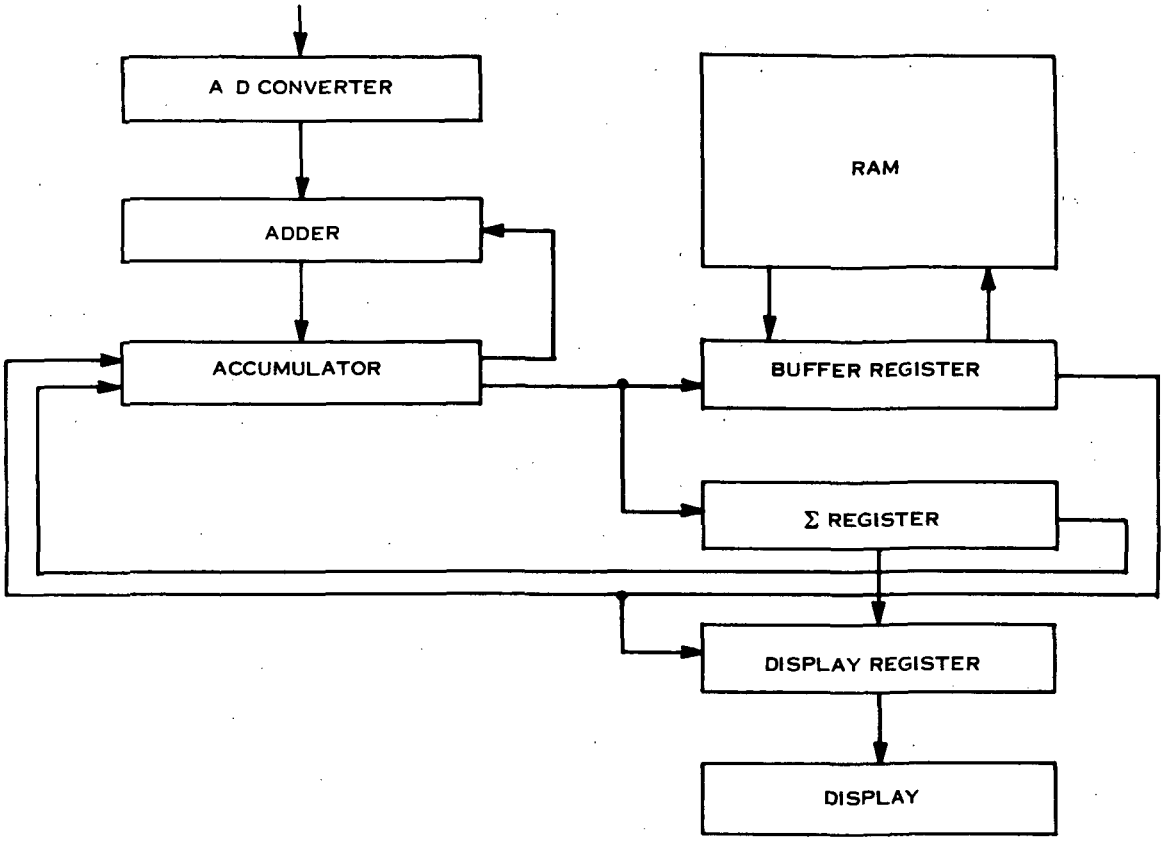

Figure 3.3.12. Arithmetic Unit Structure

The Control Panel (23) contains necessary manual controls and displays and makes the human control of the experiment possible.

Auxiliary functions are the following modules: Scan Drive (31), Chopper Drive (32), Clear and Clock Generator (33).

The breadboard design is based on wide use of transistor-transistor logic integrated circuits employing small-scale and medium-scale integration. To keep the breadboard cost reasonable and within budgetary limits, the commercial grade devices (0-70°C) temperature range were selected. The suggestions to use the same technology as for the actual satellite borne instrument was rejected for the following reasons:

1. The space verison is to be, hopefully, so far simplified, that it would resemble the breadboard very little and a completely new design, based on experimental data obtained in breadboard experiments, will be necessary anyway.

2. The idea of taming new technology could not justify itself boosting the breadboard costs many times. However it is assumed, that the design of the engineering model will implement all characteristics of the final space instrument, being as identical as possible.

Routine RUN 1 is initiated by EOI command in OPER mode:

	Program Counter		Instruction No.
RUN 1	1	READ RAM (A)	3
	2	BR TO AC	7
	3	CLEAR IF SZERO	0
	4	CONVERT	1
	5	ADD	2
	6	AC TO BR	5
	7	WRITE RAM (A)	4
	8	E TO AC	8
	9	CLEAR IF AZERO	12
	10	ADD	2
	11	AC TO E	6
	12	IF A0-1 RESET INTEGRATORS	11
	13	IF EOS DISPLAY E	10
	14	INCREMENT A	13
	15	IF A0=0 PAUSE 1	14
	0	CONTINUE	

Routine RUN 2 is initiated by the manual DISARM command in STOP mode:

RUN 2	1	READ RAM (A)	3
	2	BR TO DR	9
	3	PAUSE 2	15
	0	CONTINUE	

Figure 3.3.13. Routines: RUN 1 and RUN 2

Compared with the above, the Minicomputer Solution (Figure 3.3.11), actually used for the breadboard is much simpler, in that blocks 04 through 07, part of block 03, blocks 21, 22, 33 and most of 23 of Figure 3.3.10 are replaced by the Nova. The functioning of the remaining blocks is as described above for the hardware version.

Complete details of the breadboard electronic circuits, consisting of 12 plug-in cards plus 3 preamplifiers, power supplies and inter-card wiring is shown in Appendix C.

4. BREADBOARD CONSTRUCTION AND TESTING

4.1 Optical/Mechanical

The first step in construction of the breadboard was the fabrication of the interferometer frame from ultra low expansion (ULE) titanium silicate.* The process consists of machining the top and bottom plates and the pillars roughly to size, building up the structure by hand, and heating it in a furnace until all the parts fuse together to give a monolithic structure. This is then machined to dimensions and the required holes are drilled. This fusing process has been used to fabricate many large light-weight mirror blanks and similar structures.

While the fusing process worked well, the manufacturer experienced considerable difficulties in the finishing operations. The first frame was accidently damaged while being unwaxed from a holding fixture between steps in the machining. The second ULE frame was found to be grossly out of tolerance on many dimensions and to have several cracks. These cracks had occurred during machining of the piece after fusing and appeared to be due to excessive cutting speeds and improper support of the piece during machining. Although the cracks had been stopped by drilling, they were so extensive as to seriously weaken the structure. Further, the many dimensional errors would have necessitated extensive rework of mating mechanical components and the inclusion of extra spacers at the fixed mirror, which would further compromise the stability of the system. Design and drawing of these modifications was carried out in order to cover the contingency that the overall program schedule would not allow time for fabrication of a replacement frame. However it was decided that the frame should be rejected and the manufacturer was requested to provide a replacement.

In view of the paramount need to minimize delay to the program it was decided to have the frame bonded with adhesive rather than fused. This reduces the time to produce a frame from six weeks to two weeks. Also, according to the manufacturer, it is easier for them to maintain control of dimensions by machining the top and bottom plate of the frame as a pair, prior to assembly and this procedure also minimizes the risk of damage during machining.

In spite of the difficulties encountered by the manufacturer, the manufacturer is completely confident that they can make a fused frame of ULE titanium silicate given a reasonable time scale, the experience gained in the production of the breadboard, and more refined methods of machining.**

---

*Carried out by Corning Glass, Rensslear Falls, New York.
**This was verified in subsequent work.

Prior to producing the bonded frame a sample bond was prepared using two pieces of ULE material using Eastman Kodak 910 adhesive, which they use routinely for bonds to ULE. After bonding the test sample was examined for strain by polariscope and showed no detectable strain. The sample was treated in tension and the ULE material failed before the bond.

The completed, bonded, replacement frame has no visible flaws other than a slight chipping of some non-critical edges and all dimensions are within tolerance.

The reject frame was used to test the moveable mirror mount and the scan plate damper and to gain experience with the technique of grinding the locating surfaces on the beamsplitter locating studs. The ULE material grinds quickly and easily using the traditional methods with silicon carbide grit, water and a metal tool.

The three beamsplitter locating studs were ground until they defined a plane, which to a tolerance of ± 0.01 inch, bisected the angle formed by the two sides of the frame which were to locate the mirrors. The locating surfaces have about a 10 inch cylindrical radius and a #400 grit finish. Next, the 4 sets of invar pads were epoxied in place on the frame, viz the three on the underside for the kinematic attachment of the frame to the metal chassis, the three studs which hold the magnets for the scan plate damper, the clamp blocks for the fixed mirror and the pads which locate the adjusting screws for the movable mirror. The mirror locating pads are attached in such a way that there is no epoxy between the surfaces which control the length of the interferometer arm.

Next the mirrors were attached to the frame and a metalized glass beamsplitter temporarily installed. This allowed the mounting points on the chassis for the ULE frame to be aligned so that the axes of the interferometer (i.e., the normal to the fixed mirror through the center of its aperture and the reflection of this axis in the beamsplitter) coincide with the axes of the mounting for the input and output lenses, within $\pm$ 1 mm on position and $\pm$ 5 milliradians in angle. Due to the kinematic nature of the mounting, the ULE frame can now be removed from and replaced in the chassis without losing this alignment. Following this alignment process, which was carried out using a visible laser, inclusion of a beam expander, a diffuser and a positive lens in the beam produced Haidinger fringes. These afforded a qualitative test of the mirror adjustments. The minimum adjustment achievable on the micrometer was found to be about 1/4 fringe and the tilt adjustments permitted production of distinct fringes over the entire 5° diameter of the source. The elastic and kinematic nature of the mirror mounts was also confirmed; if a load was applied to the mirrors and removed the phase at the center of the fringe pattern returned to its original state.

The glass beamsplitter was then removed, the installation of components on the ULE frame completed and the frame installed on the chassis along with the silicon input and output lenses. Observation of auto collimated images in the focal planes of the lenses (Figure 4.1.1) produce the plots shown in Figure 4.1.2. These indicate that for a 5%

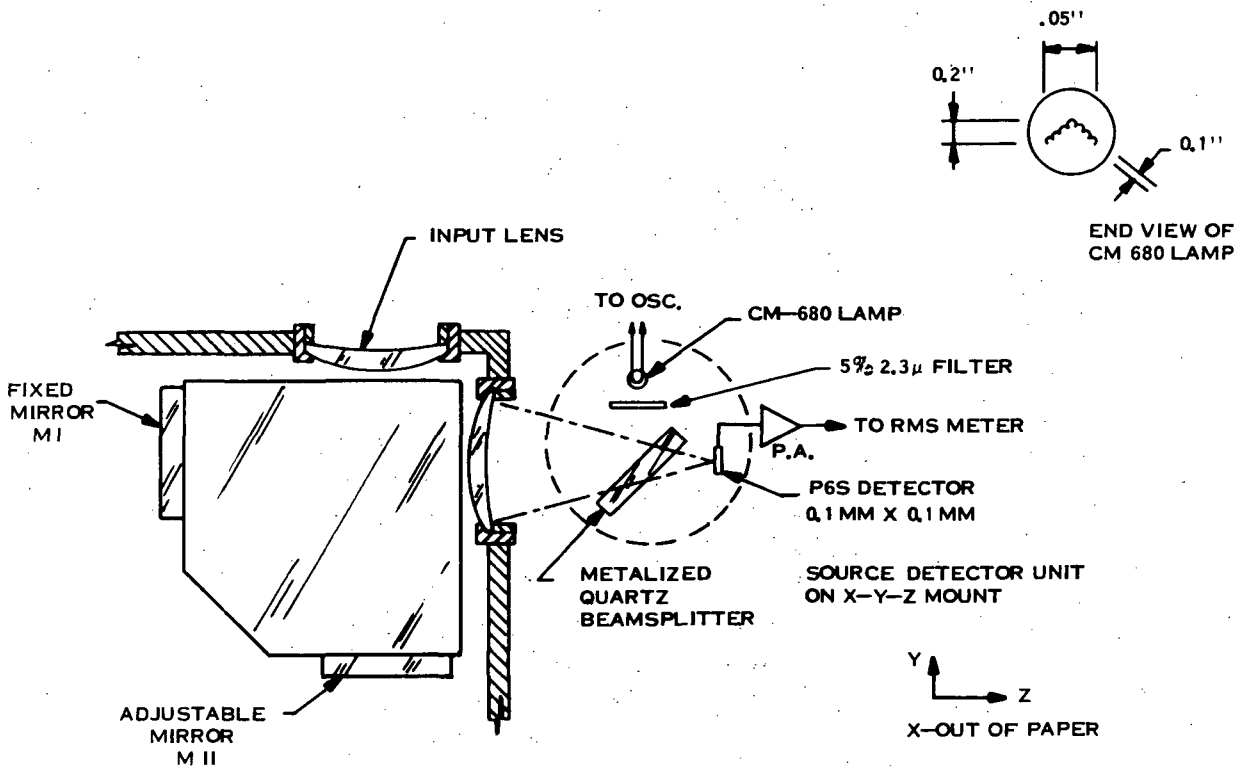

Figure 4.1.1. Measurement of Aberration

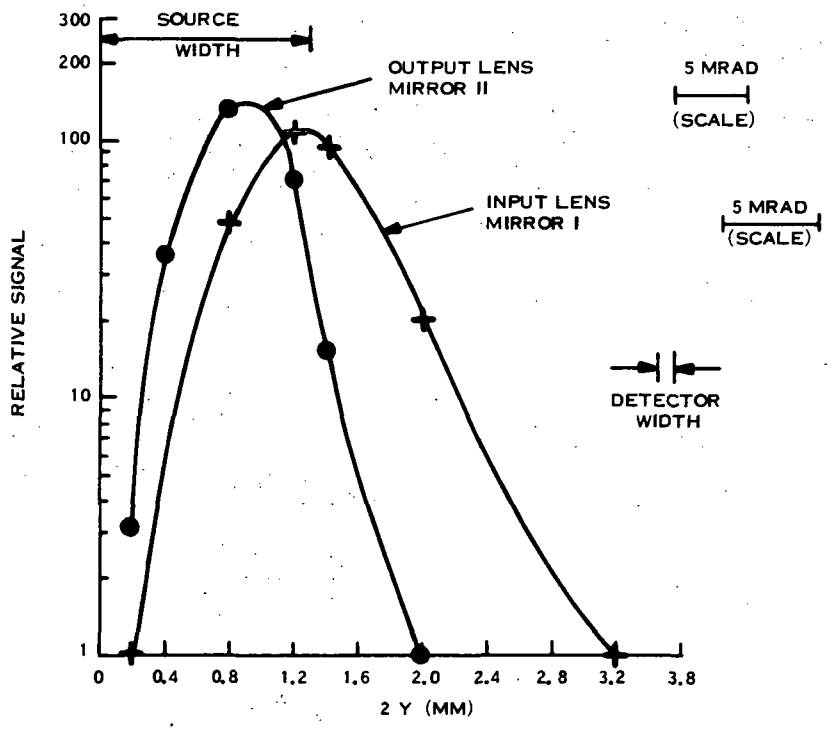

Figure 4.1.2 Lens Aberrations

spectral bandwidth at 2.35 microns, the on-axis abberations of the lenses are such that 90% of available power falls within 5 milliradians of the Gaussian image. The lens abberation from a ray trace is 3.3 milliradians.

From the relative amplitudes of the returns from the two mirrors, the reflectance: transmittance ratio of the beamsplitter was found to be 65:35 which gives an efficiency of 0.23 compared to the theoretical maximum of 0.25 and the design goal of 0.21.

Following these tests the 2.3 micron detector was installed and aligned so that its image, as seen in the focal plane of the input lens, was centered on the system axis and sharply defined. The image at this plane is 16 mm between 50% points which, allowing for the 1.3 mm width of the source used, indicates a field of view of 0.122 radian; the design figure is 0.12 radian.

The next major step, involving considerable time and effort was interferometric alignment and the measurement of fringe visibility. The initial alignment of the instrument is greatly complicated by the absence of visible transmission in the silicon optics, which were chosed as the cheapest, lightest and strongest method of achieving 4.6 micron capability. The lack of visible transmission prevents the step from "geometric" to "interferometric" alignment of the mirrors from being made by the usual method of visual observation of monochromatic wedge fringes localized on the mirrors. An attempt was made to align the mirrors using the 4321.611 cm^{-1} Argon line produced in a microwave excited plasma as described by Humphreys and Paul (ref. 10). However, the energy obtainable was low, and fluctuated due to plasma instabilities. Also, the geometry of available cavities and discharge tubes made it difficult to obtain a sharply defined source. Alignment was finally achieved as follows: the adjustable mirror was moved to the computed position for zero delay, and then very carefully aligned with the fixed mirror by superimposing the autocollimated images from both mirrors at the focus of the input lens. The exit slit of a 1/2 meter Ebert spectrometer illuminated by a quartz-iodine lamp was then used as a source, the scanning plate was oscillated and the adjustable mirror slowly scanned in delay until the zero delay fringes were found. The 300 1/mm grating and 1/2mm slits of the spectrometer made it a .1% bandwidth filter, so that the fringe pattern was visible over at least 2mm of delay. Having secured approximate alignment, the spectrometer was replaced by a variable-diameter diffuse source on an x-y-z mount and a chopper disc. Fringe visibility measurements were then made for several spectral filter widths and field and aperture stop sizes. Since the ground quartz plate used as a transmitting diffuser was not Lambertian over the full f/1.8 cone of the entrance optics, its use was confined to measurements at small aperture stops. To measure the visibility at full aperture the lamp was used directly.

Three parameters affecting visibility were noted:

1. Finite field of view: as shown in Figure 4.1.3, the fact that the system is field widened at 3 mm does not imply the same field at zero delay: with the finite size of sources used in these tests the visibility would not be expected to exceed

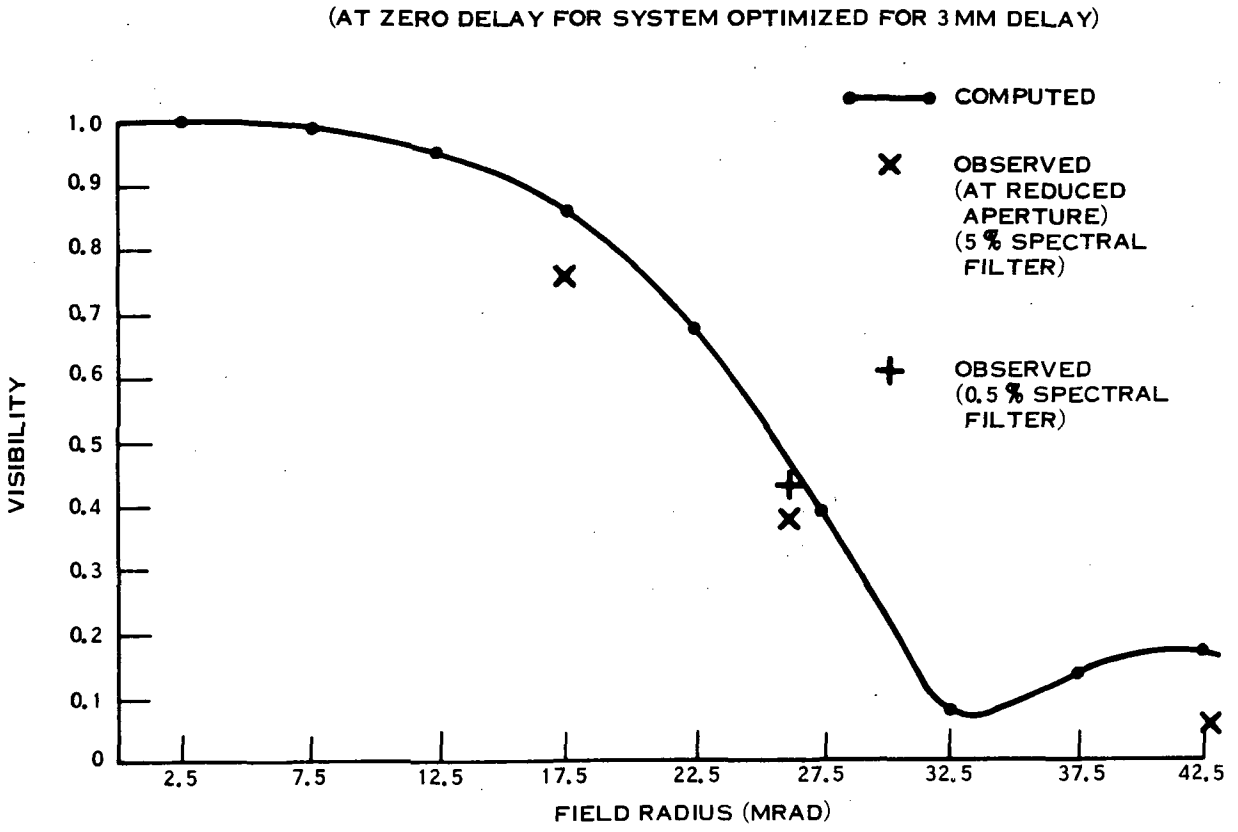

Figure 4.1.3. Visibility as a Function of Field Angle

70 to 80% and in fact, values just less than this were observed at reduced mirror aperture. Some of the reduction is due to the dispersion effects mentioned below. Since the transmission of the arms is equal within 5%, the only other effect which could reduce visibility at small mirror apertures would be polarization.

2. Dispersion: the effect of the variation in refractive index with wavelength is to distribute the modulated power through the interferogram (sometimes referred to as "chirping"). Since there is no longer a unique zero delay the maximum observed visibility is reduced while that at other points is increased. For the same (small) field and mirror stops the following were observed:

Bandwidth	20%	5%	0.5%
Visibility	31%	56%	67%

3. Mirror Aperture: as the mirror aperture is increased, the visibility decreases, so that, with the 0.5% filter, the visibility at full aperture, 34 mrad. field diameter and zero delay, is 34%. The theoretical maximum for a field of this size is 85% (see Figure 4.1.3).

The differential delay across the aperture, which causes this reduction in visibility, is shown in Figure 4.1.4. The principal effect is a roughly parabolic variation across the aperture. Since it is unaffected by changes in the spring pressures which locate the optical elements, the variation is not due to any deformation of the elements by mounting stresses. Neither can be due to departure from flatness in the elements, since it would require 3/10 of a visible wave error in the silicon elements or 7/10 wave in the mirrors and all these elements are 1/8 wave or better. The most probable cause is the combination of the lens abberrations and the absence of field widening at zero-delay. From Figure C.3 it is seen that the observed visibility would be expected if the off axis aberrations were sufficient to increase the field radius by 10 mradians. From the ray trace, the effective field from a 34 mrad diameter field stop is about 45 mrad diameter, which would give a visibility of 60% so that the observed visibility is only partly accounted for. However, the source size (34 mrad) quoted above is from a visible estimate of the size of the radiating portion of the lamp filament and this must be smaller than the effective source at 2.35 microns. If the 2.35 micron source is 1.2 mm larger than the visible, this is enough to account for the observed visibility.

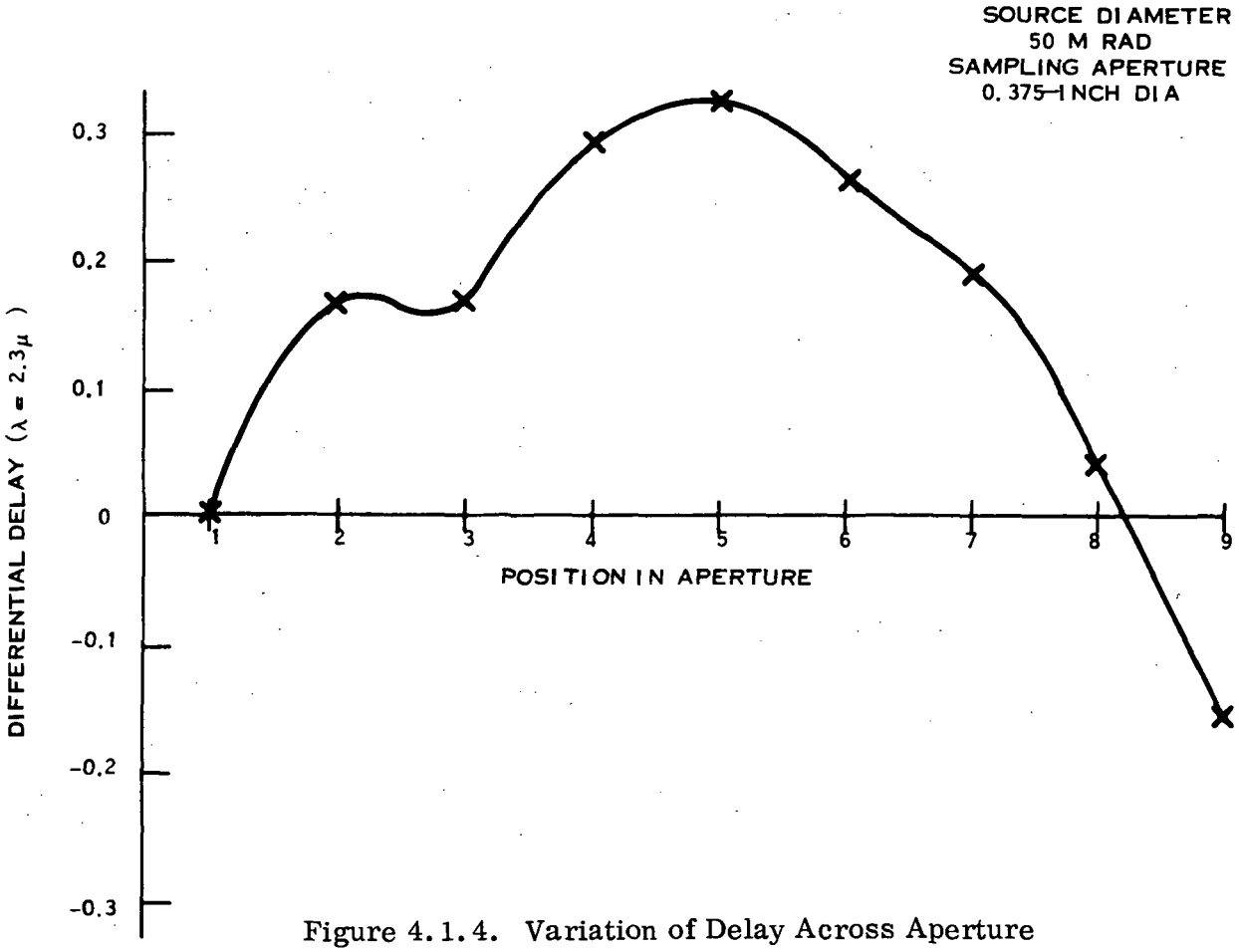

Figure 4.1.4. Variation of Delay Across Aperture

As well as the major parabolic variation in delay there are two smaller features. The rapid change near positions 2 and 3 indicates a small local deformation of one of the optical elements corresponding to a thickness variation of about 1/10 of a visible wavelength, if it is in the scan plate or beamsplitter. This is not significant, being within the 1/8 wave specified for these elements. The assymetry of .15 of the working wavelength indicates a residual wedge between the mirrors of .18 microns, which is not necessarily the direction of maximum wedge.

Having completed interferometric alignment opto-mechanical assembly was completed by attaching the telescope (fore optics) to the chassis. Prior to its installation, the telescope was aligned so that:

1. The center of curvature of the primary is on the axis of the telescope tube.

2. The reflection of the tube axis in the primary and secondary mirrors is coincident with the optic axis of the input lens, within 4 mrad.

3. The focal plane of the telescope coincides with that of the input lens of the interferometer.

With the telescope installed, the reference channel could be aligned for maximum signal amplitude. When this was done there was found to be considerable radiation leakage from the reference channel into the main channel, due principally to scatter in the field lens and windows at the telescope focal plane and in the reference channel source enclosure. This scattering occurs before the light has traversed the reference gas cell, so there is no contribution to the main channel interferogram, but, since it is modulated by the AGC chopper, it offsets the AGC setting for the main channel so that at low light levels, the gain is no longer inversely proportional to the incoming radiation level. By reducing both the aperture and field stop of the reference source optics, it was possible to reduce the leakage to 300 mv peak to peak at the preamplifier output which is less than the lowest level (expected during outdoor operation). However this was achieved at the expense of the S/N ratio in the reference interferogram, with the result that the absolute delay reference circuit would no longer reliably identify a maximum in the reference within the range ($\pm$ 3 fringes) which is required if it is to be used to provide a Beginning of Scan pulse. However, the S/N was still sufficient to permit scanning over the region of the CO signature without having extra or missing transitions in the square waves, derived from the reference, which are used to determine sample length..

These difficulties would have been avoided if the reference radiation had been injected near an aperture stop and had not shared the field stop with the main channel. The arrangement used was chosen so that both systems would use the same spectral filter and the same field of view.

However, it was observed during the thermal testing that changing the filter temperature did not significantly affect the phase of the reference relative to the scan plate position so there would seem to be no objection, in future versions of the instrument, to use separate filters permitting much better separation of the channels.

Some modifications were also required to the plate position sensor. Originally it was intended to use a light source to give a 10 micron spot which was to be chopped by a 500 lines/inch recticle as described in Section 3.2.2. However the light level provided by the source was too low for satisfactory S/N without going to the complication of a modulated source and A. C. circuitry. Accordingly, this source was replaced by a 0.002 pinhole illuminated by an LED. This did not give the pulse train originally envisaged but did give a satisfactory step function for use as a beginning of scan mark. It is possible however that some of the relative movement between the BOS pulse and the reference fringes, seen during cold chamber testing of the breadboard, may be due to the plate position sensor. These changes, though not serious, were larger than expected on the basis of the thermal properties of the interferometer itself. In subsequent instruments, several straightforward changes such as the use of a more powerful collimated LED will greatly increase the sharpness of the step and thus reduce the significance of any temperature effects in the semiconductor.

4.2 Electronic and System

Assembly and checkout of the digital electronics proceeded smoothly and without any changes being required. Apart from the inclusion of a small inductor to suppress high frequency oscillations on the scan drive card, the auxiliary circuits all operated satisfactorily as designed.

In the analog circuitry, several problems were encountered, the first being in the main preamplifier. Before the PbS detector was fabricated, the manufacturer had indicated that the impedance would lie in the range 10 to 50 megohms and thus the preamp was designed accordingly. In fact the detector is 4M when cooled, necessitating changes from the original circuit. These involved the use of low-current-noise metal-film resistors, the selection of FET's for low noise and input protection diodes for low leakage, and an increase in the value of gate resistors. In its present form the preamp with a 4M low-noise resistor in place of the detector has a noise density referred to the detector terminals of

$$0.207\ V/Hz^{1/2}$$

Combining the Johnson noise of the effective source impedance (2M), the 60 $\mu V/Hz^{1/2}$, given by the manufacturer as the voltage noise generators of the dual FETS which form the differential input stage and the Johnson noise of the resistors on the second input gives

$$0.209\ \mu V/Hz^{1/2}$$

With the cooled detector connected (unbiased) the noise is 0.170 $\mu V/Hz^{1/2}$ and with 125 volts bias applied the noise is 0.185 $\mu V/Hz^{1/2}$. This indicates that the optimum operating point is in the region of 100 volts bias, as suggested by the manufacturer.

A second problem in the analog circuitry was the use of detector bias for AGC. This proved impractical when the optical head was separated from the main electronics by a 50-foot cable, due to noise pick-up on the lead carrying the bias which was fed from a high impedance source. This problem was solved by using fixed bias and using a variable gain amplifier. This had the simplifying advantage that the same circuit could be used with the 4.6 micron detector which is operated at zero bias.

After these changes had been made a signal/noise calibration was carried out on the detector preamp combination. The light source was a 0.04 inch diameter aperture illuminated by a ribbon filament tungsten lamp. Since the distance from the aperture to the detector was 118.75 inches and from the aperture to the 3mm lamp-filament was 1.5 inches the aperture formed the effective source. The source radiance was computed from the relation between lamp current and colour temperature provided by the lamp supplier (Canadian General Electric), the emissive properties of tungsten given in the Smithsonian Tables and an auxiliary measurement of the transmission of the glass envelope at 2.3 microns. The measured NEP for the detector/preamp combination was 1×10^{-12} watt/$Hz^{1/2}$ at 125 volt bias. This is within specification but not as good as the value (5.6×10^{-12} watts/$Hz^{1/2}$ claimed by the manufacturer for the detector alone.

Following installation of the telescope, a photometric calibration of the complete system was carried out. The source for the calibration consisted of a sand-blasted aluminum plate (#80 grit), illuminated by a calibrated ribbon-filament tungsten lamp. By a subsidiary experiment it was established that the radiance of the plate (at 2.3 micron) was given by

$$N\ (\text{watts/cm}^2\ \text{sterad}\ \text{cm}^{-1})$$

$$= 0.80\ \frac{H}{\pi}\ \cos\theta_1,\ \theta_2 \qquad (1)$$

where H is the incident spectral irradiance from the lamp (watts/cm^2 cm^{-1}) and θ_1, θ_2 are the angles of incidence and reflection.

For the particular geometry used,

$$N = 9.4 \times 10^{-10} \text{ watts RMS/cm}^2 \text{ sterad cm}^{-1} . \quad (2)$$

at chopping frequency of 700 Hz and with 100 volt bias, the resulting detector output was

$$V = 256 \times 10^{-6} \text{ volt RMS} \quad (3)$$

Now, from measurements made during detector testing, the responsivity at 700 Hz, 100 volt bias is

$$R = 1.41 \times 10^{-5} \text{ volts/watt} \quad (4)$$

thus, from (3) and (4), the power received by the detector was

$$P = 1.81 \times 10^{-9} \text{ watts RMS} \quad (5)$$

Now

$$P = 1/2 \, N \, A \, \omega \, B \, T_1 \, T_2 \quad (6)$$

where

A, the etendue, = 0.36 cm^2 sterad
B, the effective filter bandwidth, = 34 cm^{-1}
T_1, the filter peak transmission = 0.48
T_2, the transmission of the optics (including the relative beamsplitter efficiency, 4 x Reflectance X Transmittance)

thus

$$T_2 = 0.66.$$

The relative beamsplitter efficiency was previously measured as approximately 0.9, so that the combined transmission of the other optical elements is about 0.72. This figure would result if the three mirror surfaces are each about 0.91 reflecting and the six silicon/air interfaces average 0.96 transmitting, which values are within the component specifications. The above measurements were made without the windows on the thermostatic enclosure for the filter; when the transmission of these elements is included, T_2 will decrease to 0.46. Dividing the detector NEP of 1.0×10^{-12} watts/$\text{Hz}^{1/2}$ by 1/2 T_1 T_2 gives the system NEP of 0.9×10^{-11} watts/$\text{Hz}^{1/2}$ at the preamplifier output.

Thermal testing of the system was carried out in a coolable environmental chamber. Initially it was found that a rearrangement of the heating elements was required to avoid large temperature gradients. When this was implemented, the following results were obtained. In a 10°C environment, the heating systems are capable of maintaining both the interferometer and filter enclosures at 28 $\pm$ 0.5°C or better, after a 90 minute stabilization period (the environment temperature was lowered, from 22°C at switch-on, to 10°C in less than 10 minutes). The shift between the mechanically derived Begin of Scan pulse and the reference interferogram was less than 1/4 fringe while the temperature was stabilized. When the environment was returned to 22°C, the interferometer enclosure temperature rose briefly to 33°C and during this time the BOS pulse advanced 1.75 fringes and then returned by 1/4 fringe, to the same position as it occupied before cool down of the environmental chamber.

Following environmental testing, the electronic system was connected to the NOVA and no difficulties were experienced in functioning under program control. Digital accumulation of large numbers of scans revealed some synchronous noises due to pick up of reference waveform and the reference square wave into the signal channel. These were reduced below the detector noise by decoupling of power supplies, rerouting of cables and inclusion of a screen between two of the circuit cards. Following this, methane and CO interferograms were observed using a diffuse source at levels approximating a 20% ground albedo and atmospheric amounts of gas in a 1 meter cell. These runs were used to adjust gains so as to ensure that detector noise dominated and that efficient use was being made of the A.D converter span.

Data taken, using two amounts of methane and three of CO, were used in a limited test of the weight generating procedure. Increments of 0.45 and 0.15 atm.-ctm. were measured with errors of about 5%. A case where the CO was changed by 2 atm.-cm. and the CH_4 by 5 atm. cm., (i.e., very large extrapolations from the cases used to determine the weights), gave errors as much as 50%. As well as involving an extreme change in CO, this case is well outside the limited array of observations used in this preliminary test and thus would not be expected to be measured accurately with those weights.

5. LABORATORY TESTS

5.1 Multiple Chamber Test Facility

The facility was designed to permit spectral absorption measurements to be made to be made by measuring the absorption of the light from an infrared source (globar) as it passed through a series of gas cells filled with appropriate amounts of test gases. The details of the facility are shown in Figures 5.1.1, 5.1.2, and 5.1.3. The facility had previously been tested by obtaining interferograms and spectra with an 0.5 cm^{-1} resolution interferometer spectrometer.

Each of the 4 primary cells which comprise the multiple chamber system is equipped with a vacuum gauge which is used in testing for leaks and with a pair of thermocouples to measure the temperature of the gas in the cell. The cells can be isolated from a common manifold which is used for evacuating the cells and for filling them with the proper gas mixture. An accurate pressure gauge measures the pressure of the gas in the pumping manifold and hence the pressure in the individual cells with the appropriate valves opened. The gauge is a Baratron capacitive sensor, which is a diaphragm type gauge, capable of measuring absolute pressure in the range 0 to 1000 torr with an accuracy of better than 0.5% of the pressure being measured.

The individual cells are constructed from stainless steel tube and are flanged at each end to permit them to be bolted together. The windows, which are clamped between the cells, are sealed with O-rings to provide a leak-free system. Potassium bromide windows were used during the tests at both 2.35 microns and 4.6 microns. The cells vary in length from 1/2 meter to 2 meter and have an inside diameter of 6.3 cm. Cells with a total length of 5 meters can be assembled into a single unit. For this series of tests, however, 4 of the cells, with a total length of 3 meters, were assembled.

Since some cells were cooled below the dew point of the ambient air for certain tests, a short extension cell was placed over the window of an end cell which was operated below the dew point. The cell was evacuated and the end window then remained free of condensation or frost.

Additional cells could be added to the system to introduce the effects of interferring gases such as methane and water vapor. The cell containing the water vapor is temperature controlled and could be heated to 100°C to enable a maximum amount of water vapor to be placed in the 1 meter cell. A "null" cell which contained dry air and was identical to the other two cells was used to eliminate the effect of the windows on the measurements. These three cells were not rigidly fastened to the multiple chamber system and could be individually placed in the optical path quickly during tests.

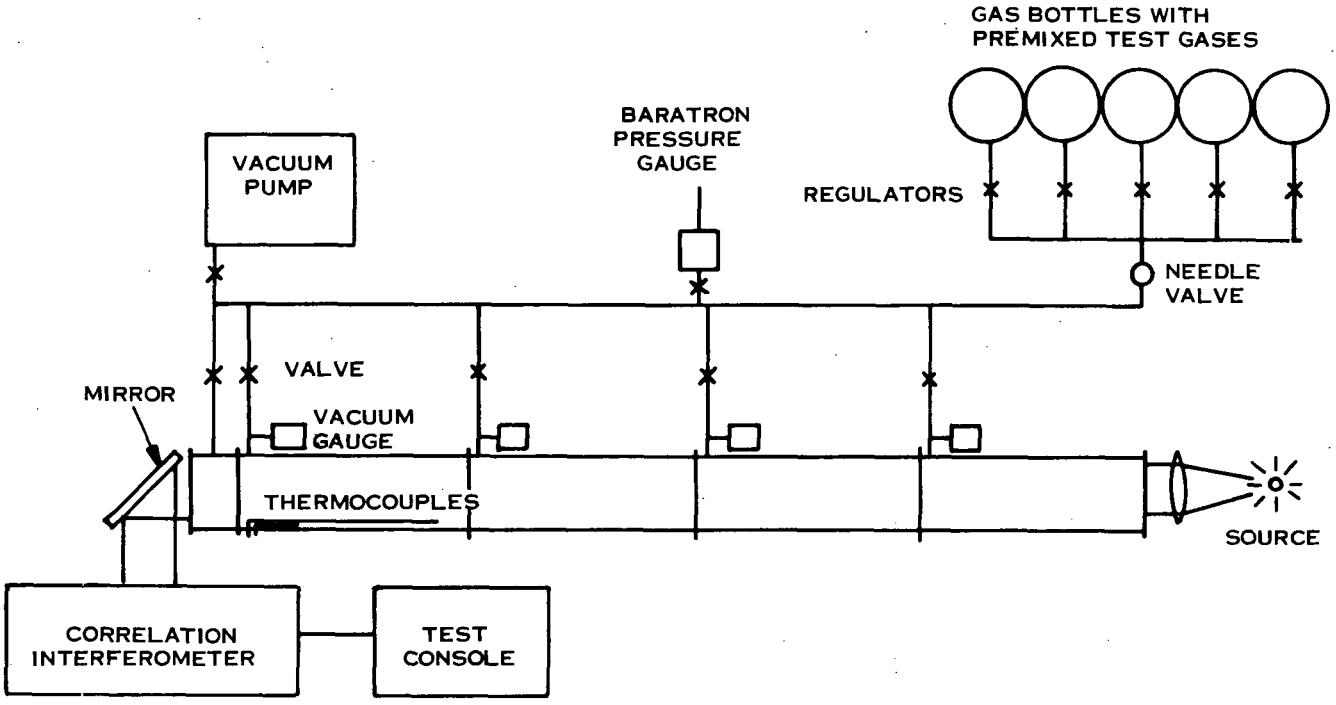

Figure 5. 1. 1. Schematic Layout of the Multiple Chamber Test Facility

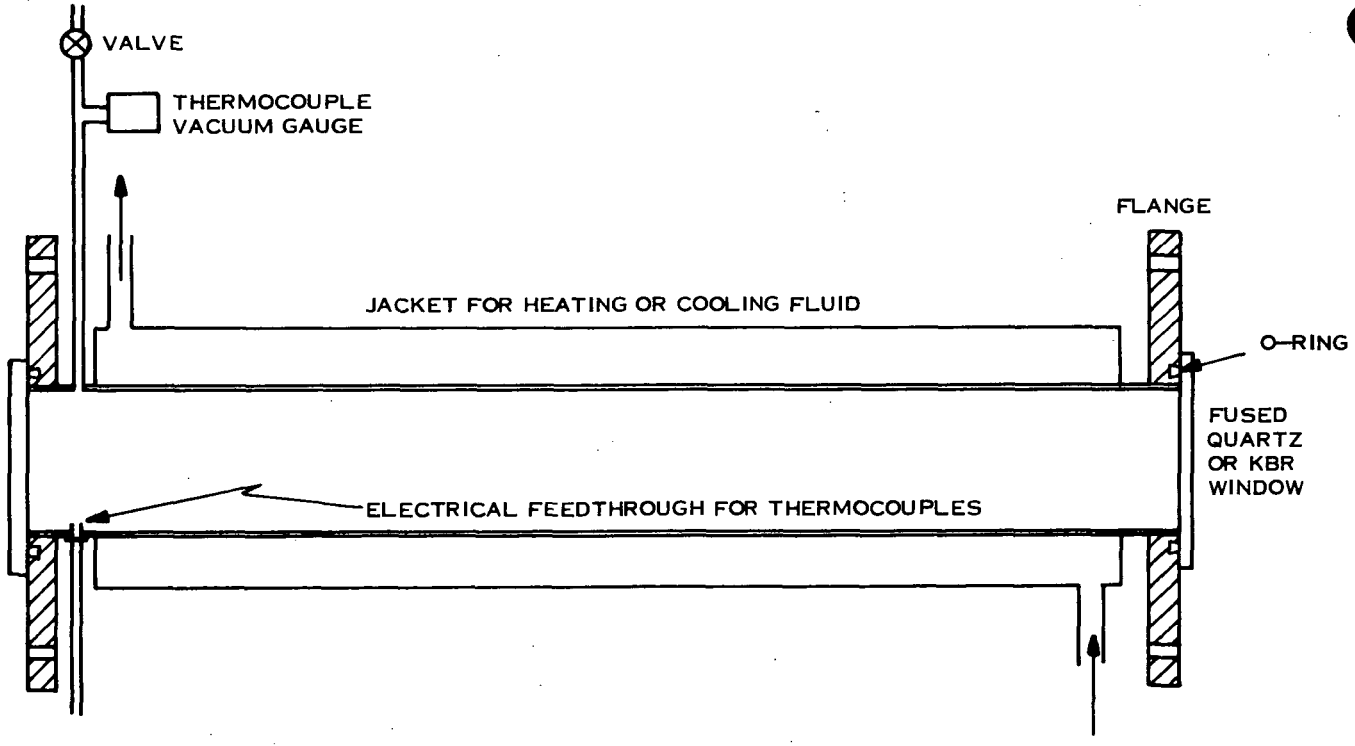

Figure 5. 1. 2. Detail of Individual Absorption Cells

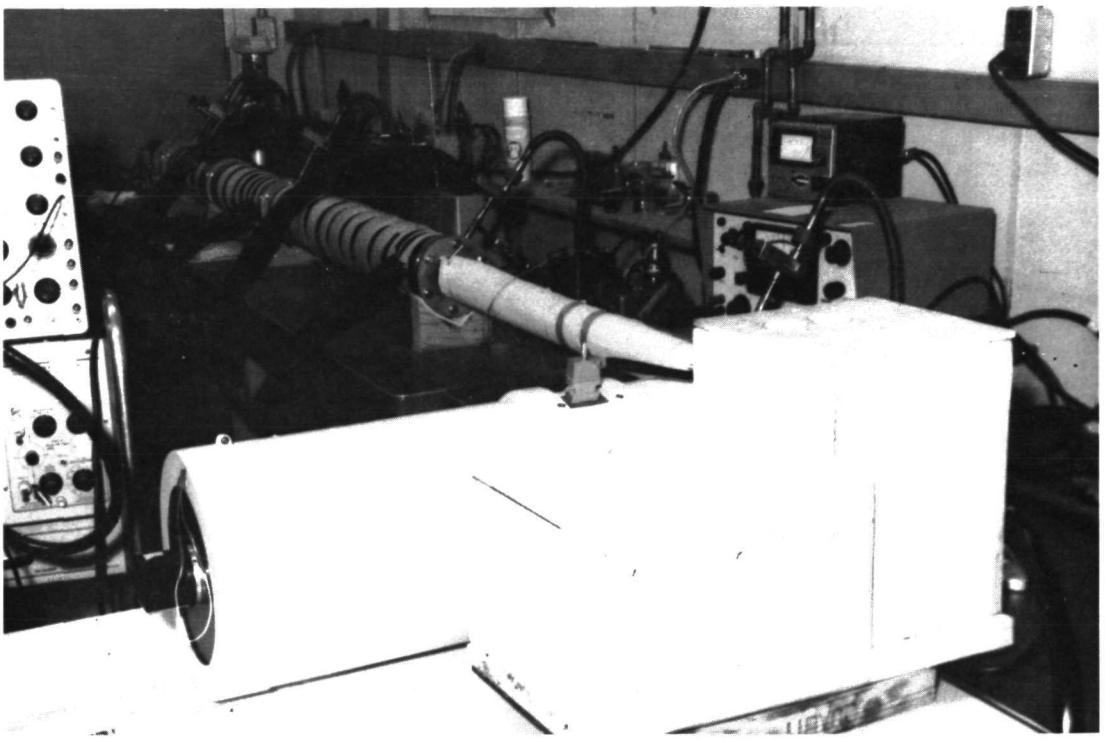

Figure 5.1.3. Multiple Chamber Test Facility

Three of the chamber sections were jacketed to permit cooled or heated fluids to circulate and control the temperature of the gas within the cell. Using a mixture of dry ice and acetone in a heat exchanger the circulating fluid in the system (methanol) could lower the chamber temperature to -58°C.

The energy from the glowing filament source is collimated by a reflecting optical system and passes through the series of absorption cells containing the test gases at the predetermined temperatures and pressures. The energy is selectively absorbed by the gages and the spectral radiant flux emerging from the system passes into the correlation interferometer.

The temperature and pressure of the test gases in the cells of the multiple chamber system could be controlled to approximate conditions to be encountered in the atmosphere. While the actual concentrations and path lengths could not be duplicated, the integrated amounts of gas over a complete or partial atmospheric path were placed in the chambers at mean temperature and pressure conditions.

While the test chambers could be evacuated to less than 50 microns and the leak rates with the system isolated from the pump were less than 4.0 microns/hour, the test cases were not run at pressures of less than 2 torr due to the uncertainties introduced in trying to mix gases at these low pressures. The atmospheric models indicate that the altitude corresponding to the pressure of 2 torr is 41 km. The atmospheric temperatures

in the 0 to 41 km altitude region range between 300°K and 190°K depending on season and latitude. The temperatures of the chambers equipped with the cooling jackets could be lowered to 215°K, which is low enough to closely approximate stratospheric temperature levels.

5.2 Laboratory Tests of the Correlation Interferometer

The tests of the instrument planned with the multiple chamber facility (described above) at GE were designed to demonstrate the instrument's ability to measure CO over the required range (i.e., 0.02 atm.-cm. to 4.0 atm.-cm.) in the presence of strong spectral interference by other atmospheric constituent gases. All of the interfering gases cannot be introduced into the optical path in the quantities present in the atmosphere. Water, which is a strong interferent at 2.3 microns, cannot be introduced in significant quantities. However, methane can be introduced in atmospheric amounts and its effect studied. At 4.6 microns, the interfering gases are nitrous oxide (N_2O), carbon dioxide (CO_2), and also water vapor. In this case, N_2O can be placed in the cells in reasonable concentrations while the cells have to be filled with pure CO_2 to get an equivalent atmospheric amount, and also significant amounts of water vapor cannot be introduced into the cells.

As a result, the laboratory tests were done with carbon monoxide and methane or nitrous oxide as the interferent gases. With these test gases a sufficient range of optical thicknesses and temperatures and pressures could be investigated to experimentally verify the basic instrument concept.

The primary limitation of the tests was that not all of the interferent gases can be studied in the GE multiple chamber system. A second limitation was that test conditions appropriate to the limb experiment could not be set up in a realistic manner. The combination of large optical thickness and low pressure meant that the gas in the chamber would be almost pure CO and CH_4 or N_2O. These conditions are better tested in the long path facility at NASA/LRC. Such tests are discussed later.

During the tests of the breadboard correlation interferometer with the multichamber facility it was important to determine the sensitivity of the measurements to changes in the interferent amounts (CH_4 and N_2O), and also to changes in the temperature and pressure of the gases in the cells.

The gases used for these tests were various premixed gases (3.0% CH_4 in N_2, 2.1% CO in N_2, and 880 ppm CO in N_2) together with various pure gases (N_2, CO_2, N_2O). These were used to give the optical thicknesses of gas desired, as described below. These gases were introduced into the system shown in Figures 5.1.1 and 5.1.2 by evacuating the system, filling one or more cells with the desired mixture, re-evacuating the filling system, and repeating until all needed cells are filled.

The nominal background amounts of CO, CH_4, and N_2O in the double vertical path through the atmosphere are given as:

1. 0.176 atm.-cm. CO

2. 2.80 atm.-cm. CH_4

3. 0.44 atm.-cm. N_2O (single atmospheric path)

The atmospheric concentration models for CO, CH_4, and N_2O from which these quantities have been computed have been discussed previously (ref. 1).

The quantity of CO in the path was varied from 0.0176 atm.-cm., which is the background amount assumed for a sink region, to 4.0 atm.-cm., which is the quantity of CO assumed for a polluted urban region. Over this range of CO optical masses, the amount of interferent gases was varied over the range

1. 1.4 to 5.6 atm.-cm. of CH_4

2. 0.44 to 0.88 atm.-cm. of N_2O

Initial tests were conducted with methane and carbon monoxide mixtures in various combinations. The basic procedure in generating a set of data to be used in determining a suitable correlation function for the methane and carbon monoxide mixture, is the following:

1. A test condition is set up in the gas cells which corresponds to a nominal background amount of the gases used. In this case 3 atm.-cm. of methane and 0.2 atm.-cm. of carbon monoxide was chosen since this corresponded to the amount of gas in a vertical atmospheric column for a double pass through the atmosphere.

2. A series of interferogram scans is then sampled and co-added at some predetermined sampling interval. In this case interferograms with 22 and 64 sampling points over the same path difference interval were collected and a punched paper tape record output from the computer system was obtained.

3. The nominal amount of carbon monoxide in the cell is then increased by a predetermined amount which was 0.099 atm.-cm. for the purposes of the tests. The interferogram for this methane and carbon monoxide condition is then sampled.

4. Then a series of test conditions is set up in which the carbon monoxide is maintained at 0.2 atm.-cm. and the methane is varied. For these experiments the methane varied from 1 to 5 atm.-cm.

The measurements were all run twice to provide duplicate measurements to be used as test cases. In addition some other combinations of methane and carbon monoxide were run as test cases.

The data is all recorded on punched paper tape and then is input through the GE time-share computer system for storage on disc.

Using these stored interferograms, various correlation functions can be computed and used with interferograms of test cases to obtain a measure of the CO in the path.

Tables 5.2.1 and 5.2.2 indicate the gas test conditions which were set up in the cells using CO and CH_4. Measurements were made in two different series. After the first series of the test matrix (Table 5.2.1) had been run, a failure of the lead sulphide detector occurred. After this problem was corrected, a second series (Table 5.2.2) was run.

Tables 5.2.3, 5.2.4, and 5.2.5 indicate the range of measuring conditions set up in the chambers for the determination of correlation functions for a CO, N_2O, and CO_2 gas combination. Since the CO spectral band at 4.6 microns is so much stronger than the overtone band at 2.3 microns, the interferent effects of N_2O and CO_2 will be correspondingly less than those of CH_4 at 2.3 microns. Thus fewer test cases were set up for the 4.6 micron tests than for the 2.3 micron tests described later. The CO amounts listed correspond to a single atmospheric path.

The same conditions were then set up with the gas pressures changed as for the 2.3 micron tests and the correlation functions again determined.

After the effects of gas quantity and pressure were evaluated, the effects of temperature were investigated with the three nominal amounts of CO and 0.44 atm.-cm. of N_2O. By heating the fluid in the constant temperature baths, the gas temperature was raised to 48°C, and by using dry ice and acetone in the heat exchangers, the temperature of the gas was dropped to about -60°C. Intermediate temperatures could also be achieved.

5.3 Long-Path Tunnel Tests at NASA/LRC

Demonstration tests of the breadboard correlation interferometer were conducted using the 435-foot tunnel at NASA/LRC. The objective of these tests was to further verify the operation of the breadboard employing a test atmosphere which contained a known amount of water vapor, approximately that of the low water atmospheric model used in the analytical studies.

Table 5.2.1. Gas Test Conditions for 2.3μ Laboratory Tests (First Series)

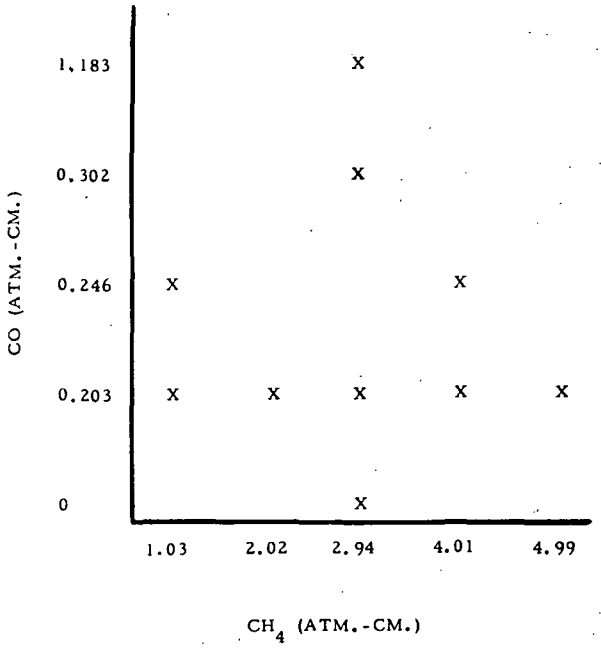

Table 5.2.2. Gas Test Conditions for 2.3μ Laboratory Tests (Second Series)

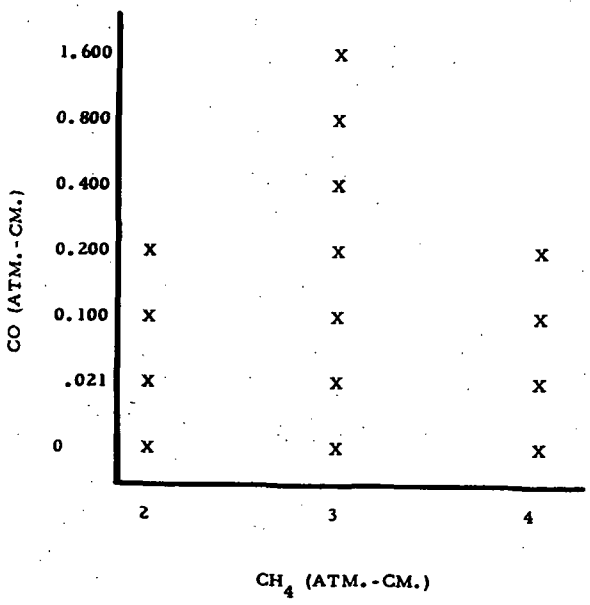

Table 5.2.3. Gas Test Conditions for 4.6μ Laboratory Tests (6 Amp Source)

PRESSURE = 740 TORR and 660 TORR
TEMPERATURE = 25°C and 44°C (T ≈ 950 K)
SOURCE CURRENT = 6 AMPS

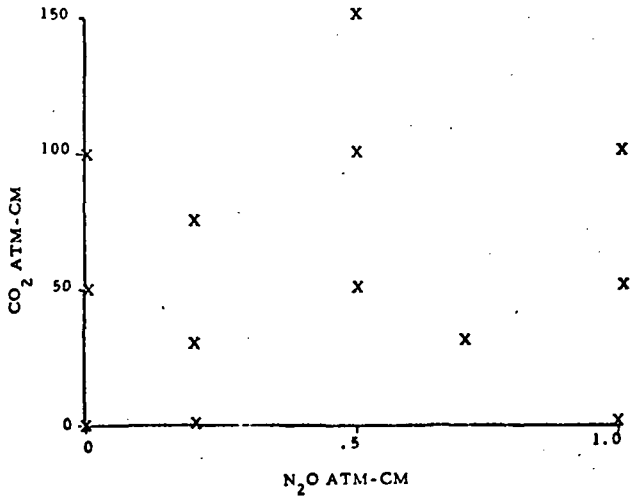

X - Test Conditions with CO from 0 to 0.084 ATM-CM.

Table 5.2.4. Gas Test Conditions for 4.6μ Laboratory Tests (1.5 Amp Source)

PRESSURE = 740 and 660 TORR
TEMPERATURE = 25°C and 44°C
SOURCE CURRENT = 1.5 AMP (T ≈ 400 K)

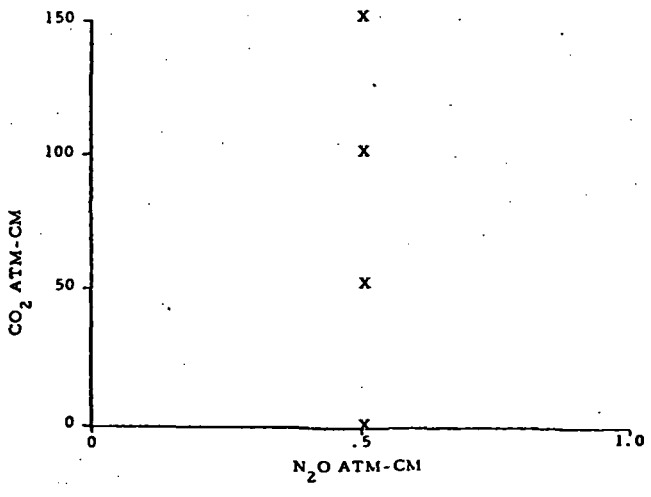

X - Test Conditions with CO from 0 to 0.25 ATM-CM.

The equipment used for these long path tests is shown schematically in Figure 5.3.1. The light source for the tests was a 1000 watt tungsten-iodine lamp. The energy is collected and collimated by a 12-inch diameter, f/4 parabolic mirror and beamed through the window at the far end of the tunnel. At each end of the tunnel, 12-inch diameter quartz windows are provided. The tunnel itself is 435 feet long, four feet in diameter, can be evacuated to approximately 500 microns pressure by means of a steam-ejector pump. The energy passing through the window is collected and focussed by another 12-inch diameter, f/4 parabolic mirror. This energy is then recollimated into a smaller beam by means of a 1-inch diameter, f/4 quartz lens to allow the beam to pass through the gas cells which are 2 $\frac{1}{2}$ inches in diameter. The beam is directed by means of flat mirrors through the gas cells and then into the correlation interferometer. It was necessary to place another lens in the optical path between the two cells in order to cause the beam to converge slightly and pass through the cells without vignetting. The gas cells used for these tests were those described in Section 5.1.

Table 5.2.5. Gas Test Conditions for 4.6μ Laboratory Tests (100°C Source)

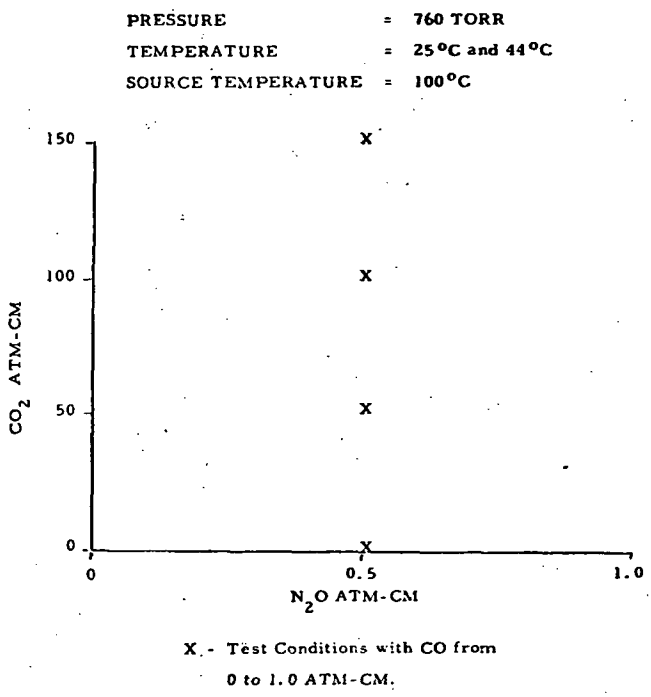

The test procedure followed was to evacuate the tunnel to its minimum pressure and check that the leak rate was not excessive. Pumping was then stopped and the tunnel isolated. Liquid water was then introduced into the tunnel and allowed to vaporize. The equilibrium vapor pressure of the water vapor was then measured. The leak rate into the tunnel was of the order of 500 microns per hour and it was possible to measure the water vapor pressure to about this level of accuracy (about 500 microns). The amount of water vapor which could be introduced into the tunnel at saturation depended on the tunnel temperature. This was monitored by means of thermocouples placed along the length of the tunnel. It was found that approximately 0.2 precipitable centimeter of water could be introduced into the tunnel optical path under the temperature conditions which prevailed at the time.

After the required amount of water vapor was placed in the tunnel, the tunnel was then pressurized to atmospheric pressure with dry nitrogen. The carbon monoxide and methane were introduced into the optical path external to the tunnel by using pre-mixed gases in the gas cells. This permitted a large matrix of CO-CH_4 gas conditions to be set up in a reasonable period of time. The test conditions are shown in Table 5.3.1.

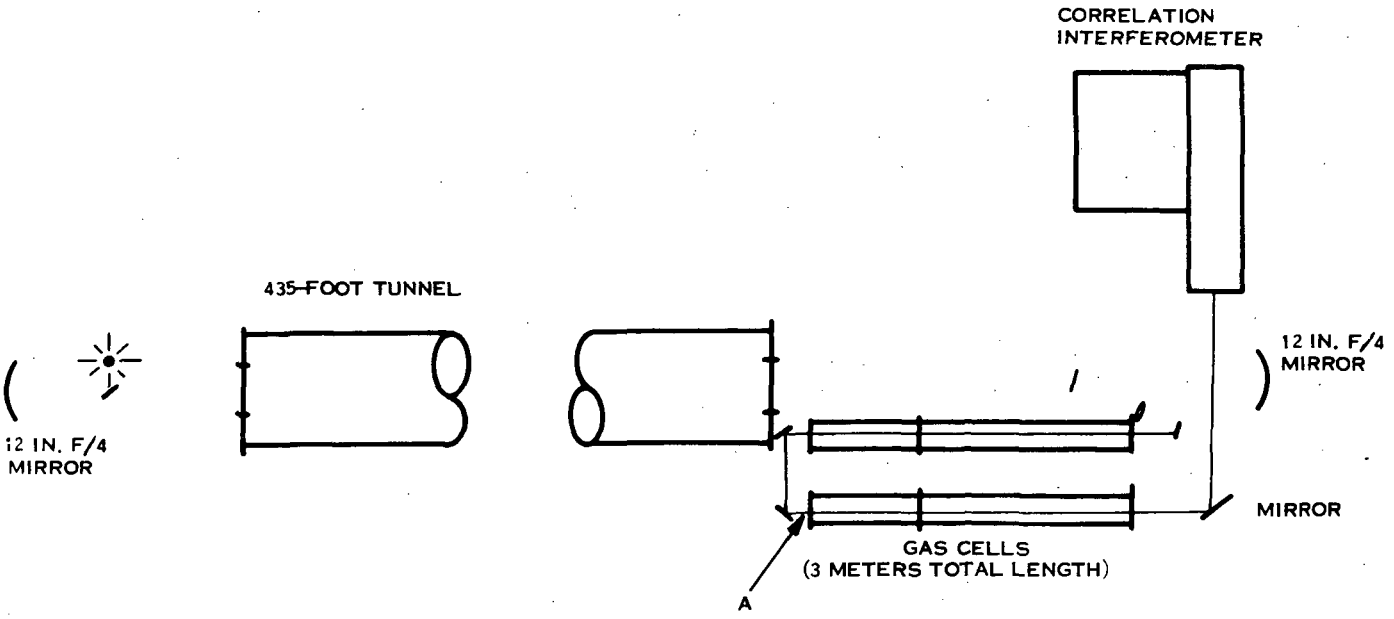

Figure 5.3.1. Long-Path Tunnel Test Facility

The test procedure followed was similar to that used at GE for the laboratory tests. In order to monitor the stability of the instrument over the period of approximately 8 hours which was required to run the tests, a standard test condition of 0.2 atm.-cm. of CO and 2.72 atm.-cm. of CH_4 was set up in the cells and a measurement made periodically using a second light source introduced in the optical path at location A (see Figure 5.3.1) after blocking off the light from the tunnel. This permitted an evaluation of instrumental variations in the measurement.

In addition a small matrix of test cases was run using 1, 10, and 100 scans per measurement to evaluate the instrument signal to noise ratio.

These data are discussed in Section 7.

Table 5.3.1. Gas Test Conditions for 2.3μ Breadboard Tests at NASA/LRC Tunnel

CO (ATM.-CM.)	0	1.80	2.72	3.61	4.52	5.44
0.914	x	x	x	x	x	x
0.457	x	x	x	x	x	x
0.200	x	x	x	x	x	x
0.100	x	x	x	x	x	x
0.02	x	x	x	x	x	x
0.01					x	
0	x	x	x	x	x	x

CH_4 (ATM.-CM.)

6. OUTDOOR BREADBOARD TESTS

After the operation of the breadboard had been verified in the laboratory, it was taken outdoors to make measurements using radiation which has traversed a real atmospheric path. The outdoor tests were designed to demonstrate the capabilities of the instrument in making measurement of CO in the presence of large amounts of water vapor, which is an interferent at 2.3 microns.

The purpose of the outdoor tests was to obtain a series of interferograms from the correlation interferometer covering a range of atmospheric conditions. The inter ferograms were then used to generate a set of correlation functions which were optimized for detecting CO against the atmospheric interferent gases over the range of test conditions. The measurement is then repeated with a known amount of CO placed in a cell in the optical path. These interferograms are then input to the BRL programs which compute the correlation functions.

The breadboard system permitted the output of interferograms for input to the weight generation program, or the input of a correlation function, or the making of a measurement using the correlation function which had been input. Each new set of observations could be used as a test of the existing correlation function and then included in the determination of an improved correlation function.

A series of outdoor measurements were made with the apparatus shown in Figure 6.1.1 using sunlight in the vicinity of the Space Sciences Laboratory. The optical path through the atmosphere covered solar elevation angles from about 10^{o} above the horizon to approximately 60^{o}. The atmospheric air mass covered varied by a factor of 5, with a corresponding variation in the range of CO and interferent gases. Making these arrangements over a period of time permitted variations in the atmospheric gas concentrations as well as changes in atmospheric temperature and pressure.

A number of auxiliary measurements were made in order to define the atmospheric properties at the time of the measurements. These were the following:

1. A measurement of the amount of CO in the optical path was made by means of a spectral absorption measurement. The solar absorption spectrum was measured at 4.6 microns with an 0.5 cm^{-1} resolution interferometer spectrometer. The measured spectrum of individual lines of the CO band was compared with spectra computed using the available theoretical absorption model to permit the amount of CO in the atmospheric path to be determined. These measurements are more easily made at 4.6 microns when the sun is used as the source because of the greater strength of the lines in the CO fundamental band. The CO line strengths and widths are known with sufficient accuracy so that theoretical calculations of band absorption agree with measured values to within 10% (refs. 11, 12).

2. In addition, the concentration of CO at ground level was monitored using a non-dispersive infrared CO analyzer which has a sensitivity of 0.25 ppm, and hence gives adequate CO measurements for ambient levels of 2.5 ppm and greater.

3. Atmospheric humidity at ground level.

4. Ground level temperature.

In these tests it should be noted that the atmospheric CO concentration did not reach the levels to be encountered in the region of a CO sink (i.e., 0.02 atm.-cm). However, the ability to reject the effects of interfering gases was tested by putting the cell with 0.02 atm.-cm. of CO in the path as an increment to the background amount of CO, and the corresponding increment in the amount of CO indicated by the correlation interferometer was observed.

Figure 6.1.1. Instrumentation for Outdoor Tests

7. RESULTS

7.1 Laboratory Tests - 2.3 Microns

The laboratory results for CO measurements using the first overtone band of CO are presented in this section. The results in the following tables (it is to be noted that these are not graphs) are shown as percent difference between the actual and measured amounts of CO for the various amounts of CO (as shown on the left) and of CH_4, the interferent (as shown at the bottom). For the case of zero CO, the absolute value (in atm.-cm.) of the measured amount of CO is given. The correlation function was calculated using the conditions enclosed in solid lines.

Table 7.1.1 shows the results for measurements made with methane amounts of 1.03, 2.02, 2.94, and 4.99 atm.-cm. The nominal amount, corresponding to amounts of these gases to be expected in unpolluted atmospheric paths, of methane is 2.94 atm.-cm. and of carbon monoxide is 0.203 atm.-cm. The target increment of carbon monoxide is 0.302 atm.-cm. The interferogram was sampled at 64 points over the path difference interval. The instrument output for a given correlation function is a single number which represents the amount of carbon monoxide in the optical path. The results are expressed here and in following tables as percent error in the measurement of CO, except for the cases of zero CO in the path for which the absolute measurement (and error) is given in parentheses since percent error is meaningless in such cases. These results generally show good agreement with the actual amount of CO in the cells. Where duplicate measured values are available the difference between the measured values is small (i.e., of the order of 0.004 to 0.006 atm.-cm. of CO) indicating that the noise in the measurements is small. The measurement of 1.183 atm.-cm. of CO is lower than the actual amount in the cells. This is due to the nonlinear absorption by the CO when the amount of gas becomes this large. Since the measurement technique basically assumes that the CO absorption is linear, the amount of CO indicated by the instrument will be less than is present since the amount of absorption is less than predicted by the linear absorption theory. It is to be noted that this amount of carbon monoxide is much greater than any in the runs used to obtain the correlation function.

The same data were treated to take a larger target increment of CO, i.e., 1.183 atm.-cm., with the nominal background amount of CO of 0.203 atm.-cm. to obtain the correlation function. These data are shown in Table 7.1.2. Using the larger target increment of CO fits the data better at the large amounts of CO than if small target increments are used. The measurements of the small amounts of CO obtained with this set of weights are not drastically different from those obtained with the smaller target increment of CO.

Table 7.1.3 presents the same basic data treated with a correlation function obtained by letting the methane vary between 2.02 and 4.99 atm.-cm. rather than between 1.03 and

4.99 atm.-cm. as above. In this case the agreement between the measured and actual amounts of CO is quite good except when methane amount is outside of the range used in generating the weights. For example, the measurements with 1.03 atm.-cm. of methane show a large offset which amounts to the equivalent of 0.123 atm.-cm. of CO. This is approximately a constant for a given amount of methane. The measurements with 1.02 atm.-cm. of methane and 0.246 atm.-cm. of CO show the same offset since if one substracts 0.123 from the total measured CO of 0.370 the result is 0.247 atm.-cm., which is the actual amount in the cells. This tends to indicate that measurements made with an amount of interferent outside of the range for which the correlation function is generated could be used if a correction is applied.

Tables 7.1.4, 7.1.5, and 7.1.6 are the results for the same gas conditions as in Tables 7.1.1, 7.1.2, and 7.1.3 except that the interferogram is sampled at only 22 points. The results in these cases are not drastically different from those obtained with the 64 sample interferograms. A few of the measurements appear to be better with the 64 sample interferograms, but there are not enough data to conclude that one should use one sampling interval over the other.

The data presented here is the initial treatment of the set of interferograms available. The same data can be treated in other ways by taking different combinations of the interferograms to generate the correlation functions thus permitting an optimization of the experiment parameters, such as sample number, range of interferogram scanned, and the range of interferent amounts over which a correlation function will accurately apply.

The remainder of the laboratory 2.3 micron experiments required a new lead sulphide detector. These consisted of several sets of runs with 23, 35, and 55 sample points per interferogram. Table 7.1.7 shows results where the correlation function was obtained using a range of methane from 2.0 to 4.0 atm.-cm. and .02 to .80 atm.-cm. of CO. The accuracies are, in general, less than 10% even with an extrapolation of a factor of two in CO.

The measurements made at 2.3 microns show a long term measurement drift which affects the final measurement accuracy. This is an instrumental effect which may be caused by the system electronics or the present design of the interferometer itself. To illustrate the drift effect a number of test interferograms were run over a long period with 3.0 atm.-cm. of methane and zero carbon monoxide in the cells of the laboratory test system. Then using a correlation function derived from a nominal test case of 3.0 atm.-cm. if CH_4 and 0.2 atm.-cm. of CO and a target amount of 0.8 atm-cm. of CO, the measurement was made on the test interferograms with 3.0 atm.-cm. of CH_4 and zero of CO. The variation of the measured amount of CO with time then gives an indication of the magnitude of the instrument drift. Table 7.1.8 shows this measurement of the zero amount of CO taken over a period of two days. There is apparently a cyclic variation to the drift with the measurement varying between about -0.043 and +0.013 atm.-cm.

Table 7.1.1. Laboratory Results, 2.3 μ, 64 Samples

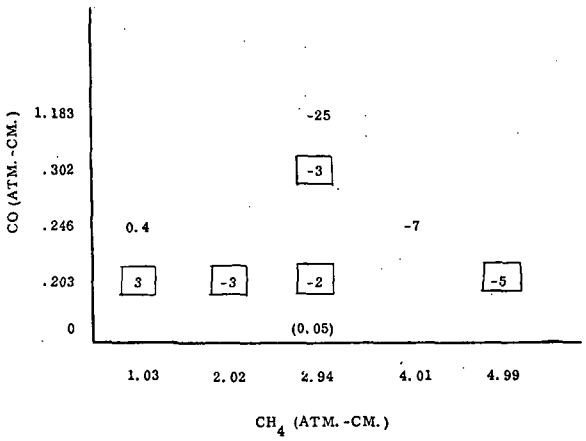

Table 7.1.2. Laboratory Results, 2.3 μ, 64 Samples

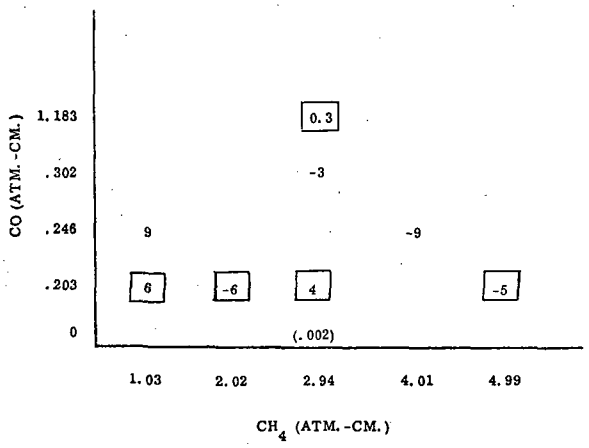

Table 7.1.3. Laboratory Results, 2.3 μ, 64 Samples

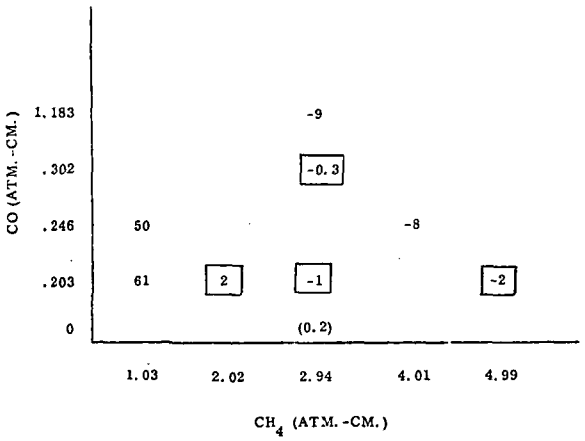

Table 7.1.4. Laboratory Results, 2.3 μ, 64 Samples

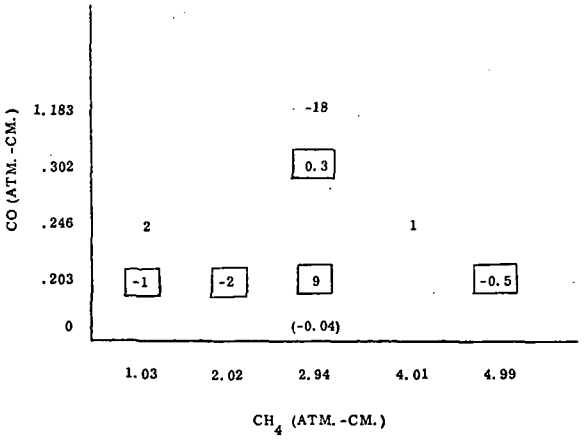

Note: Units of tabular data are % error of CO measurement except for data in parentheses which are absolute amount of CO in atm.-cm.

Table 7.1.5*. Laboratory Results, 2.3μ, 22 Samples

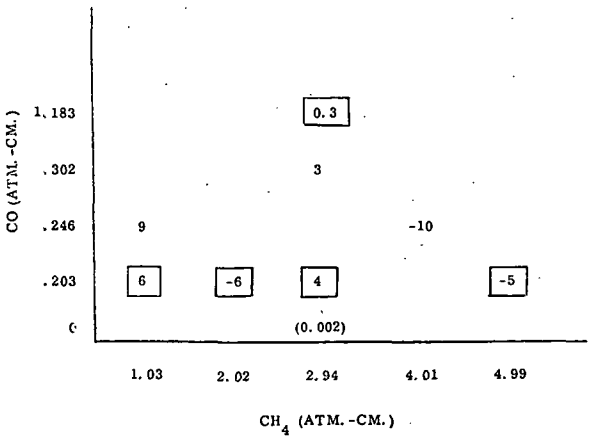

Table 7.1.6*. Laboratory Results, 2.3μ, 22 Samples

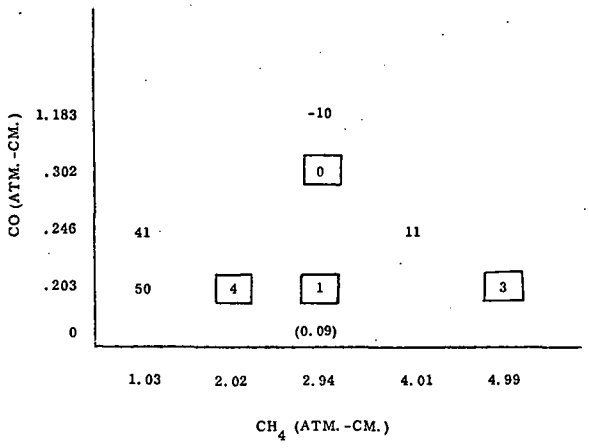

Table 7.1.7*. Laboratory Results, 2.3μ, 55 Samples

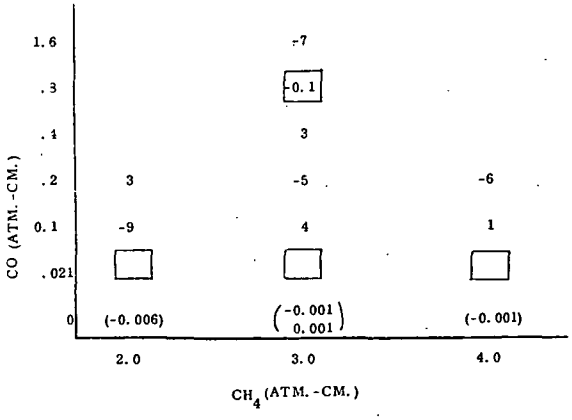

Table 7.1.8. Instrument Measurement Drift

DATE	TIME	CO MEASUREMENT (atm.-cm.)
10/19/71	8:35	-0.0288
	8:40	-0.0284
	10:00	-0.0404
	13:15	0.0093
	13:20	0.0129
	16:20	-0.0047
10/21/71	11:00	-0.0433
	11:05	-0.0424
	15:12	-0.0305
	15:16	-0.0287

*Note: Units of tabular data are % error of CO measurement except for data in parentheses which are absolute amount of CO in atm.-cm.

A comparison of results obtained with the different numbers of sample points per interferogram is shown in Table 7.1.9. The conditions used for the determination of the correlation function are given at the top of the table while the remainder of the runs, listed in the lower part of the table, were the test runs. The accuracy attained with 23 samples is about as good as that obtained with 35 samples which is about as good as that obtained with 55 samples.

The effect of temperature variations on CO measurement accuracy is shown in Table 7.1.10 for actual amounts of CO of 0 and .4 atm.-cm. Each measurement is given for temperatures of 26 and 48°C. The differences between the results for the two temperatures are very small (for each CO density).

The effect of pressure in CO measurement accuracy is shown in Table 7.1.11 for actual amounts of CO of 0 and .4 atm.-cm. Each measurement is given for pressures of 760 and 836 torr. The differences between the results for the two pressures are very small (for each CO density).

The data of Table 7.1.2 are shown graphically in Figure 7.1.1 which gives the amounts of CO measured using the correlation interferometer breadboard as a function of the actual amount of CO in the chambers. It can be seen that a one-to-one relation holds until a level of about 1 atm.-cm. above which a slight departure is seen. This linearity with the 2.3 micron band is extremely advantageous. It shows that interpolation over the range up to at least 1 atm.-cm. is reasonable for CO.

Table 7.1.9. Laboratory Results, 2.3 μ, Variation of Samples

CH_4 (ATM-CM)	CO (ATM-CM)
3.0	0.021
3.0	0.80
2.0	0.021
4.0	0.021

TEST CELL		55 SAMPLES		35 SAMPLES		23 SAMPLES	
CH_4 (ATM-CM)	CO (ATM-CM)	MEASURED CO (ATM-CM)	ACCURACY (%)	MEASURED CO (ATM-CM)	ACCURACY (%)	MEASURED CO (ATM-CM)	ACCURACY (%)
2.0	0	-0.003	-	0.0094	-	0.0058	-
2.0	0.100	0.095	-5.10	0.102	2.02	0.104	4.40
2.0	0.200	0.205	2.66	0.223	11.49	0.223	11.81
3.0	0	0.001	-	0.0035	-	-0.0041	-
3.0	0.100	0.103	2.99	0.106	5.74	0.107	6.68
3.0	0.200	0.191	-4.76	0.202	0.92	0.213	6.25
3.0	0.400	0.409	2.35	0.409	2.32	0.405	1.18
3.0	0.800	0.799	-0.09	0.812	1.44	0.790	-1.20
3.0	1.600	1.51	-5.72	1.50	-6.50	1.48	-7.22
4.0	0	-0.0012	-	0.0004	-	0.002	-
4.0	0.100	0.099	-0.67	0.088	-12.03	0.096	-3.96
4.0	0.200	0.188	-5.85	0.183	-8.47	0.200	0.27

Table 7.1.10. Effect of Temperature of Methane and CO Laboratory Measurements, 2.3 μ

CH_4 (^oC)	CO (ATM-CM)
26	0
48	0.024

CO (^oC)	CO (ATM-CM)
26	0.41
47	0.41

Table 7.1.11. Effect of Pressurizing Methane and CO Laboratory Results, 2.3 μ

CH_4 (TORR)	CO (ATM-CM)
760	0
836	0.004

CO (TORR)	CO (ATM-CM)
760	0.39
836	0.39

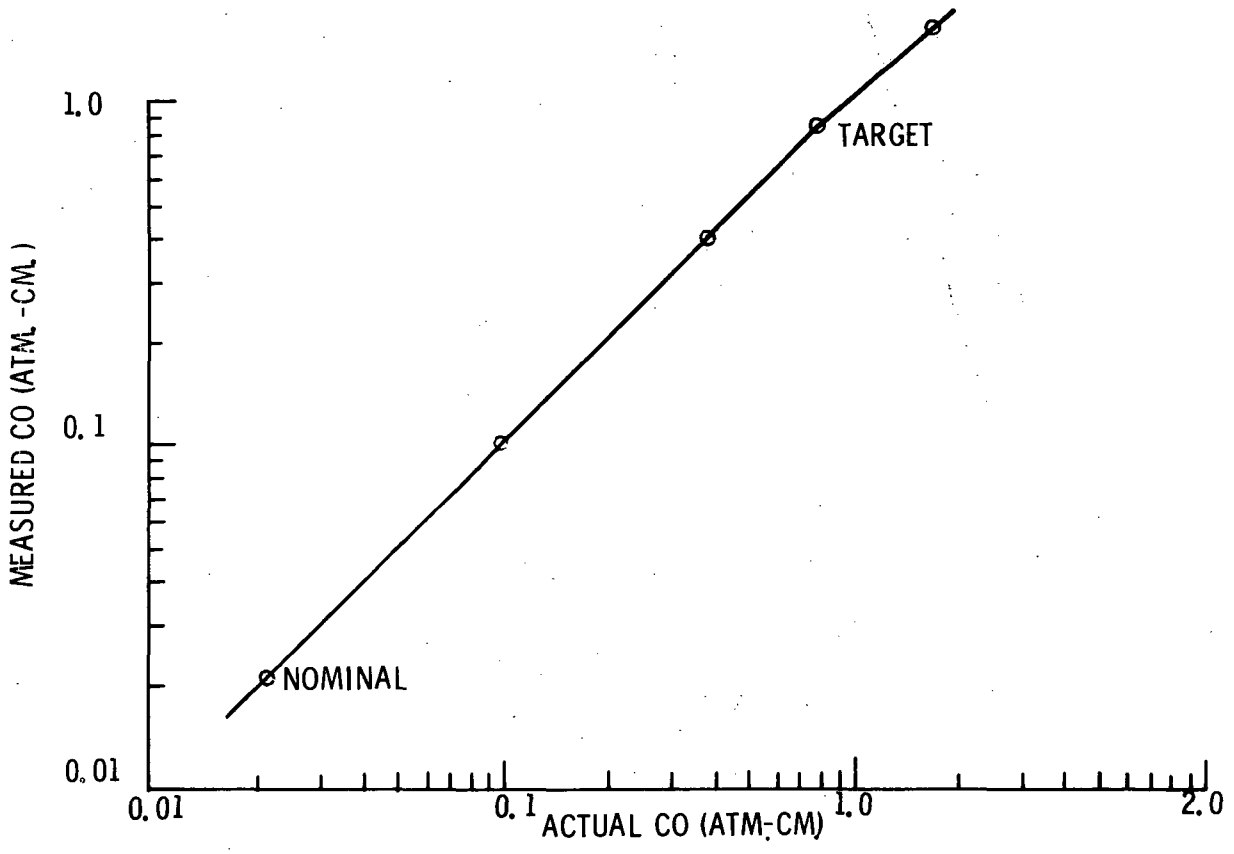

Figure 7.1.1. Variation of Measured CO with Actual CO at 2.3 μ

These data lead to certain conclusions concerning measurements of CO at 2.3 microns. Specifically,

1. The sensitivity of the breadboard at 2.3 microns is sufficient for the desired measurements. One-tenth of the normal unpolluted atmospheric burden can be detected.

2. The effect of methane can be eliminated by including in the data used to obtain the correlation function, the extreme limits of methane density over which measurements are to be made.

3. Densities of CO are measured to better than 10% accuracy in the presence of methane over a range from one-tenth to five times the normal atmospheric density.

4. The response of the instrument to CO is linear over the range up to 1 atm.-cm.

5. The number of sample points into which the section of the interferogram used is divided has little effect in variation from 23 to 55 points.

6. Temperature and pressure have little effect on the measurements.

7. Interpolation between calibration points gives better results than extrapolation beyond calibration points (conditions used to obtain the correlation function). This is more important for the range of methane than for the range of CO.

7.2 Laboratory Tests - 4.6 Microns

The laboratory results for CO measurements using the fundamental band of CO at 4.6 microns are presented in a number of tables following. The data were subjected to more treatment than the 2.3 micron data, that is they were treated with more correlation functions, since the results were not as good and improvement was sought. The reason for the poorer results can be seen by the curve giving the density of CO measured by the breadboard as a function of the actual CO density in the chambers in the optical path. This is shown in Figure 7.2.1 where drastic non-linearity is observed. It can be noted that the curve is double-valued at densities well below 1 atm.-cm. and reaches negative values at low densities.

Nitrous oxide and carbon dioxide were considered as interferents. Nitrous oxide had no significant effect as can be seen from the data of Table 7.2.1. This table shows results with and without CO_2 for CO from 0 to .08 atm.-cm. The results are given in percent accuracy, that is the agreement between actual and measured CO densities. At zero CO level, the results are given in terms of absolute amount of CO in atm.-cm. The

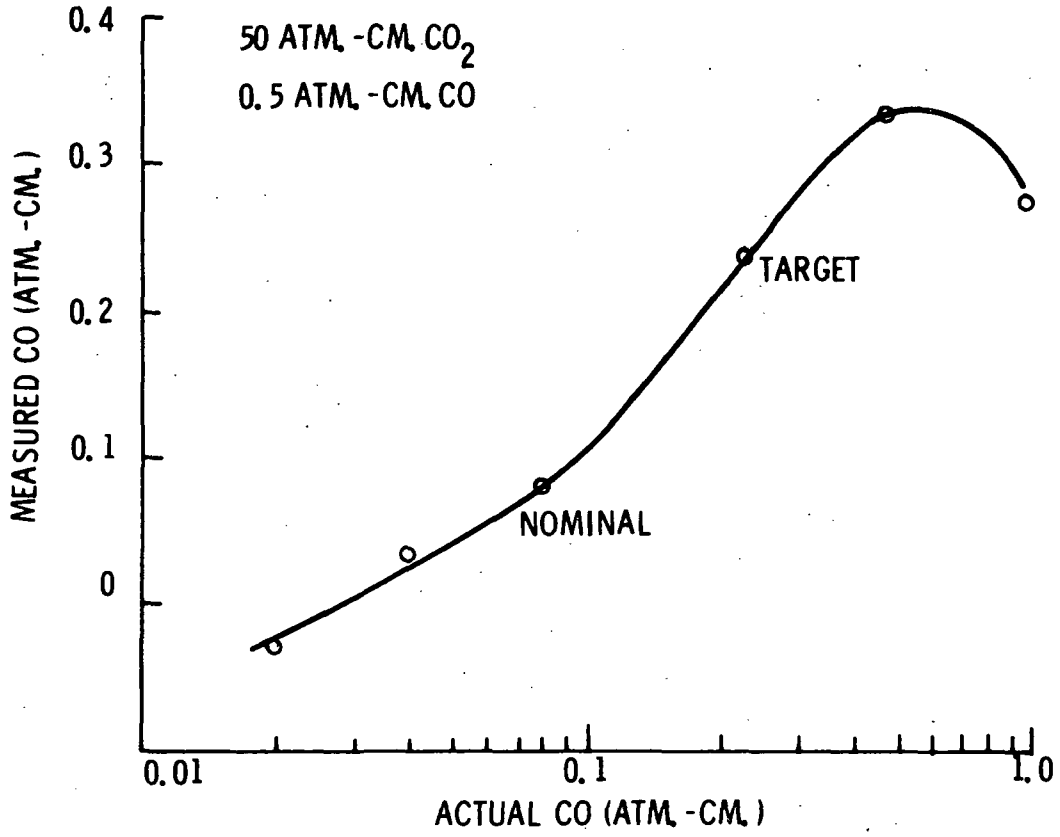

Figure 7.2.1. Variation of Measured CO with Actual CO at 4.6 μ

point to note in this table is that variation of N_2O shows very little effect on CO. This is seen by comparison of numbers in any vertical column from which it can be noted that these are approximately constant. Thus, the variation in N_2O does not appreciably affect the CO interferogram. This is expected since the line spacing of the 4.6 micron CO band is significantly different than that of the N_2O band in this band region and the effect of N_2O appears at a different delay in the interferogram.

The results in the following tables are shown as percent difference between the actual and measured amounts of CO for the various amounts of CO (as shown on the left) and of CO_2, the interferent, (as shown at the bottom). For the case of zero CO, the absolute value (in atm.-cm.) of the measured amount of CO is given. It is to be noted that these are all for relatively low amounts of CO, the density of CO in a vertical column of unpolluted air being about 0.1 atm.-cm. For higher CO densities the lack of linearity would give worse results.

Tables 7.2.2 through 7.2.11 show the results of treatment of about two hundred runs carried out with the gas at 25°C and 760 torr and a source temperature of 950°C. Each table uses the same data with a different correlation function (obtained with data for conditions shown in rectangles).

Table 7.2.1. Effect of N_2O Column Density on Accuracy of CO Column Density Measurements, 4.6 μ

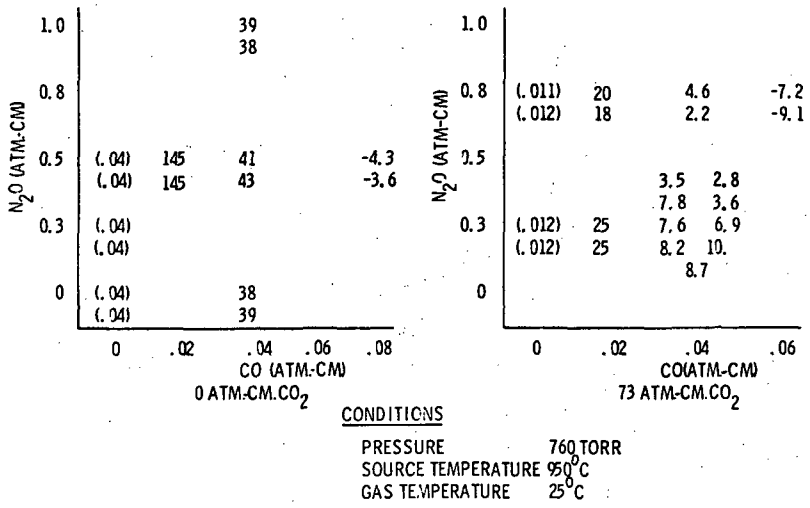

Note: Units of tabular data are % error of CO measurement except for data in parentheses which are absolute amount of CO in atm.-cm.

In Table 7.2.2 it can be seen that extrapolation from .04 down to .02 atm.-cm. of CO gives poor results. In Table 7.2.3 a lower target amount of CO (.05 atm.-cm.) is used without great differences. It can be noted that distinguishing between zero and .02 atm.-cm. is uncertain.

In Table 7.2.4 a zero CO target case was used. This did not improve the measurements at .02 atm.-cm. even though this is an interpolation. The inaccuracies at the higher CO values, e.g., .08 atm.-cm., are worse. Tables 7.2.5 and 7.2.6 show results similar to the above cases. It can be noted that interpolation over CO_2 gives reasonable results. Tables 7.2.7 and 7.2.8 show the effect of extrapolation of the CO_2 range, the results being worse at the low CO_2 values, the latter using a zero CO case for the target. Table 7.2.9 is very similar to 7.2.8 the only difference being that duplicate runs were used in obtaining the correlation functions for the data treatment. This apparently has little effect.

Table 7.2.10 gives results similar to those of 7.2.3. Note the difficulty in distinguishing between zero and .02 atm.-cm. CO. Table 7.2.11 includes a low-density CO run (.02 atm.-cm.) as the target case. Other measured values for this density are poor.

Similar results are shown for a different source temperatures, 100°C, in Table 7.2.12. Results are not as good as for the higher temperature source. There would be serious problems in attempting to accommodate both the limb and mapping experiments.

Table 7.2.2. Accuracy of Laboratory CO Column Density Measurements, 4.6 μ

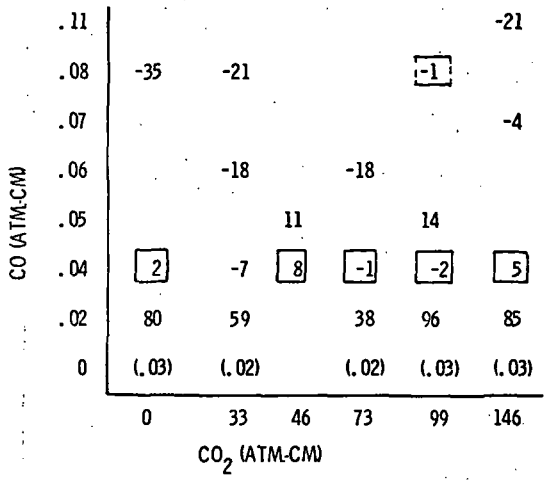

Table 7.2.3. Accuracy of Laboratory CO Column Density Measurements, 4.6 μ

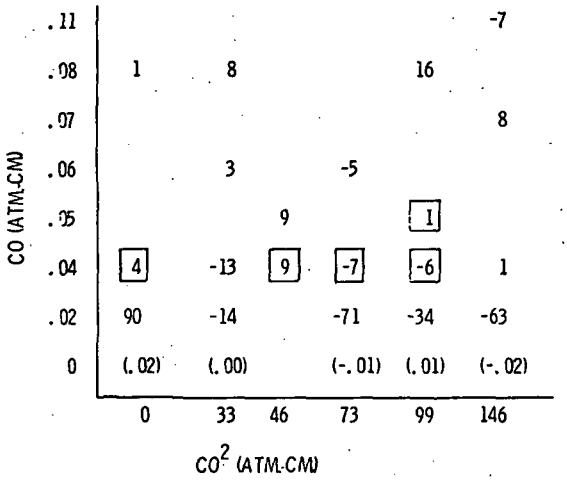

Table 7.2.4. Accuracy of Laboratory CO Column Density Measurements, 4.6 μ

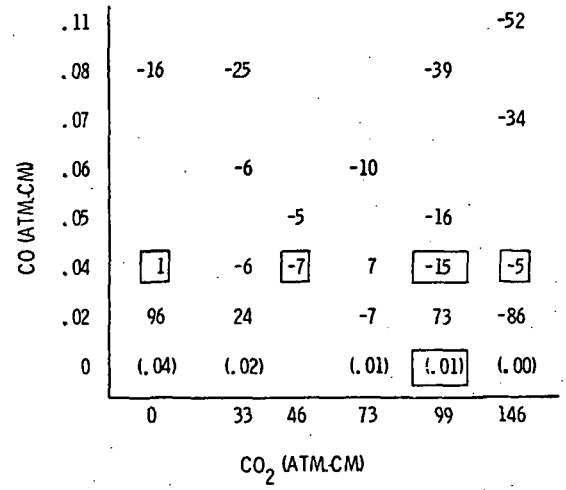

Table 7.2.5. Accuracy of Laboratory CO Column Density Measurements, 4.6 μ

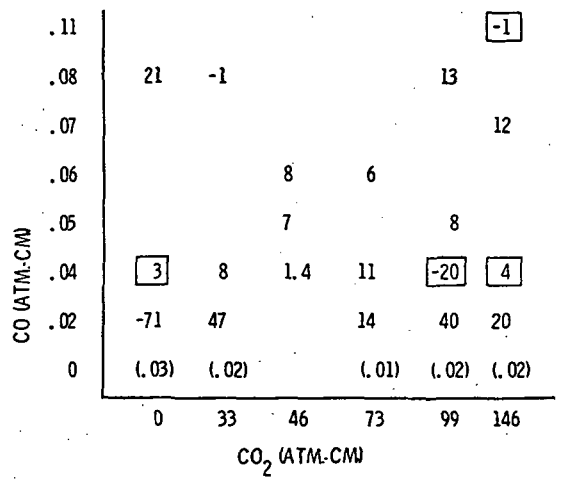

Note: Units of tabular data are % error of CO measurement except for data in parentheses which are absolute amounts of CO in atm.-cm.

Table 7.2.6. Accuracy of Laboratory CO Column Density Measurements, 4.6 μ

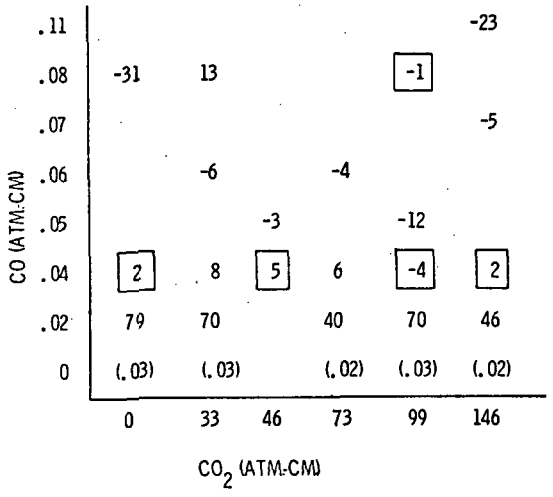

Table 7.2.7. Accuracy of Laboratory CO Column Density Measurements, 4.6 μ

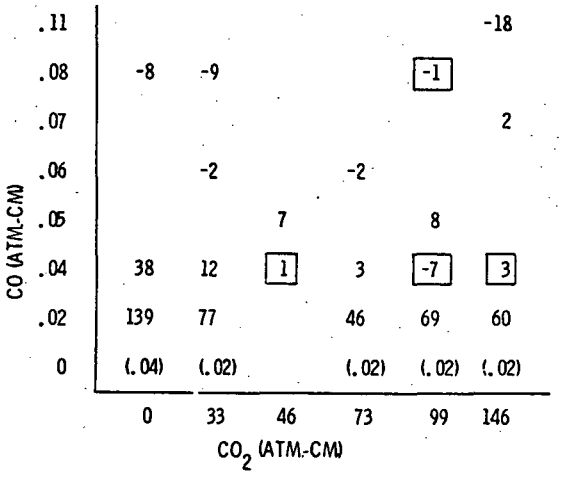

Table 7.2.8. Accuracy of Laboratory CO Column Density Measurements, 4.6 μ

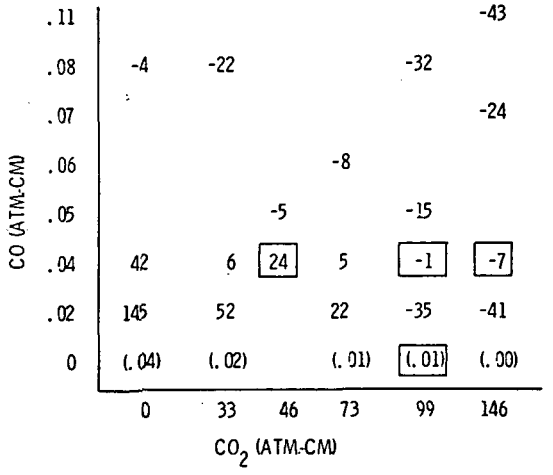

Table 7.2.9. Accuracy of Laboratory CO Column Density Measurements, 4.6 μ

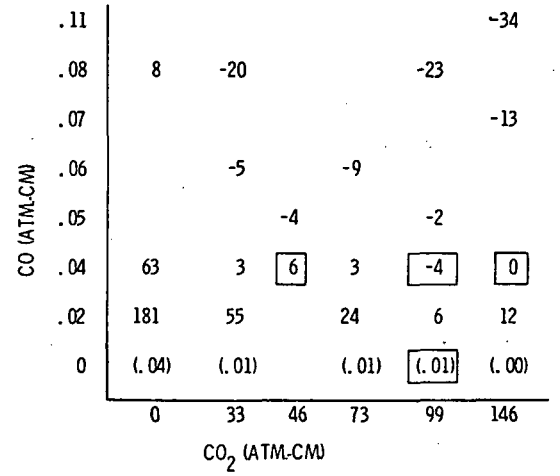

Note: Units of tabular data are % error of CO measurements except for data in parentheses which are absolute amount of CO in atm.-cm.

C - 2

Measurements were made using different source temperatures. These were a six ampere source (950°C), a 1.5 ampere source (about 400°C), a 100°C source, and for a few runs, 47°C and 25°C. Comparison of results for these source temperatures is given in Table 7.2.13. These are all based on the use of correlation functions obtained with a 100°C source.

Results for various source temperatures and gas temperatures are given in Tables 7.2.14 through 7.2.20 and 7.2.12. These are a series of calculations applying each of correlation functions derived with 950°C, 400°C, and 100°C source temperatures to measurements made at each of the temperatures of 950°C, 400°C, and 100°C. These may be summarized as follows:

Measurement Source T =	Correlation Function Source T =
950°C,	950°C
= 950°C	= 400°C
= 950°C	= 100°C
= 400°C	= 950°C
= 400°C	= 400°C
= 100°C	= 950°C
= 100°C	= 400°C
= 100°C	= 100°C

Examination of Tables 7.2.14, 7.2.15 and 7.2.16 shows that treatment of the data on the measurements with a 950°C source is, as would be expected, better when retreated with a correlation function obtained with data using a 950°C source (Table 7.2.14) than when treated with data from other correlation functions (Tables 7.2.15 and 7.2.16). Tables 7.2.17 and 7.2.18 and Tables 7.2.12, 7.2.19, and 7.2.20 show similar results. Results for one series of these are given in Table 7.2.21. This again shows the need at 4.6 microns for calibrating with the same source temperature as will be used in testing.

The effects of changing the gas temperature is shown in Table 7.2.22. The change in gas temperature from 25°C to 45°C changes the accuracy (% difference between the actual and measured CO) from 7 to 20%. Thus the gas temperature can have a significant effect.

Similarly a ten percent change in pressure changes the accuracy by about 3% for the conditions shown in Table 7.2.23.

These data lead to certain conclusions concerning measurements of CO at 4.6 microns. Specifically,

1. It is difficult to distinguish 10% of the normal atmospheric CO burden from zero CO.

Table 7.2.10*. Accuracy of Laboratory CO Column Density Measurements, 4.6 μ

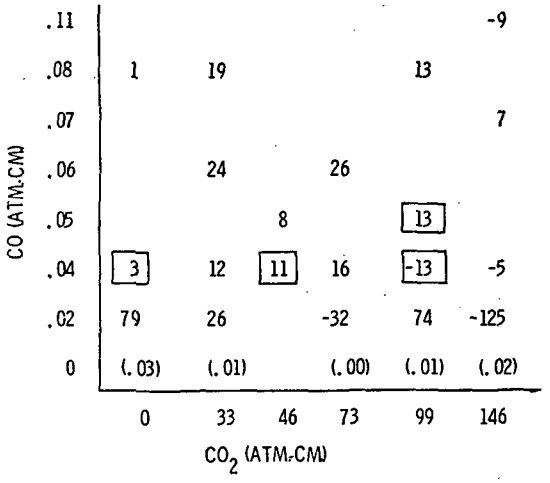

Table 7.2.11*. Accuracy of Laboratory CO Column Density Measurements, 4.6 μ

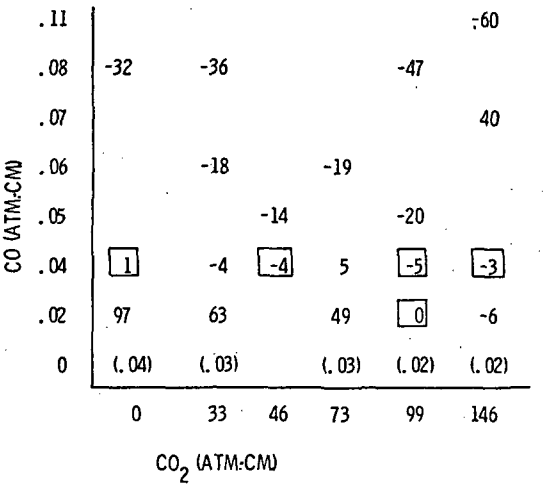

Table 7.2.12*. Accuracy of Laboratory CO Column Density Measurements, 4.6 μ

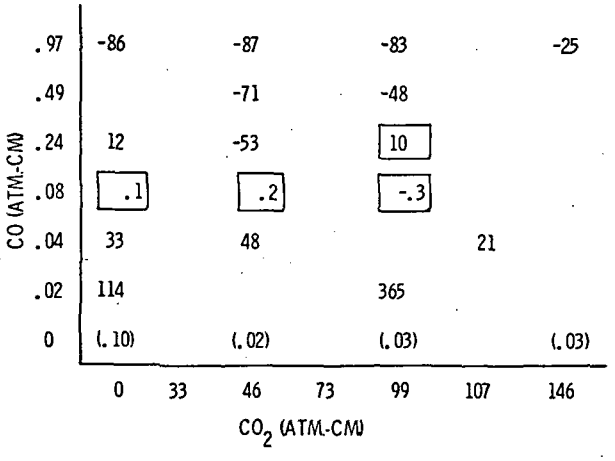

Table 7.2.13. Effect of Source Temperature, 4.6 μ

CO (ACTUAL) (Atm.-Cm.)	CO (Measured) (Atm.-Cm.) 25°C	47°C	100°C	400°C	950°C
0		-.10	.027	.046	.040
0			.027	.041	.038
.04	-.19	-.16	.042	.14	.15
.04			.042	.14	.15
.08			.082	.17	.20
.08			.080	.18	.18

*Note: Units of tabular data are % error of CO measurement except for data in parentheses which are absolute amount of CO in atm.-cm.

Table 7.2.14. Accuracy of CO Laboratory Measurements, 4.6 μ

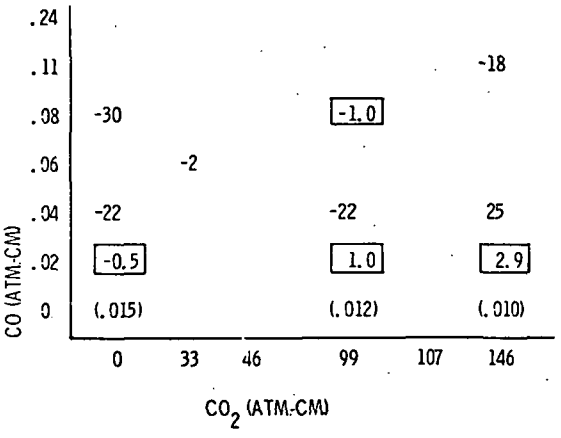

Table 7.2.15. Accuracy of CO Laboratory Measurements, 4.6 μ, at 950°C Source Temperature Using 400°C Source Weighting Function

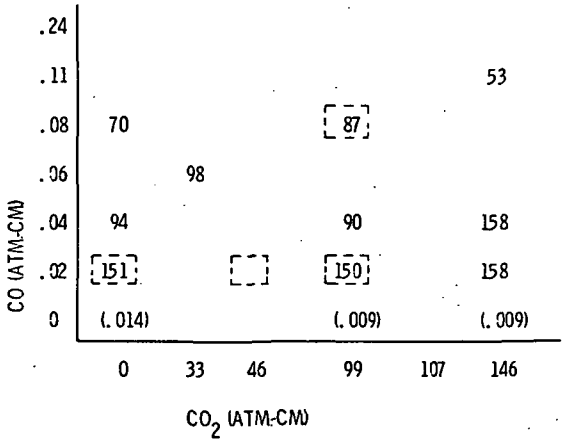

Table 7.2.16. Accuracy of CO Laboratory Measurements, 4.6 μ

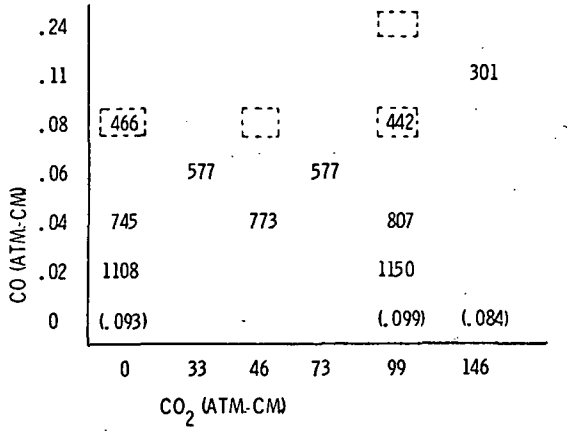

Table 7.2.17. Accuracy of CO Laboratory Measurements, 4.6 μ, at 400°C Source Temperature Using 950°C Source Weighting Function

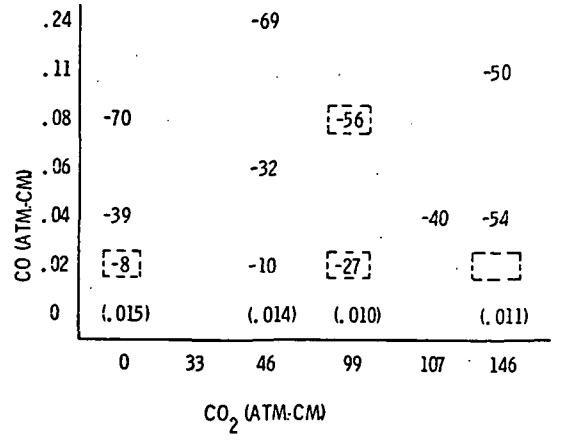

Note: Units of tabular data are % error of CO measurement except for data in parentheses which are absolute amount of CO in atm.-cm.

Table 7.2.18. Accuracy of CO Laboratory Measurements, 4.6 μ

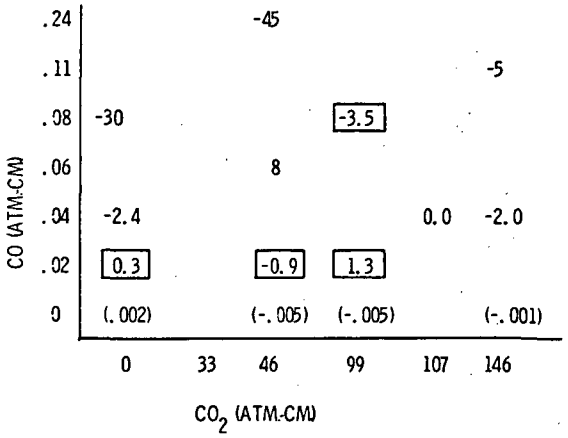

Table 7.2.19. Accuracy of CO Laboratory Measurements, 4.6 μ, at 100°C Source Temperature Using 950°C Source Weighting Function

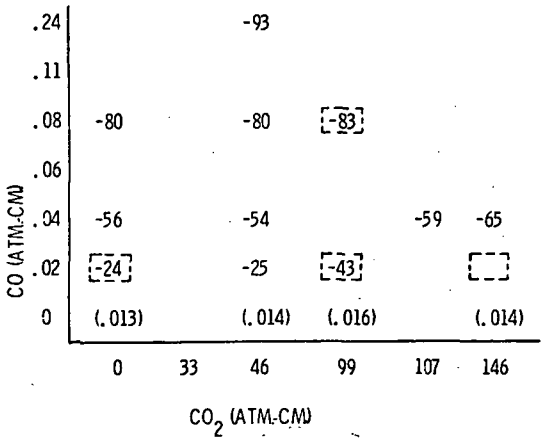

Table 7.2.20. Accuracy of CO Laboratory Measurements, 4.6 μ, at 100°C Source Temperature Using 400°C Source Weighting Function

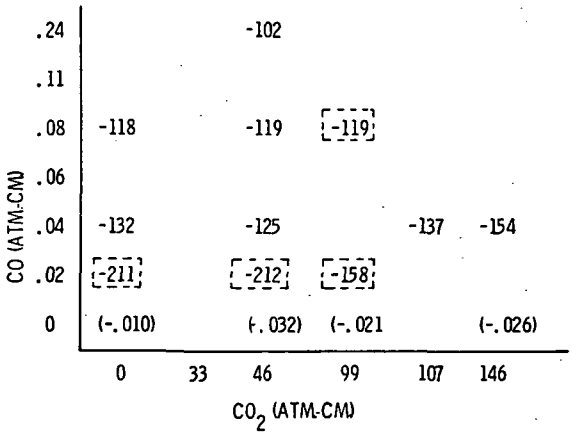

Note: Units of tabular data are % error of CO measurement except for data in parentheses which are absolute amount of CO in atm. -cm.

Table 7.2.21. Effect of Source Temperature on Accuracy of CO Column Density Measurements, 4.6 μ, Using 950°C Source Weighting Function

SOURCE TEMPERATURE (°C)	ACCURACY (%)
950	0.0, -1.1
400	-47.1, -47.6
100	-53.5, -54.1

CONDITIONS
.08 ATM-CM CO
.5 ATM-CM N_2O
99 ATM-CM CO_2
PRESSURE 760 TORR
GAS TEMPERATURE 25°C

Table 7.2.22. Effect of Gas Temperature on Accuracy of CO Column Density Measurements, 4.6 μ, Using 25°C Gas Weighting Function

GAS TEMPERATURE (°C)	ACCURACY (%)
25	-6.8, -7.3
45	-21.0, -19.0

CONDITIONS
.04 ATM-CM CO
.5 ATM-CM N_2O
46 ATM-CM CO_2
PRESSURE 670 TORR
SOURCE TEMPERATURE 400°C

Table 7.2.23. Effect of Pressure on Accuracy of CO Column Density Measurements, 4.6 μ, Using 760 Torr Weighting Function

PRESSURE (TORR)	ACCURACY (%)	CONDITIONS
760	0.0, 2.5	.04 ATM-CM CO
670	3.1, 5.6	.5 ATM-CM N_2O
		46 ATM-CM CO_2
		SOURCE TEMPERATURE 950°C
		GAS TEMPERATURE 25°C
760	-10.6, -9.0	.04 ATM-CM CO
670	-6.8, -7.3	.5 ATM-CM N_2O
		46 ATM-CM CO_2
		SOURCE TEMPERATURE 400°C
		GAS TEMPERATURE 45°C

2. The effect of N_2O is negligible. The effect of CO_2 can be eliminated by including in the data used to obtain the correlation function the extreme limits of CO_2 density over which measurements are to be made.

3. The accuracy of measured CO densities is somewhat worse than 10% and much worse at burdens greater than 0.1 atm.-cm.

4. The response of the instrument is quite non-linear. Calibration would have to be done over smaller ranges of CO than at 2.3 microns.

5. Gas temperature and pressure have significant effects on the measurements.

6. Source temperatures has serious effects on the measurements.

7. Interpolation between calibration points gives better results than extrapolation beyond points both for CO and CO_2.

7.3 Outdoor Tests

Tests of the breadboard continued with outdoor tests at 2.3 microns. These were carried out to determine if the instrument was capable of making measurements of CO in the presence of water vapor and other interferents of the atmosphere. The results showed that the instrument was definitely capable of this. The tests were carried out making measurements with a cell containing from zero to 0.5 atm.-cm. of CO interposed in front of the instrument. The instrument was able to measure an addition of 0.02 atm.-cm. of CO to about 20% (of the added CO). This is just 10% of the atmospheric amount. The results from data obtained in a two-hour period of one day (noted here as Day 2) are given in Table 7.3.1. The data compare the actual amount of added CO in the cell with the measured amount. This is the amount above that already in the stmospheric path which is about 0.2 atm.-cm. Very good agreement is found even when the amount of CO added is only 10% (.02 atm.-cm.) of the atmospheric burden. This is the CO-density region of most interest. This illustrates the major point which the outdoor experiments were intended to prove - that accurate CO measurements can be made in the presence of water and other atmospheric interferents. Similar results are given for data of Day 3 in Table 7.3.2. In each case the correlation function was obtained from data taken during the period when the test measurements were obtained. The data used for calculation of the correlation function are enclosed in rectangles.

The results obtained were very good as long as the conditions of the correlation functions were about the same as those of the test runs. Since during the day and from day to day the path length, the amount of CO, the amounts of water vapor, methane and other interferents, the temperature, the source strength, the amounts of clouds and haze, and the wind changed, the conditions of the calibration runs are extremely

Table 7.3.1. Short Term Measurements, 2.3 μ, (Day 2)

CONDITIONS

TEMPEATURE	12°C
RELATIVE HUMIDITY	48%
WATER	6500 PPM

TIME OF DAY	ADDED CO (ATM-CM)	MEASURED ADDED CO (ATM-CM)
1150	0.10	0.101
1158	0.021	0.024
1202	0	0
1305	0.20	0.20
1314	0.10	0.108
1322	0.021	0.023
1329	0	-0.006
1333	0	0

Table 7.3.2. Short Term Measurements, 2.3 μ, (Day 3)

CONDITIONS

TEMPERATURE	4°C
RELATIVE HUMIDITY	48%
WATER	4000 PPM

TIME OF DAY	ADDED CO (ATM-CM)	MEASURED ADDED CO (ATM-CM)
1120	0.105	0.116
1133	0.025	0.057
1145	0	0
1150	0.525	0.525
1200	0.210	0.214
1210	0.105	0.118

important. Results were much better when calibration runs included data from several days rather than just one. This confirms the results obtained theoretically and in the laboratory. That is, much better results are obtained when the calibration runs cover the entire range of variables of the test cases, which means that it is much better to interpolate between, rather than extrapolate beyond calibration points. The data which show this are presented in Tables 7.3.3, 7.3.4, and 7.3.5. The data from the four days of outdoor tests are presented with the data treated with correlation functions obtained from data of one of the days. In each case the measurements are best for the day on which the calibration data were obtained. Those of the other days are not nearly as good. This is similar to extrapolation.

Table 7.3.6 shows the results where the data of all four days are treated with a correlation function obtained from data of two days. The results for these two days are reasonably good while those for the other two days are poor.

In Tables 7.3.7 and 7.3.2 results are shown for the data of all four days treated with a correlation function obtained from data of three days. The results for all four days are reasonably good. The data are all as good as, and most are better than, in the case of the treatment with a correlation function taken from data of only one day.

These data lead to certain conclusions concerning measurements of CO at 2.3 microns. Specifically,

1. CO can be measured in the atmosphere in the presence of the natural interferents of the atmosphere.

2. The correlation function should be obtained using as wide a range of conditions as possible.

3. The accuracy of the results is reasonable for the conditions under which the data were obtained.

7.4 Long-Path Breadboard Demonstration at NASA/ LRC

During the course of the long-path tests at NASA/ LRC a total 454 interferograms were collected and stored in the LRC computer for processing.

The first set of data processed consisted of a matrix of test cases in which the carbon monoxide and methane ranged from 0 to 0.914 atm.-cm. and 0 to 5.44 atm.-cm., respectively. The 434-foot tunnel was completely saturated with water vapor and contained about 230 atm.-cm. (or 0.185 precipitable-cm.). Initial processing of the data was carried out to verify that the instrument was operating properly. The test data with the tunnel saturated with water show good agreement between the measured and

Table 7.3.3. Accuracy of Outdoor Measurements, 2.3 μ, Weighting Function Based on Data of Day 2

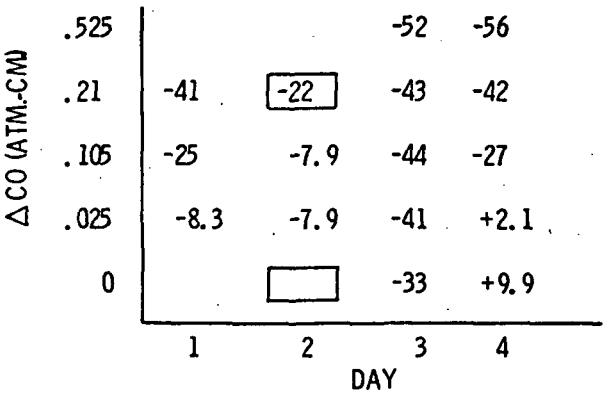

Table 7.3.4. Accuracy of Outdoor Measurements, 2.3 μ, Weighting Function Based on Data of Day 3

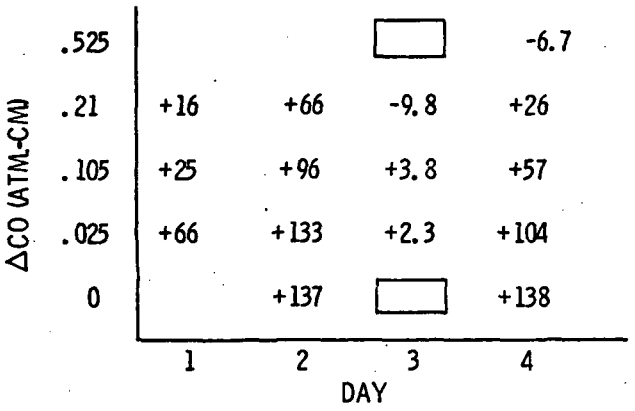

Table 7.3.5. Accuracy of Outdoor Measurements, 2.3 μ, Weighting Function Based on Data of Day 4

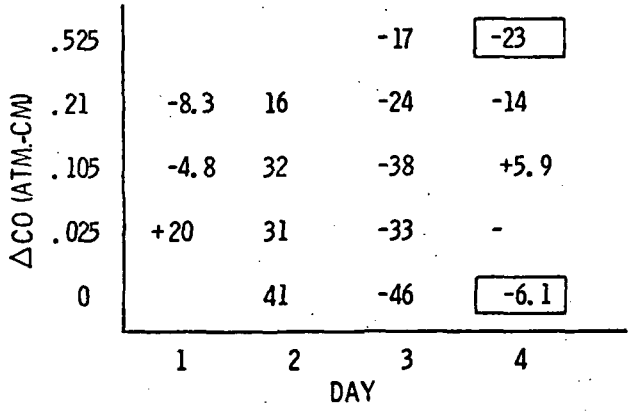

Table 7.3.6. Accuracy of Outdoor Measurements, 2.3 μ, Weighting Function Based on Data of Days 3 and 4

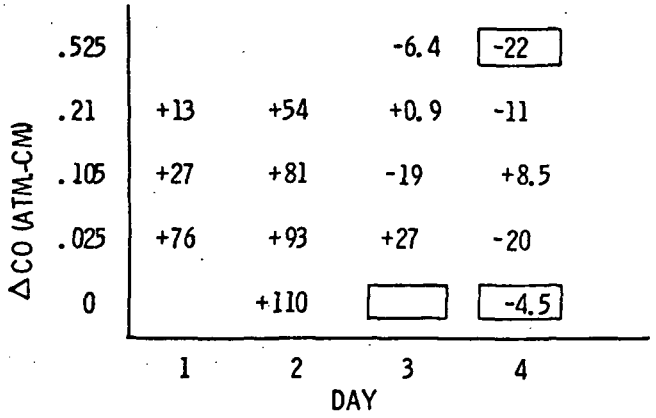

Note: Units of tabular data are % error of CO measurement except for data in parentheses which are absolute amount of CO in atm.-cm.

Table 7.3.7. Accuracy of Outdoor Measurements, 2.3μ, Weighting Function Based on Data of Days 2, 3 and 4

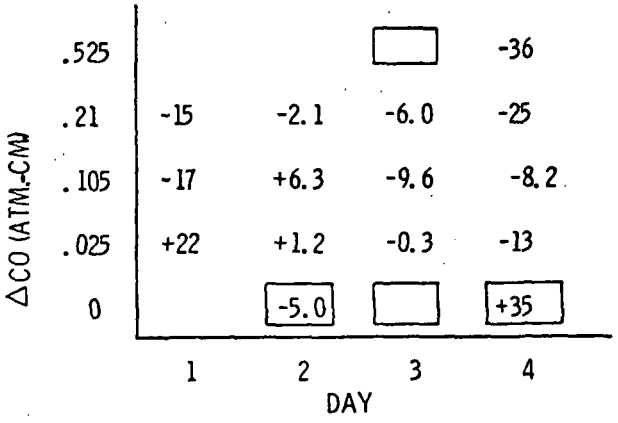

Table 7.3.8. Accuracy of Outdoor Measurements, 2.3μ, Weighting Function Based on Data of Days 2, 3 and 4

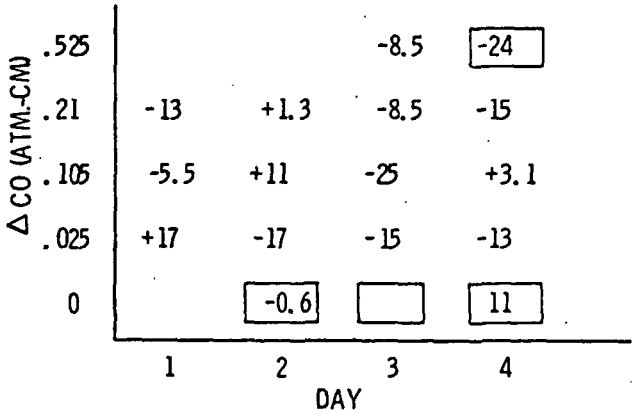

Note: Units of tabular data are % error of CO measurement except for data in parentheses which are absolute amount of CO in atm.-cm.

actual amounts of carbon monoxide when allowance is made for the slight measurement drift noted in the instrument. In this case the drift was measured by setting up a standard set of gas conditions (i.e., 0.201 atm.-cm. of CO and 2.72 atm.-cm. of CH_4) in the gas cells introduced into the optical path which included the 434-foot tunnel. Table 7.4.1 indicates the variation of the measurement of the standard condition over a period of time which extended over two days. The variation amounted to a maximum of only -0.01832 atm.-cm. of CO during the tests. It should be noted that the measurement variation can be caused by an instrument effect or a slight change in the water vapor content of the tunnel. In either case the effect is small compared with the nominal atmospheric amount of 0.20 atm.-cm. of CO.

Applying the same correlation function to the set of measurements as was used for the standard measurements in Table 7.4.1, the CO was measured very accurately (Table 7.4.2). These tabulated data are all for a methane amount of 2.72 atm.-cm. The measurements of the small amounts of CO, i.e., 0.0202 atm.-cm., show a measurement offset which is consistent with the variation shown in Table 7.4.1. It should, however, be noted that the difference between 0.0 and 0.0202 atm.-cm. of CO amounts to 0.01888 atm.-cm. of CO is one takes the difference between the average measured values given in Table 7.4.2. The measurements of 0.914 atm.-cm. of CO were in error by about 10% due to the measurement being made by extrapolation to CO amounts larger than the target amount of 0.457 atm.-cm.

Table 7.4.1. Time Dependent CO Measurement Variations, Tunnel Tests

TEST CASE NO.	DATE DATE	TIME TIME	MEASURED CO (atm.-cm.)	ACTUAL CO (atm.-cm.)	ΔCO (atm.-cm.)
1	2/1/72	13:48	.20100	.20100	0
2		13:52	.20008		- .00002
19		16:05	.20457		+ .00357
20		16:15	.20016		- .00084
25	2/2/72	8:15	.20514		+ .00414
26		8:20	.20797		+ .00697
29		9:03	.18413		- .01687
30		9:10	.18268		- .01832
43		10:45	.18873		- .01227
44		10:50	.18985		- .01115
83		16:05	.20168		+ .00068
84		16:10	.20476		+ .00376
89	2/3/72	9:43	.19547		- .00553
90		9:49	.20100		0
124		14:44	.21487		+ .01387
125		14:47	.20954		+ .00854

Table 7.4.2. CO Measurements in the Presence of CH_4 and H_2O
(0.201 atm.-cm. of CO - nominal; 0.457 atm.-cm. of CO - target)

TEST CASE NO.	MEASURED CO (atm.-cm)	ACTUAL CO (atm.-cm)	PERCENT ERROR
93	- .00936	0.00	---
94	- .01527	0.00	---
95	.00733	0.0202	- 63.72
96	.00582	0.0202	- 71.19
54	.09925	0.1005	- 1.25
55	.09161	0.1005	- 8.84
89	.19547	0.2010	- 2.75
90	.2010	0.2010	0.0 Nominal
71	.45411	0.457	- 0.63
70	.457	0.457	0.0 Target
5	.81553	0.914	- 10.77
6	.81777	0.914	- 10.53

In addition to the computed data presented in Table 7.4.1, correlation functions were calculated for the following cases:

Correlation Function	Nominal CO (atm.-cm.)	Target CO (atm.-cm.)
1	0.201	0.914
2	0.201	0.457
3	0.0202	0.914
4	0.0202	0.457
5	0.00	0.914
6	0.00	0.457
7	0.100	0.914
8	0.100	0.457

In general the CO measurements made with the other correlation functions show the show the same trends as the data presented. Using the correlation function No. 1, which uses the larger target amount of CO, the measurements show better agreement for the large amount of CO (Table 7.4.3). The measurement errors for amounts of CO smaller than 0.201 atm.-cm. are larger than in Table 7.4.2 where the target amount of CO was 0.457 atm.-cm. Extending the CO range to the larger target amount makes the measurement more non-linear than when 0.457 atm.-cm. was used for the target. This means that measurements which try to extrapolate outside the range from 0.201 to 0.914 atm.-cm. will have greater errors. In addition there is also the measurement drift which was previously noted. It should again be noted that the difference between 0.0 and 0.0202 atm.-cm. of CO amounts to 0.02107 atm.-cm. of CO if one takes the difference between the average measured values given in Table 7.4.3.

Further carbon monoxide measurements in the presence of methane and water vapor are shown in Tables 7.4.4 and 7.4.5. These data cover the CO range from 0 to 0.914 atm.-cm. and the CH_4 range from 0 to 5.44 atm.-cm. In all cases the tunnel was saturated with water vapor and the optical path contained about 230 atm.-cm. of water vapor. The numbers shown on the tables indicate the precentage error in the measured CO or CH_4 except that those numbers in parentheses indicate the measured value of CO or CH_4 in atm.-cm. The nominal and target cases used in the data reduction are indicated in the tables by the square boxes.

In Table 7.4.4 the nominal CO amount is taken at 0.201 atm.-cm. and the target CO is 0.457 atm.-cm. Extrapolation to larger CO amounts gives an error of the order of 10% which is due primarily to the non-linear CO absorption at CO levels of 0.914 atm.-cm. Extrapolation to CO amounts less than 0.201 atm.-cm. indicates a small measurement offset introduced which is of the order of -0.0123 to +0.0127 atm.-cm. indicated when no CO was present in the test cells. However, the measurements with 0.020 atm.-cm. In Table 7.4.5 the target amount of CO was taken as 0.914 atm.-cm. and the nominal amount was 0.100 atm.-cm. The measured values of CO within the range are

Table 7.4.3. CO Measurements in the Presence of CH_4 and H_2O (0.201 atm.-cm. of CO - nominal; 0.914 atm.-cm. of CO - target)

TEST CASE NO.	MEASURED CO (atm.-cm)	ACTUAL CO (atm.-cm)	PERCENT ERROR
93	-.03927	0.00	---
94	-.04597	0.00	---
95	-.02078	0.0202	-202.85
96	-.02232	0.0202	-210.50
54	.08197	0.1005	- 18.44
55	.07186	0.1005	- 28.50
89	.19482	0.2010	- 3.07
90	.201	0.2010	0.0 Nominal
70	.47943	0.457	4.91
71	.47782	0.457	4.56
5	.914	0.914	0.0 Target
6	.91732	0.914	0.36

Table 7.4.4. CO Measurement Accuracy with CH_4 and 230 atm.-cm. H_2O in the Optical Path

CO (ATM.-CM.)	0	1.80	2.72	3.61	4.52	5.44
.914	-6.34	-9.72	-10.65	-10.51	-11.34	-11.20
.457	10.47	4.07	-0.63 T	-0.41	-5.90	-5.75
.200	-2.83	-3.51	-5.83 N	-2.84	-2.96	-1.91
.100	(.1275)	(.1024)	(.0954)	(.1069)	(.0939)	(.1169)
.02	(0424)	(.0279)	(.0066)	(.0131)	(.0177)	(-.0005)
.01					(.0092)	
0	(.0217)	(.0035)	(-.0123)	-.0036	(-.0047)	-.0083

CH_4 (ATM.-CM.)

Table 7.4.5. CO Measurement Accuracy with CH_4 and 230 atm.-cm. H_2O in the Optical Path

CO (ATM.-CM.)	0	1.80	2.72	3.61	4.52	5.44
.914	3.45	1.60	1.20 T	-0.39	-1.66	1.17
.457	9.0	11.34	8.00	8.03	5.71	6.30
.200	-1.84	10.39 4.47	-4.47 0.74	5.54 -1.52	-0.0 4.99	14.09
.100	(.10164)	(.1064)	N	(.0920)	(.0942)	(.1136)
.02	(.0132)	(.0300)	(.0137)	(.0107)	(.0125)	(.0137)
.01					(-.0047)	
0	(-.0118)	(.0002)	(.0041)	(-.0092)	(-.0192)	(.0040)

CH_4 (ATM.-CM.)

Note: Units of tabular data are % error of CO measurement except for data in parentheses which are absolute amount of CO in atm.-cm.

generally within 10% with a few exceptions. The measured values of CO below 0.100 atm.-cm. show the same trend as discussed above in Table 7.4.4. The small measurement of offsets observed are not inconsistent with the long term drift effects noted in the long term stability measurements.

A series of laboratory tests was conducted with the instrument in which a range of test cases was set up using the cells and a collimated incandescent source. A set of interferograms was collected using 100 scans, 10 scans, and 1 scan for each interferogram case in order to determine the effect of reducing the measurement time on the measurement. Repeated measurements were made on a test case which had 0.20 atm.-cm. of CH_4 in the cells. The data were analyzed to show the mean measured CO and the standard deviation and these are tabulated below:

No. of Scans	Mean Measured CO (atm.-cm.)	Standard Deviation (atm.-cm.)
100	0.2145	0.0035
10	0.2109	0.0064
1	0.2179	0.0165

Thus, it is seen that the noise level is about twice as bad at 10 scans as it is at 100 scans, and 5 times worse at 1 scan as the noise level at 100 scans.

In addition to the investigation of measurement S/N variation with the number of scans (measurement time), the data were also processed to determine the effect of using smaller portions of the interferogram in the calculation of the correlation functions. A set of test cases was examined in which the nominal CO level was 0.100 atm.-cm. and the target amount was 0.914 atm.-cm. The methane range and water vapor amount are the same as discussed previously. The test cases computed were those shown in Table 7.4.6.

Table 7.4.6. Test Cases for Effect of Number of Sample Points

Table Number	Sample Points
7.4.7	2 to 33
7.4.8	4 to 33
7.4.9	6 to 33
7.4.10	8 to 33
7.4.11	2 to 31
7.4.12	2 to 29
7.4.13	2 to 27
7.4.14	4 to 31
7.4.15	6 to 29

Table 7.4.7 CO Measurement Accuracy with CH_4 and 230 Atm.-Cm. H_2O in the Optical Path

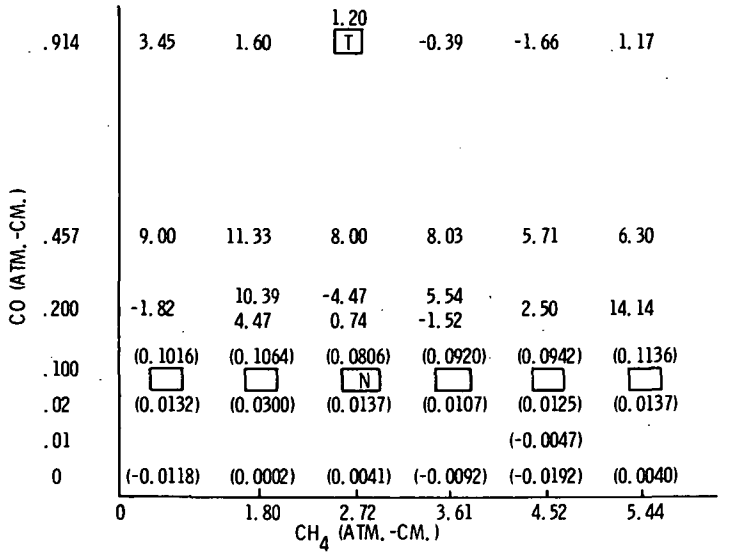

Note: Samples 2 to 33.
Units of tabular data are % error of CO measurement except for data in parentheses which are absolute amount of CO in atm.-cm.

Table 7.4.8 CO Measurement Accuracy with CH_4 and 230 Atm.-Cm. H_2O in the Optical Path

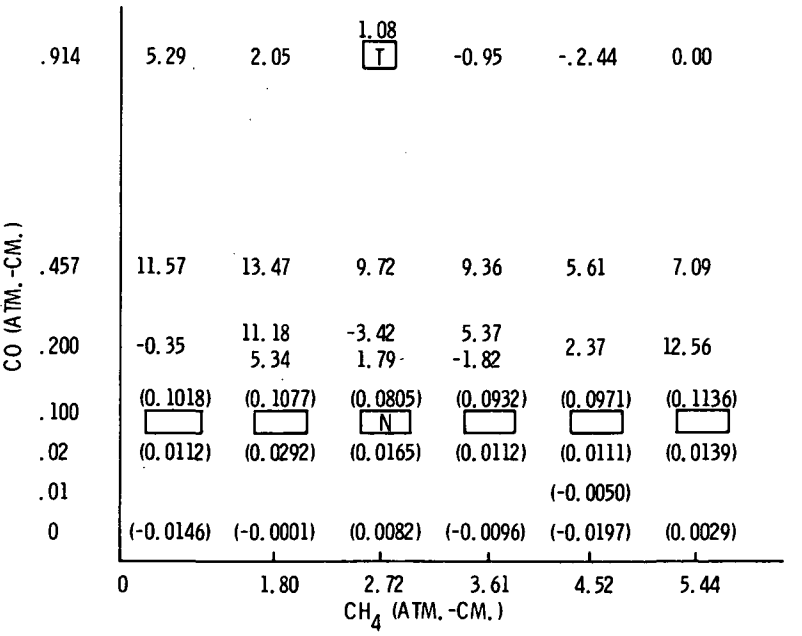

Note: Samples 4 to 33.
Units of tabular data are % error of CO measurement except for data in parentheses which are absolute amount of CO in atm.-cm.

Table 7.4.9 CO Measurement Accuracy with CH_4 and 230 Atm.-Cm. H_2O in the Optical Path

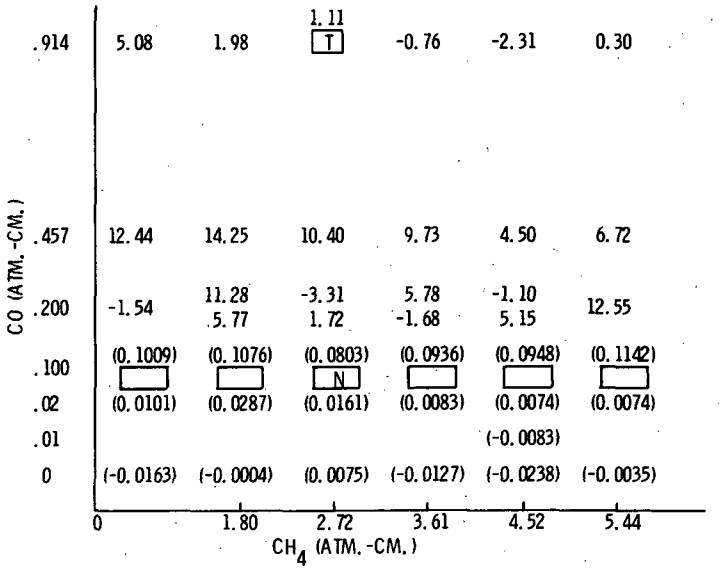

Note: Samples 6 to 33.
Units of tabular data are % error of CO measurement except for data in parentheses which are absolute amount of CO in atm.-cm.

Table 7.4.10 CO Measurement Accuracy with CH_4 and 230 Atm.-Cm. H_2O in the Optical Path

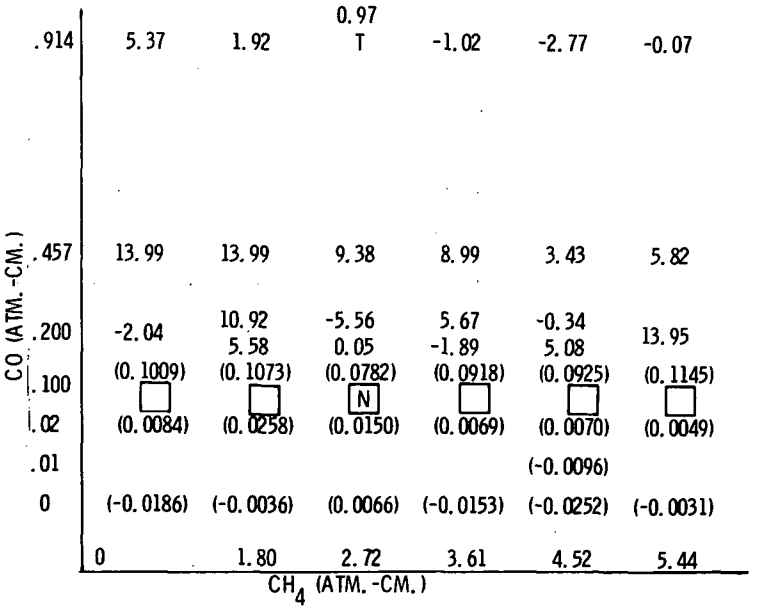

Note: Samples 8 to 33.
Units of tabular data are % error of CO measurement except for data in parentheses which are absolute amount of CO in atm.-cm.

Table 7.4.11 CO Measurement Accuracy with CH_4 and 230 Atm.-Cm. H_2O in the Optical Path

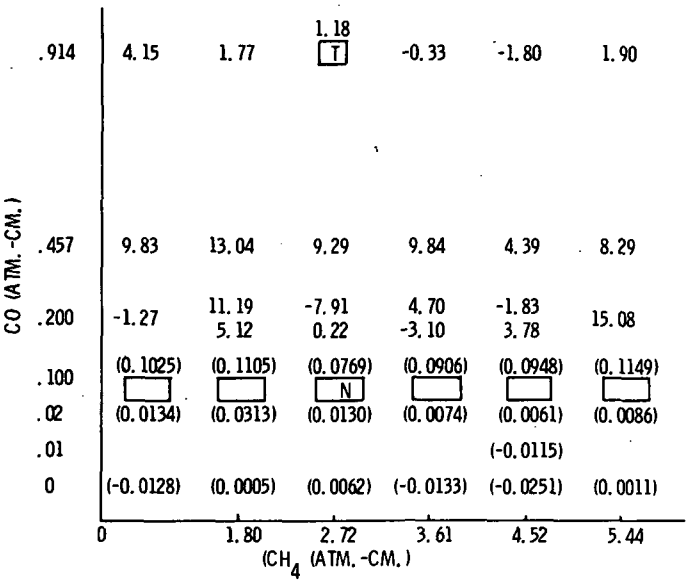

Note: Samples 2 to 31.
Units of tabular data are % error of CO measurement except for data in parentheses which are absolute amount of CO in atm.-cm.

Table 7.4.12 CO Measurement Accuracy with CH_4 and 230 Atm.-Cm. H_2O in the Optical Path

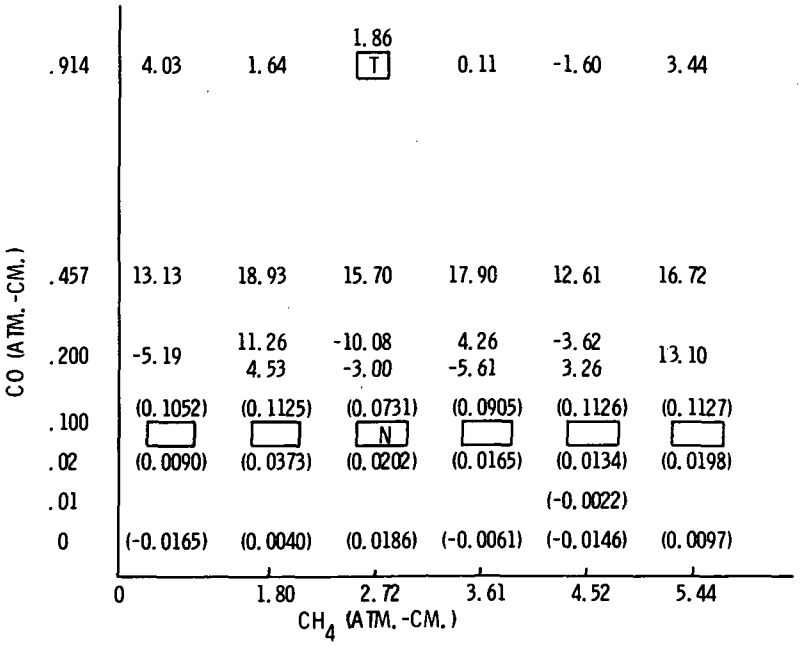

Note: Samples 2 to 29.
Units of tabular data are % error of CO measurement except for data in parentheses which are absolute amount of CO in atm.-cm.

Table 7.4.13 CO Measurement Accuracy with CH_4 and 230 Atm.-Cm. H_2O in the Optical Path

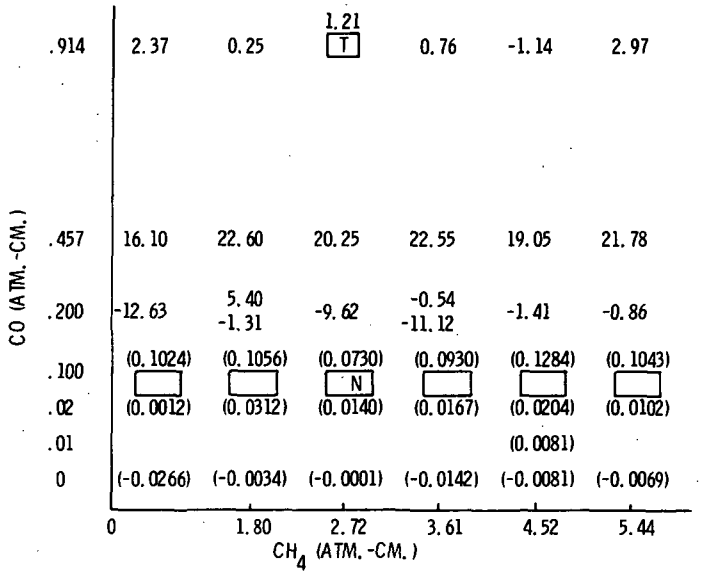

Note: Samples 2 to 27.
Units of tabular data are % error of CO measurement except for data in parentheses which are absolute amount of CO in atm.-cm.

Table 7.4.14 CO Measurement Accuracy with CH_4 and 230 Atm.-Cm. H_2O in the Optical Path

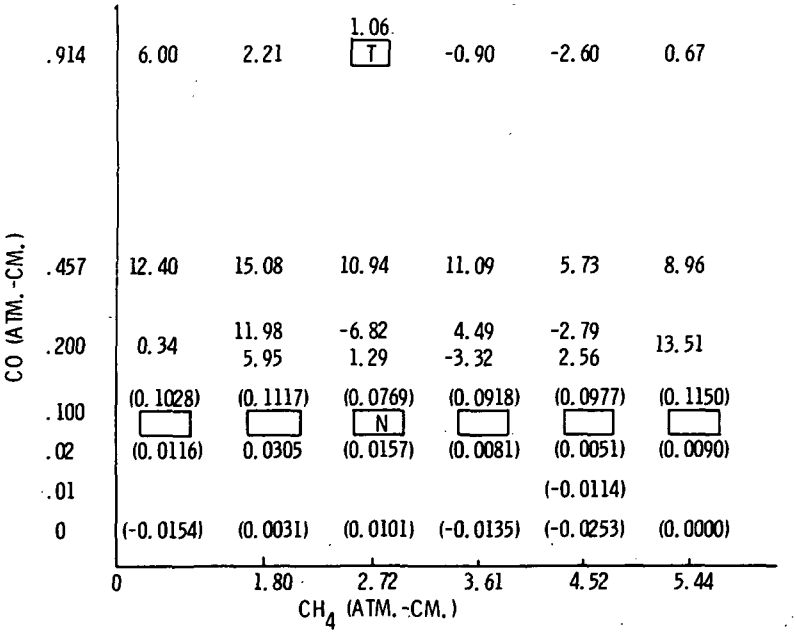

Note: Samples 4 to 31.
Units of tabular data are % error of CO measurement except for data in parentheses which are absolute amount of CO in atm.-cm.

Table 7.4.15 CO Measurement Accuracy with CH_4 and 230 Atm.-Cm. H_2O in the Optical Path

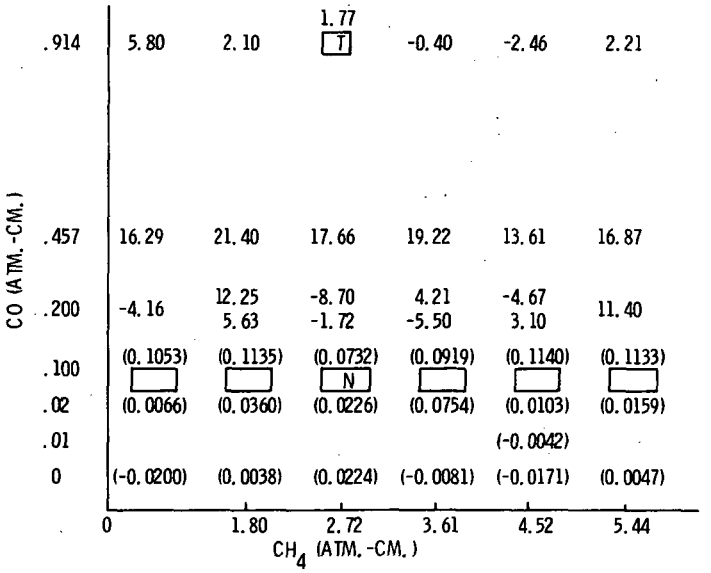

Note: Samples 6 to 29.
Units of tabular data are % error of CO measurement except for data in parentheses which are absolute amount of CO in atm.-cm.

In most cases the measurement accuracy is degraded by using fewer sample points. This is not as significant when the sample points deleted are in the initial part of the interferogram, but when the sample points are deleted from the end of the interferogram the result is more important. Since the measurements shown are averages of pairs of duplicate measurements in most cases, a quantity which is not shown is the difference between the measurements. In the case of the measurements of 0.200 atm.-cm. of CO, the two measurements are shown if they differ by 5%. In general it appears that a reduction of the sample points used results in a larger difference between pairs of duplicate measurements.

7.5 Methane Measurements with the Correlation Interferometer

Since the theory behind the operation of the correlation interferometer indicates that the technique can be applied to any species with an interferogram in the instrument delay region, the collected set of interferograms was processed to yield a methane measurement. In this case the methane is the target species of interest and the carbon monoxide and water vapor are treated as interferrents. Correlation functions for a number of combinations of nominal and target amounts of methane were computed, and the results of these calculations are shown in Tables 7.5.1 to 7.5.8.

Table 7.5.1. CH_4 Measurement Accuracy with CO and 230 Atm.-Cm. H_2O in the Optical Path

CO (ATM.-CM.)		CH_4 (ATM.-CM.)				
		0	1.80	2.72	3.61	4.52	5.44
.914	(1.55)	0.08	-7.88	-6.09	-1.95	0.80
.457	(1.47)	-0.14	-7.01	-5.78	-0.10	2.34
.201	(1.47)	0.27 N	-7.01	-3.95	-0.21 T	3.89
.100	(1.44)	-0.19	-6.72	-5.09	-0.90	2.88
0	(1.42)	-0.05	-7.29	-5.13	-1.64	2.19

Table 7.5.2. CH_4 Measurement Accuracy with CO and 230 Atm.-Cm. H_2O in the Optical Path

CO (ATM.-CM)		CH_4 (ATM.-CM.)				
		0	1.80	2.72	3.61	4.52	5.44
.914	(2.66)	23.65	-0.22	-4.86	-3.86	-2.20
.457	(2.52)	22.36	0.14	-4.39	-2.11	-0.82
.201	(2.52)	22.55	0.18 N	-3.69	-2.57	-0.16 T
.100	(2.48)	22.30	0.35	-4.13	-2.75	-0.60
0	(2.44)	22.07	-0.04	-3.79	-3.05	-0.91

Note: Units of tabular data are % error of CH_4 measurement except for data in parentheses which are absolute amount of CH_4 in atm.-cm.

Table 7.5.3. CH_4 Measurement Accuracy with CO and 230 Atm.-Cm. H_2O in the Optical Path

CO (ATM.-CM.)	0	1.80	2.72	3.61	4.52	5.44
.914	(0.0)	50.75	34.08	20.51	10.11	-0.11
.457	(0.0)	52.29	34.78	20.43	12.09	0.75
.201	(0.0) N	45.60	35.81	19.84	8.80	-.03 T
.100	(0.0)	47.63	30.55	18.07	8.17	-1.55
0	(0.0)	48.97	33.45	17.89	6.41	-1.75

CH_4 (ATM.-CM.)

Table 7.5.4. CH_4 Measurement Accuracy with CO and 230 Atm.-Cm. H_2O in the Optical Path

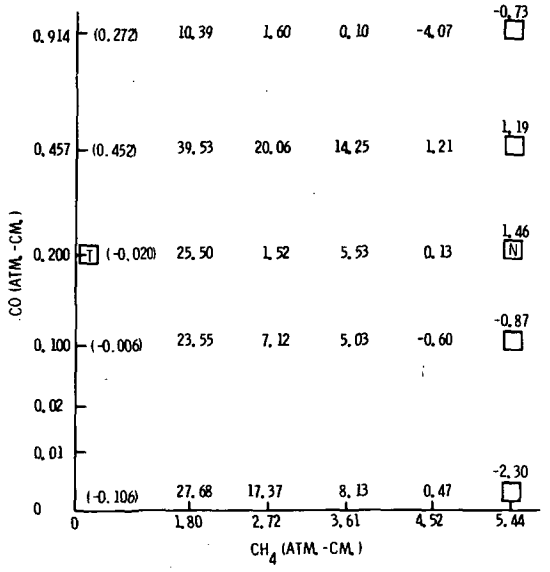

Note: Units of tabular data are % error of CH_4 measurement except for data in parentheses which are absolute amount of CH_4 in atm.-cm.

Table 7.5.5. CH_4 Measurement Accuracy with CO and 230 Atm.-Cm. H_2O in the Optical Path

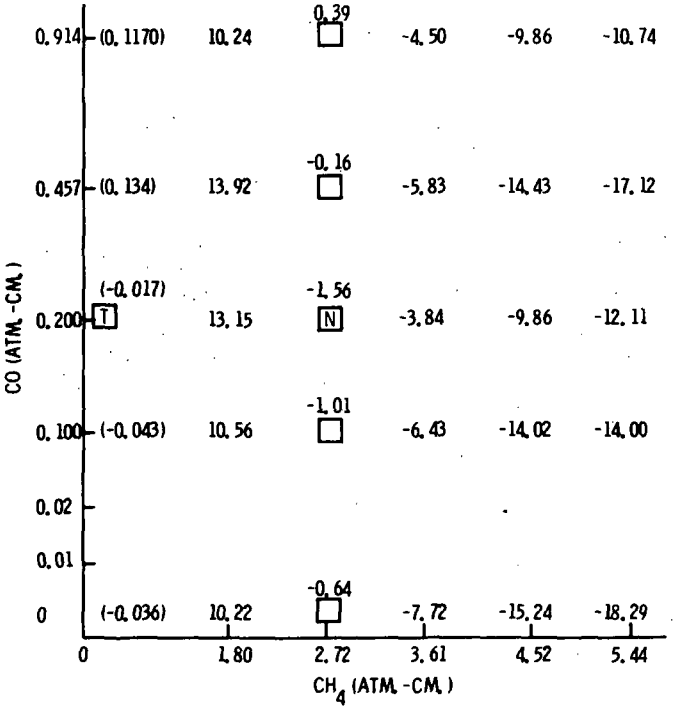

Table 7.5.6. CH_4 Measurement Accuracy with CO and 230 Atm.-Cm. H_2O in the Optical Path

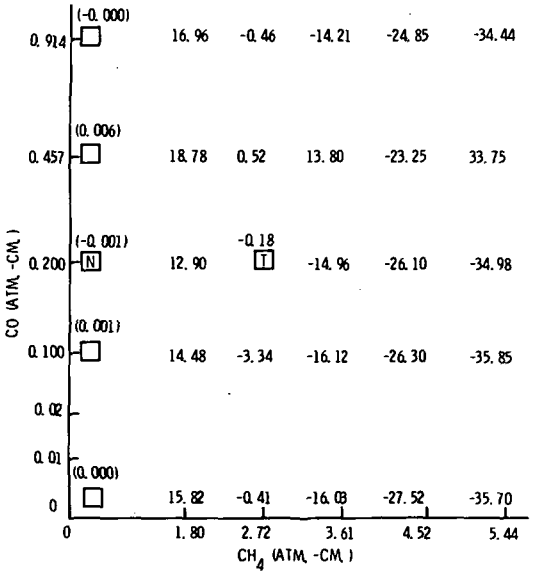

Note: Units of tabular data are % error of CH_4 measurement except for data in parentheses which are absolute amount of CH_4 in atm.-cm.

Table 7.5.7. CH_4 Measurement Accuracy with CO and 230 Atm.-Cm. H_2O in the Optical Path

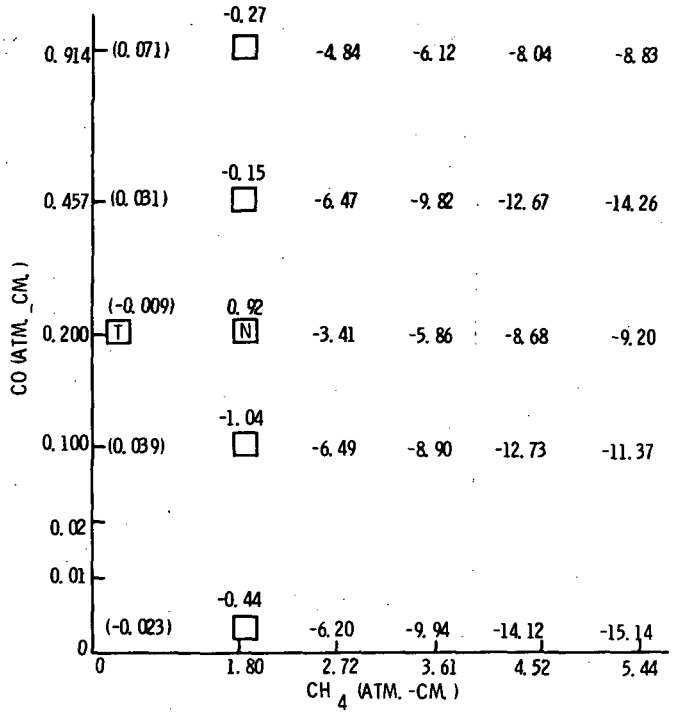

Table 7.5.8. CH_4 Measurement Accuracy with CO and 230 Atm.-Cm. H_2O in the Optical Path

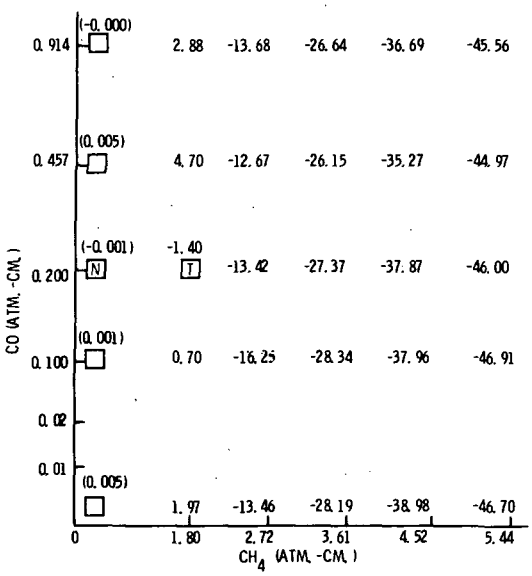

Note: Units of tabular data are % error of CH_4 measurement except for data in parentheses which are absolute amount of CH_4 in atm.-cm.

In the case of methane the tables indicate that, if the nominal and target cases are taken in the range from 1.8 to 4.5 atm.-cm. of CH_4, the methane within this range can be measured with better than 8% accuracy. Restricting the range from 2.7 to 5.4 atm. -cm. produces 22% error), but acceptable results for the larger methane amounts (e.g., extrapolation from 4.5 to 5.4 atm.-cm. produces less than 4% error). If one attempts to cover too large a range of methane (e.g., zero to 5.4 atm.-cm. in Table 7.5.3) the results are relatively poor throughout the range. However the useful range for the methane measurements is probably in the 1.8 to 5.4 range and this can apparently be covered adequately with one correlation function. If an extremely accurate methane measurement were required, then two correlation functions should cover the methane range adequately.

8. CONCLUSIONS

The testing of the correlation interferometer has shown that this technique is capable of making the desired measurements over the important range of CO in the presence of atmospheric gases.

It has been found the atmospheric amounts of CO can be measured with an error of 10% or better. The instrument tests confirmed the conclusion reached analytically (ref. 1) that the use of the overtone band at 2.3μ gives much better results than does that of the fundamental band at 4.6μ. The range of sensitivity at 2.3μ is much larger, the absorption being nearly linear from 0 to above 1 atm.-cm. and usable to at least 10 atm.-cm., whereas at 4.6μ near linearity is very limited to a factor of about five in the range of densities of interest. The effects of gas temperatures and pressures and source temperatures are negligible using the 2.3μ band but quite significant using the 4.6μ band.

Carbon monoxide can be measured accurately in the presence of the major interferents for this spectral region - methane and water. The methane effect has been found to be completely separable from that of CO. These same data can be used to measure methane as well as CO with errors of less than 10% over the range of 1 to 5 atm.-cm. which covers that to be expected in atmospheric measurements with this technique. The effect of water was studied in the long-path tunnel tests and in outdoor measurements. The tunnel tests showed that, for water densities up to 230 atm.-cm., the effect on CO accuracy is separable and minimal. The outdoor tests showed that the effect of atmospheric amounts of water can be overcome by a proper choice of correlation functions. The choice of conditions used to determine correlation functions is critical. The conditions should cover the range of variation of interferents and atmospheric parameters which affect the measurement. The use of a wide range of conditions in obtaining correlation functions and interpolation between these gives much better results than use of a narrow range with extrapolation. The outdoor tests showed that using a broad range of appropriate conditions for these functions greatly improves results.

The technique can be shown to be readily adaptable to the measurement of many other trace species through minor instrumental changes which are expected to be capable of accomplishment in flight.

The breadboard experimental results gave good and necessary data for obtaining design parameters for the engineering model.

APPENDIX A

SIGNAL PROCESSING IN THE CORRELATION INTERFEROMETER

A. 1 Signal Processing

In order to extract a measurement from the interferogram produced on scanning the refractor plate, the signal must be processed to minimize the effects of the various interferents and noises. Appendix A outlines the theory by which an optimum correlation function or matched filter may be determined for the measurement of a particular quantity from the signal for some specified range of interferent conditions and for given noise severities. (The procedure reduces to a matrix inversion.)

Computer programs have been generated embodying the theory. These are built around one subroutine, "WHOP", which when given a specified scan function, a selection of interferograms, and noise severities, produces an optimal correlation function and also a measurement of the signal to noise ratio for that correlation function. One group of programs, "MAPEM", is designed to examine the possible choices of scan range for the purpose of identifying that scan range which provides best signal to noise ratio. The large number of correlation functions produced in running this group are not retained, most being of no interest.

A second group, "RUNEM", may be used to either generate an optimal correlation function for some specified conditions or to pick up a previously generated and stored function, and use the function to carry out measurements on specified interferograms. This, in conjunction with a noise evaluation section of the same programs, allows signal processing with the function to be evaluated for both systematic errors (variations with interferent conditions) and random errors.

In running either group of programs, it is necessary to provide interferograms delimiting a range of interferent conditions within which actual measurements should be made. (Measurements with a correlation function for conditions much outside the range for which it was generated generally results in large systematic errors.) The target quantity for each of these interferograms should be the same; however, an additional interferogram must be provided for conditions similar to one of the other cases but with a variation of the target. The interferogram used may be the measured output of an actual instrument or the results of computations on synthetic spectra.

A.2 Relation Between Radiation Spectrum and Interferogram

In this section the relationship between the spectrum of the radiation incident upon an interferometer system, and output of the system will be outlined.

A.2.1 Incident Radiation. - The radiation incident at the instrument will have a dependence with a spectral frequency which may be conveniently represented

$$S(\nu, \bar{Q}) = S_o \times T(\nu, \bar{Q})$$

The vector $\bar{Q}$ has been used to represent all the parameters which determine the detailed structure of the spectrum; things such as quantities and profiles of various absorbers along the optical path, temperature pressure structure along the path, gradient of any non-flat reflectors (in short, anything which results in structure). The results of all such parameters may be considered as a dimensionless transmission factor $T(\nu, \bar{Q})$. The received spectral radiance S and the background radiance S_o on the otherhand have dimensions of [watts/cm^2 sterad. wavenumbers]

Defined in this manner, S is independent of the interferometer system. However, it is convenient to include in $\bar{Q}$ the characteristics of any spectral filter used in the instrument to isolate the region of interest in the spectrum. Thus T will include the filter transmission function.

The remainder of the interferometer system is characterized by its light grasp or etendu E (cm^2 steradians), its efficiency e (dimensionless) and of course the delay setting x (centimeters). (The efficiency e may be used to account for variation in x over the interferometer aperture by including a fringe visibility term.) For a given setting of the interferometer, the radiation available to the detector is

$$I(x, \bar{Q}) = e\,E \int_{\nu=0}^{\infty} [1 + \cos(2\pi\nu x)]\; S(\nu, \bar{Q})\, d\nu$$

$$= e\,E\,S_o \left[\int_{\nu=0}^{\infty} T(\nu, Q)\, d\nu + \int_{O}^{\infty} \cos(2\pi\nu x)\, T(\nu, Q)\, d\nu \right]$$

We may define $P_o = e\,E\,S_o$ (nominal available spectral power, [watts/wavenumber]), and

$$W(x, \bar{Q}) = \int_{\nu=0}^{\infty} \cos(2\pi\nu x)\, T(\nu, Q)\, d\nu$$

(equivalent width of optical path + interferometer system for delay setting x, in wave number).

Then

$$I(x, \bar{Q}) = P_o\, [W(x, \bar{Q})]\ (\text{watts}) + P_o \int_{\nu=0}^{\infty} T(\nu, Q)\, d\nu$$

The equivalent widths $W(x, \bar{Q})$ depend only on the characteristics of the optical path and the spectral filter, and may be evaluated independently of considerations of the gross parameters S_o, e, and E.

It is generally desired to operate under a range of conditions for $\bar{Q}$. Signal processing will have as its object the measurement of one or more of the parameters comprising $\bar{Q}$, in such a manner as to be insensitive to variation of the remaining parameters within their anticipated range. In developing a procedure for making this measurement it is useful to consider approximations for the variation of the spectra and interferograms with the parameters $\bar{Q}$.

If nominal conditions are defined by parameters $\bar{Q}_o$, it is possible to write

$$S(\nu, \bar{Q}) = S(\nu, Q_o) + \Sigma\, (Q_i - Q_{oi})\, S_i(\nu) + \ldots\ldots\ldots\ldots$$

$$= S_{oo}(\nu) + \Sigma\, q_i\, S_i(\nu) + \Sigma\, q_i q_j\, S_{ij}(\nu) + \ldots\ldots$$

where

q_i = change in the amount of the ith constituent from the nominal condition.

If the terms of such an expression are obtained from a Taylor expansion, one has

$$S_i = \left[\frac{\partial S(\nu, \bar{Q})}{\partial Q_i} \right] \bar{Q}_o$$

$$S_{ij} = \left[\frac{\partial^2 S(\nu, \bar{Q})}{\partial Q_i\, \partial Q_j} \right] \bar{Q}_o$$

etc.

In the case of Q_i representing the concentration path products for absorber with absorption coefficients

$$S(\nu, \bar{Q}) = S_o e^{-\Sigma_i \alpha_i}$$

$$= S_o e^{-\Sigma_{io} \alpha_i} [1 - (\Sigma q_i \alpha_i) + (\Sigma q_i \alpha_i)^2/2 !.....]$$

$$= S_{oo} + \Sigma q_i S_i + ...$$

This gives

$$S_{oo} = S_o e^{-\Sigma Q_{io} \alpha_i} \qquad \text{and} \qquad S_i = S_{oo} a_i$$

A. 2. 2 Expansion of the Interferogram. - Because of the linear property of Fourier transformation, any expansion of the spectrum as a sum of components results in an interferogram which is the sum of the interferograms of the individual spectral components.

Thus,

$$S(\nu, Q) = S_{oo}(\nu) + \Sigma q_i S_i (\nu) + \Sigma q_i q_j S_{ij}(\nu) + ...$$

gives an interferogram

$$I (x, \bar{Q}) = I_{oo}(x) + \Sigma q_i I_i (x) + \Sigma q_i q_j I_{ij}(x) + ...$$

where

$$I_{oo}(x) = \int_{\nu=0}^{\infty} [1 + \cos (2\pi\nu x)] S_{oo} (\nu) dv.$$

It is instructive to consider the case where only the linear terms are important. If there are m parameters q_i (i = 1, ...m), and if the interferograms is observed at n points x_K (K = 1, ... n), then the observations are

$$\begin{aligned} I(x_1) &= I_{oo} (x_1) + q_i I_1 (x_1) .... + q_m I_m (x_1) \\ &\vdots \qquad\quad \vdots \qquad\quad \vdots \\ I(x_n) &= I_{oo} (x_n) + q_1 I_1 (x_n) .... + q_m I_m (x_n) . \end{aligned}$$

If there are just m observation points, and if the I_{oo} terms are known, then the observations constitute m equations in m unknown (the q_i), and may be solved by matrix inversion. The equations may be written

$$I(x_k) = I_{oo}(x_k, \bar{Q}) = \sum_{i=1}^{m} q_i I_i(x_k)$$

$$= \Sigma q_i I_{ik}$$

which have the solutions

$$q_i = \sum_{k=1}^{m} I_{ik}^{-1} [I(x_k) - I_{oo}(x_k, Q)] .$$

In the case that there are more observation points than there are variables, the linear least squares technique is applied.

A.3 Determination of Correlation Functions

A.3.1 Basic Principles. - In the linear approximation, it may be assumed that the interferogram may be represented in terms of the interferogram obtained for some nominal set of conditions (nominal atmospheric parameters and nominal composition), to which are added differential interferograms according to the deviations of the conditions from nominal. For example, if the parameters which determine the spectral distribution of the incident light are represented by some array of values $\bar{Q}$, i. e.

$$S = S(v, \bar{Q}), \quad (\bar{Q} = Q_1, Q_2, \ldots . Q_N)$$

then at least for small deviations of $\bar{Q}$ from some nominal set of values $\bar{Q}_o$ we may write

$$S(v, \bar{Q}) \simeq S(v, \bar{Q}_o) + \sum_{1}^{N} q_i (dS/dQ_i)_{\bar{Q}_o}$$

$$\equiv S(v, \bar{Q}_o + \Sigma q_1 S_i(v),$$

where

$$q_i = Q_i - Q_{io}$$

Now the interferogram observed $I(x, \bar{Q})$ is the cosine Fourier transform (CFT) of $S(v, \bar{Q})$. As Fourier transformation is a linear operation, we may write to the same approximation.

$$I(x, \bar{Q}) \simeq I(x, \bar{Q}_o) + \sum_{1}^{N} q_i I_i(x),$$

where

$I_i(x)$ are the CFT's of $S_i(v)$.

(Non-linear effects may be included by adding terms of the form $q_i q_j I_{ij}(x)$).

It is desired to measure one of the parameters, Q_j say. Unfortunately variation of the other parameters from nominal values as well as this one result in variation of the interferogram. The problem is to make a measurement on the interferogram which is sensitive only to variations in the target parameter, q_j, and not to the other q_i.

Signal processing theory has dealt with the application of a linear filter or correlation function $H(x)$ to the interferogram to make the measurement. An additional degree of freedom may be available in the length of time $D(x)$ (duration) spent at each interferogram point ($D(x)$ must be positive). The measurement made is then

$$M(\bar{Q}) = \int H(x)\, D(x)\, I(x, \bar{Q}) dx$$

$$= \int M_o + \Sigma q_i\, Mi;$$

where

$$M_i = \int H(x)\, D(x)\, I_i(x)\, dx,$$

$$M_o = \int H(x)\, D(x)\, I(x, \bar{Q}_o) dx.$$

It is relatively simple to produce a correlation function which gives zero for all the M_i, except for the target M_j. It is only necessary that the range of x considered contains at least as many points which exhibit different variation (with the parameters $\bar{Q}$) as there are parameters. This requires that the matrix B_{iu}

$$B_{ij} = \int I_j(x)\, I_j(x) dx$$

be non singular

The wide degree of freedom remaining in the choice of a filter function (after requiring $M_1 = 0$ for $i \neq j$) may be used to minimize the noise or uncertainty obtained in making the measurement.

A. 3. 2 Representation of Noise. - The noises can be divided into four groups, according to whether they are random in time, or synchronous with the scanning of the interferometer delay, and according to whether they are basically additive or multiplicative in their affect on the interferometer output. The table below gives examples of sources for the various noises.

	Random	Synchronous
Additive	1. Detector noise, photon noise;	3. Unanticipated interferents;
Multiplicative	2. Random vibrations;	4. Synchronous vibrations, scan sweep rate deviations, incorrect specification of weighting function

The difference in these noise sources is due to the way in which they affect the measurement. Any point of the interferogram x supplies a contribution to the measurement

$$\Delta M(x) = dM/dx$$

$$= H(x)\, D(x) \Sigma\, q_i I_i(x). \qquad (M = \int \Delta M(x)\, dx).$$

Associated with this contribution there is an uncertainty, $\Delta N(x)$, which adds in an RMS manner with the uncertainties or noises at all other points give the total uncertainty.

$$N^2 = \int (\Delta N)^2\, dx,$$

For synchronous noises, ($\Delta N(x)$ increases directly with the length of time the point is observed (the duration D(x)). For non-synchronous noises, ΔN increases only with the square root of D, i. e.

$$\Delta N(x) \propto \begin{cases} D(x) & \text{synchronous noises} \\ D^{1/2}(x) & \text{non-synchronous noises.} \end{cases}$$

In the case of additive noises, ΔN is independent of the signal amplitude, while in the case of multiplicative noises N is proportional to the expected size of the signal at that point:

$$\Delta N = \propto < I(x) >$$

$$= (\Sigma < q_i^2 > I_i^2 (x))^{1/2}$$

The notation

$$r^2 (x) \equiv \Sigma < q_i^2 > I_i^2 (x)$$

will be used in representing this portion of the multiplicative noises.

In addition to the factors outlined above, each of the contributors to ΔN is weighted by the full weighting function H(x). The various noises will again add up in an RMS manner; i. e.

$$\Delta N^2 (x) = \sum_{k=1}^{4} \Delta N_k^2 (x).$$

The table below then shows the way in which the various noise sources contribute to $\Delta N_i^2 (x)$ (apart from constant factors which indicate the total severity of the sources).

	Random	Synchronous
Additive	1. $H^2 (x)D$	3. $H^2(x)D^2(x)$
Multiplicative	2. $H^2 (x)D(x)r^2 (x)$	4. $H^2(x) D^2(x) r^2(x)$

In the constant factors are a_i (i = 1..4 as indicated in the table), then we may write

$$\Delta N^2 = H^2 [(a_1 + a_2 r^2) D + (a_3 + a_4 r^2) D^2]$$

$$= H^2 D [G_1(x) + G_2(x)D].$$

where

$$G_1(x) = [a_1 + a_4 r^2(x)]$$

$$G_2(x) = [a_3 + a_4 r^2(x)] .$$

The total expression for the noise is then

$$N^2 = \int H^2(x)\, D(x)\, [G_1(x) + G_2(x)\, D(x)]dx;$$

where

$$G_1 = a_1 + a_2 r^2,$$

$$G_2 = a_3 + a_4 r^2,$$

and

$$r^2 = \Sigma < q_i^2 > I_i^2(x)$$

A.3.3 Optimization of M/N; D Specified. - Of the various factors which affect the signal to noise ratio M/N achieved in making measurement, only the correlation function H(x) may be varied in an attempt to optimize the ratio once the basic system has been specified.

It is fairly straightforward to find a correlation function H(x) which is optimum for a specified duration function D(x). This will be outlined now.

It is desired to find a correlation function H(x) which gives

$$M_i = \int H(x)\, D(x)\, I_i(x)dx$$

$$= \begin{matrix} 0 & i \neq 1 \\ 1 & i=1 \end{matrix}$$

This will give a measurement

$$M = \int H\, D\, q_i\, I_i\, dx$$

$$= q_1.$$

H is to be chosen so as to minimize N^2

$$N^2 = \int [H(x)\ D(x)]^2\ G(x)dx$$

where

$$G(x) = G_1/D + G_2$$

Defining $H'(x) = H(x)\ D(x)$, the problem is to minimize

So that

$$\int H'(x)^2\ G(x)dx = N^2 \qquad (1)$$

$$\int H'(x)\ I_i(x)\,dx = \delta_{i1} \qquad (2)$$

The equations (2) may be multiplied by Lagrange multipliers m_i and added to equation (1), to require

$$\int H'^2\ G dx + \Sigma m_i \int H'\ I_i dx = \text{minimum.}$$

Varying any particular H' (x) will result in zero variation of this expression when H' is optimized: i. e.

$$\frac{\partial}{\partial H'(x_o)} \left[\int H'^2\ G dx + \Sigma\ m'_i \int H'\ I_i\ dx\right] = 0 \text{ for all } x_o,$$

or

$$2H'(x_o)\ G(x_o) + \Sigma m_i\ I_i(x_o) = 0.$$

This gives

$$H'(x_o) = \Sigma m'_i\ I_i\ (x_o)/G(x_o)$$

where

$$m'_i = m_i/2.$$

The m_i may be determined by substituting for H' in the equations (2) and solving:

$$\int H'(x)\, I_j\,(x)\, dx \;=\; \delta_{i1} \;=\; \Sigma m_i' \int (I_i\, I_j/G)dx$$

or

$$\Sigma m_i' A_{ij} \;=\; \delta_{j1}$$

where

$$A_{ij} \;=\int (I_i\, I_j)/G\; dx$$

This set of linear equations has the solution

$$m_i' \;=\; \Sigma_j\; A^{-1}_{ij}\; \delta_{j1}.$$

where

A^{-1} is the inverse of matrix A.

Thus we may write

$$H'(x) \;=\; HD \;=\Sigma\; A^{-1}_{i1}\; I_i\,(x)/G(x)$$

or

$$H(x) \;=\; \Sigma\; A^{-1}_{i1}\; I_i\,(x)/[G_1 + DG_2]x.$$

This H(x) can be shown to be the same one which would be used to find those values of q which give the best fit to an observed interferogram I(x), i. e. those q which minimize

$$\int [\, I(x) \;-\; \Sigma q_i\, I_i\,(x)]^2/N^2(x)\; dx,$$

when

$$N^2\,(x) \;=\; G_1\,(x)/D + G_2(x) \;=\; G.$$

The following points should be noted:

- If a given function H(x) is used, function $H_1(x) = CH(x)$ may be used to give a larger measurement $M_1 = CM$; but the signal to noise ratio remains unchanged $(M_1/N_1 = M_1/N_1)$.
- If there are synchronous noises only, $(G_1 << G_2)$, then any combination of H and D which give the same product HD will give the same signal to noise ratio. Increasing observation time in such a case does not improve the signal to noise ratio.

Paragraph A. 3. 4 outlines an algorithm for finding optimum dwell function D(x) as well as H(x), but only for the case $G_1 >> G_2$ (random noises only). The result is to give D(x) = 0 except at a small number of points. No algorithm has been produced for the general case. (The implementation of any system in which D(x) is programmable will be awkward.) The flow chart for a program implementing the algorithm for the case of D(x) specified is shown in Figure A. 3. 3. 1.

A. 3. 4 Optimization of M/N; D Variable, Random Noise. Consider a signal composed of a target signal and several interferent signals, which is essentially stationary in time but which depend on an independent variable x (interferometer delay).

We may write

$$S(x) = \sum_{i=0}^{N} q_i I_i(x)$$

i = 0 for target

≠ 0 for interferents

where

$I_i(x)$ are the shapes of the signals, and q_i their relative strengths.

Given a finite length of time to make a measurement of the target strength, being limited to observations at only a single value of x at any instant, and having present additive white random noise of constant power density N_o^2, it is desired to make a measurement of q_o with minimum uncertainty due to the noise. The parameters available for carrying out the measurement are a correlation function (H(x) which may be applied to each observation point S(x), and the duration for each observation point $D^2(x)$. $D^2(x)$ is used to force positive values for the duration.

The measurement of q_o is

$$q_o' = \int D^2(x)\, H(x)\, S(x)\, dx$$

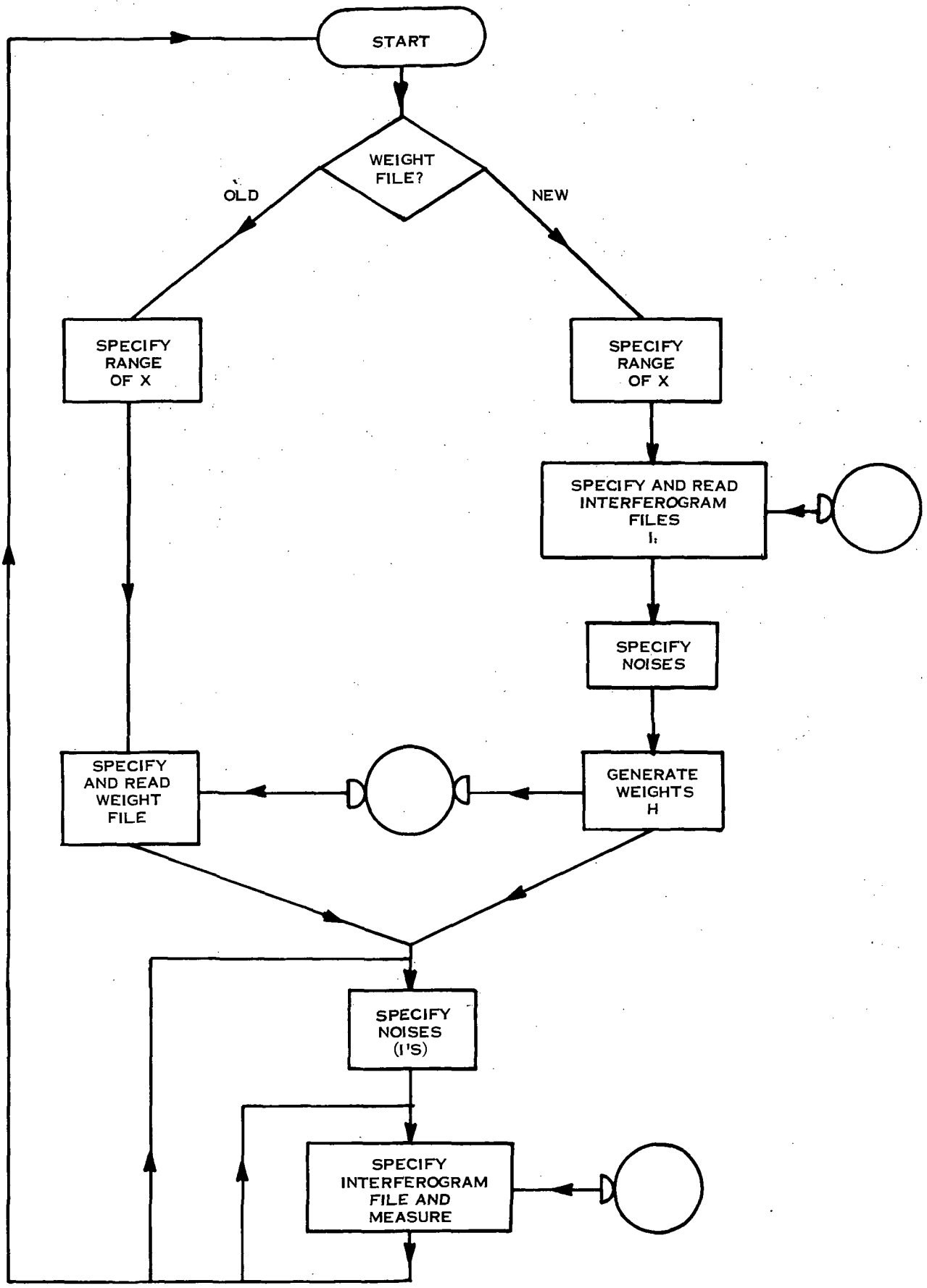

Figure A.3.3.1. Flow Chart for Program to Generate Weights, RUNEM

and has a mean square uncertainty

$$N^2 = N_o^2 \int D^2(x)\, H^2(x)\, dx$$

or

$$N^2 = N_o^2\, N'^2 \qquad (N' = N/N_o)$$

subject to the constraint

$$\int D^2(x)\, dx = T \quad \text{(the total time available for the measurement).}$$

Now q_o' may be expanded* as

$$q_o' = q_o \int D^2(x)\, H(x)\, I_o(x)\, dx$$

$$+ \Sigma\ q_i \int D^2(x)\, H(x)\, I_i(x)\, dx.$$

The sensitivities to the various signal constituents are

$$S_i = \frac{\partial q_o'}{\partial q_i}$$

$$= \int D^2\, H(x)\, I_i(x)\, dx.$$

The problem is to maximize S_o/N', while making the measurement independent of the interferents; i. e.,

$$(S_o/N')^2 = \max \tag{1}$$

$$S_i = 0 \qquad i \neq 0, \tag{2}$$

keeping in mind T = constant = 1, say. (3)

---

* Summation over the index i will be from 1 to N, unless a lower limit of 0 is explicitly indicated. $(\Sigma \rightarrow \overset{N}{\underset{1}{\Sigma}}\ ;\ \Sigma \rightarrow \overset{N}{\underset{0}{\Sigma}})$

In terms of D^2 and H, these conditions may be written as

$$\frac{\left(\int D^2 H I_o dx\right)^2}{\int D^2 H^2 dx} = (S_o / N)^2 = \max \tag{4}$$

$$\int D^2 H I_i dx = 0 \qquad i \neq 0 \tag{5}$$

$$\int D^2 dx = 1 \tag{6}$$

Variational techniques may be applied: multiplying (5) by m_i, (6) by m_t, and adding all of these to (4), we have

$$\frac{\left(\int D^2 H I_o dx\right)^2}{\int D^2 H^2 dx} + \Sigma m_i \int D^2 H' I_i dx + m_t \int D^2 dx = \max \tag{7}.$$

If small variations are applied to D^2 (x) and to H (x), the following expressions are obtained:

for

$$\delta D: \quad D(2k HI_o - k^2 H^2 + \Sigma m_i HI_i + m_t) = 0; \tag{8}$$

$$\delta D: \quad D^2 (2k I_o - 2k^2 H + \Sigma m_i I_i) = 0, \tag{9}$$

where

$$k = \left(\int D^2 H I_o\right)/\left(\int D^2 H^2\right) = S_o/N'^2 .$$

These expressions may be satisfied for any x by either the portions within the brackets simultaneously vanishing for each equation, or else by D = 0. At these points for which $D \neq 0$, the bracketed portion of (9) gives

$$H(x) = I_o/k + \Sigma m_i I_i/2k.$$

On the other hand, the bracketed portion of the first expression gives

$$H^2(x) = H(x) \cdot (2 I_o/k + \Sigma m_i HI_i/k^2) + m_t/k^2$$

$$= 2\,[H(x)]^2 + m_t/k^2;$$

i.e.,

$$H^2(x) = -m_t/k^2.$$

This gives 3 results for points at which D is non-zero: first, $H^2(x) = C$ (constant); second, $m_t < 0$; and third, $I_o/k + \Sigma m_i I_i/2K^2 = H(x) = \pm\sqrt{C}$.

Now if one inspects the expression (4) to be maximized, it is seen that if there is found one set H(x) giving a maximum, any other set $H'(x) = aH(x)$ will give the same maximum. Thus the constant C is arbitrary.

Further, as $H^2(x)$ = constant, the expression for the relative noise N' is

$$D^2\,C\,dx = C$$

Thus, we may arbitrarily set C=1, giving N' = 1
and

$$k = S_o^2/N' = S_o^2/N^2 \qquad (10).$$

The third result for points with non-zero duration is

$$I_o/k + \Sigma m_i'\,I_i = H(x) = \pm 1. \qquad (11). \qquad (m_i' = m_i/2k)$$

If one now considers the functions $I_o(x)$ and $I_i(x)$ to be plotted along orthogonal axes of an N+1 dimension hyperspace, the relationships $I_o(x)$ and $I_i(x)$ are parametric equations for a curve I(x) within the space (see Figure A. 3. 4. 1). Furthermore, for a given K and m_i', equation (11) defines a pair of hyper-planes in this space; one being the inverse of the other, H being +1 on one and -1 on the other. The constant k being $(S_o/N')^2$ and positive, the intercepts of the two planes with the I_o axis give the magnitude of $(S_o/N')^2$. The intersections of the hyper-planes with the $\bar{I}(x)$ curve give the corresponding points x at which observations may be made for this (k, m_i') set.

It is thus desired to find the hyperplane pair which intersects the I_o axis with the largest intercepts. However, the choice of planes must be restricted by the condition that: the points of intersection with the $\bar{I}(x)$ curve, x_j say, must be such that values $D_j^2 = D^2(x_j)$ may be found satisfying the conditions

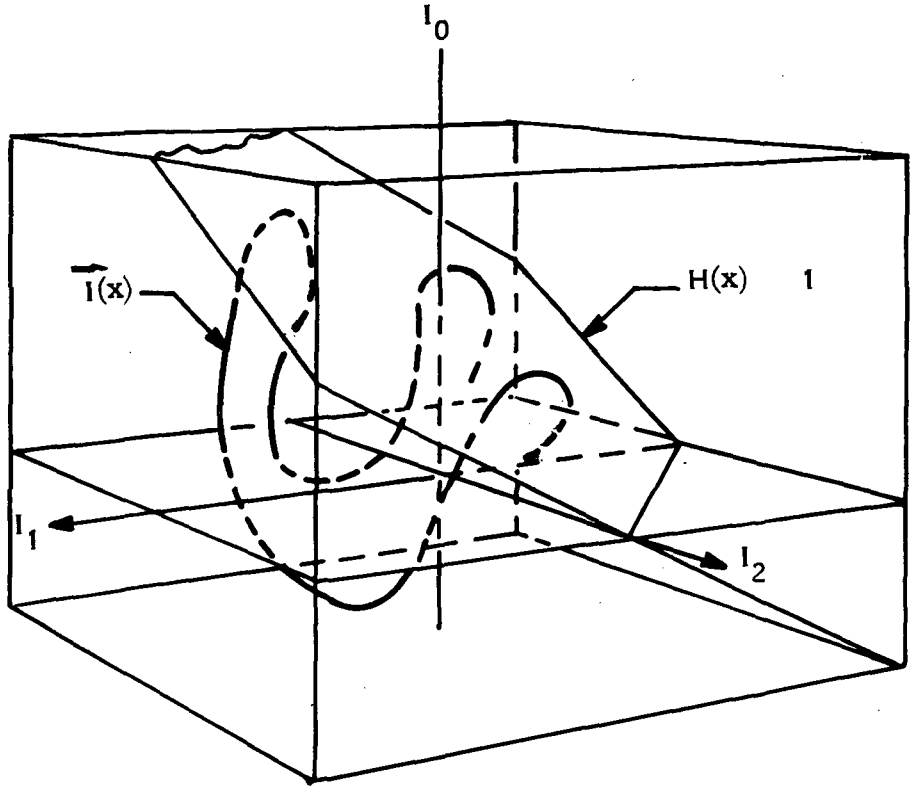

Figure A. 3. 4. 1. Parametric Plot of Interferogram

$$S_i = \sum_j D_j^2 \, H(x_j) \, I_i(x_j) = 0 \qquad i \neq 0$$

and (12)

$$\sum_j D_j^2 = 1.$$

It is possible to eliminate the plane with negative I_o intercept by adding to the curve I(x) its inversion in the origin. If we consider the inverse curve

$$\bar{I}^*(x) = -\bar{I}(x),$$

then the conditions (11) may be written

$$\Sigma m_i' \, I_i(x) = 1 \qquad (H = 1)$$

$$\Sigma m_i' \, [-I_i(x)] = \Sigma m_i' \, I_i^*(x) = 1 \qquad (H = -1)$$

$$(m_o' = 1/k').$$

Thus by considering a composite curve composed of both $\bar{I}$ and its inverse $\bar{I}^*$, one plane defined by the same m_i and having positive I_o intercept may be used to select all points satisfying equations (11). However for the points on the $\bar{I}^*$ section of the curve, $H = -1$ is used, and the observations are actually of $\bar{I} = -\bar{I}^*$. If the points on the $\bar{I}$ sections are denoted x_j, and those on the I^* x_k, then the first of equations (12) may be written

$$\sum_j D_j^2 I_i(x_j) + \sum_k D_k^2 (-1) I_i(x_k)$$

$$= \sum_j D_j^2 I_i(x_j) + \sum_k D_k^2 \times (-1) \times [-I^*(x_k)]$$

$$= \sum_j D_j^2 I_i(x_j) + \sum_k D_k^2 I^*(x_k) = 0.$$

If $\bar{I}$ is assumed to be defined on the range $(0, x)$, the composite curve $\bar{I}$, $\bar{I}^*$ may be expressed as simply $\bar{I}$, by defining

$$\bar{I}(-x) = \bar{I}^*(x) = -\bar{I}(x). \tag{13}$$

The condition (11) may be written simply

$$\sum_{i=0}^{N} m'_i I_i(x) = 1, \tag{14}$$

defining x_i for given m', and (12) becomes

$$\sum_j D_j^2 I_i(x_j) = 0 \quad i = 1, N, \tag{15}$$

$$\sum_j D_j^2 = 1$$

The problem is then to choose the plane in $\bar{I}$ space for which the I_o intercept is maximum, such that equations (15) by its intersections with the composite $\bar{I}$ curve can be satisfied.

A technique for determining this plane will be outlined below. However, some general comments may be made. First, in order to satisfy the equations (15), there

must be at least N + 1 intersection points x_j. Second, for each of the I_j there must be at least one point for which the sign of I_j is different from the rest of the points: with all $D_j^2 > 0$, (15) cannot otherwise be satisfied. This result may be generalized intuitively to require that the I_o intercept of the hyperplane must lie within the convex polyhedron defined by the points x_j.

Once N + 1 points satisfying this condition have been found, equations (15) may be most easily solved by arbitrarily specifying $D_1^2 = 1$, and then solving the first set of N equations for the remaining N values D_j^2. As these should turn out to be positive, they will not satisfy the second equation: however, a new set of D_j^2 satisfying this equation as well may then be found by dividing each D_j^2 by the sum of all D_j^2.

A. 3. 5 Determination of Optimum Plane. - Consider a curve in N dimensional space, defined parametrically as $\bar{I}(x)$. It is desired to determine an N-1 dimensional hyperplane.

$$\bar{m} \cdot \bar{I} = 1 \qquad (1)$$

(where m_i are the inverses of the intercepts) such that its intercept with a specified axis, (I_o, say), is maximum, and such that this intercept lies within the convex figure formed by the intersections of the plane with the curve $\bar{I}(x)$ (condition 'A'). (There must be at least N such intersections.)* It should be noted that if the figure contains the intercept, then its projection in the hyperplane $I_o = 0$ will contain the origin $\bar{I} = 0$.

Using this last property, the first approximation to the desired plane may be found as follows. All of the positive extrema in $I_o(x)$ ($d I_o(x)/dx = 0$) are found. (Only points with $I_o > 0$ need be considered, if $\bar{I}(x)$ is its own inverse). Of these, the N-1 points having largest I_o are identified. The projection in $I_o = 0$ of these N-1 points, plus the origin, may be used to define N-1 bounding 'planes' or order N-2 (defined within the hyperplane $I_o = 0$, each being defined by omitting one of the N-1 selected points. (The origin being include, N-1 points still remain, sufficient to define an N-2 dimensional surface.)

As the final point is chosen such that it is 'interior' to the space enclosed by these N-1 bounds, but on the side of the origin remote from the other points, than condition 'A' will be satisfied. This will be called condition 'B'. Figure A. 3. 5. 1 demonstrates the situation for N = 3. N-1 points p_1 and p_2 are found and projected in the plane $I_o = 0$. The N-1 bounds of dimension N-2 (2 lines) are found by considering the first

*Note: in the derivations of the conditions for optimum sampling, there were N interferents and one target (N + 1) signals in all). In this section there are N-1 interferents, giving N signals in all.

p_2 and the origin, and then p_1 and the origin. Any points p_3 within the shaded region will form with p_1 and p_2 a figure containing the origin. If the point is outside the region, the origin will not be contained by the figure.

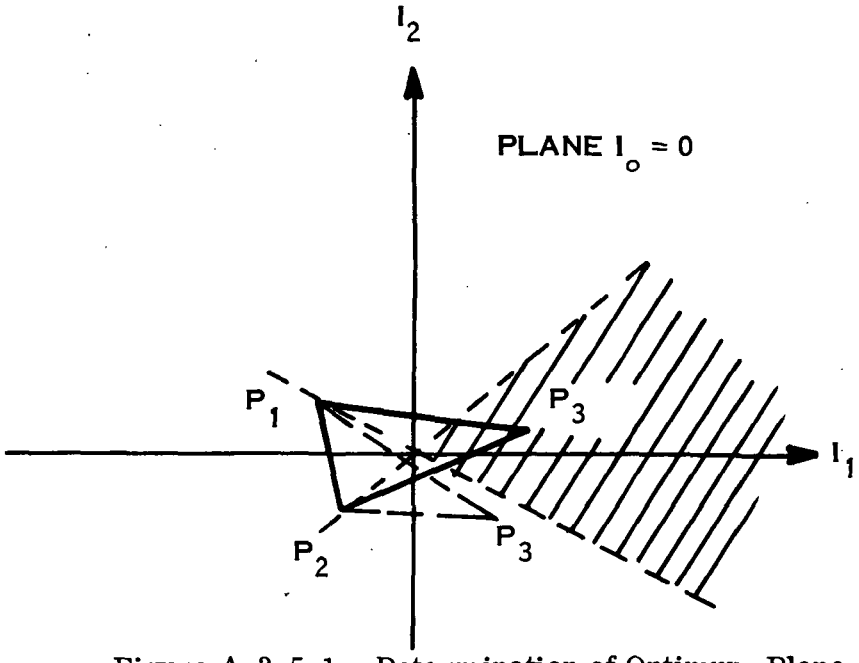

Figure A.3.5.1. Determination of Optimum Plane

Thus, after the first N-1 points have been selected, the next problem is to define the N-1 bounds of dimension N-2. The bound defined by omitting the k^{th} point may be expressed in terms of an N-1 dimensional vector $\bar{a}_k$

$$\bar{a}_k \cdot \bar{I} = 1$$

This equation must be satisfied by each of the points except the k^{th}, and also by the origin;

$$\bar{a}_k \cdot \bar{I}_i = 0 \qquad j = 0 \ldots N-1; \qquad j \neq k \tag{2}$$

where

$$\bar{I}_o \equiv 0.$$

The zero equation makes the set indeterminate and must be removed by arbitrarily specifying one of the $\bar{a}_k$. The set then becomes a set of N-2 equations in N-2 unknowns; e.g., specifying $a_{1k} = 1$

$$\sum_{i=1}^{N-1} a_{ik} I_{ij} = -I_{1j} \quad j = 1, \ldots N-1; \quad j \neq k. \tag{2'}$$

(I_{ij} is the ith coordinate of the jth point).

The arbitrariness of the signs of the a_{1k} is removed when condition B is formulated. Any point in the $I_0 = 0$ plane may be defined as being on one side or the other of the k^{th} bound by substituting its coordinates in the

$$f_k = \bar{a}_k \cdot \bar{I}. \tag{3}$$

Points for which f_k is positive are on one side of the bound, those for which f_k is negative are on the other side. Now if one point (not necessarily on the curve $\bar{I}(x)$ is found for which condition 'B' is satisfied, its position may in this manner be found with respect to each of the bounds. For those bounds giving negative f_k with this point, the signs of $\bar{a}_k$ may all be changed to give f_k positive. Once this has been done, any point giving f_k positive for all k satisfies condition 'B'.

The simplest way of obtaining one point $\bar{I}_B$ satisfying condition 'B' is to find the centroid of the N-1 points already chosen, and then to invert this point in the origin:

i.e. $$\bar{I}_B = -\left(\sum_{1}^{N-1} \bar{I}_i\right)/(N-1). \tag{4}$$

Once the $\bar{a}_k$ have been redefined, it is necessary only to search the remaining extrema in I_0 to find the largest which gives all f_k positive in equation (3). The result is then N points which define an N-1 dimensional hyperplane. Substituting their full coordinates in equation (1) gives N equations in N unknown which may be solved for $\bar{m}$, and the plane defined by the points will be specified.

The plane defined by the above procedure is a first approximation to the 'optimum' plane: its 'quality' being defined by its I_0 intercept, $1/m_0$ (which will be positive if the curve $\bar{I}(x)$ contains its own inverse). In general, this intercept will be not much smaller than for the optimum plane; however, with a fairly simple iteration procedure the optimum plane itself may be found.

If the coordinates of the origin are substituted in equation

$$f = \bar{m} \cdot \bar{I} - 1, \tag{5}$$

then the result will be $f = -1$.

Thus any point for which f is positive is located on the side of the plane remote from the origin, and those points with largest positive f are farthest from the origin. If N points may be found for which f is positive, and which satisfy condition 'A', then they will define a new hyperplane having a larger I_0 intercept than did the previous plane. The procedure is thus similar to that used in finding the first approximation, except the set of points considered is much reduced (those for which f is positive), and the condition that I_0 be extreme is replaced by the condition that f be extreme. When the data points are discrete, the process may be iterated until there are only N points left. Convergence should be rapid.

Problems may arise for certain cases in which the above procedure cannot be carried out. It may not be possible to find N maxima in I_0; or after choosing the N-1 largest maxima, it is possible that none of the remaining points satisfies condition 'B'. A method for proceeding in cases such as these must still be developed.

It should be noted that although a D varying with X was considered in the design of this instrument, the actual design of the instrument was confined to a constant D.

APPENDIX B

FIELD WIDENING

B.1 The Path Difference in a Refractively Scanned Interferometer

The change in optical path due to the introduction of a flat slab of material of thickness t and refractive index n into one arm of a Michelson interferometer can be shown to be

$$Pd = 2\,n\,t\cos\psi_n - 2\,t\cos\psi$$

Where ψ is the angle of incidence of the ray on the dispersive slab, ψ_n is the angle of refraction. For two plates plus an air path difference due to the positioning of the mirrors the overall path difference becomes

$$Pd = 2n_1 t_1 \cos\psi_{n_1} - 2t_1\cos\psi - (2n_2 t_2 \cos\psi_n - 2t_2\cos\psi) + 2T_3\cos\phi \tag{1}$$

The tilt angle θ of the plate and the ray off axis angle ϕ are related to ψ by the spherical triangle relation (see Figure B.1.1)

$$\cos\psi = \cos\theta\cos\phi + \sin\phi\sin\theta\cos\omega \tag{2}$$

ψ_n and ψ are related by Snells law

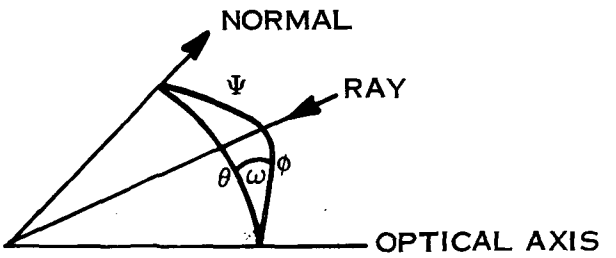

Figure B.1.1. Angle Relations in Path Difference Equations

$$n\sin\psi_n = \sin\psi \tag{3}$$

When t_1 and t_2 are unequal it is possible to field widen the interferometer at some path difference. The amount of widening possible is a function of the optical aberrations present, and a function of the scanning range. To gain some insight into the mode of

operation of such an interferometer the optical path of rays in two planes will be calculated. These planes are defined here as

1) tangential plane, where $W = O, \pi$

2) sagittal plane, where $W = \pm \pi/2$

B.2 The Small Angle Approximation (Retaining terms only to the second power)

B.2.1 The Tangential Plane ($W = O, \pi$). - In this plane, equation (2) and (3) can be approximated to $\cos \psi \simeq 1 - \frac{\psi^2}{2} = \cos \theta \cos \phi \simeq 1 - \frac{\theta^2}{2} - \frac{\phi^2}{2} (1 - \theta^2/2)$

$$\sin \psi \simeq \psi = n \sin \psi n \simeq n \psi n$$

If plate 1 is scanned by a rotation δ from some mean angle θ, plate 2 is fixed at the angle θ, and both plates have the same n, it is easily shown that the ϕ dependence is minimum for

$$PD_T = \Delta_o + \Delta_s - \Delta_s \frac{\phi^2}{2} \quad \text{where,} \tag{4}$$

$$\Delta_o = 2 (n - \frac{1}{n}) (t_1 - t_2), \quad \text{the axial path differences for } \delta = o. \tag{5}$$

$$t_3 = (1 - \frac{1}{n}) (t_1 - t_2) (1 - \frac{\theta^2}{2}) \text{ the air thickness,} \tag{6}$$

$$\Delta_s = t_1 (1 - \frac{1}{n}) (2 \theta \delta + \delta^2) \quad \text{the scan distance} \tag{7}$$

due to rotation of plate 1.

Under these conditions and to the accuracy of the small angle approximation, the off-axis angle is limited by the scanning distance. This is very like the usual Michelson case but now the scanning begins at some path difference Δ_o which is different from zero.

If the criterion is used that the on-axis ray and the off-axis ray should not differ by more than $\lambda/2$

$$PD - \Delta_o - \Delta_s \leq \lambda/2,$$

and the usuable solid angle subtended at the instrument is $\Omega = \pi\phi^2$, then

$$\Omega_T \leq \frac{\pi\lambda}{\Delta_s} \tag{8}$$

This is very like the ordinary Michelson scanning limitation

$\Omega_{MI} \leq \frac{\pi\lambda}{\Delta_{MI}}$, where Δ_{MI} is the path difference from zero. Equation (8) shows that (to the $\phi 2$ approximation) the useful field dimension in the tangential plane is limited only by the scanning range.

B. 2. 2 Sagittal Plane ($W = +\pi/2$). - In this plane the small angle approximation contains $\phi\theta$ terms.

$$\cos\psi \simeq 1 - \frac{\psi^2}{2} = \cos\theta\cos\phi + \sin\theta\sin\phi \simeq 1 - \frac{\theta^2}{2} - \frac{\phi^2}{2}\left(1 - \frac{\theta^2}{2}\right) + \theta\phi$$

An analysis like that just given for the tangential plane and assuming t_3 is given by the expression shown in equation (6) gives

$$PD_s = \Delta_o + \Delta_s - \Delta_s\left(\frac{\phi^2}{2} + \frac{\delta\theta}{2}\right) - \Delta_o\phi\theta\left(\frac{n-1}{n^2-1}\right) - 2\Delta_s\phi \tag{9}$$

Here the ϕ dependence is much more severe and for a small scanning range is determined by the second last term in expression (9). This is, however, overly pessimistic because the interferometer mirrors are in this case focussed for minimum ϕ dependence in the tangential plane. A lesser ϕ dependence in the Sagittal plane may be obtained at the expense of a somewhat greater ϕ dependence in the tangential plane. Writing the change in the focus position of the mirror as t'' one can write

$$PD_T = \Delta_o + \Delta_s(1 - \phi^2/2) + 2t''(1 - \phi^2/2) \tag{10}$$

$$PD_s = \Delta_o + \Delta_s(1 - \phi^2/2) - \Delta_s\left(\frac{\delta\theta}{2} - 2\phi\right) - \frac{\Delta_o\theta(n-1)}{(n^2-1)}\phi + 2t''(1 - \phi^2/2) \tag{11}$$

and t'' may be chosen to reduce some of the ϕ dependence of the PD_S equation, i.e., the t'' terms will completely cancel the ϕ dependent terms for some ϕ_c and δ value

$$2t'' \frac{\phi_c^2}{2} = -\Delta_s \left(\frac{\delta\theta}{2} - 2\phi_c\right) - \frac{\Delta_o \theta (n-1)}{(n^2 - 1)} \phi_c \qquad (12)$$

The small angle approximation solution given in equation (8) was compared with the maximum useful off-axis rays found using the computer solution of the exact path difference equation. The test parameters were

$t_1 = 0.945$ cm

$t_2 = 0.9$ cm

$n_1 = n_2 = 3.4425$

$\theta_1 = 45^o \pm \delta$

$\theta_2 = 45^o$

The allowable off-axis angle derived from (8) is shown as a function of tilt angle δ in Figure B.2.2.1.

The path difference as a function of angle (Figure B.2.2.2) was calculated from (5) and (7).

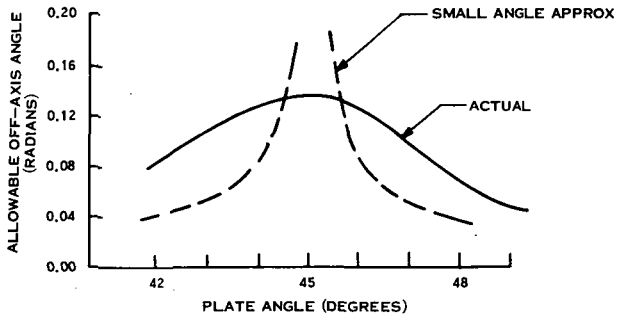

Figure B.2.2.1. Off-Axis Angle as a Function of Tilt Angle

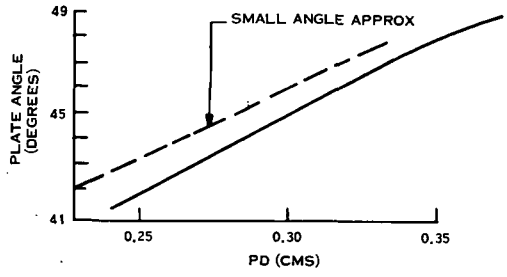

Figure B.2.2.2. Path Difference as a Function of Angle

B.3 The Effect of Aperture

For an ordinary Michelson interferometer the integrated effect of aperture is to reduce the fringe modulation amplitude according to the sin x/x function, and to introduce a phase which is a linear function of wavenumber.

Both the visibility and the phase distortion are more involved for the field widened refractively scanned Michelson than for the ordinary Michelson. The integrated effects of aperture may be found as follows. Each element, dA, of aperture contributes to the total interferogram I (Δ) according to

$$I(\Delta) = 2I_o \left\{ 1 + \frac{\int_A \cos(2\pi\sigma\Delta + \phi')\, dA}{\int_A dA} \right\} \tag{13}$$

The path difference Δ is a function of off-axis angle as shown in equation (1). Without loss of generality the integration may be performed where the axial path difference Δ_o is such that $\sigma\Delta_o$ is an integer. ϕ' is a phase angle which is an function of aperture size. If I (Δ) is derived at a maximum then ϕ' is zero for a very small aperture, and grows in size with the aperture.

Writing $\Delta = \Delta_o + \delta\Delta$, *equation (13) may be re-written as*

$$I(\Delta_o) = 2I_o \left\{ 1 + \frac{\cos\phi'}{\int_A dA} \int_A \cos(2\pi\sigma\,\delta\Delta) - \frac{\sin\phi'}{\int_A dA} \int_A \sin(2\pi\sigma\,\delta\Delta)\, dA \right\}$$

$$= 2I_o \left\{ 1 + \alpha\cos\phi' - \beta\sin\phi' \right\}$$

This may be changed to the form

$$I(\Delta_o) = 2I_o \left\{ 1 + V_A \cos(\phi' - \psi) \right\} \tag{14}$$

where the aperture visibility parameter V_A is

$$V_A = \sqrt{\alpha^2 + \beta^2} \tag{15}$$

and the phase function is

$$\psi = \tan^{-1}(\beta/\alpha). \tag{16}$$

Obviously (14) is maximum when $\psi = \phi'$. The result of numerical computer solutions for the aperture visibility and phase are shown in Figures B.3.1 and B.3.2, respectively, for the geometry $t_1 = 0.9455$ cm, $t_2 = 0.90$ cm, $n_1 = n_2 = 3.4425$ $\theta_1 = 45^o \pm \delta$, $\theta_2 = 45^o$.

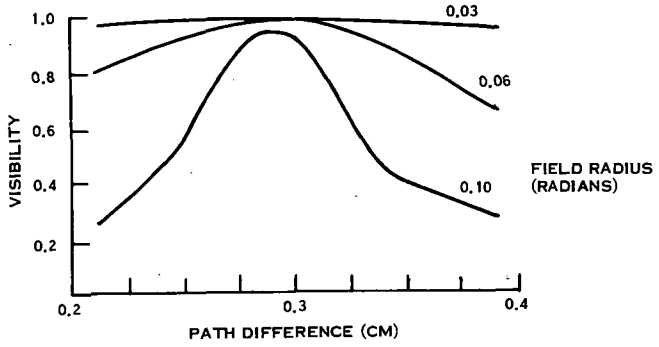

Figure B.3.1. Aperture Visibility Solutions

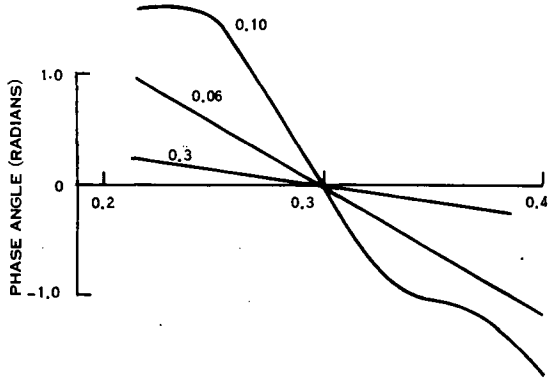

Figure B.3.2. Aperture Phase Angle Solutions

It is seen that the phase function due to aperture is essentially linear over the path difference region of interest for apertures as large as 0.06 radians. When computing the Fourier transform of a spectral distribution this phase distortion involves the product $\sigma\Delta$ and can therefore be incorporated into the computed interferogram by premultiplying the spectrum by the phase function $e^{j\psi}$ prior to performing the Fourier transform.

However, if the reference spectrum has the same aperture dependence, the path difference monitored with this reference will automatically correct the aperture phase error. The reference fringes and spectral fringes also self compensate for some other effects such as non-uniform motion in the rotating refractor plate.

B.4 Dispersion

Dispersion acts so as to yield path differences which are one function of wavelength. The axial ray path difference is given by equation (1) (or (4) in the small angle approximation). One may write the axial path difference as

$$\Delta_a = 2t_1 \sqrt{(n^2 - 1) + \cos^2\theta_1} - 2t_1 \cos\theta_1 - 2t_2 \sqrt{(n^2 - 1) + \cos^2\theta}$$

$$+ 2t_2 \cos\theta - 2t_3 \qquad (17)$$

and forming the differential to obtain the change in path differences due to dispersion (neglecting the dispersion of the air) gives

$$\delta\Delta_a = \frac{t_1 \cdot 2n\, dn/d\lambda}{\sqrt{(n^2 - 1) + \cos^2\theta_1}} \delta\lambda - \frac{\lambda_2 \cdot 2n\, dn/d\lambda}{\sqrt{(n^2 - 1) + \cos^2\theta}} \delta\lambda$$

If $\theta_1 = \theta \pm \delta$ and $\theta = 45$ degrees, $\delta < 5$ degrees, then to a good approximation $\cos^2\theta_1 = 1/2 \mp \delta$ and

$$\delta\Delta_a = \frac{2n}{\sqrt{n^2 - 1}} \frac{dn}{d\lambda} \delta\lambda \left\{ t_1 \left[1 + \frac{(1/2 \mp \delta)}{(n^2 - 1)} \right]^{-1/2} \right.$$

$$\left. - t_2 \left[1 + \frac{1/2}{(n^2 - 1)} \right]^{-1/2} \right.$$

$$\doteq 2 \left(\frac{dn}{d\lambda}\right) \delta\lambda \left[1 + \frac{1}{2n^2} \right] \left[t_1 - t_2 \right] \left[1 - \frac{1}{4(n^2 - 1)} \right] \pm \frac{2dn}{d\lambda}$$

$$\delta\lambda \left(1 + \frac{1}{2n^2}\right) \frac{t_1 \delta}{(n^2 - 1)} \qquad (18)$$

For silicon at 2.3 microns, $n = 3.4425$, $(dn/d\lambda) = -9.024$ micron^{-1}, $\delta = 3$ degrees and for features separated by $\delta\lambda = 0.02$ micron (the distance between 1/2 power points of a 1% interference filter) one obtains

$$\delta\Delta_a \doteq (0.2 \pm 0.02) \text{ wavelengths.}$$

Therefore, absorption features separated by 0.02 micron have an additional phase shift of about 70 degrees due to dispersion alone.

Interestingly at 4.6 microns for silicon the dispersion is ~ -0.0029 micron^{-1}, nearly a factor of 10 less than the value at 2.3 microns. Hence for reasonably narrow interference filters the dispersion of the interferometer at 4.6 microns may be neglected.

The effect of dispersion can be incorporated into the synthesized interferograms as follows:

$$I(\Delta) = \int_{-\infty}^{\infty} B(\sigma)\, e^{-2\pi j\sigma\,(\Delta + \delta\Delta_a)}\, d\sigma$$

$$I(\Delta) = \int_{-\infty}^{\infty} B(\sigma)\, e^{-2\pi j\sigma\,\delta\Delta_a}\, e^{-2\pi j\sigma\Delta}\, d\sigma \qquad (19)$$

The convolution theorem enables one to write

$$I(\Delta) = I'(\Delta) * T(\Delta), \qquad (20)$$

where $I'(\Delta)$ is the interferogram with dispersion neglected and

$$T(\Delta) = \int_{-\infty}^{\infty} e^{-2\pi j\sigma\Delta_a}\, e^{-2\pi j\sigma\Delta}\, d\sigma$$

is the Fourier transform of the phase function $e^{-j\phi_D}$ due to dispersion.

$$\phi_D = 2\pi\sigma\,\delta\Delta_a \qquad (21)$$

Interferograms which include the effects of dispersion may therefore be obtained in two ways. Probably the most direct method is to multiply the spectral input by the phase function prior to performing the Fourier transform. The second method is to convolve the undispersed interferograms with the function $T(\Delta)$ defined above.

Care should be used with the first method if the scanning range is large. This can be seen if the phase function is written explicitly. Equation (18) may be written in the form

$$\phi_D = (a + b\Delta)\, \delta\sigma. \tag{22}$$

In this case, the interferogram may be written as

$$I(\Delta) = \int B(\sigma)\; e^{-2\pi j \sigma a\, \delta\sigma}\; e^{-2\pi j \sigma\, (1 + b\, \delta\sigma)}\, d\sigma$$

Therefore, the first term in (22) is multiplicative in spectral space, and the second term can be incorporated by applying a scaling shift to the spectrum prior to performing the Fourier transform.

APPENDIX C

BREADBOARD ELECTRONIC CIRCUITS

APPENDIX C

BREADBOARD ELECTRONIC CIRCUITS

The following figures (C. 1 through C. 16) give the complete details of the breadboard electronic circuits, consisting of twelve plug-in cards, three preamplifiers, power supplies, and inter-card wiring.

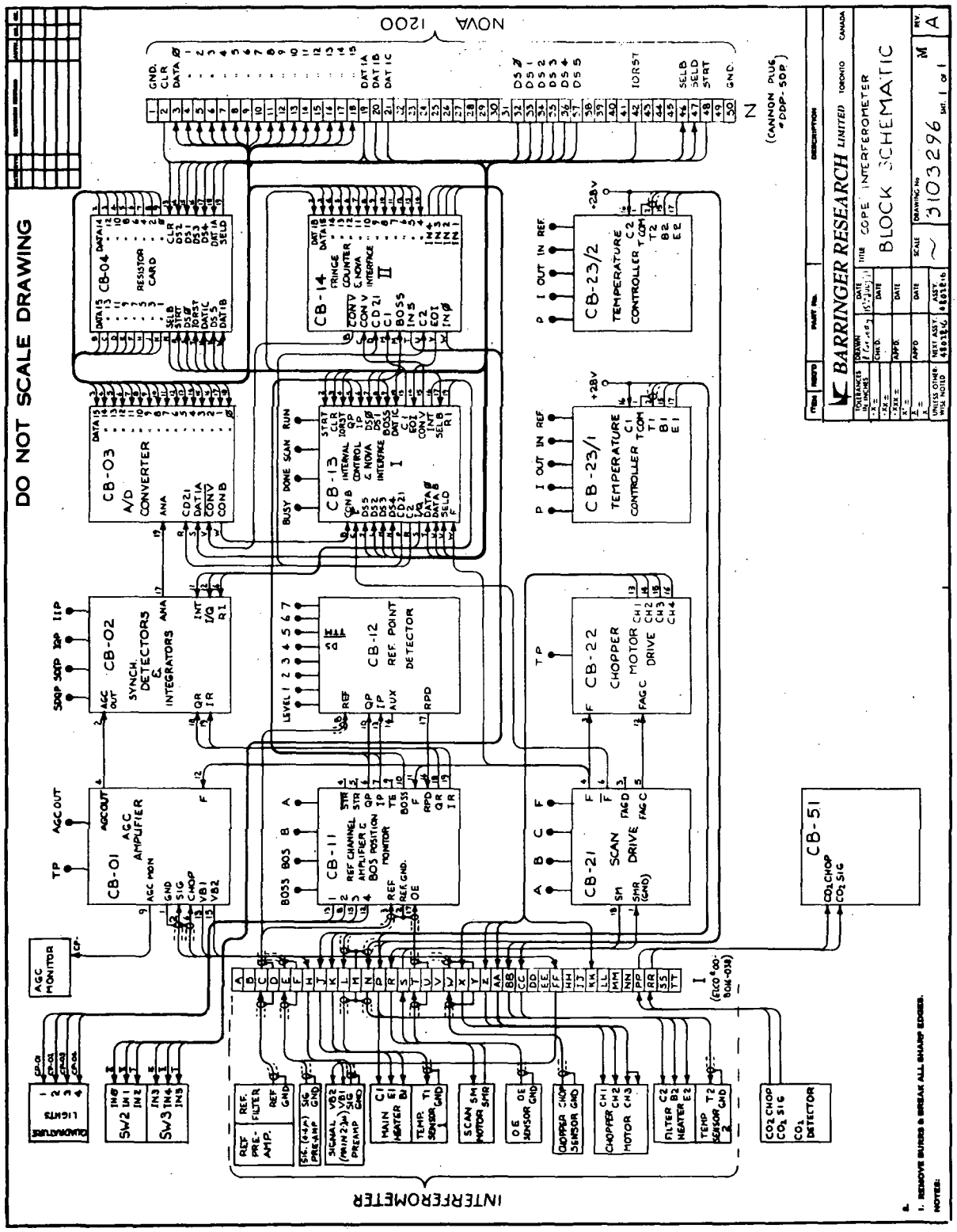

Figure C.1. Block Schematic

ORIGINAL PAGE IS
OF POOR QUALITY

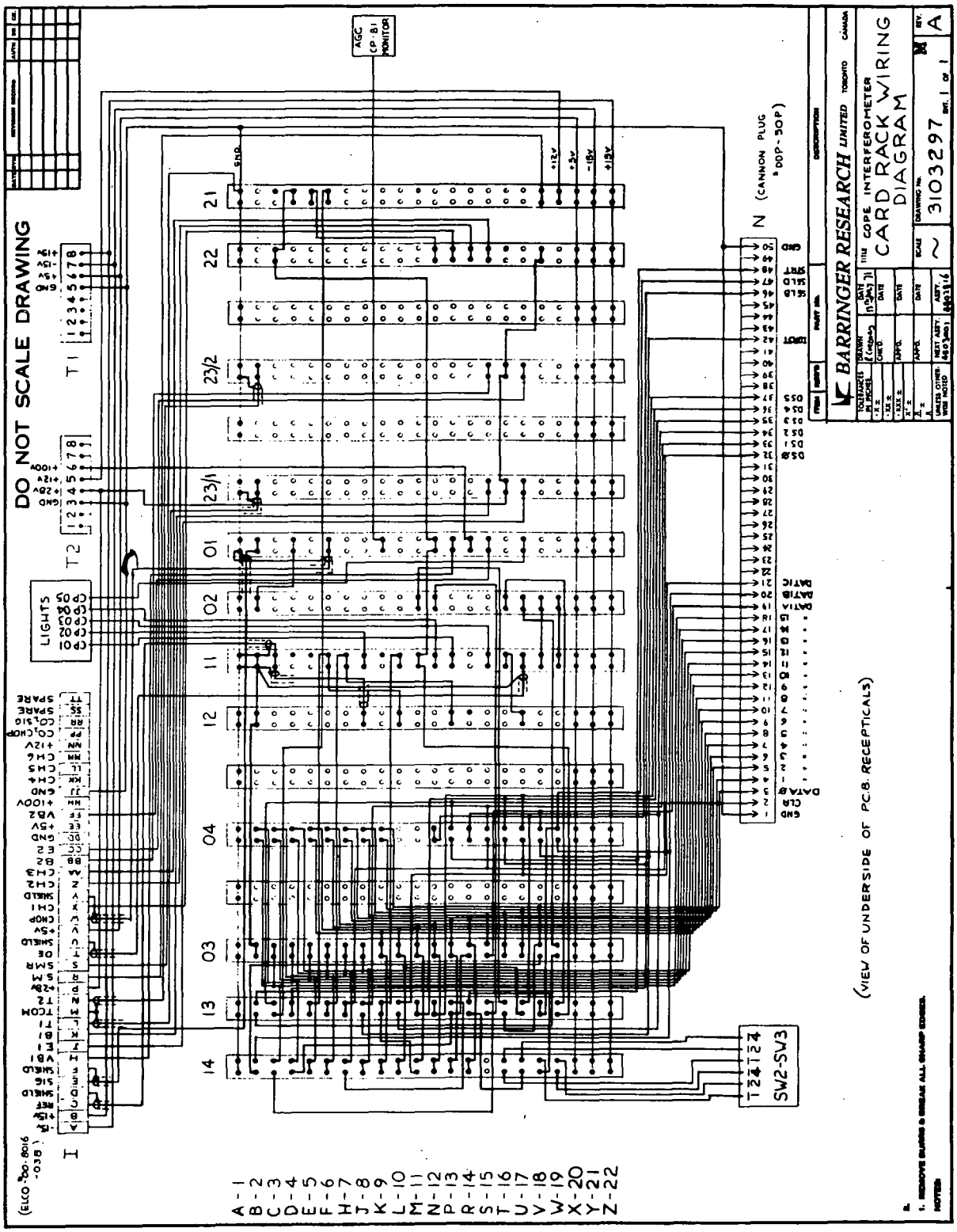

Figure C.2. Card Rack Wiring Diagram

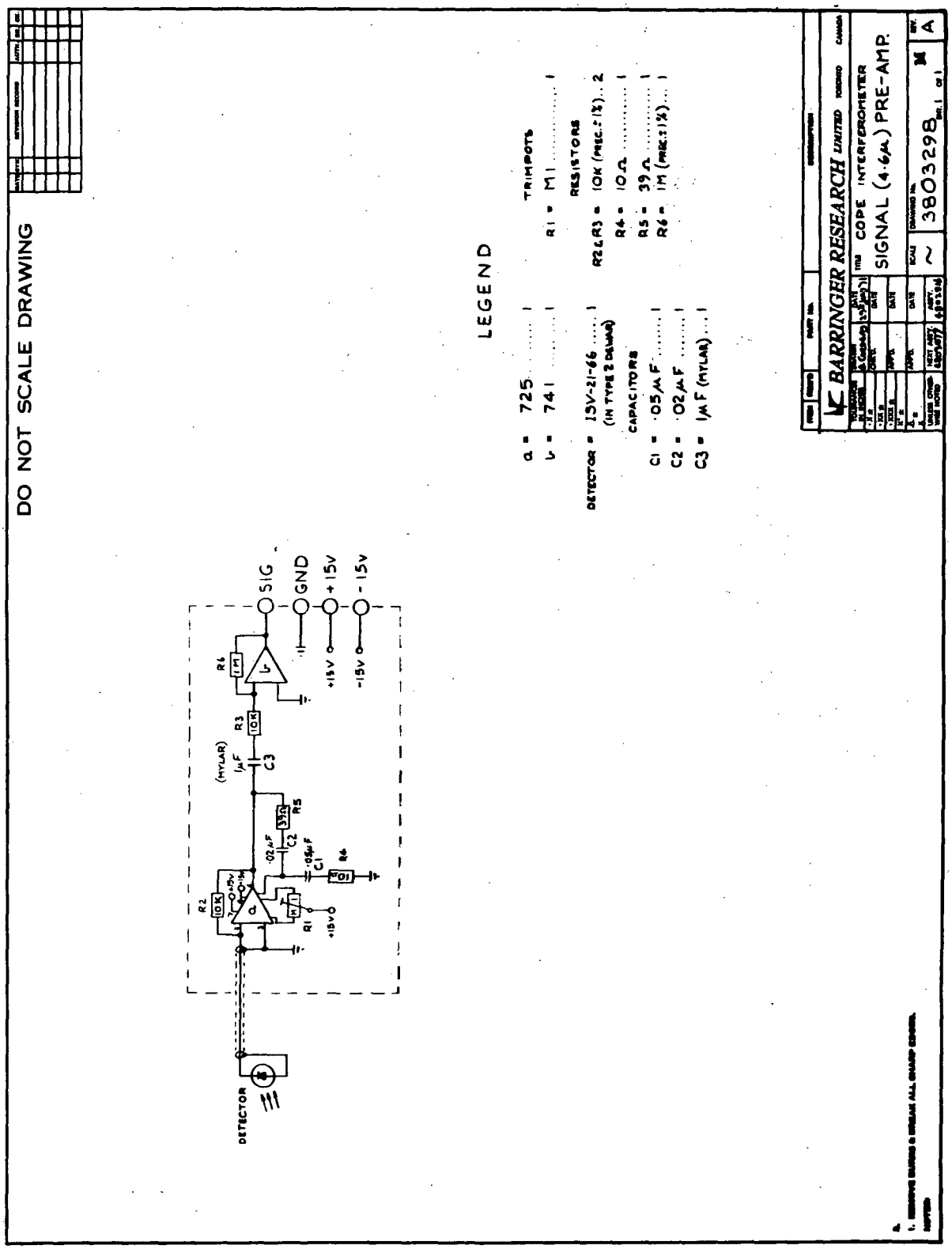

Figure C.3. Signal (4.6μ) Preamp

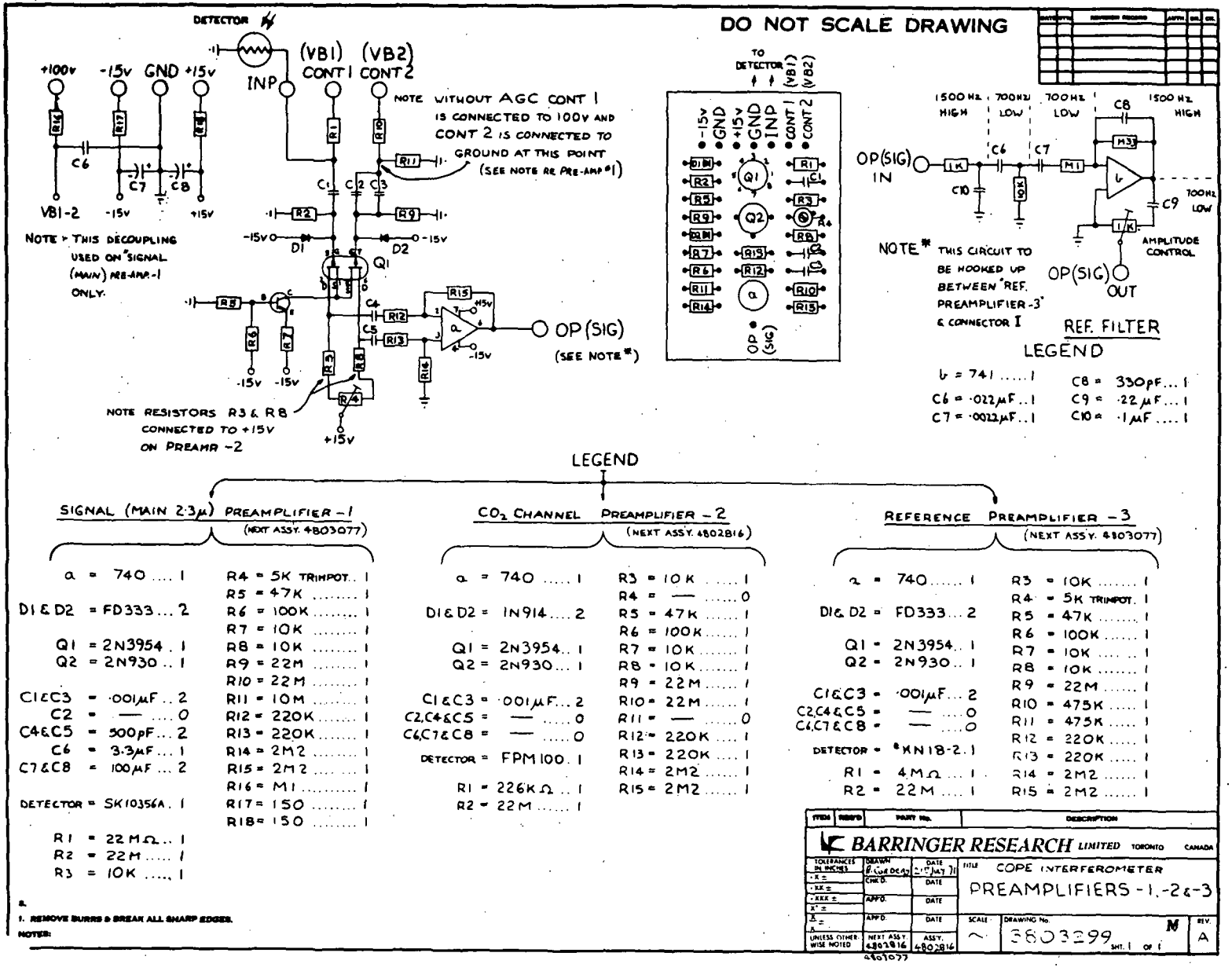

Figure C.4. Preamplifiers 1, 2, and 3

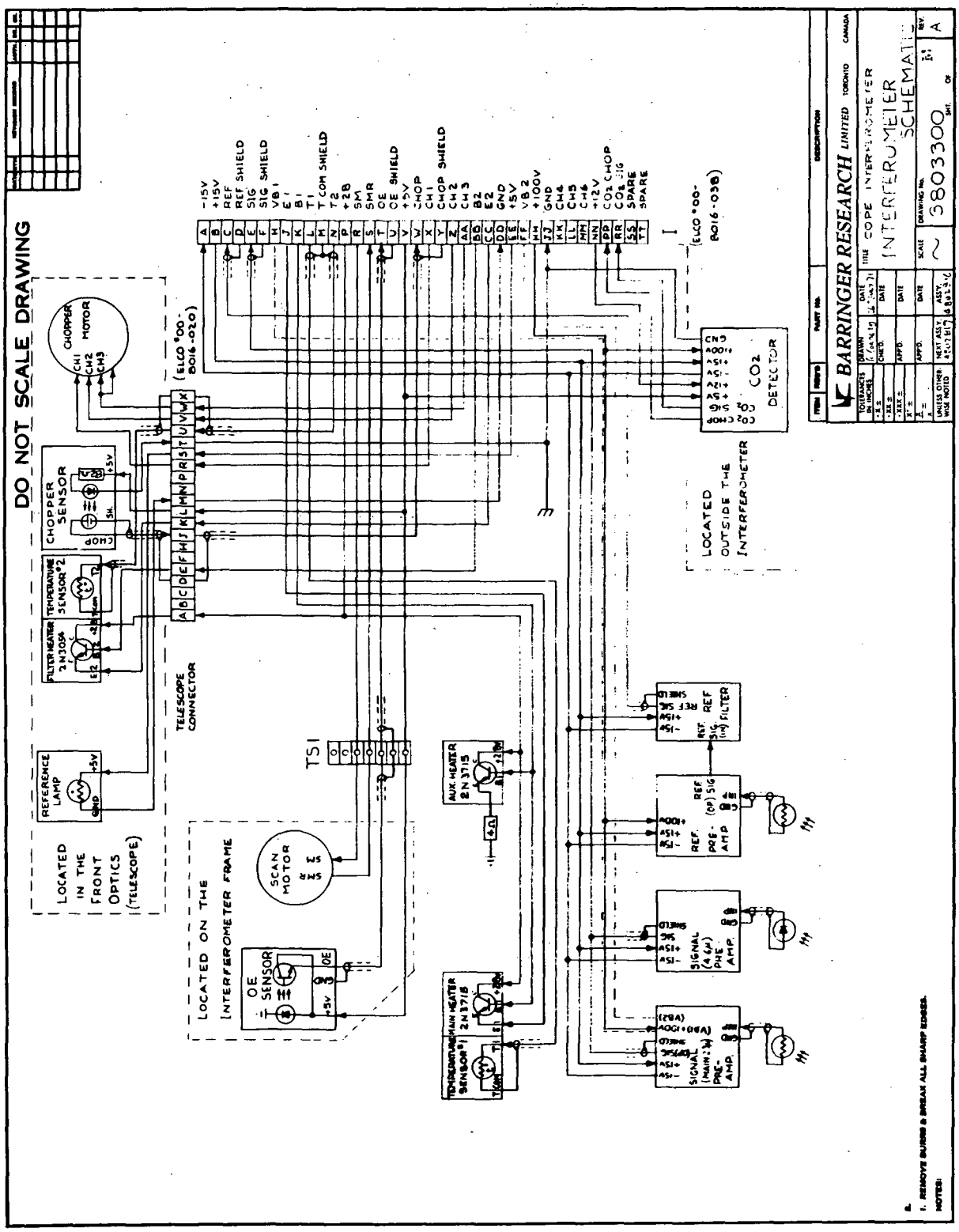

Figure C. 5. Interferometer Schematic

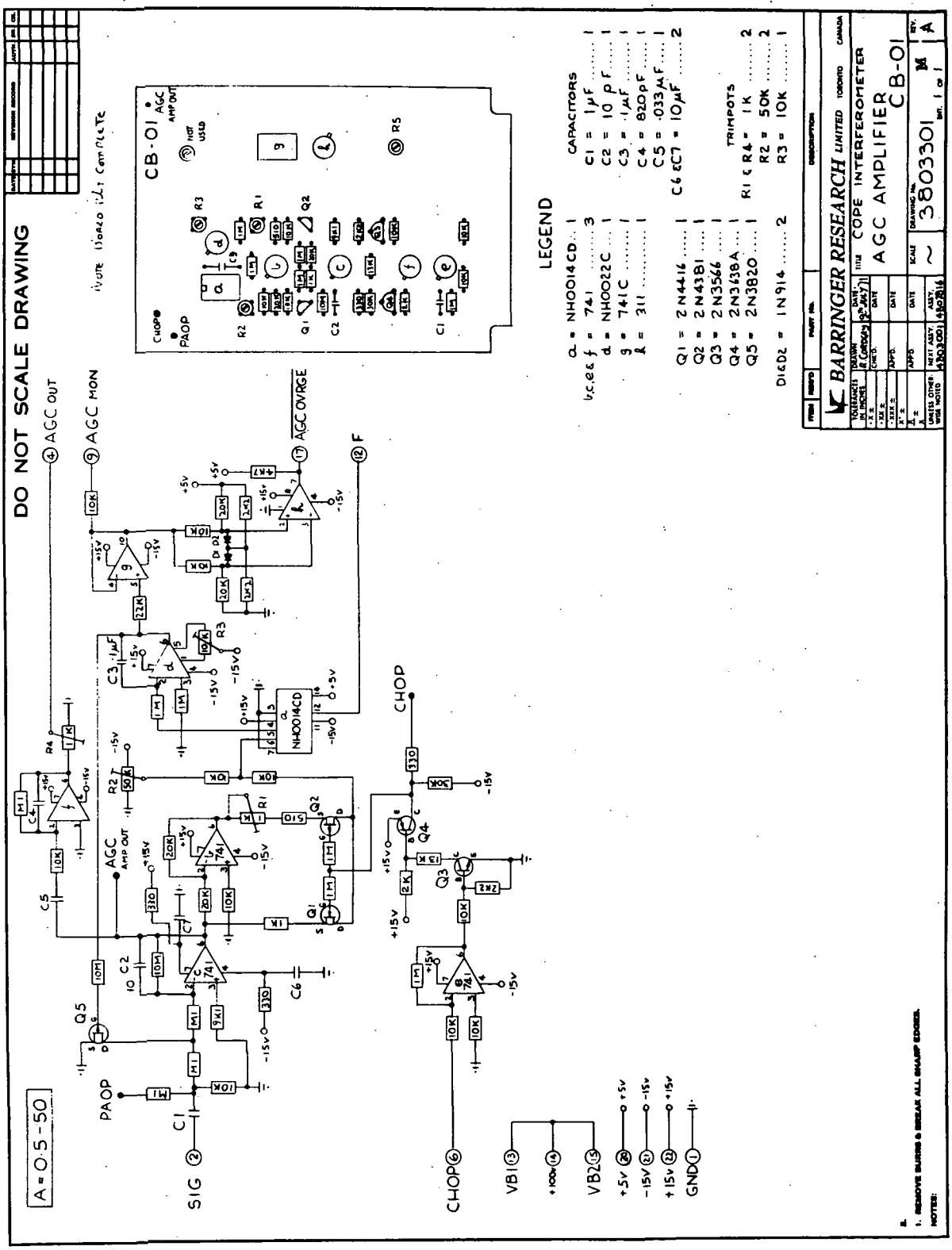

Figure C. 6. AGC Amplifier

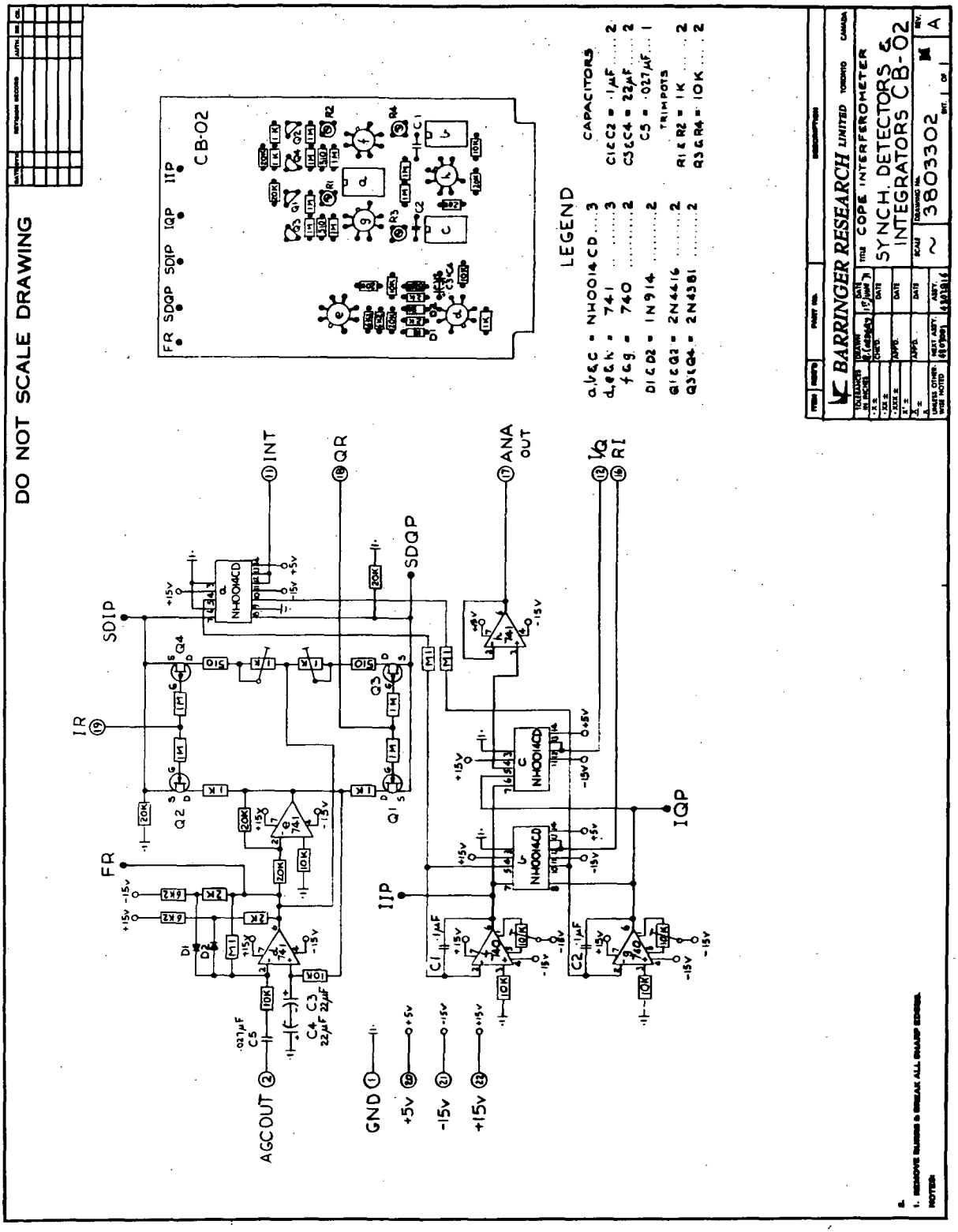

Figure C. 7. Synchronous Detectors and Integrators

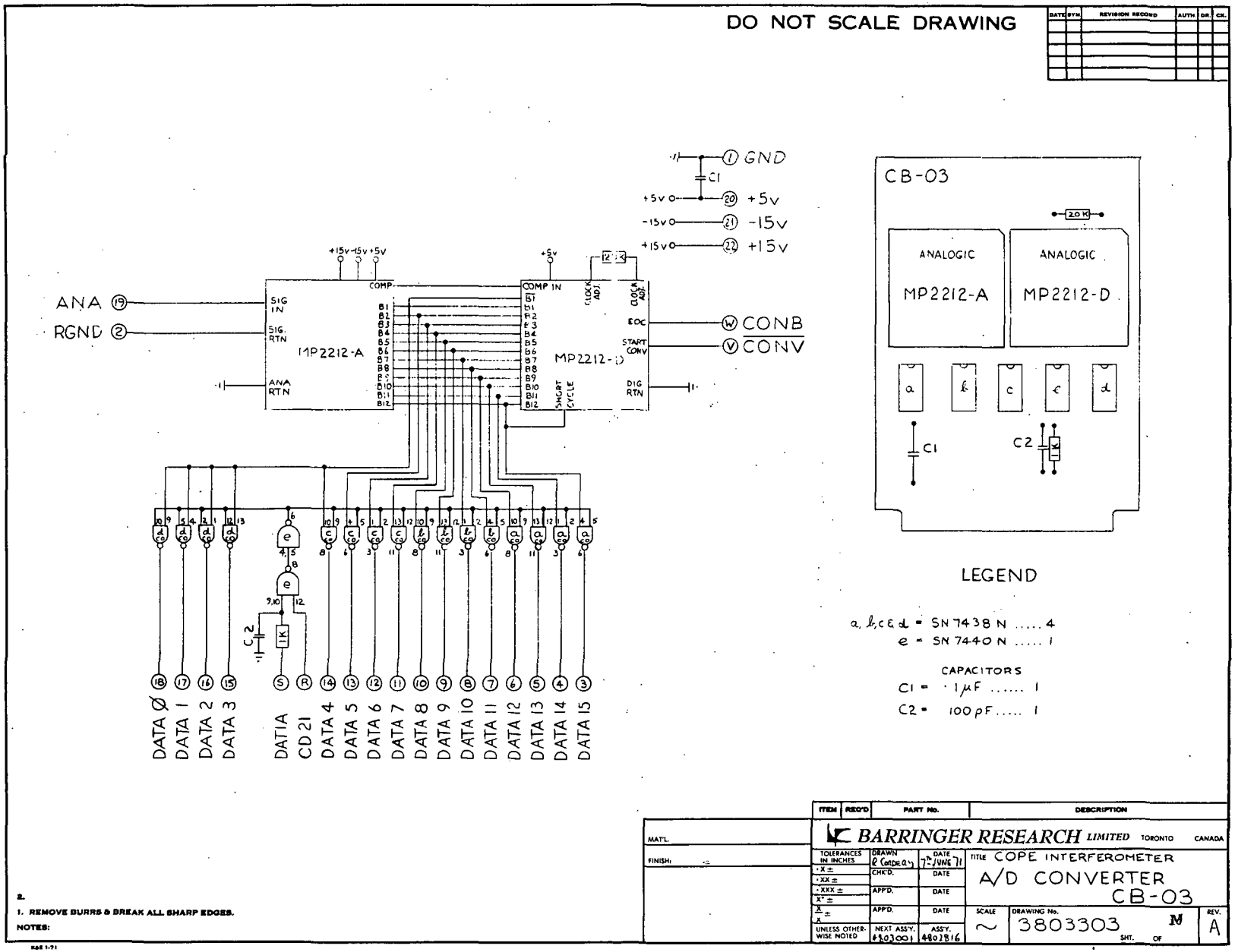

Figure C. 8. A/D Converter

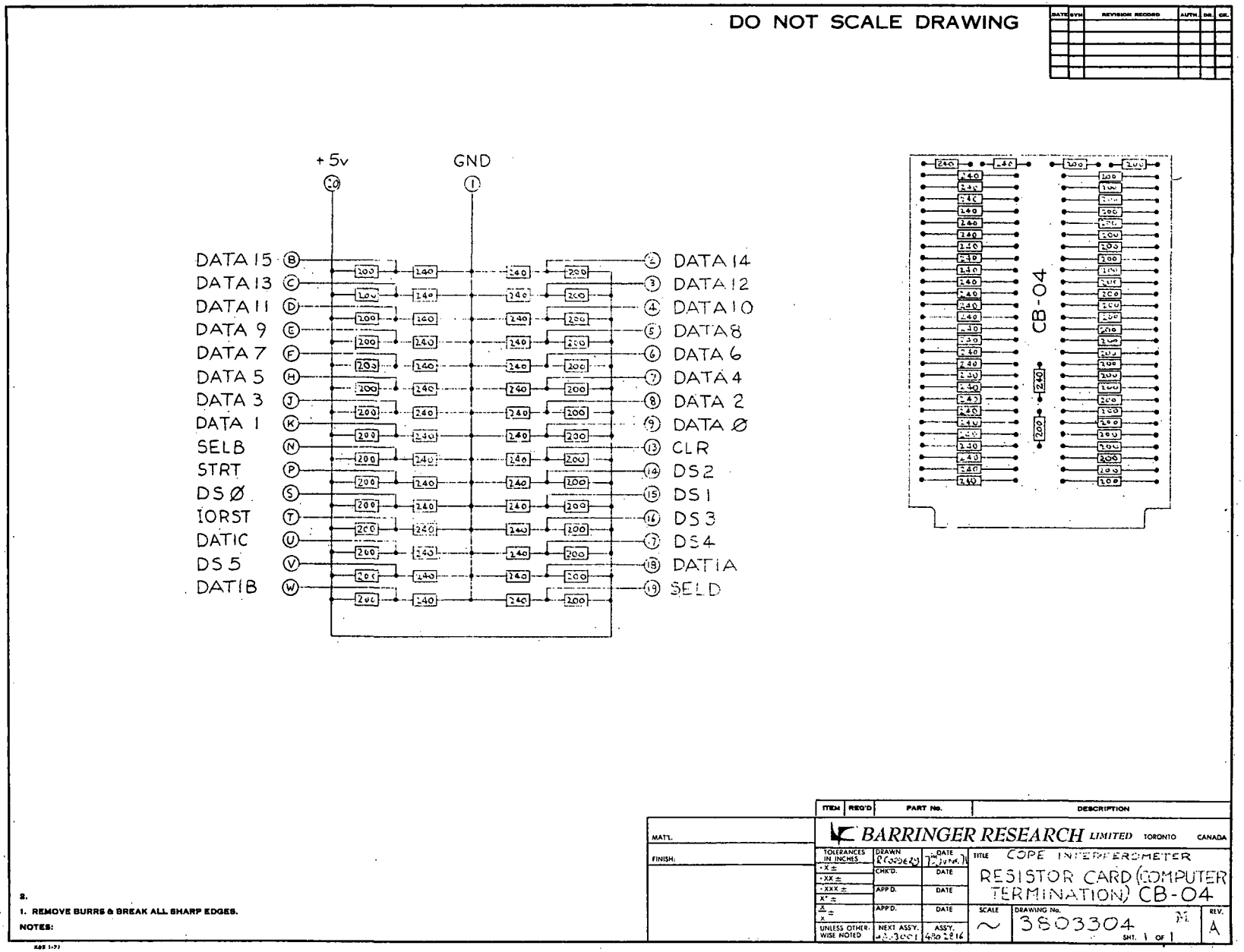

Figure C. 9. Resistor Card (Computer Termination)

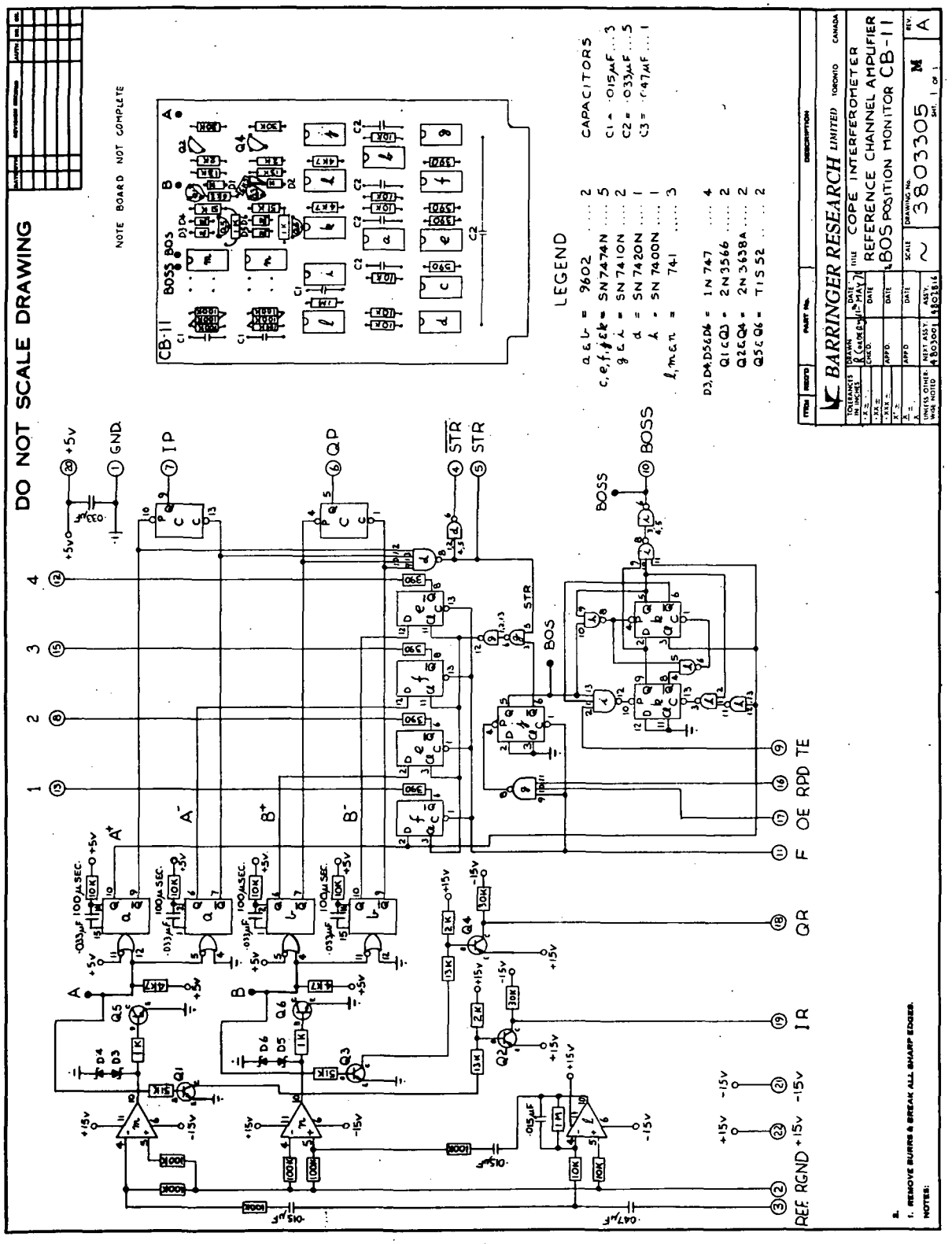

Figure C.10. Reference Channel Amplifier and BOS Position

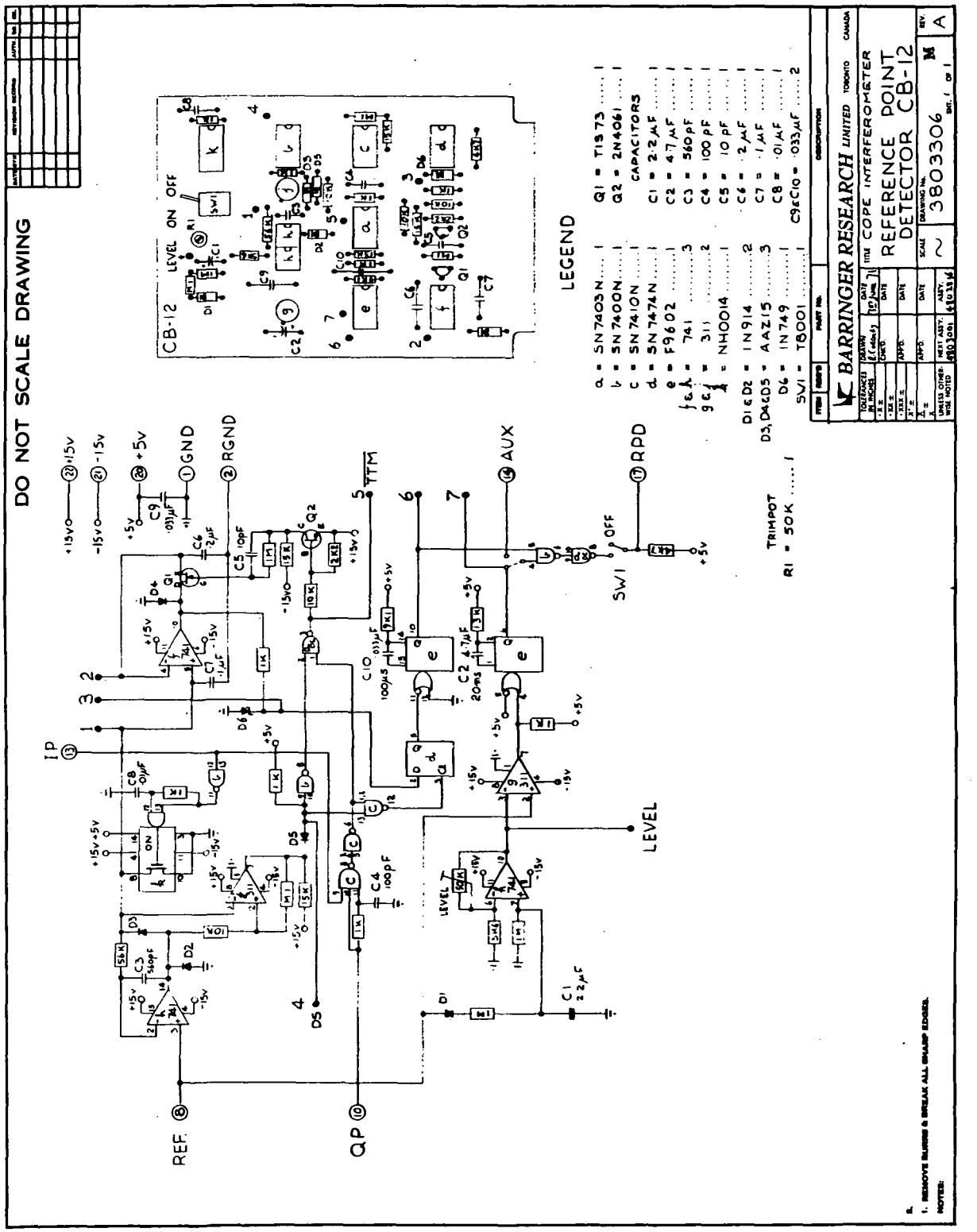

Figure C.11. Reference Point Detector

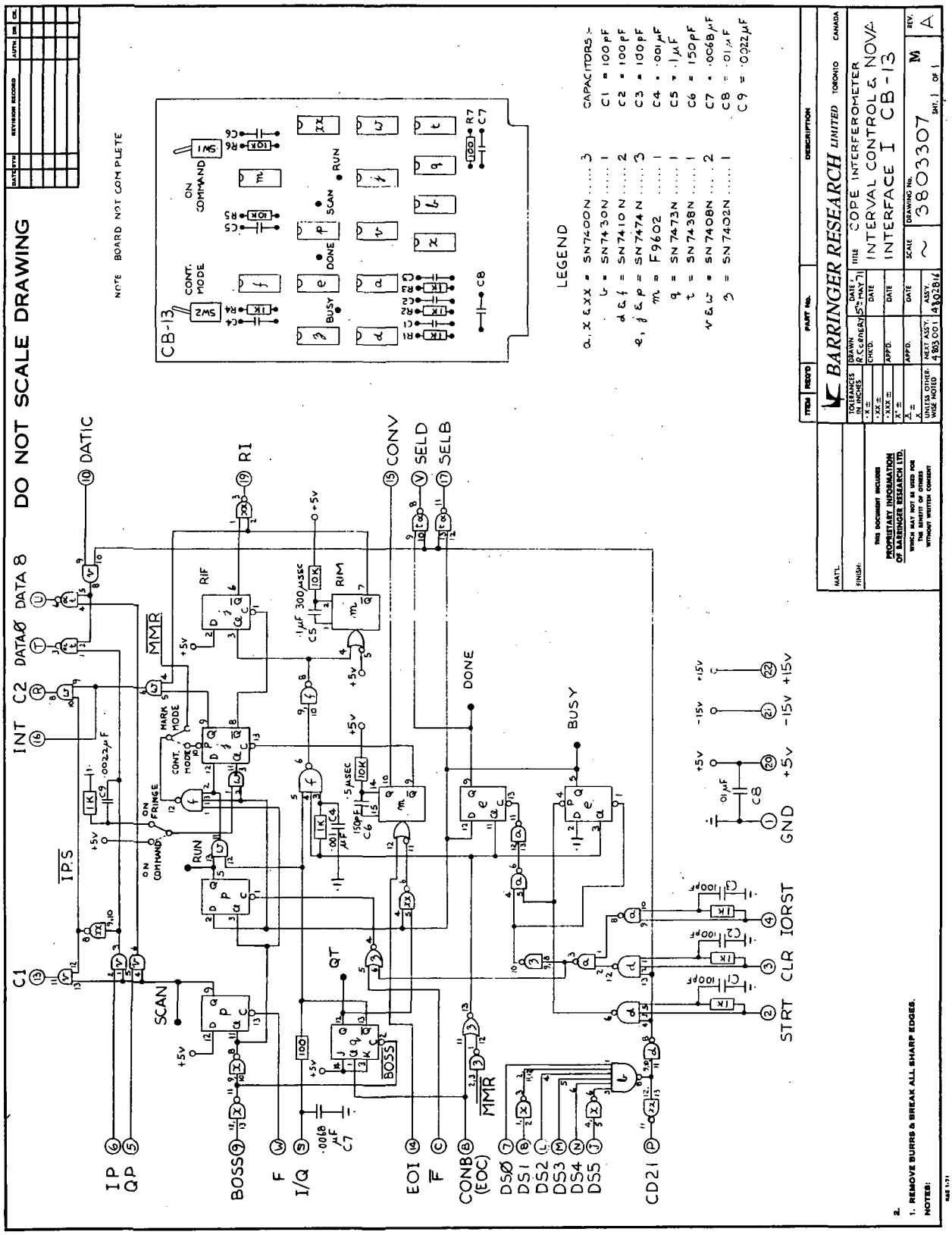

Figure C.12. Interval Control and NOVA Interface I

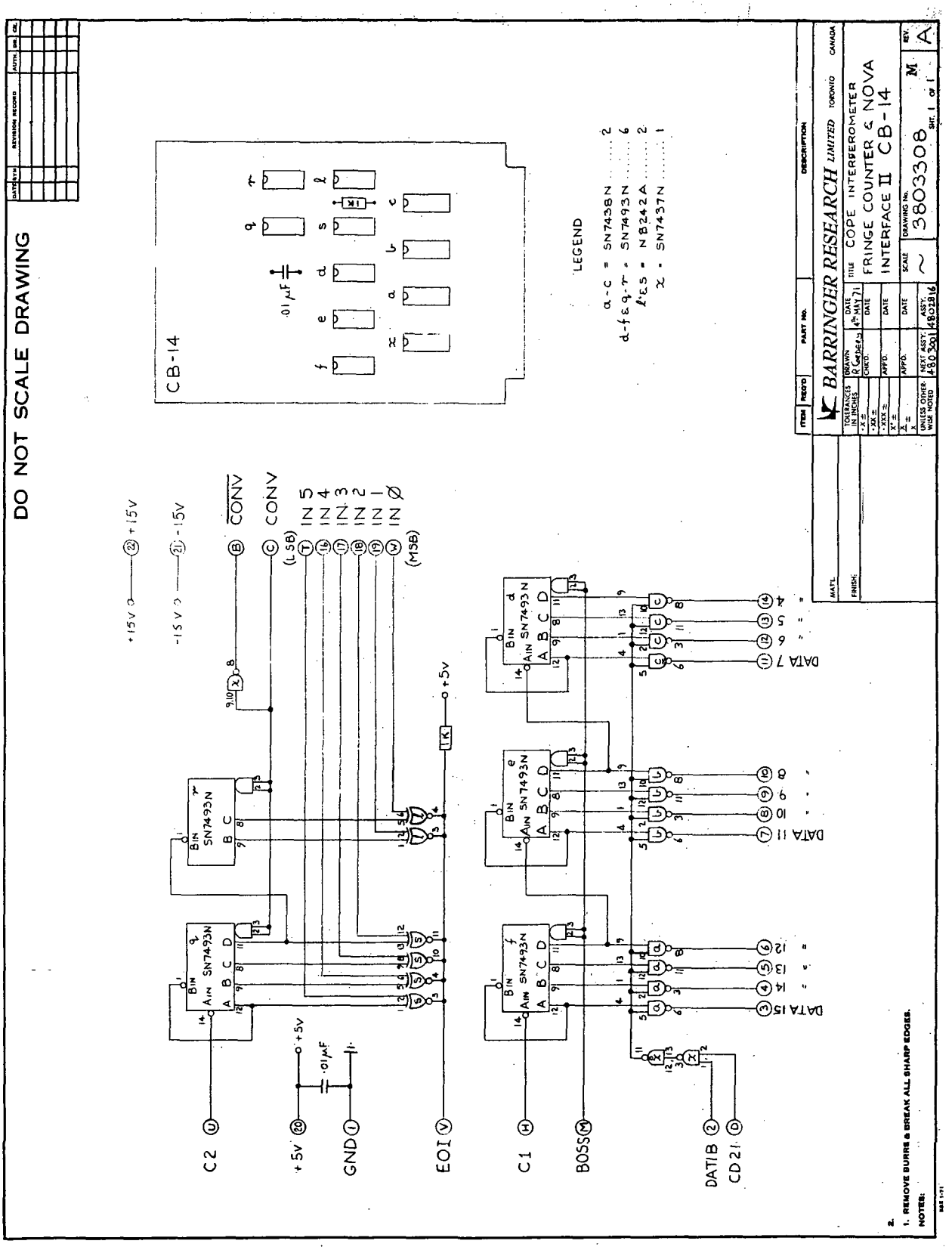

Figure C. 13. Fringe Counter and NOVA Interface II

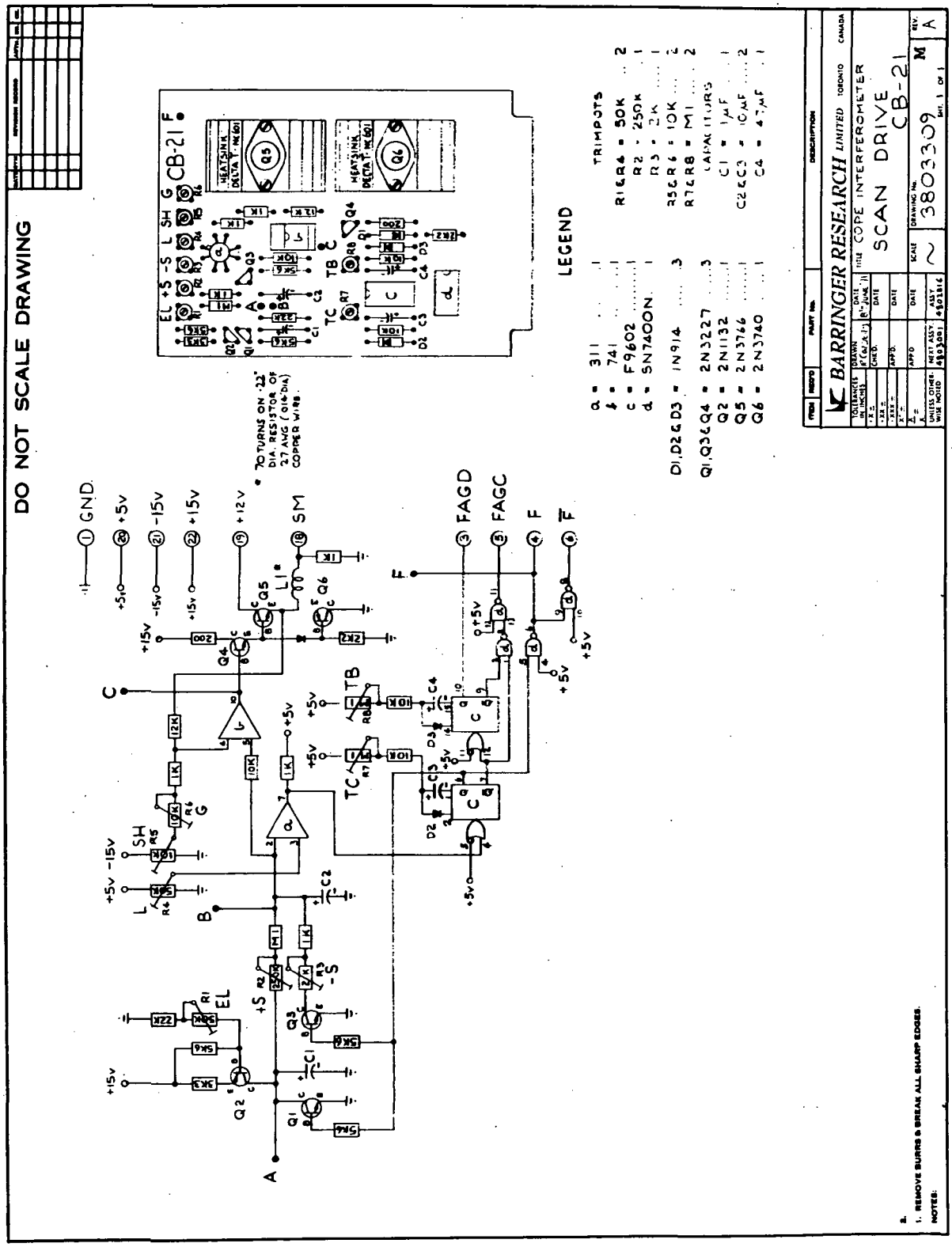

Figure C. 14. Scan Drive

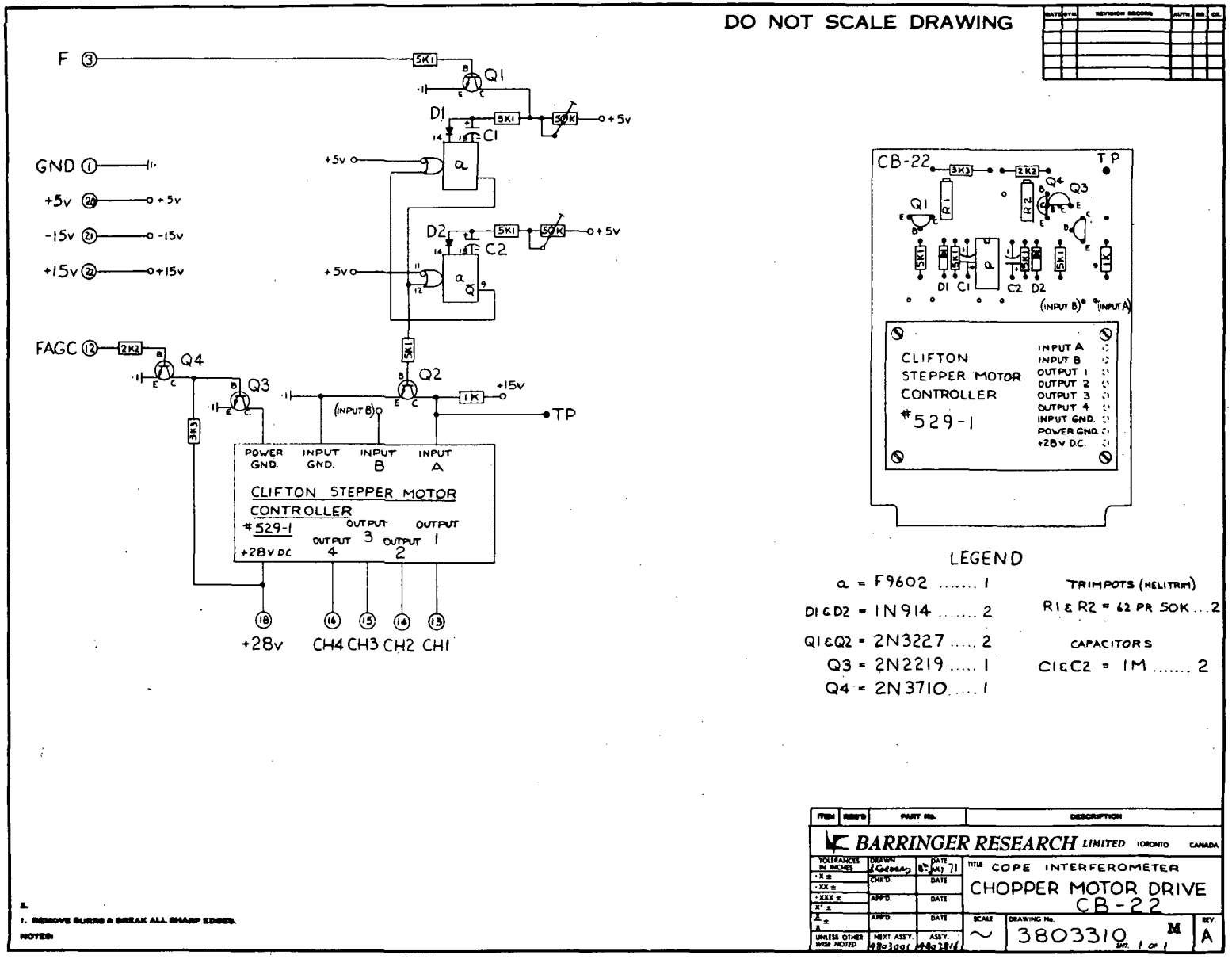

Figure C. 15. Chopper Motor Drive

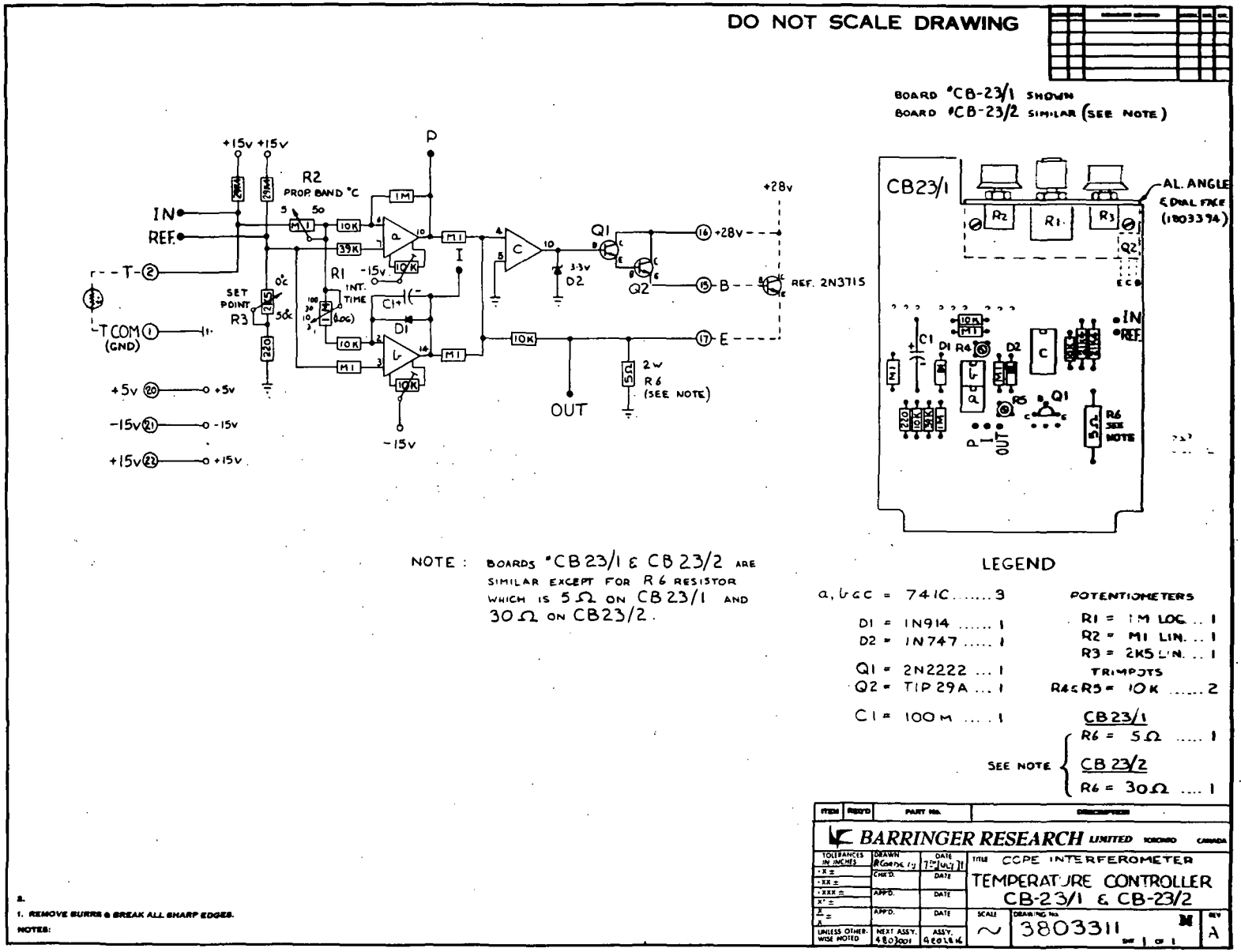

Figure C. 16. Temperature Controller

APPENDIX D

REFERENCES

1. Bortner, M. H. Alyea, F. N. ; Grenda, R. N. ; Levy, G. M. ; and Liebling, G. R. : "Analysis of the Feasibility of an Experiment to Measure Carbon Monoxide in the Atmosphere," GE Report on Contract NAS 1-10139, March 1973.

2. Bortner, M. H. ; Kummler, R. H. ; and Jaffe, L. S. ; "A Review of Carbon Monoxide Sources, Sinks, and Concentrations in the Earth's Atmosphere," NASA CR-2081, June 1972.

3. Barringer, A. R. ; "Chemical Analysis by Remote Sensing," Paper presented at Twenty-third Annual ISA Instrumentation Automation Conference (New York, N. Y.), Oct. 1968.

4. Dick, R. ; and Levy, G. : "Correlation Interferometry," AFCRL-71-0019, Paper presented at Aspen International Conference on Fourier Spectroscopy (Aspen, Colo.), 1970.

5. Grenda, R. N. ; Bortner, M. H. ; et al: "Carbon Monoxide Pollution Experiment - (1). A Solution to the Carbon Monoxide Sink Anomaly," Paper No. 71-1120, Joint Conference on Sensing of Environmental Pollutants (Palo Alto, Calif.), Nov. 1971.

6. Mertz, L. : Transformations in Optics, John Wiley and Sons, New York, N. Y. , 1965, p. 60.

7. Smith, R. A. : IEE Monograph, No. 6, Aug. 15, 1951.

8. Templin, H. A. ; Talbert, W. W. ; and Morrison, R. E. : IRIS, III, No. 4, AD305118, Univ. of Michigan, Dec. , 1958.

9. Skolnik, M. I. : Introduction to Radar Systems, McGraw Hill, New York, N. Y. , 1962, p. 20.

10. Humphreys, C. J. ; and Paul, E. : Applied Opt. 2, 691 (1963).

11. Shaw, J. H. ; and Houghton, J. T. : "Total Band Absorption of CO Near 4. 7μ," Applied Opt. , June 1964, p. 773.

12. Kostkowski, H. J. ; and Bass, A. M. : "Direct Measurement of Line Intensities and Widths in the First Overtone Band of CO," J. Quant. Spect. and Rad. Transfer 1, 177 (1961).

GENERAL ELECTRIC

Space Division / Headquarters: Valley Forge, Pennsylvania ☐ Daytona Beach, Fla. ☐ Cape Kennedy, Fla. ☐ Evendale, Ohio ☐ Huntsville, Ala. ☐ Bay St. Louis, Miss. ☐ Houston, Texas ☐ Newport Beach, Calif.